Radboud Repository

Radboud University Nijmegen

PDF hosted at the Radboud Repository of the Radboud University Nijmegen

The following full text is a publisher's version.

For additional information about this publication click this link.
http://hdl.handle.net/2066/204190

Please be advised that this information was generated on 2019-07-08 and may be subject to change.

Emergent phenomena in Weyl, nodal line and one-dimensional semimetals

Maarten van Delft

Copyright © 2019, by Maarten van Delft

Printed by Ipskamp Printing, Enschede

ISBN: 978-94-028-1495-8

A digital version of this thesis can be downloaded from http://repository.ubn.ru.nl

Emergent phenomena in Weyl, nodal line and one-dimensional semimetals

Proefschrift

ter verkrijging van de graad van doctor
aan de Radboud Universiteit Nijmegen
op gezag van de rector magnificus prof. dr. J.H.J.M. van Krieken,
volgens besluit van het college van decanen
in het openbaar te verdedigen op dinsdag 4 juni 2019,
om 16:30 uur precies

door

Maarten Ruud van Delft

geboren op 7 juni 1991
te 's-Hertogenbosch

Promotor: Prof. Dr. Nigel Hussey

Copromotoren: Dr. Steffen Wiedmann
Dr. Alix McCollam

Manuscriptcommissie:

Prof. Alexander Khajetoorians

Prof. Hae-Young Kee
University of Toronto

Dr. Suchitra Sebastian
University of Cambridge

Het werk beschreven in dit proefschrift is uitgevoerd aan de faculteit der Natuurwetenschappen, Wiskunde en Informatica van de Radboud Universiteit Nijmegen en is gefinancierd door de Nederlandse Organisatie voor Wetenschappelijk Onderzoek (NWO).

Preface

The thesis you have in your hands at the moment is quite different from what I envisioned when I started my PhD. The initial plan was to develop a focused ion beam based device for the measurement of mesoscopic single crystals, electrically at first, then thermally. To this end, many a long day during the first year of my PhD was spent in front of the FIB machine at MESA+, some times writing a too-detailed description of FIB, some times watching Southpark, while the machine did its work. This, however, did not lead to a working device until Steffen came to me one day asking if I could try to FIB this oddly shaped TaP crystal he had.

What happened with that crystal took a while to understand, but eventually lead to my first successful project, while simultaneously laying the foundations for the next project(s). For this, as well as for the fruitful and enjoyable collaboration that followed, Steffen deserves full credit. Along the same line of good collaboration, I should mention Sergio as well. We worked together for most of the magnet time I had during my PhD, and this was always a pleasure. Not only is Sergio a great guy to have around in the lab, he should also be acknowledged as a certified good friend, always taking care of the Aperol Spritz. For the TaP story, I should also mention Paul, whose XRD work was instrumental to the conclusion of this work.

The most exciting project of my PhD has definitely been the work on nodal-line semimetals. This was very much a team effort, with important contributions from within HFML coming from Thomas and Claudius, in addition to the aforementioned Sergio and Steffen. I very much enjoyed both the labwork as well as the discussions we had together. Of course, none of that would have been possible without the excellent samples provided to us by Leslie, the indispensable calculations performed by Tony or the theoretical support by Misha and Maxim. I have certainly learned a lot from each of the members of this team.

For my last project, I owe much to Ulrike. Three times I came to the MPI in Dresden for us to work together on the dilution fridge. During my first visit, she performed the experiments while I assisted; during the last visit, I ran the experiments while she remained available to help me if needed. The data may not have been entirely consistent, but the experience has still been useful. The lithium molybdate data was not the only good result from my visits to Dresden, however, and I would like to acknowledge Markus and Andy for their help with EDX. In general, the people at the MPI deserve a mention for making me feel welcome at their lab, with frequent barbecues during my first visit.

Having mentioned each of my collaborators, it is time to mention my supervisor, Nigel (as it is on the author list of a paper, the supervisor is named last). Nigel is the only other person involved with each of my three projects, and has been invaluable to each of them. You were always there to answer any of my questions and guide me in the right direction. In particular, I would like to thank you, Nigel, for always encouraging me to improve myself and my work. I will also remember you for your ability to improve the grammar, punctuation, structure and wording of any text.

Not always acknowledged, but always indispensable, is the technical staff that supports us in our experiments. In particular, I should mention Henk for teaching me how to use the FIB at MESA+ and fixing the machine whenever it had problems. Furthermore, especially in the early stages of my PhD, Peter has been a huge help. Together, we cleared out the mess in the cleanroom and set everything up for it to actually be a clean room (the fact that nearly nobody respected this is another matter).

As any person doing experiments at the HFML, I could not have done any of it without the help of Lijnis, Michel and Tom making probes and fixing problems; or without the excellent team of engineers building, maintaining and repairing the magnets; or without Hung, of course. Also, I should not forget the people who organize everything in HFML: Ine, Thera and Martin.

Naturally, my time at HFML has not solely been devoted to hard work. There has always been time to have some fun as well, in the form of the annual labtrip and barbecue, or the monthly borrels (for which I would like to extend a special thanks to all current and former members of the esteemed Borrel Committee. Despite the fact that you some times forgot to provide sufficient cola, you made a major contribution to the social life at the HFML.)

I also have good memories of the travels I made while working at HFML. First and foremost of these is, of course, Ameland. There we did the most exciting things, such as watching Lisa try to catch a rabbit, or going mud walking in a torrential downpour. There were trips to further away, more exotic places as well though, such as Hong Kong (where I developed a taste for dim sum) or Boston (where Nigel and Steffen just wanted to watch football).

Special events or travels were not required in order to have a good time, however. Every day at HFML there was time for a chat or a joke. I have had good times with my office mates Francesca, Salvo, Anderson, Jonathan, Alessandro, Rava, Maryam, Anatol, Matija, Alex and Marion. With some of you, I have shared an office for years and others just a short time, but all deserve to be mentioned. Furthermore, not just my office-mates, but also all other friends I made during my PhD (inside or outside of the lab) should be acknowledged for all the fun we had in this time, in particular my paranymphs Lisa and Michael.

Finally, I should mention the most important result of my PhD, which you will not find in any of the following chapters: my marriage to Mariana. You came all the way from Brazil to do your PhD at the HFML, and ended up making this Dutch guy very happy.

Contents

CHAPTER 1

Basic introduction

Within this thesis, a number of different material systems is discussed, with various physical phenomena being studied, such as superconductivity, Klein tunneling, magnetic breakdown and one-dimensionality. At first glance, it might appear that some of the chapters are unrelated. However, that impression would be incorrect, as there exist many connections between the different subjects. Some important connections are discussed in this introductory chapter.

As suggested by the title "Emergent phenomena in Weyl, nodal line and one-dimensional semimetals", all of the studied material systems are semimetals, which will be explained in Sec. 1.2. First, however, the concept of emergent phenomena warrants an introduction.

1.1 Emergent phenomena

No single definition exists for what is considered "emergent". In some cases, a system is emergent when it cannot be described by simply adding together its ingredients, but its properties arise from the complex behavior of the microscopic constituents. This, however, would include almost anything beyond an elementary particle. For this reason, we also require that an emergent phenomenon be novel.

We consider emergence in the context of condensed matter, as is most relevant to this thesis. Emergence is quite natural in this context, as each of the properties of a crystal arises from complex interactions between its constituents, and can never be described merely by solving the Schrödinger equation for all of these particles. Therefore, condensed matter is in general emergent. Because of the requirement of novelty, however, we do not speak of emergence when considering well-understood basic properties of crystals, but reserve this term for more complicated phenomena.

The systems in question are often strongly correlated electron systems, which can exhibit emergent phases such as superconductivity, novel magnetic states or strange metallic behavior. Another form of emergence in condensed matter is related to topology. Topological materials can often be described in terms of emergent quasiparticles.

For each of the different topics of study included in this thesis, we can see some type of emergent phenomenon. These are phenomena at the edge of our current understanding of physics, and of great interest to fundamental research.

1.2 What is a semimetal?

Within any crystalline solid, the electrons are arranged in energy bands separated by regions in which no electron orbitals exist. These forbidden regions are called band gaps and arise from the interaction of the conduction electrons with the lattice [1]. The level up to which the bands are filled with electrons is called the Fermi level (E_F). This is the level near which electrons are able to move into free states and conduct electricity.

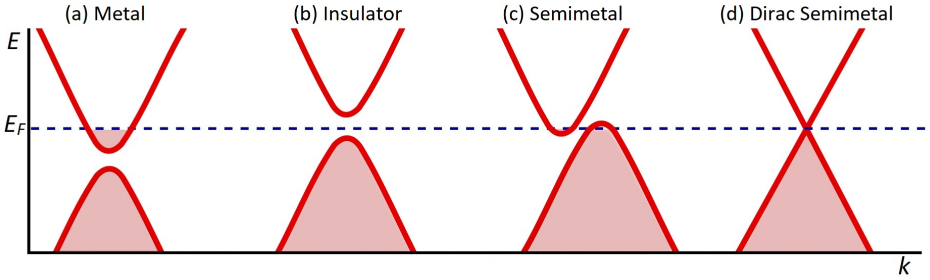

Figure 1.1: *Simplified illustration of the band structures of (a) a metal, (b) an insulator or semiconductor, (c) a semimetal and (d) a Dirac or Weyl semimetal.*

The way these bands are filled, determines the level of conductivity of the material. In a metal, one or more of the bands are partly filled and electrons can easily move (Fig. 1.1(a)). In an insulator, on the other hand, all bands are either completely filled or completely empty (Fig. 1.1(b)). In order for an electron to have freedom to move, it needs to be excited to another band, crossing the band gap. In an insulator, this band gap is so large that the electrons essentially cannot move, resulting in a very high resistance. When the band gap is small (typically less than 3 electronvolt), we speak of a semiconductor. In a semiconductor, carriers may still be thermally excited or doped into a higher band leading to a finite conductivity.

In a semimetal (Fig. 1.1(c)), there exists a small overlap in energy between the bands and they are slightly filled or slightly empty. Semimetals are distinguished by of the fact that there is a very small density of states at the Fermi level.

1.2.1 Dirac and Weyl Semimetals

Dirac and Weyl semimetals (WSM) form a subset of semimetals, whose bands disperse linearly around points (referred to as Dirac nodes) where the bands touch, as illustrated in Fig. 1.1(d). Due to the linear dispersion, the bands form cones with their apex at the Dirac nodes. These band touchings may occur in many different materials, but only have physical consequences when they occur at, or close to, the Fermi level, and only then do we consider a material to be a Dirac or Weyl semimetal. A comprehensive review of Dirac and Weyl semimetals can be found in Ref. [2].

The difference between a Dirac semimetal and a WSM, is that in a WSM either time-reversal or inversion symmetry is broken. This means that, either the system no longer maps onto itself upon reversing the direction of time, or the system is no longer the same after the operation that inverts all spatial coordinates as $(x, y, z) \rightarrow (-x, -y, -z)$. The former happens naturally in magnetic systems or can be induced with the application of a magnetic field (an example is GdPtBi [3]), the latter simply depends on the crystallographic structure of the material. Although the case of time reversal symmetry breaking is more frequently studied theoretically, it is the other case of inversion symmetry breaking that is more commonly encountered in experiments. A well known example of this case, is the family of mono-pnictides such as TaAs, NbAs, NbP and TaP [4–7].

As a consequence of the symmetry breaking, the spin degeneracy is lifted and each Dirac node splits into a pair of so-called Weyl nodes with opposite chirality. These Weyl nodes are stable against small perturbations because their chirality is conserved. This situation provides the conditions for the unusual physical effects of Weyl physics to manifest themselves.

Weyl semimetals come in two different guises, depending on the level of tilting of the cone formed by the linear dispersion around the Weyl node. In a type-I WSM, this cone has negligible tilting, such that there is a point-like Fermi surface at the node [8]. Type-II WSMs, on the other hand, posses strongly tilted cones, the node appearing at a touching point between open electron and hole pockets. In that case, tunneling between these pockets may be possible [9].

The first Weyl type-I semimetals to be identified experimentally, and those most studied to date, are included in the TaAs-family of compounds. Known type-II WSMs include for example WTe_2 [10] and MoP_2 [11]. Within this thesis, we study the type-I Weyl semimetal Tantalum Phosphide (TaP). In Chapter 5, we report the observation of superconductivity in this material.

1.2.2 Nodal line semimetals

The concept of a Dirac semimetal, with bands touching at particular points and dispersing linearly, can be extended to higher dimensions of band degeneracy. In the case of two dimensions, such that the bands are touching along a line or loop in the Brillouin zone, the material is called a nodal line semimetal (NLSM). In Fig. 1.2, we illustrate the touching of bands in a NLSM.

The topology is different in this configuration, and thus a NLSM may present properties that are distinct from those associated with Weyl semimetals (WSMs).

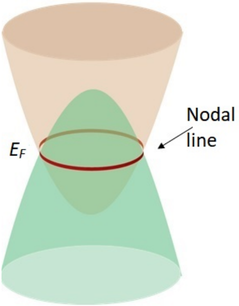

Figure 1.2: *Illustration of the band structure of a NLSM, with two bands touching along a line.*

Additionally, it is claimed that the Coulomb interaction in NLSMs may be unscreened due to the vanishing density of states near the Fermi level. Together with the metallic nature of the materials, this may lead to enhanced correlation effects that drive NLSMs towards various types of order. This is of particular interest when combined with topological features in the band structure giving rise to possible novel phenomena.

Experimentally verified material systems belonging to the class of NLSMs include $PbTaSe_2$ [12], $PtSn_4$ [13] and compounds with a general formula of WHM (W = Zr, Hf; H = Si, Ge, Sn and M = S, Se, Te) [14] that are of particular interest as they reveal a number of distinct features predominantly investigated in the Dirac NLSM ZrSiS [15]. Within this thesis, we study two of these NLSMs, belonging to the WHM compounds: Zirconium Silicon Sulphide (ZrSiS, Chapter 4) and Hafnium Silicon Sulphide (HfSiS, Chapter 3). For both of these materials, we present the results of an extensive quantum oscillation study, demonstrating Klein tunneling in momentum space and many other new physical effects.

1.2.3 $Li_{0.9}Mo_6O_{17}$ as a one-dimensional semimetal

$Li_{0.9}Mo_6O_{17}$ (see chapter 6) stands apart from the other materials discussed in this thesis, because it is not normally considered a semimetal. However, this material, which is a one-dimensional (1D) metal at higher temperatures, undergoes a transition around $T_m = 100$ K. Below this temperature, Coulomb repulsion causes more charge carriers to be destroyed, leading to a change of the Fermi surface. While the original Fermi surface is essentially composed of two flat sheets, below T_m it consists of small electron and hole pockets and resembles a semimetal.

In Chapter 6, we present low-temperature thermal and electrical conductivity measurements of $Li_{0.9}Mo_6O_{17}$. Based on these, we address the nature of the superconductivity in this material as well as its one-dimensionality.

1.3 Quantum oscillations

As mentioned previously, the Fermi level is the energy up to which all available electronic states are filled (at $T = 0$ K). Above this level, all states are empty. The intersection of this level with the electronic bands in a metal spans the Fermi Surface (FS). In a Dirac semimetal where the Fermi level intersects with a node, the FS is simply a dot. If the Fermi level is above or below the nodes, then it will have a pocket with electron or hole character, respectively. The FS is unique to any (semi)metal, and is primarily responsible for its electronic properties [16].

We study the FS through quantum oscillation measurements. Quantum Oscillations (QOs) arise because in a magnetic field, the electronic states are quantized into tubes in k-space, called Landau tubes [17]. Under the influence of the magnetic field, charge carriers then make so-called cyclotron orbits within these tubes, which are aligned with the direction of the magnetic field, $\vec{H}$. The cross-section of the tubes normal to $\vec{H}$, a, is proportional to its magnitude:

$$a = (n + \frac{1}{2})\frac{2\pi e H}{\hbar}, \tag{1.1}$$

where n is an integer.

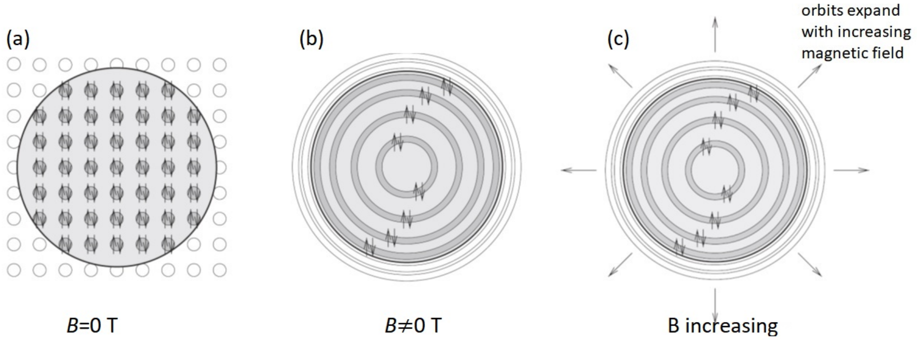

Figure 1.3: *Illustration of the origin of quantum oscillations. (a) Two-dimensional slice of an example FS with circular cross-section at zero magnetic field. Here, all states within the Fermi surface are occupied and all outside are empty. (b) When a magnetic field is turned on, the carriers make quantized circular orbits. (c) As the magnetic field is increased, so do the diameters of the orbits. When an orbit passes through the FS, it is emptied. Figure adapted from Ref. [18]*

The concept of the FS is still applicable in this situation, so any electron orbit on the Landau tubes (with a given $n = m$) is filled if it is inside the FS, and empty otherwise. Now, as the magnetic field is increased, the size of the orbit grows. Because of this, the orbit will at a certain H pass through the FS. When this happens, the orbit is depleted and the electrons in it are no longer available to the system. As we continue to increase the magnetic field, the same will happen with the next orbit ($n = m - 1$), and the next ($n = m - 2$), until $n = 0$. In this way, the occupation of electrons in the system periodically drops with a period that is regular in $1/H$. This corresponds to a frequency that is measured in tesla and proportional to the extremal cross-sectional area of the FS, A, via the Onsager relation:

$$F = \frac{\hbar A}{2\pi e}. \tag{1.2}$$

The relevant area has to be extremal (i.e. $a = A$), because this is when the tube falls completely outside the FS. As long as the tube is still partially inside the FS, its occupied length will shrink as H increases, but it is not fully depleted. For this reason, only the extremal area counts towards the oscillation frequency.

In a real material, the FS often has multiple pockets and multiple extremal areas, which lead to several different frequencies. A special case is possible when there are two pockets that are separated by only a small gap in momentum space, and the extremal orbits are in the same plane. Then, a carrier making an orbit around one of these pockets may tunnel to the other pocket. The total orbit then results in a frequency proportional to the sum of the two separate pockets if they have the same character (electron or hole), or the difference if they have opposite character. This effect is called magnetic breakdown (MB). In order for MB to be possible, a sufficiently large magnetic field is required, depending on the size of the gap between the pockets.

When the system has a nonzero temperature, the boundary between occupied and unoccupied states becomes blurred. The depletion process is then less abrupt and as a result, the oscillation amplitude is decreased [17]. The size of this reduction then depends on the level of blurring (of order $\mathrm{k}_B T$) compared to the separation between adjacent tubes ($\propto H/m^*$, where m^* is the cyclotron mass). Similarly, the Landau tubes are also being blurred by the presence of a finite relaxation time. Specifics for both of these amplitude reduction factors can be found in Appendix B. These can be used to extract important physical properties of the system.

The oscillations of the charge carrier occupation described in this section, manifest themselves in several ways in measurable properties of a material. The best known of those are the magnetic susceptibility through the de Haas–van Alphen (dHvA) effect and the electrical resistance through the Shubnikov–de Haas (SdH) effect. Both of these effects are utilized for this thesis, by way of magnetoresistance (see Sec. 2.3) and magnetic torque (see Sec. 2.6.1) measurements. By studying the different oscillation frequencies observed through these techniques, we are able to gain information about the FSs of the materials we work with.

The study of the Fermi surface through quantum oscillations is key to the chapters on ZrSiS (Chapter 4) and HfSiS (Chapter 3), but also plays an important role for TaP (see Chapter 5), where QOs are used in order to demonstrate a high degree of crystalline quality.

1.4 Superconductivity

Superconductivity (SC) is central to our experiments on the WSM TaP (Chapter 5) and an important property of the 1D material $\mathrm{Li}_{0.9}\mathrm{Mo}_6\mathrm{O}_{17}$. Furthermore, it has been predicted to occur in NLSMs as well (and under some circumstances, actually observed [19]). Considering this, an introduction of the relevant theory is in order.

A superconductor is a material that exhibits zero electrical resistance below a certain critical temperature [20]. An important aspect of SC is the exclusion of magnetic fields from the interior of the superconductor, up to a certain critical field. Above this field, the SC is suppressed. The conventional description of superconductivity is the Bardeen-Cooper-Schrieffer (BCS) theory, which states that at sufficiently low temperature, electrons may form Cooper pairs under the influence of an attractive potential, even if it is a very weak potential [21]. Contrary to single electrons, which are fermions, these Cooper pairs have bosonic properties, which means that they can occupy the same state.

An important aspect of a superconductor is the existence of a gap in the allowed energy states of the electrons, caused by the formation between Cooper pairs near the Fermi level. As the two electrons in a pair may be a relatively large distance apart and there is a large number of pairs, there is significant overlap between different pairs. This overlap results in coherence and produces the condensed state in a superconductor, leading to the above-mentioned energy gap.

In non-superconducting materials, electrons can scatter into empty states, which leads to an electrical resistance. Such scattering processes cannot happen in a superconductor, as they would require breaking up a pair. To break a pair, both of the electrons in the pair must be excited across the gap, disturbing the entire correlated system. There is no scattering process available that can provide sufficient energy to do this. As a consequence, scattering is suppressed and there is no electrical resistance.

Nothing has been said so far about the origin of the aforementioned attractive potential. Conventionally, this attraction is due to electron-phonon (e-ph) interactions. In a simplified view, they may be understood as follows: an electron moves through the lattice and attracts nearby positive ions. The lattice is slightly deformed in the process and a higher positive charge appears in the trail of the electron. A second electron is then attracted to this area and forms a pair with the first electron. This is one of the possible ways of forming a Cooper pair. Another way can be a direct interaction between electrons.

BCS theory is the simplest theory for SC and describes many systems adequately. However, there exists a plethora of superconductors that cannot be explained with BCS theory, including those that exhibit high temperature superconductivity. Discussion of alternative theories of unconventional superconductivity, however, is beyond the scope of this thesis.

References

[1] C. Kittel. *Introduction to solid state physics.* John Wiley & Sons, Inc, 8th edition, 2005.

[2] N. P. Armitage, E. J. Mele, and A. Vishwanath. *Reviews of Modern Physics*, 90(1):15001, 2018.

[3] M. Hirschberger, S. Kushwaha, Z. Wang, et al. *Nature Materials*, 15:1161–1165, 2016.

[4] S.-Y. Xu, I. Belopolski, N. Alidoust, et al. *Science*, 349(6248):613–617, 2015.

[5] S.-Y. Xu, N. Alidoust, I. Belopolski, et al. *Nature Physics*, 11:748–754, 2015.

[6] C. Shekhar, A. K. Nayak, Y. Sun, et al. *Nature Physics*, 11:645–649, 2015.

[7] S.-Y. Xu, I. Belopolski, D. S. Sanchez, et al. *Science Advances*, 1(10):e1501092, 2015.

[8] A. A. Soluyanov, D. Gresch, Z. Wang, et al. *Nature*, 527(7579):495–498, 2015.

[9] T. E. O'Brien, M. Diez, and C. W. J. Beenakker. *Physical Review Letters*, 116(236401), 2016.

[10] Y.-Y. Lv, X. Li, B.-B. Zhang, et al. *Physical Review Letters*, 118(096603), 2017.

[11] N. Kumar, Y. Sun, N. Xu, et al. *Nature Communications*, 8(1642), 2017.

[12] G. Bian, T.-R. Chang, R. Sankar, et al. *Nature communications*, 7:10556, 2016.

[13] D. Wu, J. Liao, W. Yi, et al. *Applied Physics Letters*, 108(042105), 2016.

[14] J. Hu, Y. Zhu, X. Gui, et al. *Physical Review B*, 97(155101), 2018.

[15] L. M. Schoop, M. N. Ali, C. Straßer, et al. *Nature Communications*, 7(11696), 2016.

[16] S. B. Dugdale. *Physica Scripta*, 91(053009), 2016.

[17] D. Shoenberg. *Magnetic Osillation in metals.* Cambridge University Press, 1984.

[18] C. Bergemann, A. P. Mackenzie, S. R. Julian, D. Forsythe, and E. Ohmichi. *Advances in Physics*, 52(7):639–725, 2003.

[19] L. Aggarwal, C. K. Singh, M. Aslam, et al. *ArXiv*, 1802.07993, 2018.

[20] M. Tinkham. *Introduction to superconductivity.* McGraw-Hill, Inc., 2nd edition, 1996.

[21] J. Bardeen, L. N. Cooper, and J. R. Schrieffer. *Physical Review*, 108(5):1175–1204, 1957.

CHAPTER 2

Experimental techniques

We begin this chapter with a detailed description of the Focused Ion Beam (FIB) fabrication procedure that we use for some of our samples. We describe first the whole process from preparing the sample and substrate to cutting and contacting the sample in Sec. 2.1 and then we give an overview of all the different materials that we processed with this technique, in Sec. 2.2. Additionally, we have prepared an exhaustive explanation of the FIB technique, given in Appendix A, so that this thesis may serve as a reference for future users of FIB at the High Field Magnet Laboratory.

After this, we proceed to talk about different types of measurement techniques used in this thesis, beginning with electrical resistivity measurements in Sec. 2.3, followed by thermal conductivity in Sec. 2.4. We then describe the systems used for our experiments in high magnetic fields, both steady and pulsed, in Sec. 2.5. Finally, at the end of the chapter, we mention some methods used to support our main experiments.

2.1 FIB Fabrication procedure

The fabrication process for the devices used in this work typically starts in one of two ways. In some cases, there is a small crystal (having its largest dimension less than 100 μm) that cannot be contacted conventionally using gold wires attached with silver paste. In order to measure the transport properties of such a crystal, it has to be contacted using FIB. In other cases, the starting point is a bigger piece of material. This crystal can be in such an irregular shape that it not clear how to measure its properties reliably along any particular axis. In that case, the FIB can be of assistance by shaping a small part of the crystal into a well-defined geometry, so that measurements can be performed on this piece. It is also possible that the crystal does have a well-defined shape with clear axes, but its properties may be size-dependent or difficult to measure in a large crystal. In that case, it is better to cleave a small piece off the crystal and use FIB to reduce it to the desired dimensions.

2.1.1 Preparing the substrate

Regardless of whether the sample starts out as a microscopic piece, or is cut to those dimensions, it needs to be placed on a substrate. For this, a (5x5) mm^2 piece of Si/SiO$_2$ is typically used. This substrate has large pads of gold with lines converging to a central spot in order to be able to connect the sample to measurement equipment after it has been contacted. The sample will be placed in this spot, so that only a short line of FIB-deposited Pt is necessary to connect the sample to the gold pads and no long deposition time is required. The pads in turn can be contacted with silver paste and gold wires to create connections to, for example, current sources or lock-in amplifiers.

The gold pads are fabricated by photolithography using a negative photoresist to define their geometry, followed by evaporation of 5 nm of Ti and 100 nm of Au. The photoresist layer and the excess metal are then removed in a lift-off process. After this, the substrate is ready to host a sample.

2.1.2 Preparing a microscopic sample

When working with very small crystals, either in a powder sample, such as in Fig. 2.1a, or slivers cleaved from a larger crystal, the first step is to find a sample that has a well defined geometry so that the different axes can be identified by sight. It has to be done by sight, as these samples are too small to employ a technique like X-ray crystallography to identify the axes. It is important to pay attention to this in order to ensure uniaxial current flow in any subsequent transport measurements.

Once a suitable crystal has been identified, it needs to be picked up and transferred to the substrate. The crystals are too small to use

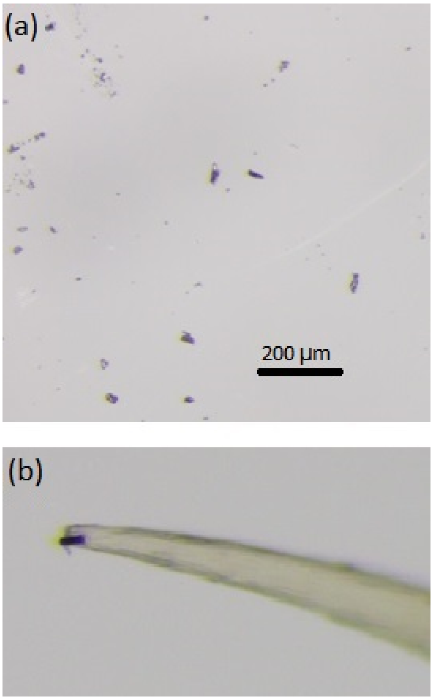

Figure 2.1: *(a) Picture of typical microsamples, in this case $PrBa_2Cu_4O_8$. From these samples, one is selected that has a well-defined geometry and no visible defects. That crystal is then picked up using the needle of a cactus. (b) Picture of a crystal sticking to a cactus needle.*

tweezers to do this, so a different method is required. Lacking an advanced micromanipulation system, it can be done using a needle from a cactus [1], see Fig. 2.1b. The tips of these needles can have a diameter of some tens of microns (depending on the species) and can be used to pick up samples. The tip is simply brought in contact with the sample and the sample sticks to it via electrostatic attraction. This method works frequently with many different kinds of crystals. Since the tips are fairly soft, they also do not damage the samples.

On the substrate, the sample should be glued down so that it remains in a stable position. Because of this, a small drop of glue has to be placed first on the position where the sample will be placed. The drop should ideally be about as large as the sample, so again the cactus needles can be useful here. Sticking a needle into a bigger drop of glue and then touching it onto the substrate will usually generate a drop of glue that is less than 100 μm in size. The sample can then be placed gently onto this drop of glue, without submerging it into the drop. It sticks much more strongly to the glue then to the needle, and once the glue has dried, the sample is ready for processing in the FIB.

The type of glue that is used is Araldite rapid. This kind of glue has a good consistency to achieve droplets of the right size and takes about 5-10 minutes to dry, which is enough time to orient and place a sample onto it. It can also survive cryogenic temperatures without problems, even when cooled down several times. Importantly, it does not cause any problems in the FIB either. Milling it or depositing platinum onto it works well, and it does not compromise the vacuum of the FIB chamber through outgassing.

2.1.3 Cutting a sample from a large crystal

When starting with an irregularly shaped crystal, such as shown in Fig. 2.2a, the first step is to determine its axes using X-ray crystallography. Then, in order to be able to align a small piece of this crystal in the right orientation, it needs to be glued onto the FIB sample holder in such a way that the right plane is exposed and faces upwards. It is important that the glue is conducting, so that all the charge generated by the FIB can dissipate without damaging the crystal or making it impossible to image or mill it. For this reason, the sample is attached to the holder (a grounded metal stub) with ample silver paste, as shown in Fig. 2.2b.

Then the FIB cutting process can begin. To cut a well defined rectangular piece of material, it is necessary to rotate the sample stage frequently in order to mill in two directions: both parallel to the sample surface and perpendicular to it. In this part of the processing, the FIB is used with an acceleration voltage of 30kV and the highest available current of 20nA to limit the amount of time it takes. Once the piece is completely detached from the main crystal (except in one point where a thin bridge of material keeps it in place) as shown in Fig. 2.2d, the micromanipulator is placed in the FIB chamber. The stage motion is restricted when the micromanipulator is in the chamber, so additional milling is difficult at this point.

The tip of the micromanipulator is then brought into contact with the (almost detached) sample. Here the different perspectives of the SEM and FIB (due to the 52° angle difference

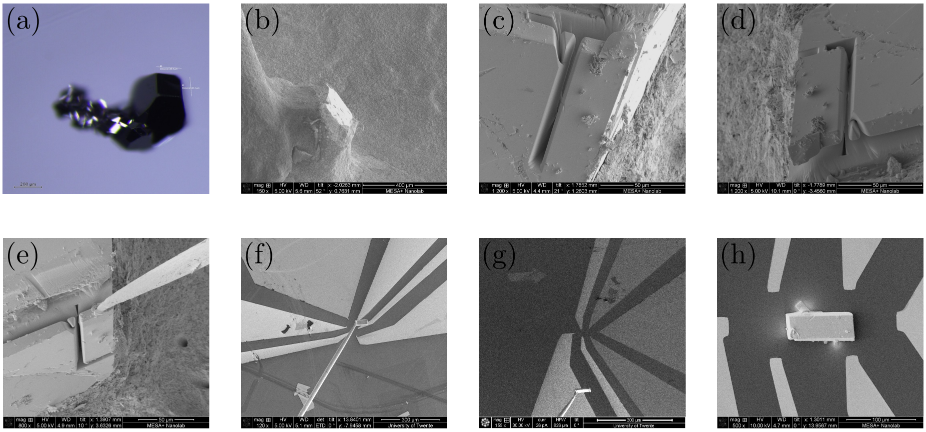

Figure 2.2: *Illustration of the different steps involved in the process of cutting a small piece from a large crystal. (a) The original crystal (the material is TaP) before FIB. (b) The crystal is attached to the FIB sample holder with ample silver paste. (c) Grooves are milled with the FIB in order to define the piece to be taken out. (d) Here the piece is only attached to the large crystal through a thin bridge. (e) The micromanipulator tip is brought into contact with the piece and attached with platinum deposition. Then the bridge is cut. (f) and (g) The piece has been lifted out of the big crystal and positioned above the substrate. The different perspective of the SEM (image (f)) and the FIB (image (g)) is nicely visible here. (h) The crystal is in position and ready for contacting.*

between them) are very useful. The SEM gives a top view, allowing the tip to be accurately positioned above the sample. The FIB additionally gives information about the height of the tip above the sample. Together, the two points of view make it possible to gently touch the sample with the tip, as shown in Fig. 2.2e. A thick layer of platinum is then deposited over the point where the tip and sample touch in order to solidly attach the two. If the sample breaks from the tip during transfer, it is usually not possible to find it again, so it is very important to deposit enough platinum for a strong connection. Once this is done, the thin bridge connecting the sample to the larger crystal can be milled through and the sample lifted out and moved to the substrate. This step is the most risky one, and samples are frequently lost when trying to place them onto the substrate. The reason for this is the fact that the micromanipulator does not allow for rotation of the sample, so that it is above the substrate with the same angle as it was in the large crystal. Placing it flat on the substrate then requires some very careful manipulation, after which the sample can be fixed onto the surface and the micromanipulator tip removed. At that point, it is ready for shaping and contacting.

2.1.4 Shaping and contacting the sample

For very anisotropic samples, the contacting is a delicate process. In order to get a reliable measurement along one particular axis, the other axes need to be electrically shorted so that the measurement is not contaminated with orthogonal voltages. This can be achieved by having the current contacts fully cover the ends of the crystal, over the whole width and height. The voltage contacts are then prepared on the sides, covering the full height of the crystal, and the current flows only along the its length. This allows a measurement of the resistivity along this axis without interference caused by currents flowing in other directions. Of course, this procedure can also be followed for samples that are not anisotropic. In that case, coverage of the contacts over the entire sample is not so crucial.

Before making contacts with the FIB, the samples first undergo some structuring. As the crystal may have a rough sidewall which is not easily accessible for deposition on the side, or it may be partially submerged in glue, the first step is to bevel the ends of the crystal so that a smooth surface is exposed. This beveling is typically done at an acceleration voltage of 30 kV and a current of 0.9-6.5 nA, with the stage tilted to 7°. Since the FIB column is positioned at 52° to the normal, this level of tilt means the ions impact the sample under a 45° angle, creating a bevel with the same angle.

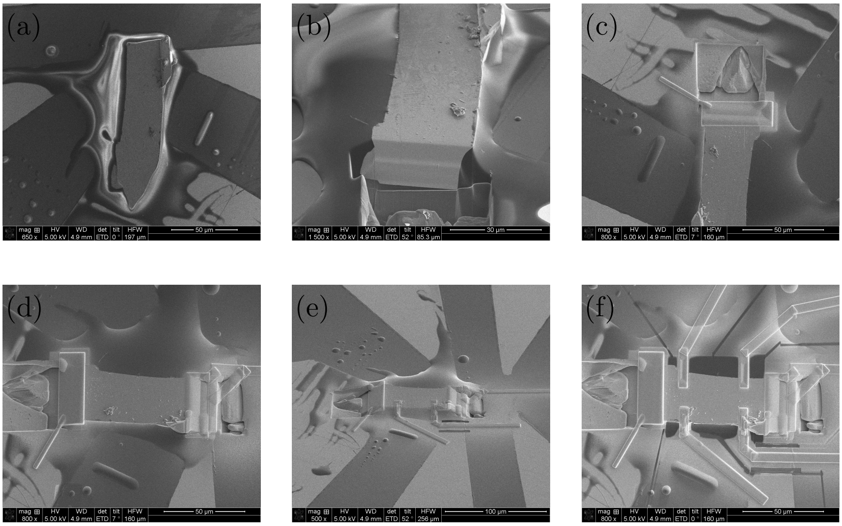

Figure 2.3: *Illustration of the different steps of the fabrication process. (a) The sample is glued to the substrate, ready to be processed. (b) The sample is (b), beveled and (c), contacted on one of the short sides. The opposite side is beveled and contacted in the same way (d), as are the contacts on the side (e). (f) The contacts are all ready and some cleanup is performed around the sample to prevent any shortcuts.*

The relatively high voltage and current will induce a damaged layer on the surface that can lead to unexpected effects depending on the material. Often, this layer is the reason for large contact resistance and it manifests itself as sudden jumps in the measured resistance as the system temperature is varied, or as an increased level of noise. In order to avoid these issues, it is important that the beveled surfaces are additionally milled at a low voltage of 8 kV with a current of about 0.2 nA, removing approximately the top 50 nm. This does not completely remove the damaged layer, but reduces its thickness and mitigates its effects. Nevertheless, for some materials this layer still has significant consequences, as will be discussed later.

The next step is to deposit the platinum for the contacts. Because damage to the sample can also occur in this step, the first 100 nm of platinum is deposited on the sample at 8 kV instead of the standard 30 kV. After this, an extra 1 μm of platinum is deposited at 30 kV creating a line between the sample and the gold contacts.

This whole procedure is executed consecutively on both ends of the crystal to create two current contacts and on smaller sections of the other sides of the crystal to make voltage contacts. In most cases, the samples are made in a standard configuration with four voltage contacts (two on each side, opposing the ones on the other side). This gives two sets of contacts to measure longitudinal voltages, and two to measure Hall voltages. Of course, the FIB contacting procedure is not limited to this configuration, but it is very versatile and allows for a nearly unlimited number of configurations.

Once the sample is prepared in the right shape with the desired number of contacts, thin lines are milled at 30 kV to a depth of about 100 nm between each of the platinum lines going to the gold pads, isolating all of the contacts, removing any electrical shortcuts created during milling and deposition processes. The top of the sample is also milled (at 8 kV) to remove any shortcut there as well. After this the sample is ready for measurement.

2.2 Materials worked on with FIB

2.2.1 Cuprates

The first compound we worked on with FIB was $PrBa_2Cu_4O_8$ (Pr124). This material is a member of the cuprate family, but does not superconduct. Pr124 is a quasi-one-dimensional metal with extremely anisotropic conductivity (ρ_a/ρ_b 1000 at 4.2 K [2, 3]) and so great care has to be taken to prepare the contacts in such a way that they cover the sides of the sample completely. We chose Pr124 as a first sample for FIB in order to demonstrate the ability to work with very anisotropic samples.

We invested a great deal of time and effort into contacting this material with FIB, trying many possible variations of different procedures. However, in all cases, the sample became insulating and no reasonable data could be obtained. During this time, we also attempted to contact another cuprate, $Bi_2Sr_2CaCu_2O_{8+x}$ (BSCCO). BSCCO is naturally superconducting, yet showed much the same behavior as the Pr124 after FIB processing.

A definite explanation for this behavior was only found after all variations of the FIB procedure were exhausted. It was revealed to us [P. J. W. Moll, private communication], that FIB contacting of cuprates is completely prohibited by the aforementioned thin damage layer that the FIB leaves behind on the sample surface. In the case of cuprates, this layer forms a strong insulator. Knowing this, we decided to terminate this project. It turns out that one way to succeed in electrically contacting to cuprate crystals is to first contact onto the pristine surfaces with silver paint and then to post-fabricate the crystals into the appropriate geometry. This technique, however, requires large crystals that can be mounted by hand.

2.2.2 SnTe

SnTe is a candidate topological crystalline insulator [4], i.e. a material that combines electronic topological properties with crystalline symmetry. We investigated it for a very different reason, namely the temperature dependence of its resistance, which is linear over a very wide temperature range [5]. Such a temperature dependence is potentially useful as a thermometer, which, with FIB, could be on the micrometer scale.

We worked on SnTe samples from two different sources. One powder sample of pure SnTe, from which we took small crystals to contact with FIB; and one 2 μm thick film of SnTe grown on a BaF_2 substrate. From the latter sample, we polished away the substrate using sandpaper and picked a piece of SnTe from the broken fragments that remained. The two types of samples showed similar results, although the transport data on the film fragment was much cleaner.

The electrical transport data obtained from the SnTe FIB samples is peculiar. Firstly, the linear temperature dependence seen in macroscopic samples is no longer there. And, secondly, the samples are showing an unexpected drop in resistance when going down to low temperature, as shown in Fig. 2.4. Applying a small magnetic field is enough to remove this drop, and the effect

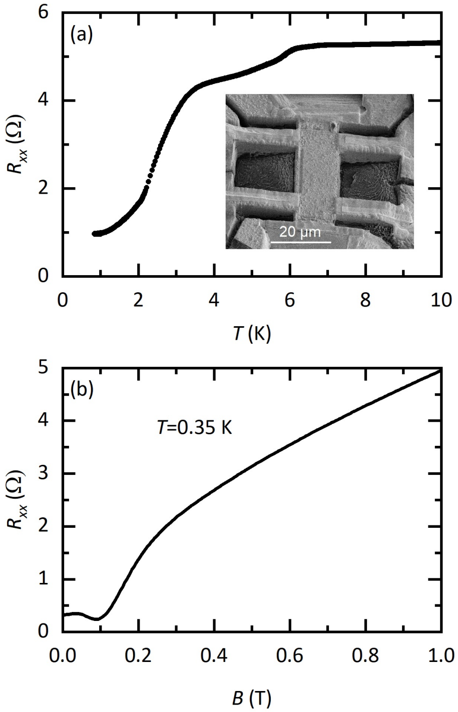

Figure 2.4: *(a) Temperature sweep of the FIB-contacted SnTe sample prepared from the polished film, showing a drop in resistance at low temperature. Inset: SEM image of the sample. (b) Field sweep up to 1 T of the same sample.*

could suggest a partial superconducting transition. Superconductivity in SnTe is not expected for these samples, but not unheard of either; it is known to occur, for example, in both self-doped [6] and in indium-doped [5, 7] samples. In our case, there is no indium present in the system and the bulk samples do not naturally show any resistance drop. A possible explanation may be doping with gallium ions implanted by the FIB.

Another unusual effect that occurs in SnTe after FIB can be seen from the inset of 2.4(a). In this SEM image, it is clear that the surface of the crystal is very rough. This was not the case before FIB processing, so it appears the surface structure of SnTe changes strongly under the influence of FIB.

2.2.3 SmB_6

For SmB_6, the FIB processing worked without additional complications. A small crystal of this material was contacted and measured in order to investigate the difference between it and macroscopic pieces and perhaps identify a signature of its topological surface states. However, no clear difference between micro- and macroscopic samples was found in the data, except for a reduction in the magnitude of the low temperature resistance plateau. This reduction may be explained by the opening of a parallel conduction channel due to the FIB processing. The results of this study were reported by Shahrokhvand *et al.* [8].

2.2.4 Topological semimetals

We also used FIB to contact a number of topological semimetals, beginning with the Weyl semimetal TaP, which will be discussed in detail in chapter 5. Aside from this, two nodal line semimetals were contacted, ZrSiS and ZrSiTe. The former is a straightforward material to work with, and the two FIB prepared samples showed very similar results to those obtained on macroscopic samples. ZrSiS is discussed in detail in chapter 4.

ZrSiTe, on the other hand, was found to be very hard to work with. This material oxidizes rapidly when exposed to air; even if a good quality contact is made with silver paste after removing the oxide layer, it degrades within minutes. As our setup does not allow for the sample to be prepared and inserted into the cryostat without coming into contact with air, this is a serious problem. One way we attempted to deal with this problem was to prepare contacts with FIB. These contacts did not degrade in air, but they did present a high resistance and failed at low temperatures. In the end, a quantum oscillation study of ZrSiTe was completed, but on a macroscopic crystal contacted using a different technique.

2.3 Resistivity measurements

2.3.1 Four-point measurements

The standard configuration for resistivity measurements throughout this thesis is the four-point configuration. For this setup, the two short ends of the typically rectangular sample are contacted and used as source and drain for the electrical current. In between these two contacts, two other contacts are made and used for voltage sensing. Separating current and voltage leads in this way eliminates the contributions of line and contact resistances to the measurements, so that in principle only the sample resistance is measured. If a Hall voltage is to be measured as well, an additional two contacts are added in line with the existing two voltage contacts, on the opposite face. This has the additional advantage that if one contact or a pair of them fails, the ones on the other face can still be used. All FIB prepared samples are made in this configuration.

For measurements, an AC current of the order of 100 μA (microsamples) or a few mA (macrosamples) is supplied by a current source at a typical frequency of several tens of Hertz. The voltage is measured with a lock-in amplifier.

2.3.2 Sample preparation

Electrical contacts to macroscopic samples can simply be defined with silver conductive paste (we use Dupont 4929). This is satisfactory in many cases, but it can be beneficial (and sometimes essential) to optimize the contacting procedure for minimal contact resistance.

In order to do this, it is important that the sample has a fresh surface to contact. This is true for all tested samples, but in particular for those prone to oxidation. When working with crystals of $Li_{0.9}Mo_6O_{17}$ or HfSiS, for example, measurements can give noisy and irreproducible results if the native oxide layer is not taken care of. For this reason, the sample needs to be cut or cleaved along the direction of interest. Polishing the sample is also possible, but not preferred, as it introduces considerable damage to the surface. For the most sensitive samples (i.e. HfSiS), the samples were prepared under a constant flow of Ar or N_2 gas to prevent new oxidation.

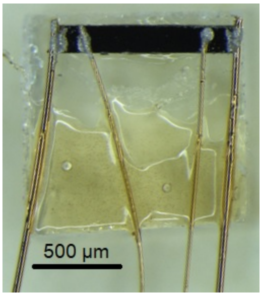

Figure 2.5: *Example of a sample (in this case ZrSiS) prepared for minimal contact resistance.*

After this, a masking layer is defined directly on the sample. This is done with silver paste, which is used to cover those parts of the crystal that should *not* be contacted. Then, the sample is placed in the vacuum chamber of the evaporator system and 10 nm of Ti (ZrSiS and HfSS) or Cr ($Li_{0.9}Mo_6O_{17}$) and 50 nm of Au are evaporated onto the sample. Subsequently, the silver paste is dissolved with acetone and only the evaporated metal remains. The contact resistances are now typically less than 10 Ω.

Finally, Au wires can be attached directly to the Au strips with a drop of silver paste. If the sample is being prepared for use in a pulsed field, we still need to take a great deal of care in this phase. First of all, the sample itself needs to be well fixed with GE varnish. The same applies to the wires; their ends are of course stuck to the sample, but also away from the ends; nothing should be able to move. Any movement, of sample or wire, can degrade the quality of a measurement. The position in which the wires are glued also matters. Specifically, the voltage wires should have as little area between them as possible, in order to minimize induction voltages under the influence of the rapid field change.

To reduce eddy currents, the minimal amount of conductive material should be used for the contacts. It is also better to use thinner Au wires for this reason. The minimum for that is set by the need for thermalization, however, since cryogenic temperatures as low as 0.3 K are often required. With two of the four wires being at least 50 μm in diameter, there can be enough conduction of heat away from the sample to cool it down to base temperature. The other two wires may be as small as 25 μm.

2.3.3 Differential resistance

For superconductors, it can be useful to measure differential resistance in order to determine the critical current and its evolution with temperature and magnetic field, as is done for TaP in chapter 5. To do this, the standard setup for resistivity measurements has to be expanded with a source of DC current. For this purpose, we employed a voltage source in series with a resistor (10 or 100 kΩ). The voltage is then swept between negative and positive voltages, thereby varying the bias current on the sample. At the same time, a 10 μA AC current is supplied to the sample by a lock-in amplifier in series with a resistor. The same lock-in amplifier is used to record the AC voltage on the sample, which is the differential resistance dV/dI. In parallel, a multimeter measures the DC voltage in order to make an IV-curve.

2.4 Thermal conductivity

2.4.1 The setup

Measurements of thermal conductivity of $\mathrm{Li_{0.9}Mo_6O_{17}}$ were done at the Max Planck Institute for Chemical Physics of Solids (MPI CPFS) in Dresden, Germany (the results are described in chapter 6). At the MPI CPFS, there is a dedicated dilution refrigerator setup for thermal transport experiments at very low temperatures (described in detail in the PhD thesis of S. Hartmann [9]). This setup has an operational range of about 40 mK to 7 K, in magnetic fields up to 8 T.

For the experiments, the sample is prepared with Cr/Au contacts as described earlier. One end of the sample is then covered in silver paint and clamped onto the cold finger by means of a screw and a specially designed washer (as shown in Fig. 2.6). A 50 μm gold wire, leading to a platform with a heater, is connected to the other end of the sample by means of silver paint. This platform is conducting and can be connected to a current source in order to perform electrical measurements. On top of the platform, but electrically isolated from it, a resistive heater is mounted that can be used to heat up one end of the sample.

Two platforms with thermometers are connected to the two intermediate contacts on the sample, in the same way as the heater platform. For electrical measurements, these platforms are used for voltage sensing. This setup allows for measurement of both conductivities with the exact same geometry, thus creating the ideal circumstances for checking the Wiedemann-Franz law, which relates the ratio between the two to a constant and the temperature. In this way, when taking the ratio of the thermal and electrical conductivities, any errors arising from geometrical factors are minimized.

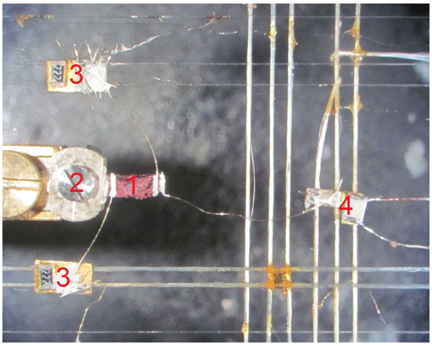

Figure 2.6: *Picture of a sample of* $Li_{0.9}Mo_6O_{17}$ *mounted onto the sample holder of the low-T thermal conductivity setup. Marked in the picture are: 1, the sample; 2, the clamp fixing the sample in place; 3, thermometer platforms and 4, the heater platform.*

For the measurement of thermal conductivity κ, it is assumed that thermal energy from the heater flows uniformly through the sample along its long axis to the heat sink, which maintains a constant temperature. A steady-state temperature gradient then develops along the sample and can be measured with the two thermometers, separated by a known distance. From this, it is possible to determine κ as

$$\kappa = \frac{L}{A}\frac{\dot{Q}}{\Delta T}, \tag{2.1}$$

where L is the distance between the contacts on the samples, A the cross-sectional area, $\dot{Q}$ the heat power injected into the sample, and ΔT the difference between the temperatures recorded by the hot and cold thermometers.

In order to ensure that as much as possible of the thermal energy produced by the heater actually goes through the sample, the setup is optimized to reduce heat losses. Since the measurements take place below 100 K, losses due to thermal radiation can be safely neglected. Losses due to thermal conduction are minimized by working under high vacuum conditions and by an appropriate choice of materials in the design of the sample holder.

The platforms of the heater and thermometers are suspended by nylon threads in a frame of Vespel, both materials having extremely low thermal conductivities. Electrical connections to the heater and thermometers themselves are made with NbTi wires, which are superconducting in the temperature range of the experiment. It is known that superconductors exhibit a very low thermal conductivity well below T_c, which helps to isolate the platforms thermally. Conduction from the platform is further reduced by the fact that the superconductivity renders it necessary to use only two wires to connect the thermometers instead of four. With these considerations, it is ensured that effectively all of the heat produced by the heater flows through the sample into the heat sink.

2.4.2 Measurement procedure

For a successful experiment, it is crucial that the thermometers attached to the samples give an accurate reading of the temperature. For this reason, they are calibrated against a thermometer on the cold finger during every measurement run. The cold finger thermometer itself is well calibrated in the range of 20 mK $\leq$ T $\leq$ 10 K. The measurement procedure is then as follows.

The temperature of the setup, measured at the cold finger, is stabilized to a chosen value using the setup heater on the mixing chamber. Once the temperature at the cold finger is stable, it is expected to be the same for the whole setup, because of the good thermal contact between cold finger, sample and sample thermometers. All the temperatures are then recorded after which a current is applied to the sample heater and a temperature gradient is established. The temperatures are again stabilized and recorded. This is repeated for several increasing values of the sample heater current after which the cold finger is heated to the next temperature using the setup heater, with zero current applied to the sample heater. At this point, the procedure repeats itself.

The data points taken at zero sample heater current are used to calibrate the hot and cold thermometers, while the other points give data relevant to the sample. The thermal conductivity is then calculated with Eq. 2.1.

Typically, a very large number of data points is generated for each data set. Some of these have to be thrown away, because the temperature gradient was not large enough or because the calibration does not work well in some temperature range. The remaining points are averaged over at least two datasets per temperature range to produce reliable data.

2.5 High magnetic fields

2.5.1 High Field Magnet Laboratory (HFML)

The bulk of the measurements discussed in this thesis were performed at the High Field Magnet Laboratory (HFML) in Nijmegen, using several of the available high field Bitter magnets. These magnets are built up of multiple coils, each consisting of stacked plates made of an alloy of Cu and Ag. A total of up to 40 kA can be passed through these coils to generate magnetic fields up to a maximum of between 33 and 38 T. A great deal of heat is produced in this process, and so the magnets need to be cooled in order to prevent them from melting down. For this reason, 140 liters of cool water is pumped through the magnets during every second of operation.

The water heats up significantly during its short passage through the magnet. For this reason, the time that the magnet can remain in operation is limited. A sizable buffer of cold water is present at the HFML, but some hours at high fields can warm up even this large volume of water. At that point, the magnet needs to be shut down and the water re-cooled.

Inside each magnet, there is a bore 32 mm in diameter that can be used to perform the experiment. This space is further reduced by the insertion of a ^{4}He cryostat, which should not touch the magnet at any point, in order to minimize vibrations. Inside this cryostat, either a ^{3}He system, for measurements down to 0.3 K, or a flow cryostat, for good temperature control between 1.4 and 300 K, is placed. The sample is then attached at the end of a long stick with a rotatable head and wires going from the top down to the sample. This stick is inserted into the cryostat.

For measurements at fields up 16 T, a superconducting magnet was also used. Control of the sample temperature and measurements work in the same way for this magnet as for the Bitter magnets. Operation of the magnet itself, is however much simpler.

2.5.2 Pulsed magnetic fields

For measurements at even higher magnetic fields than 38 T, a pulsed field facility is needed. Such measurements were done for this thesis on HfSiS and ZrSiS (see Sec. 4.5), at the Laboratoire National des Champs Magnétiques Intenses in Toulouse, France. Pulsed magnetic fields up to nearly 100 T can be generated at this laboratory, but for our project no more than 66 T was used.

Pulsed magnets work quite differently from Bitter magnets. A current is passed through the coils of these magnets for only a few hundred ms, as the capacitor banks are discharged into the magnet. The maximum field is reached once the capacitors are fully discharged, after which the field decays. The decay time is slower than the discharge time, and so this part of the pulse provides more time for a measurement and thus generates the best data. Nevertheless, the time at high field is still limited to tens of ms, approximately once per hour. In between pulses, the heat generated inside the magnet, which is placed in a liquid N_2 bath, needs to be dissipated and the bath needs to be refilled.

The pulsed field magnet is a far more demanding environment for the sample than the Bitter magnet, due to the very large dB/dt. This can cause an induced EMF that is much larger than that induced in a Bitter magnet. This is the reason that special care needs to be taken when preparing the samples, as discussed in Sec. 2.3.2.

2.6 Other techniques

2.6.1 Torque magnetometry

Torque magnetometry is a sensitive probe to study the magnetic properties of a material. It measures a torque, $\vec{\tau}$ acting on the magnetic moment, $\vec{m}$, of a sample due to a magnetic field, according to:

$$\vec{\tau} = \vec{\nabla}(\vec{m} \cdot \vec{B}) \times \vec{d} + \vec{m} \times \vec{B}. \tag{2.2}$$

For this technique, the sample is mounted on a cantilever and the deflection of this cantilever is determined from a capacitance measurement. The measured quantity is not a direct measure of the magnetization of the sample, but it can be used to study, for example, phase transitions or quantum oscillations.

We use torque magnetometry for the latter, measurements of quantum oscillations or the so-called de Haas-van Alphen effect. This is used to complement our data on the quantum oscillations (Shubnikov-de Haas effect) in our electrical transport measurements of ZrSiS (described in chapter 4).

2.6.2 Energy-dispersive X-ray spectroscopy (EDX)

Energy-dispersive X-ray spectroscopy (EDX) is a technique that is used for elemental analysis of materials. A beam of electrons is focused onto a sample, stimulating the emission of X-rays. The energies of the X-rays are measured and, since they are characteristic for each element, can be used to find which elements are present inside the material. The quantities of each element can in principle also be determined, but to do this with any reasonable degree of accuracy adds considerable complication to the measurement.

The primary requirement for an accurate quantitative measurement, is a pure reference sample of the material under study, with a well known composition. The sample that is to be investigated then needs to be measured together with the reference, so that it can be compared to it. It is important that both crystals then present a flat face to the electron beam, such that the beam is perpendicular to the surface. Any discrepancies remaining in the angle between the electron beam and the crystal can result in errors in the measurement. Only if the angle is small, is it possible to correct for it by measuring each crystal twice with a 180° in-plane rotation in between and averaging the two measurements.

For this thesis, EDX was used for compositional analysis of TaP (see chapter 5). The EDX equipment that we used, is installed inside a FIB/SEM machine at the Max Planck Institute for Chemical Physics of Solids in Dresden.

2.6.3 X-Ray Diffraction (XRD)

X-Ray Diffraction (XRD) is used to determine the orientation of the axes of a crystal as well as the crystallographic structure. We use the former to decide along which direction to cut or measure samples and the latter to gain direct information about the materials. XRD works by illuminating the crystal with a focused beam of X-rays under different orientations. The resulting diffraction patterns can be measured and a three-dimensional real-space model of the electron density can be calculated from this using Fourier transforms. From this model, the positions of the atoms within the unit cell can also be derived.

For the work described in this thesis, XRD was mainly employed for the TaP project (see chapter 5). The reflections were measured on a Bruker D8 Quest diffractometer with a sealed tube and a Triumph monochromator ($\lambda = 0.71073$ Å). The unit cell was found using the software CELL_ NOW [10]. Other XRD work was done to characterize single crystals of ZrSiS and HfSiS, using a Bruker Apex II x-ray diffractometer.

2.6.4 Density Functional Theory (DFT)

Density functional theory (DFT) is a computational method that can be used to investigate the electronic structure of many-body systems, for example in condensed matter. This theory uses functionals of the electron density to determine the properties of the system

Specifically, for this thesis, calculations were performed by Prof. Carrington (University of Bristol, UK) for ZrSiS (chapter 4) and HfSiS (chapter 3) using a full-potential linearized augmented plane-wave plus local orbital method as implemented in the Wien2K package [11]. The experimental structure was used along with the PBE-GGA exchange correlation potential [12]. The spin-orbit interaction was included using a second variational method [11]. The calculation was converged with 10^4 k-points in the full Brillouin zone. For rendering of the Fermi surface, the energy eigenvalues were evaluated on a much denser grid of 4-25 $\times$ 10^6 k-points in order to minimize interpolation errors which become severe when the Fermi level approaches the nodal line.

References

[1] P. J. W. Moll. *The role of anisotropy in iron-pnictides addressed by focused ion beam sample fabrication.* Phd thesis, ETH Zurich, 2012.

[2] N. E. Hussey, M. N. McBrien, L. Balicas, et al. *Physical Review Letters*, 89(086601), 2002.

[3] M. N. McBrien, N. E. Hussey, P. J. Meeson, S. Horii, and H. Ikuta. *Journal of the Physical Society of Japan*, 71(3):701–704, 2002.

[4] T. H. Hsieh, H. Lin, J. Liu, et al. *Nature Communications*, 3:982, 2012.

[5] G. Balakrishnan, L. Bawden, S. Cavendish, and M. R. Lees. *Physical Review B*, 87(140507(R)), 2013.

[6] J. K. Hulm, C. K. Jones, D. W. Deis, H. A. Fairbank, and P. A. Lawless. *Physical Review*, 169(2):388–394, 1968.

[7] A. S. Erickson, J. H. Chu, M. F. Toney, T. H. Geballe, and I. R. Fisher. *Physical Review B*, 79(024520), 2009.

[8] M. Shahrokhvand, S. Pezzini, M. R. Van Delft, et al. *Physical Review B*, 96(205125), 2017.

[9] S. Hartmann. *Thermoelectric Transport in Correlated Electron Systems*. Phd thesis, Technischen Universität Dresden, 2009.

[10] G. M. Sheldrick. *CELL_NOW*. Georg-August-Universität Göttingen, Germany, 2008.

[11] P. Blaha, K. Schwarz, G. K. H. Madsen, et al. *WIEN2k*. Technische Universität Wien, Austria, 2018.

[12] J. P. Perdew, K. Burke, and M. Ernzerhof. *Physical Review Letters*, 77(18):3865–3868, 1996.

CHAPTER 3

Electron-hole tunneling revealed by quantum oscillations in the nodal-line semimetal HfSiS

3.1 Introduction

Within the wider family of topological semimetals, there exist many branches which may have properties in common. One such property is shared by both the family of nodal-line semimetals introduced in chapter 1 and a class of materials called type-II Weyl semimetals (WSM). That is, both have a band structure in which pairs of electron and hole pockets coexist.

Type-II WSMs exhibit the same topologically protected crossing of valence and conduction bands at a Weyl point as found in the more conventional type-I WSMs. The difference is in the fact that the Weyl cone in a type-II is strongly tilted, resulting in the coexistence of electron and hole pockets. For this situation, a new type of quantum oscillation has been theoretically predicted to occur due to tunneling between these pockets of different character. This phenomenon has been termed 'Klein tunneling in momentum space' [1].

Usually, Klein tunneling is considered as a phenomenon in which a Dirac particle has a perfect transmission in a *p*-*n* junction in real space. This effect is mainly known in graphene [2, 3],

---

Part of the work presented in this chapter has been published in: M. R. van Delft *et al.*, *Electron-hole tunneling revealed by quantum oscillations in the nodal-line semimetal HfSiS*. Physical Review Letters 121:56602 (2018).

but it is not exclusive to this system. It may occur in any situation where electron and hole states with a Dirac-like dispersion are separated by a potential barrier. However, until now, it has never been observed in momentum space, neither in type-II WSMs nor in other classes of topological semimetals.

In this chapter, we report on quantum oscillations in the nodal-line semimetal (NLSM) HfSiS that demonstrate the first experimental confirmation of the momentum-space analog of Klein tunneling. HfSiS is a member of the ZrSiS family, but has so far received much less attention than other members of the family [4–6], despite having a similar structure. In sections 3.1.1 and 3.1.2 we will discuss the structure of HfSiS.

The momentum-space Klein tunneling effect is identified by the characteristic frequency $f_\beta - f_\alpha$ of the 'figure of eight' breakdown orbit that encloses one electron pocket β and one hole pocket α. The details of this orbit will be described in Sec. 3.2.1. In Sec. 3.2.3, we show that this orbit is only present if $\mathbf{B} \parallel c$ and in Sec. 3.2.2 that it has a cyclotron mass which is equal to the sum of the individual masses of the two pockets, as is theoretically predicted.

In addition to this 'figure of eight' breakdown orbit, we also observed high frequency oscillations due to tunneling across multiple energy gaps. These oscillations happen in the presence of sufficiently high magnetic fields and resemble those seen in ZrSiS [7] and reported in Chapter 4. We discuss their complex frequency spectrum in Sec. 3.3.

In Sec. 3.4, we then study the Berry phases of the different orbits to gain information about their topological character. Finally, in order to exclude an alternative explanation for the observed frequencies, we consider in Sec. 3.5 the effect of magnetic interaction (MI), a phenomenon that can also explain the observation of combination and difference frequencies.

3.1.1 Band structure and Fermi surface

As with all the materials in the ZrSiS family, HfSiS has a PbFCl-type structure (tetragonal space group $P4/nmm$) with layers of Hf and S sandwiched between Si square nets extending in the *ab*-plane. This is shown in Fig. 3.1(a), while in Fig. 3.1(b) the electronic band structure, calculated using Density Functional Theory (DFT, see Sec. 2.6.4), is presented. Rather uniquely for this family of nodal-line semimetals, only linearly dispersing bands are visible around the Fermi level, E_F, that extend over a large energy range of more than 1 eV.

A three-dimensional representation of the cage-like Fermi surface (FS) is presented in Fig. 3.2(a), with the electron and hole pockets colored in green and blue respectively. The corners of the diamond shape are occupied by warped cylindrical hole pockets. Elongated electron pockets additionally exist at the top and bottom of the Brillouin zone. Around the Γ point, a small spherical electron pocket is predicted. However, the presence or absence of this pocket depends on the accuracy of the calculations, as it is very sensitive to the lattice parameters and internal positions of the Hf and S atoms. Any slight variation in these parameters (which can be determined experimentally) can cause this pocket to disappear. Currently, there is no experimental evidence for its existence.

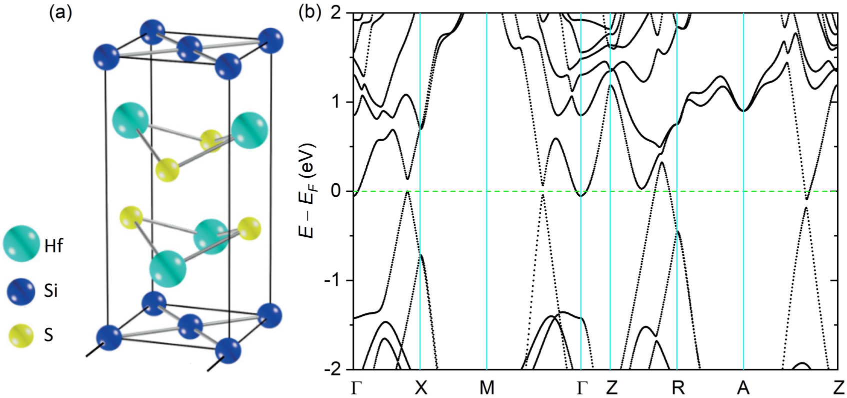

Figure 3.1: *(a) Lattice structure of HfSiS. Adapted from Ref. [5]. (b) DFT calculation, including spin-orbit coupling, for the bulk band structure of HfSiS, calculated by Prof. Antony Carrington from Bristol University.*

The Γ-M-X plane (shown in Fig. 3.2(b)) of HfSiS contains thin hole pockets that trace the contour of the nodal line and have an additional gap around the Γ-X line. The magnitude of these gaps suggest that magnetic breakdown (MB) in this plane is unlikely.

For the purposes of this investigation, the most important parameter in the Fermi surface of HfSiS is the size of the gap, k_g (indicated in Fig. 3.2(c)), between the electron and hole pockets in the Z-R-A plane. This gap is calculated to be about $k_g = 13 \times 10^{-3}$ 1/Å. This is 2-3 times larger than for the related compound ZrSiS [8], due to the larger spin-orbit coupling expected in HfSiS as a consequence of the higher mass of Hf compared to Zr.

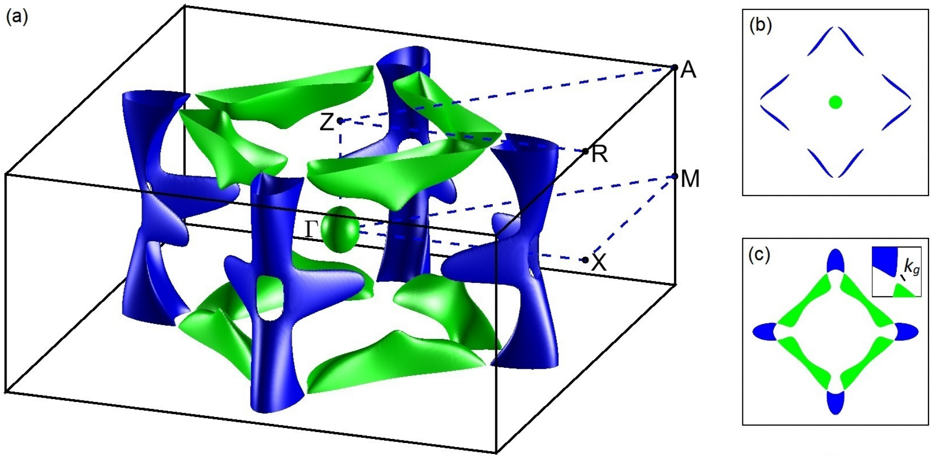

Figure 3.2: (a) Calculated 3D Fermi surface of HfSiS, showing the symmetry labels. Hole pockets are shown in blue and electrons pockets in green. (b) 2D plot of the Fermi surface in the Γ-X-M-plane and (c) in the Z-R-A-plane. The breakdown gap k_g is indicated in (c).

3.1.2 Sample synthesis and characterization

Our single crystals of HfSiS were grown by Leslie Schoop from Princeton University using iodine vapor transport. Stoichiometric amounts of the individual elements and a small amount of iodine were placed in a carbon coated quartz tube and heated to 1100°C with a 100°C temperature gradient for one week. The obtained crystals were subsequently annealed at 600°C for a period of four weeks and the composition was confirmed with EDX (Energy-Dispersive X-ray Spectroscopy, see Sec. 2.6.2).

	X	Y	Z
Hf	$\frac{3}{4}$	$\frac{3}{4}$	0.2299(1)
Si	$\frac{3}{4}$	$\frac{1}{4}$	$\frac{1}{2}$
S	$\frac{1}{4}$	$\frac{1}{4}$	0.1191(6)

Table 3.1: *Determined structural parameters for HfSiS at $T = 90$ K. The spacegroup is P4/nmm (No. 129), and the lattice parameters are $a = b = 3.5176(2)$Å and $c = 7.9479(4)$Å.*

The structure was analyzed using XRD (X-Ray Diffraction, see Sec. 2.6.3) around $T = 90$ K. It is important to do this at low temperature, so that the structural parameters are found under conditions as close as possible to the regime where the quantum oscillation experiment takes place. This is because these parameters feed directly into the electronic structure calculations, which sensitively depend on them. The more accurately the structure is determined, the more accurate the calculation will be. The experimentally relevant temperature range is still lower than 90 K, but this is the lowest temperature at which the XRD can be performed.

The resulting structure was found to be similar to that reported previously [9] at room temperature (see Table 3.1). While the difference between our determined low temperature structural parameters and those of Ref. [9] may be small, it is nevertheless significant for the electronic structure calculations.

3.2 Results and analysis

Fig. 3.3 shows a series of resistance sweeps as a function of the magnetic field up to 31 T on a HfSiS single crystal at different temperatures between 1.3 and 80 K. The magnetic field is applied parallel to the *c*-axis. As seen in the figure, HfSiS displays clear Shubnikov-de Haas (SdH) oscillations with multiple frequencies superimposed on a positive magnetoresistance (MR). Above 15 T, additional high frequency oscillations are observed which will be discussed in Sec. 3.3.

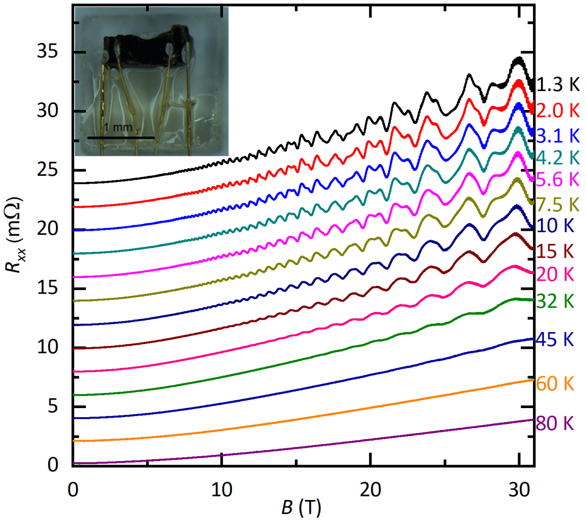

Figure 3.3: *Longitudinal resistance* R_{xx} *as a function of the magnetic field for temperatures between 1.3 and 80 K up to 31 T with* $B \parallel c$*. Each successive curve is offset by 2 m*Ω *for clarity. The inset shows an image of a typical HfSiS single crystal with attached current and voltage probes.*

3.2.1 Identification of oscillation frequencies

In Fig. 3.4(a), we present the result of a Fast Fourier Transform (FFT, see Appendix C for a discussion of FFT procedures) analysis of the 1.3 K sweep in Fig. 3.3. For now, we concentrate on the low-frequency part of the spectrum. In the figure, several clearly resolved peaks are visible. We label the two peaks with the largest amplitude, 264 T (which was reported previously in Ref. [6]) and 473 T as α and β, respectively.

We can relate the different frequencies to specific parts of the Fermi surface by considering their dependence on the angle between the magnetic field direction and the *c*-axis, θ, and comparing it with theoretical predictions. Fig. 3.4(b) shows the experimental frequencies (red dots) determined while rotating from $B \parallel c$ (0°) to $B \parallel a$ (90°) as well as DFT calculations (black dots). All frequencies up to 800 T are taken into account.

The frequency and angle dependence of α show a good agreement with the predictions for the hole pocket located at the vertex of the diamond-shaped Fermi surface in the Z-R-A plane (Fig. 3.5(a) illustrates this pocket in blue). The DFT calculations only slightly overestimate the absolute frequency. For β, the θ dependence is very similar to that predicted for the electron pocket running parallel to the top rung of the nodal loop (green in Fig. 3.5(a)), including the splitting for $\theta > 20°$. Despite the fact that the predicted frequency is about 30% larger than the experimentally observed one, the agreement is still good enough to confidently assign this orbit. Having identified these two, α and β, as fundamental frequencies, we can find most of the others as harmonics or combination/difference frequencies. We can discount any of the other frequencies as possible fundamentals, as they are all either suppressed for angles greater than 10° or clearly harmonics of the fundamental frequencies.

The exception is the low-frequency orbit at ~32 T labeled γ (also seen in Ref. [6]), which we attribute to a closed orbit in a plane between the Z-R-A and the Γ-M-X planes. The DFT calculations also account for this frequency, and predict that it will vanish for angles larger than 20°. Unfortunately though, our angle-dependent data (which was measured with a different sample than that used for Fig. 3.4(a)) does not have sufficient resolution to trace this peak in angle. Additionally, the predicted weakly angle dependent frequency of 130-150 T is not observed in any configuration.

The peaks at 734 T and 1000 T, marked with asterisks in Fig. 3.4(a), match the frequencies of $f_\beta + f_\alpha$ and $f_\beta + 2f_\alpha$, respectively. Such orbits should be semi-classically forbidden because they require the sudden reversal of the electron momentum. Nevertheless, "forbidden" frequencies have been observed in the context of magnetic breakdown in magnesium [10] and organic conductors [11] and might be caused, for example, by oscillations in the chemical potential [12, 13] or B-dependent oscillation damping [14]. Another possible explanation for these frequencies can be magnetic interaction, which we discuss in Sec. 3.5.

The key observation in Fig. 3.4 is that of a peak in the FFT spectrum at a frequency of 207 T, which is consistent with the assignment $\beta - \alpha$. A frequency set by the difference between these two pockets can result from a semi-classically allowed orbit that includes both [1, 15–17]. In principle, this orbit could be observed in any semimetal with adjacent electron and hole pockets due to quasi-particle tunneling, but generally the gap between the pockets is too large for this peculiar effect to be observed at experimentally accessible fields.

In the context of TSMs, such an orbit has been predicted to appear in type-II Weyl semimetals and referred to as the momentum space counterpart of Klein tunneling at a p-n junction [1]. The specific shape of the Fermi surface of HfSiS gives us a similar condition for this momentum space Klein tunneling, as the electron and hole pockets are sufficiently close to allow tunneling between them. Fig. 3.5(b) shows a sketch of the resulting orbit, which we refer to as the 'figure of eight' orbit, in the Z-R-A-plane in momentum space. Here, the gap that needs to be tunneled across in order to make the orbit, is indicated as k_g and the direction of the cyclotron rotation around the orbits is shown with blue arrows.

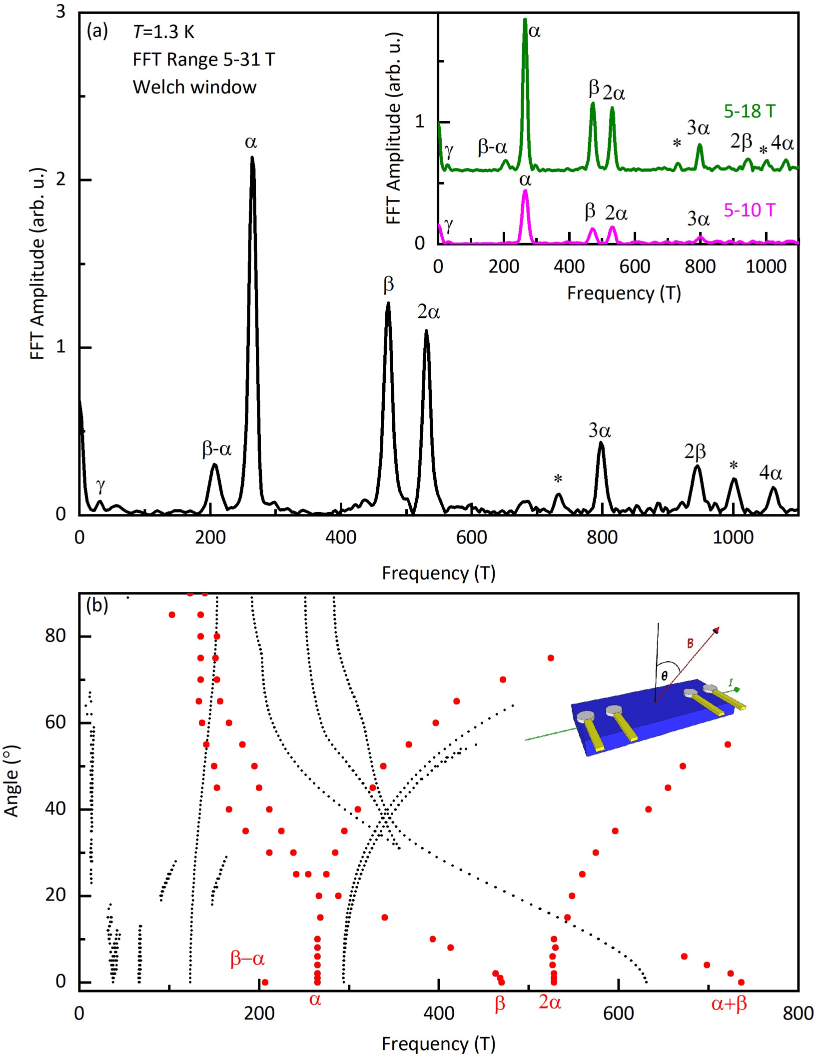

Figure 3.4: *(a) Fast Fourier transform of the data from 5 to 31 T at $T = 1.3$ K and low-frequency FFT spectrum for different field ranges (inset). The FFT peaks corresponding to individual extremal orbits are labeled α, β and γ. The 'figure of eight'-orbit with the frequency $\beta - \alpha$ is also indicated. Forbidden frequencies are marked with an asterisk. (b) Angle dependence of the quantum oscillation frequencies observed experimentally (red dots) and calculated with DFT (black dots). Inset: Configuration of the sample in a tilted magnetic field.*

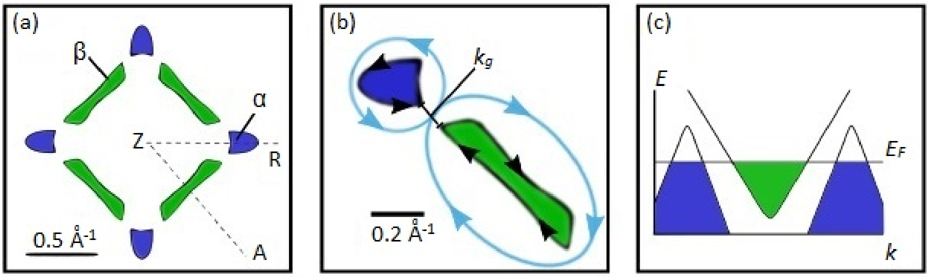

Figure 3.5: *(a) Sketch of the projection of the diamond-shaped Fermi surface in the Z-R-A plane in the first Brillouin zone for* $B \parallel c$ *(*$\theta = 0°$*). The gap* k_g *between the orbits is exaggerated here for illustration. The electron pockets,* β *are indicated in green; the hole pockets,* α *in blue. (b) Expanded view that highlights the 'figure of eight'-orbit in momentum space created by an individual electron and hole orbit. The arrows indicate the direction with which charge carriers can move around the pockets and* k_g *represents the separation in k-space between the adjacent pockets. (c) Schematic of the dispersion relation E(k). The horizontal line indicates the Fermi level* E_F*.*

As shown in the inset of Fig. 3.4(a), where we present FFT spectra calculated for different magnetic field ranges, the $\beta - \alpha$ orbit only appears at sufficiently high fields. This is in agreement with the picture of MB [15, 18], as below a certain critical field, B_0, its probability is exponentially suppressed ($\propto \exp -B_0/B$). A general expression for B_0 is:

$$B_0 = n\frac{h}{e}\left(\frac{k_g}{C}\right)^2, \tag{3.1}$$

with n the number of breakdown events and C a constant that depends on the local band curvature. Carter et al. [19] calculated C for high-T_c cuprates and found that it varied between 1.8 and 3.5. Locally the bands in their simulation are reasonably similar to those of ZrSiS, so we may estimate B_0 by taking $C = 2$.

For the 'figure of eight', B_0 can then be predicted to be approximately 35 T. Considering this, it is quite surprising that MB can be observed in HfSiS at all, according to DFT calculations. However, we note that more precise calculations using exact diagonalization of a tight binding model on the lattice, are required for a better determination of B_0. Variations in local Fermi surface curvature, for example, can easily change B_0 by a factor of 4.

3.2.2 Cyclotron masses

The experimental masses associated with each of the observed frequencies below 800 T are determined from the temperature dependence of the amplitude of the peak in the FFT, via the Lifshitz-Kosevich formalism (see Appendix B). The data and LK fitting are shown in Fig. 3.6.

In the ideal case, this procedure should be applied to the amplitude of one period of the oscillation in the raw data, at a well defined field. However, since we have many frequencies, it is impossible to identify a single period in the raw data and as such the FFT needs to be used. Using the FFT, the choice of the field window is very important. It should be such that the frequency of interest exists within the whole window; if it does not, this will dampen the amplitude in the FFT and lead to an unreliable mass determination. For our analysis, we choose a field window 10 T $\leq B \leq$ 31 T, leading to an average $\overline{B} = 15.12$ T, according to Eq. B.7. The results are shown in Table 3.2.

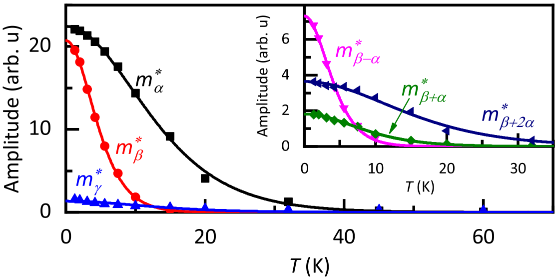

Figure 3.6: *Mass plot for the individual orbits α, β and γ, as well as the $\beta - \alpha$, $\beta + \alpha$ and $\beta + 2\alpha$ orbits (inset). The resulting cyclotron masses are specified in Table 3.2.*

The error margins in these results are estimated based on the noise level in the FFT as well as any interference from nearby peaks or side-lobes of the FFT window function, as discussed in Appendix C. This leads to, for example, the error of $m^*_{\beta+\alpha}$ being quite large due to the presence of the 3α peak at a nearby frequency. The error of m^*_α on the other hand, is very small as this peak is much larger and lighter than any other peak nearby. Additionally, errors arising due to the quality of the fitting are an order of magnitude smaller still than the estimated error.

Comparing the experimental masses with the DFT predictions, we see that the cyclotron mass for the α-pocket is in agreement with the calculation, but that of the β-pocket is found to be 24% smaller than expected. This discrepancy, however, is proportional to the DFT overestimate of the frequency.

For the 'figure of eight' orbit, the cyclotron mass $m^*_{\beta-\alpha}$ is theoretically predicted to be

$$|m^*_{\beta-\alpha}| = \left| \frac{\hbar^2}{2\pi} \frac{d}{dE} |A_\beta - A_\alpha| \right| = \left| \frac{\hbar^2}{2\pi} \frac{d}{dE} A_\beta - \frac{\hbar^2}{2\pi} \frac{d}{dE} A_\alpha \right| = |m^*_\beta| + |m^*_\alpha|, \tag{3.2}$$

where for the third equality we used $dA_\alpha \big/ dE < 0$ and $dA_\beta \big/ dE > 0$. As seen in Table 3.2, we find that $m^*_{\beta-\alpha}$ indeed agrees with the sum of the cyclotron masses of α and β, within the limit of our experimental uncertainties. The observed mass and frequency of $\beta - \alpha$ are in all consistent with the theoretical predictions for Klein tunneling in momentum space[1, 15].

For the classically forbidden orbit $\beta + \alpha$, a similar calculation as Eq. 3.2 yields $m^*_{\beta+\alpha} = |m^*_\beta| - |m^*_\alpha|$. In this case, it requires the assumption that it is indeed formed by two pockets with electron- and hole-like character and not the result of another effect leading to the same frequency. Within the error margins, this agrees with our observation, as does the $\beta + 2\alpha$ orbit, with mass $m^*_{\beta+\alpha} = |m^*_\beta| - 2|m^*_\alpha|$. However, this requires a mechanism reversing the direction of circulation of the carriers around the orbit while preserving the sign of dA/dE. Such a mechanism is difficult to explain physically.

Orbit	FFT analysis	DFT	Plane	m^*/m_e (exp.)	m^*/m_e (DFT)
α	264 T	294 T	Z-R-A	0.177 ± 0.003	0.17
β	473 T	631 T	Z-R-A	0.48 ± 0.02	0.63
γ	32 T	38 T	in between	0.17 ± 0.06	-
2α	528 T	-	Z-R-A	0.32 ± 0.02	-
3α	800 T	-	Z-R-A	0.51 ± 0.02	-
2β	945 T	-	Z-R-A	0.83 ± 0.05	-
$\beta - \alpha$	207 T	-	Z-R-A	0.59 ± 0.06	-
$\beta + \alpha$	734 T	-	-	0.22 ± 0.08	-
$\beta + 2\alpha$	1000 T	-	-	0.15 ± 0.03	-

Table 3.2: *Observed frequencies and extracted cyclotron masses in the field range from 10 to 31 T from the FFT analysis in comparison to DFT calculations, divided in three categories. First the fundamental frequencies and their harmonics, then the figure of eight orbit and finally the forbidden orbits. Here,* m_e *is the free electron mass.*

Another thing to consider is the fact that the reported masses of forbidden orbits tend to be far off from the theoretically expected values in organic conductors [20, 21] and so this theory may not be an accurate description of the physics behind these orbits. It is also interesting to note that the masses associated with $\beta - \alpha$, 2α and 2β are by a factor of 0.9 smaller than predicted by the theory. This deviation might be a consequence of the quasi-2D character of the α pocket, which can cause enhanced oscillations in the chemical potential [22, 23]. This effect is not included in the standard LK theory, but is considered as a possible origin of mass deviations in quasi-2D organic conductors [11, 21].

An enhancement of the mass with increasing field was observed in ZrSiS [7]. As HfSiS is a related compound, one might expect to see similar effects here. No mass enhancement is observed in HfSiS, however, in any configuration.

3.2.3 Suppression of the figure of eight with angle

Fig. 3.7 shows the angle dependence at 1.3 K for small angles close to $B \parallel c$. Interestingly, the $\beta - \alpha$ orbit vanishes completely within two degrees of misalignment between the magnetic field and the c-axis. This can be explained as follows: When the field is rotated away from the c-axis, the area of the orbit is extremal for different constant energy contours, perpendicular to the field. That means that the orbit will cross a slightly different part of the Brillouin zone when tunneling from one pocket to another, than it did before the rotation. One may naively expect that from the eight gaps, four would increase rapidly and four only slowly, but because of this effect, all relevant gaps increase strongly with angle. This effect is very similar to what was predicted for type-II Weyl semimetals in Ref. [1].

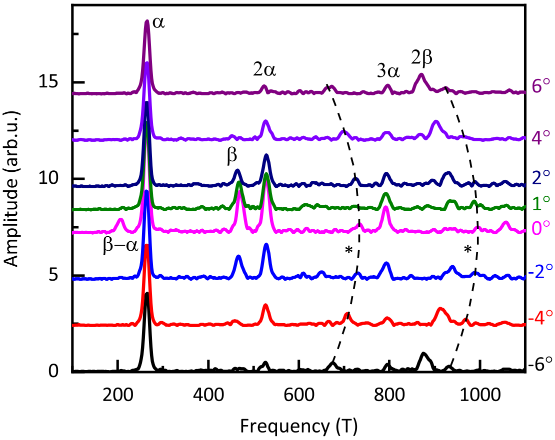

Figure 3.7: *FFT spectra at* $\boldsymbol{B} \parallel c$ *(*$\theta = 0°$*) and at small tilt angles for* $T = 1.3$ *K. While the individual orbits disperse differently with increasing tilt angle, the* $\beta - \alpha$ *orbit can only be observed at* $\theta = 0°$*. The dashed lines are guides to the eye, following the* $\beta + \alpha$ *and* $\beta + 2\alpha$ *frequencies, marked with asterisks.*

The gap size can be calculated from the DFT-predicted FS. First of all, we compute maxima and minima of the areas of the FS perpendicular to the field; these give the extremal quantum oscillation frequencies shown in Fig. 3.7(a). Then, at the value of the momentum parallel to the field ($k_{\parallel}$) where the area of $\beta - \alpha$ is extremal, we can determine the sizes of the gaps. In Fig. 3.8(a), we show the minimum gap size found this way. The minimum gap is the relevant parameter here, as that is the one that will be involved in the most probable $\beta - \alpha$ orbit. Clearly, this gap grows strongly with increasing angle.

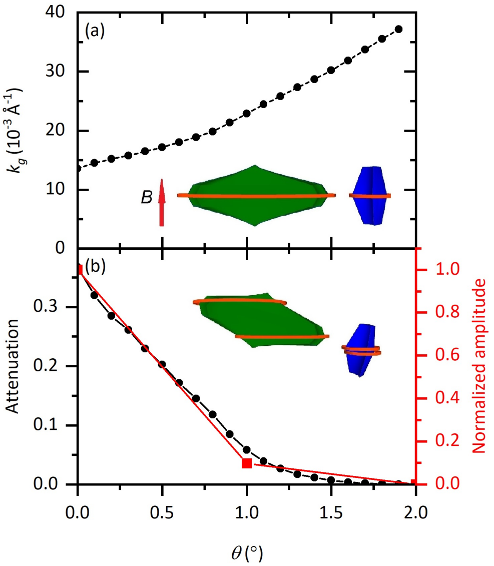

Figure 3.8: *(a) DFT calculated angle dependence of the minimal gap size between the* α *and* β *pockets. Inset, sketch of the* β *and* α *pockets from the side. The orange loops indicate possible extremal orbits perpendicular to the field. (b) In black: attenuation factor of the quantum oscillation amplitude for the* $\beta-\alpha$ *orbit, scaled to be equal to* e^{-1} *at* $\theta=0°$*. In red: amplitude of the* $\beta-\alpha$ *orbit, normalized to its amplitude at* $\theta=0°$*. Inset, sketch of the* β *and* α *pockets, but tilted and showing how the extremal orbits change.*

Beyond some angle, the $\beta-\alpha$ is no longer extremal and no more gap can be calculated, as illustrated in the insets of Fig. 3.8. The top image depicts the case for $B \parallel c$. In that case, the β and α pockets exist at the same $k_{\parallel}$, giving rise to the $\beta-\alpha$ orbit. This remains true for small angles, although the gap grows rapidly, but not for larger angles. That situation is shown in the bottom inset. Here, there is a rotation of the c-axis 15° away from the field direction, causing the orbits to shift to different values of $k_{\parallel}$.

As mentioned previously, the amplitude of the quantum oscillations due to breakdown, is attenuated by factor of $\exp(-1/k_g^2)$. In Fig. 3.8(b), we show this attenuation factor, scaled so that it is equal to e^{-1} at $\theta=0°$, which is equivalent to setting the magnetic field to the breakdown field. Comparing the calculated angle dependence of the attenuation factor with that of the $\beta-\alpha$ orbit from Fig. 3.7(b), we see an excellent agreement. These calculations very well explain the vanishing of the orbit in a tilt of less than two degrees.

In contrast to the $\beta-\alpha$ orbit, the orbits with the "forbidden" frequencies $f_\beta+f_\alpha$ and $f_\beta+2f_\alpha$ survive up to 6° and disperse strongly with angle. This could be due to a breakdown orbit, made possible by an additional effect beyond the standard breakdown physics [10, 11], or due to magnetic interaction (see Sec. 3.5).

Finally, we can compare the angle dependence of the two fundamental frequencies with that of the combinations. We then see that f_α is nearly constant in the low-angle range of Fig. 3.7(b) while f_β changes more strongly. Between 4° and 8° of tilt, no β orbit is observed, while 2β interestingly does survive. This is likely a consequence of a splitting of the Fermi surfaces for spin-up and spin-down that occurs under high magnetic fields. Interference between these two dampens the oscillations and may lead to a so-called spin zero, where a particular orbit is not observed at all (see Appendix B). Assuming $g=2$ and the spin mass is the same as the thermal mass, we can use Eq. B.4 to calculate the attenuation. Doing so, we find a strongly suppressed β around 2°, while the harmonic is almost unaffected. With a more accurate calculation, this

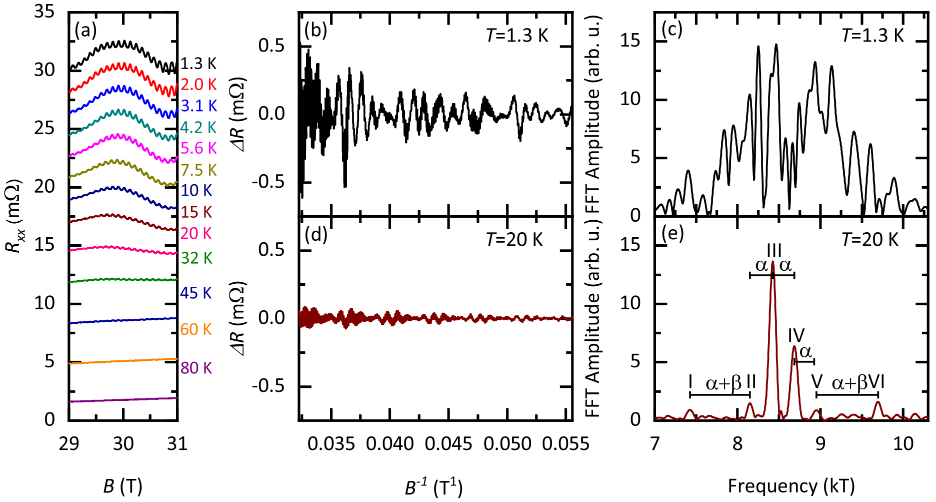

Figure 3.9: *High-frequency quantum oscillations. (a) R_{xx} as a function of B between 29 and 31 T for fixed temperatures ranging from 1.3 to 80 K ($\mathbf{B} \parallel c$). The curves are offset for clarity by 2 mΩ. (b,c) and (d,e) Oscillatory resistance ΔR versus $1/B$ and FFT analysis for 1.3 and 20 K, respectively. The spacer markers for the 20 K FFT indicate that the frequencies are separated by different combinations of the α and β frequencies.*

angle will likely turn out larger.

The disappearance of β beyond 4° provides no explanation for the vanishing of $\beta - \alpha$ within 2°, and neither does the behavior of α. Since this vanishing is not related to either pocket individually, it is therefore most likely an effect of the magnetic breakdown. In addition, the dispersion of $\beta + \alpha$ cannot be reasonably accounted for by the dispersions of β and α, as $f_{\beta+\alpha}$ changes too strongly with angle. Thus, the origin of the $\beta + \alpha$-orbit demands further investigation. The same is true for $\beta + 2\alpha$, which shows very similar behavior.

3.3 High frequency oscillations

We now discuss the high frequency oscillations that appear above 15 T. As an illustration, Fig. 3.9(a) shows an enlarged view of these oscillations between 29 and 31 T, using the same data as presented in Fig. 3.3. For Fig. 3.9(b), we removed both the smoothly varying background due to magnetoresistance and that arising from the low-frequency oscillations. What remains, plotted as a function of $1/B$, reveals a complex pattern of oscillations particularly at low temperature ($T = 1.3$ K).

This is also clear from the corresponding FFT spectrum (Fig.3.9(c)). Here, a series of peaks

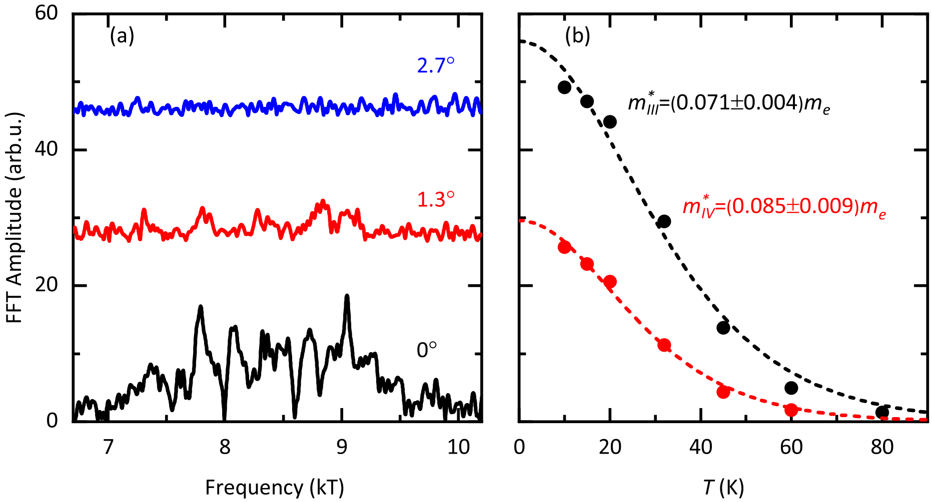

Figure 3.10: *Temperature and angle dependence of the high frequency oscillations. (a) Angle dependence at $T = 0.45$ K. This data is from a different sample. (b) Temperature dependence of the amplitude of peaks III and IV, starting from $T = 10$ K, with LK fit.*

appears ranging from 7 to around 10 kT with the most pronounced ones around 8 and 9 kT. These frequencies are so high that there are no individual orbits in the DFT derived Fermi surface with areas that match them. Such large areas can only arise from orbits that encircle the full diamond shaped FS, most likely in the Z-R-A-plane. Contributions from the Γ-M-X plane are unlikely, as there the gaps between pockets are extremely large (see Fig. 3.2).

The attribution of the high frequencies to MB orbits around the diamond is further supported by the fact that they are again strongly suppressed with small tilt angles away from the c-axis, as shown in Fig. 3.10(a). This is similar to what was observed in ZrSiS [7], although there the high frequency spectrum consists of two groups of peaks with slightly different behavior. Additionally, the fact that these frequencies only appear above 15 T, a higher minimum field than what is required for any of the low frequency orbits, also lends credibility to this scenario.

Unfortunately, the resolution of the low-temperature FFT spectra of this high frequency part of our data does not allow us to investigate individual peaks in detail as their close spacing leads to a considerable overlap of adjacent peaks. For this reason, we consider the data at $T = 20$ K, see Figs. 3.9(d) and (e). At this temperature, only six peaks (numbered I to VI) remain in the FFT spectrum, making it easier to analyze. Between each consecutive peak from II to V, there is a spacing of 264 T (i.e. f_α) while the spacing between I and II and between V and VI is approximately 734 T ($f_\alpha + f_\beta$). This suggests that these peaks correspond to orbits that incorporate different multiples of the α and β pockets.

The amplitude of peaks III and IV is noteworthy. At $T = 20$ K, it is almost as large as at 1.3 K.

This suggests there may be an anomalous behavior as was reported for ZrSiS [7] also in HfSiS. However, since we are not able to disentangle the individual peaks at low temperatures, our current data does not allow us to confirm this, but we can investigate the T-dependence of the quantum oscillation amplitude for $T \geq 10$ K. This is shown for peaks III and IV in Fig. 3.10(b). The other four identified peaks do not survive up to high temperatures and thus do not offer sufficient data points for an accurate fitting.

From the LK fitting, we find $m^*_{III} = (0.071 \pm 0.004)m_e$ and $m^*_{IV} = (0.085 \pm 0.009)m_e$. These masses are smaller than what was observed for any low frequency, which seems to be at odds with allowed breakdown frequencies. For such a frequency, one would expect a mass that is the sum of the masses associated with the different components of the orbit. Since we observe such a low mass, however, there may be another mechanism responsible for or contributing to these peaks in the FFT. Further investigation is required to properly address this issue.

3.4 Berry phase and Dingle temperature

One way to demonstrate the topological character of an orbit is to analyze the Berry phase, Φ_B, associated with the orbit. Specifically, a Dirac fermion is expected to carry a Berry phase of π [24] and in general, a non-zero Berry phase can be associated with the presence of a band touching point. This may be due to a Dirac or Weyl point, but can also be a consequence of a nodal line, as is present in HfSiS. Because of this, it is of interest to extract this phase.

The Berry phase is commonly extracted from experimental quantum oscillation data in two ways, through a Landau level index plot, or by direct fitting with the Lifshitz-Kosevich (LK) equation (see Appendix B) applied to one pocket of the FS. The former method involves plotting the $1/B$ values of the maxima or minima of the oscillations against their Landau level index, n, and extrapolating to $n = 0$. This method is most accurate when low values of n can be attained, which is not the case for our data. In literature, it is also frequently interpreted in inconsistent ways.

The LK fitting method does not suffer from these shortcomings and it is easier to judge the quality of this fitting than is possible using the Landau index extrapolation, as was also pointed out in Ref. [25]. For these reasons, it gives a more reliable result. Furthermore, the LK fitting should in theory work for systems with multiple frequencies, unlike the Landau index plot. In practice, however, the fitting often fails to converge. In our case, it is necessary to use a bandpass FFT filter on the data in order to isolate just one frequency before attempting the fitting. Fig. 3.11 shows the results of this procedure for the α and β orbits. For the others, it proved unsuccessful.

For the α orbit, we find $\Phi_B = 0.61\pi$, in rough agreement with the value reported in Ref. [6], and for β, we find $\Phi_B = 1.21\pi$. Both values are non-zero, suggesting some non-trivial band topology. However, they are quite distinct from π and as such the interpretation is not straightforward.

An additional advantage of the LK fitting method, is that it allows us to find the Dingle

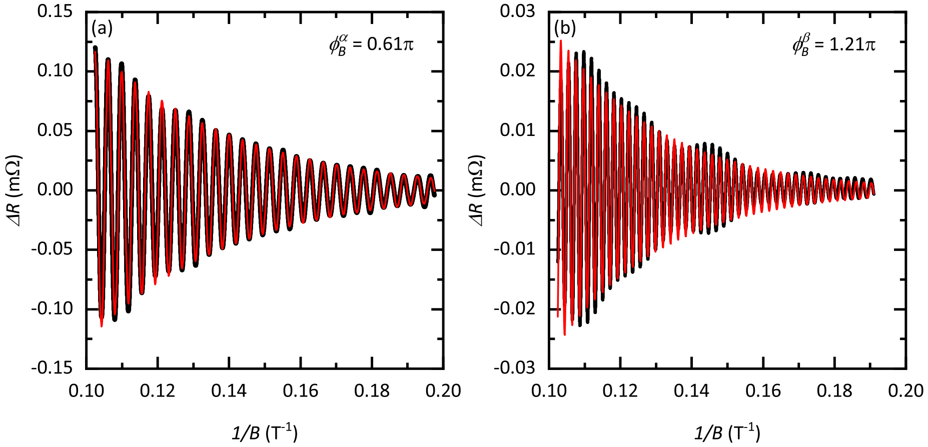

Figure 3.11: *Lifshitz-Kosevich fitting (Eq. B.1) of (a) the α frequency and (b) the β frequency.*

temperature for each orbit. From our fitting, we find for α, $T_D = 29.1 \pm 0.1$ K and for β, $T_D = 37.9 \pm 0.4$ K. With these values, we can use $k_B T_d = \frac{\hbar}{2\pi\tau}$, with τ the scattering time, to estimate the mobility as $\mu = \frac{e\tau}{m^*}$. This gives us approximately 400 and 100 cm^{2}V^{-1}s^{-1} for α and β respectively. Compared to the mobilities of similar materials, these values are very low.

3.5 Magnetic interaction

The magnetic interaction (MI) effect can result in FFT spectra that resemble those produced by magnetic breakdown (MB), since it can generate both harmonics and combinations of fundamental frequencies[26]. The physics behind this phenomenon is fundamentally different from that behind MB, however, so it is important to distinguish between the two effects. This can be done by simulating the spectra generated by MI and comparing them with the experimental data. The dependence on field, temperature and angle should be quite different for MI and MB, so they can be easily distinguished.

The MI effect arises from the fact that the diameters of the Landau tubes on which the quasi-particles are confined1 depend on the magnetic field B rather than H, related by $B = \mu_0(H + M)$. As the magnetization, M, is itself an oscillating quantity, additional frequencies can arise.

For the simulation of MI, we first calculate the magnetization M_{calc} using the conventional LK formula with $B = \mu_0 H$ and summing the contributions from only the two fundamental frequencies (α and β). We include the reduction factors R_T and R_D with the experimentally determined masses and Dingle temperatures, while the spin-splitting factor does not depend on magnetic field and so can be considered as a constant. Then, we calculate again, but this time with $B = \mu_0(H + M_{calc})$ and we assume the magnetoresistance oscillations are proportional to the susceptibility M/H.

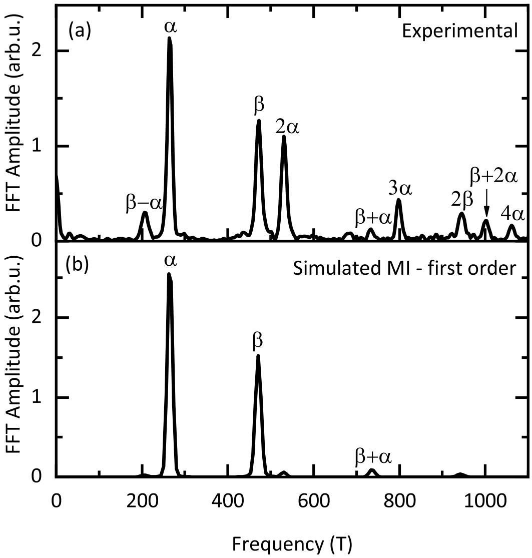

Figure 3.12: Fast Fourier Transforms from 5 to 31 T at 1.3 K: (a) Experiment and (b) simulation taking into account magnetic interaction to first order.

In order to make an accurate simulation, we also need two amplitudes A_α and A_β. A_α is set using the low field magnetization data for HfSiS reported in Ref [6], adjusted for the higher Dingle factor in our sample and A_β was chosen in such a way as to reproduce the relative height of the α and β peaks in the FFT.

The result of the simulation is shown in *Fig.* 3.12. Clearly, the MI effect is quite weak in our sample. It produces only a slight bump at $f_\beta - f_\alpha$, much smaller than what is observed experimentally, and hence cannot explain this frequency. Therefore, we conclude that $\beta - \alpha$ is indeed due to MB. The situation is different for $f_\alpha + f_\beta$. There, the simulated and experimental peaks are of similar size, so MI may be the reason that this "forbidden" peak is observed. The frequency $f_{\beta+2\alpha}$, however, does not appear in the simulated MI spectrum and remains unexplained.

The effect of temperature on the MI peaks (not shown here) was also included in our simulations. When determining $m^*_{\beta-\alpha}$ from this, we find that it is not a simple combination of m^*_α and m^*_β, meaning MI cannot explain the mass we observe. This is another confirmation of our claim that $\beta - \alpha$ arises due to magnetic breakdown. Finally, we remark that the very high frequencies (discussed in Sec. 3.3) cannot be generated by MI and can only be produced by magnetic breakdown orbits that encircle the whole Fermi surface in the Z-R-A-plane.

3.6 Conclusion

We have demonstrated the first experimental confirmation of Klein tunneling in momentum space in the NLSM HfSiS. This special type of magnetic breakdown is only present in HfSiS if the magnetic field is oriented precisely parallel to the *c*-axis and a magnetic field in excess of 10 T is applied. As theoretically predicted, the cyclotron mass associated with this orbit is found to be the sum of the masses of the individual electron and hole pockets that it consists of. Although MB has been extensively studied in simple elements and organic metals, this special type of magnetic breakdown between electron and hole pockets has not been observed previously.

The phenomenon of momentum space Klein tunneling was initially predicted for type-II WSMs, but our observation in the NLSM HfSiS implies that it is not confined to this system. Instead, our results suggest that this may be a generic property of semimetals with adjacent electron and hole pockets, separated by a sufficiently small gap.

In addition to those arising from Klein tunneling, we also discovered frequencies of semi-classically forbidden orbits. These orbits include hole and electron pockets, but instead of the difference between these, the sum is seen in the frequency spectrum. Such an orbit requires the reversal of the electron momentum, which is physically difficult to account for. Magnetic interaction rather than breakdown can partially explain the observation, but at least one frequency remains unexplained. For this, it may be necessary to invoke oscillations of the chemical potential or other mechanisms outside the standard theory.

Finally, we identified high frequency oscillations similar to those reported in ZrSiS. These oscillations present a complex FFT spectrum with peaks between 7 and 10 kT. There are indications that an unusual temperature dependence may be present, but further study is required to be verify this.

References

[1] T. E. O'Brien, M. Diez, and C. W. J. Beenakker. *Physical Review Letters*, 116(236401), 2016.

[2] M.I. Katsnelson, K.S. Novoselov, and A.K. Geim. *Nature Physics*, 2:620–625, 2006.

[3] A. F. Young and P. Kim. *Nature Physics*, 5:222–226, 2009.

[4] D. Takane, Z. Wang, S. Souma, et al. *Physical Review B*, 94(121108), 2016.

[5] C. Chen, X. Xu, J. Jiang, et al. *Physical Review B*, 95(125126), 2017.

[6] N. Kumar, K. Manna, Y. Qi, et al. *Physical Review B*, 95(121109(R)), 2017.

[7] S. Pezzini, M. R. van Delft, L. Schoop, et al. *Nature Physics*, 14:178–183, 2018.

[8] M. B. Schilling, L. M. Schoop, B. V. Lotsch, M. Dressel, and A. V. Pronin. *Physical Review Letters*, 119(187401), 2017.

[9] V. H. Onken, K. Vierheilig, and H. Hahn. *Zeitschrift für anorganische und allgemeine Chemie*, 233(267), 1964.

[10] J. W. Eddy and R. W. Stark. *Physical Review Letters*, 48(4), 1982.

[11] F. A Meyer, E Steep, W Biberacher, et al. *Europhysics Letters*, 32(8):681–686, 1995.

[12] N. Harrison, R. Bogaerts, P. Reinders, et al. *Physical Review B*, 54(14):9977–9987, 1996.

[13] J.-Y. Fortin, J. Bellissard, M. Gusmão, and T. Ziman. *Physical Review B*, 57(3):1484–1497, 1998.

[14] V. M. Gvozdikov, Y. V. Pershin, E. Steep, A. G. M. Jansen, and P. Wyder. *Physical Review B*, 65(165102), 2002.

[15] M. I. Kaganov and A. A. Slutskin. *Physics Reports*, 98(4):189–271, 1983.

[16] A. Alexandradinata and L. Glazman. *Physical Review Letters*, 119(256601), 2017.

[17] A. Alexandradinata and L. Glazman. *Physical Review B*, 97(144422), 2018.

[18] M. H. Cohen and L. M. Falicov. *Physical Review Letters*, 7(6):231–233, 1961.

[19] J.-M. Carter, D. Podolsky, and H.-Y. Kee. *Physical Review B*, 81(6):2–9, 2010.

[20] M. V. Kartsovnik, G. Y. Logvenov, T. Ishiguro, et al. *Physical Review Letters*, 77(12):2530–2533, 1996.

[21] S. Uji, M. Chaparala, S. Hill, et al. *Synthetic Metals*, 85:1573–1574, 1997.

[22] K. Kishigi and Y. Hasegawa. *Physical Review B*, 72(045410), 2005.

[23] M. A. Itskovsky. *Physical Review B*, 68(054423), 2003.

[24] J. Hu, J. Y. Liu, D. Graf, et al. *Scientific Reports*, 6:18674, 2016.

[25] J. Hu, Y. L. Zhu, D. Graf, et al. *Physical Review B*, 95(205134), 2017.

[26] D. Shoenberg. *Magnetic Osillation in metals.* Cambridge University Press, 1984.

CHAPTER 4

Quantum oscillatory behavior of the nodal line semimetal ZrSiS

4.1 Introduction

In most topological semimetals, the linear Dirac-like elements of the electronic structures coexist with other bands that cross the Fermi level. This is the case for Dirac [1], Weyl [2, 3] and Nodal Line Semimetal (NLSM, see Sec. 1) systems [4]. The situation is very different in ZrSiS, a member of the materials class ZrSiX (X= S, Se, Te) that has been found to contain NLSMs, as it has no band features crossing the Fermi level other than a line of Dirac nodes. The consequence of this is that the properties of ZrSiS are governed by electronic states close to the nodes, both in the bulk and on the surface. Furthermore, the range of linear dispersion in the band structure of ZrSiS extends up to at least 0.5 eV for all bands and up to 2 eV in some regions of the Brillouin zone. This range is much larger than found in other Dirac-like compounds.

Evidence for the Dirac-like dispersion and its energy range in ZrSiS was acquired through ARPES measurements [5–12], while the presence of the Dirac nodal loop and its topological character were demonstrated by quantum oscillation measurements. This was done not just

---

Part of the work presented in this chapter has been published in: S. Pezzini, M. R. van Delft *et al.*, *Unconventional mass enhancement around the Dirac nodal loop in ZrSiS.* Nature Physics 14:178–183 (2018) for ZrSiS [13–16], but also for the related compounds ZrSiSe and ZrSiTe [15, 17]. The authors of these studies observed phase shifts in the quantum oscillations associated with the Berry phase of the orbit and attributed this to the topological character of the nodal loop.

In this way, the topological nature of NLSMs has been well demonstrated. However, also an enhancement of correlation effects has been predicted theoretically [18], and sought after experimentally. These effects may occur due to the long-range Coulomb interaction [19–21], which arises from a vanishing density of states at the Fermi level. In that case, Coulomb interaction is only partially screened, and therefore long-ranged. Such enhanced correlation effects are particularly interesting in NLSMs due to the combination with topology, and may have several experimentally observable consequences.

Theoretical studies of these effects predict, for example, a unique momentum dependence of sound wave propagation and phonon dispersion [19] as well as various types of spin and/or charge ordering [20]. Some predictions directly concern the electrical conductivity of NLSMs. This was expected to be very high at low temperatures due to a high mobility [21], which was indeed seen experimentally [6, 14]. Furthermore, even superconductivity has been mentioned as a possibility [20], and observed upon contact with a sharp, metallic tip [22]. Finally, it was also suggested that a type of interaction-driven surface ordering as well as bulk quantum oscillations in the magnetic susceptibility can occur [18].

In our own work (Ref. [23]), we reported signs of correlation effects in ZrSiS in the form of a field-induced enhancement of the quasiparticle mass. Such enhancement is reminiscent of what is observed in known correlated electron systems, such as $YbRh_2Si_2$ [24] or $CeCoIn_5$ [25], which can be tuned to a quantum critical point (QCP) by a magnetic field. The quasiparticle masses in these materials diverge as the QCP is approached, due to a dressing by quantum fluctuations associated with the ordered state. In the case of ZrSiS, theoretical follow-up studies related the mass enhancement to an excitonic instability [26, 27].

In this chapter, we aim to elaborate on the physics of the compound ZrSiS. We begin by introducing the structure and Fermi surface of ZrSiS in Sec. 4.1.1 and its synthesis in Sec. 4.1.2. After this, we introduce our measurements with a short overview of the magnetoresistance data (Sec. 4.2), before we delve into the details of the quantum oscillatory phenomena that we observe.

We then divide our discussion into two parts, one for the oscillations below 1 kT (Sec. 4.3), and one for those between 7 and 12 kT (Sec. 4.4). The former correspond to orbits around individual pockets of the Fermi surface (FS) as well as orbits formed by magnetic breakdown (MB) between individual pockets. In this way, breakdown can lead to oscillations with frequencies made up of combinations of the fundamentals. It is then key to identify which frequencies are the fundamentals, which we do in Sec. 4.3.1 via the dependence of the oscillation frequencies on the angle with the magnetic field. Following this, we explain each of the remaining frequencies through MB in Sec. 4.3.2. The assignment that we make in this way is further confirmed via the effective masses, and their comparison to theoretical predictions in Sec. 4.3.3.

The probability of MB depends strongly on the size of the gap between pockets and on the applied magnetic field. For this reason, we study the effects of small changes in the angle with the field (which corresponds to small changes in the gap size) in Sec. 4.3.4 and the dependence on the field itself in Sec. 4.3.5. We then finalize the explanation of all observed frequencies in a discussion of the effect of magnetic interaction in Sec. 4.3.6. We conclude the discussion of the low frequency oscillations with an analysis of the mass enhancement effect.

The high frequency oscillations cannot arise directly from the fundamentals or combinations thereof. Such large orbits can only be formed by including the momentum space in between the pockets and so the high frequencies require magnetic breakdown that connects all of the individual pockets, forming a loop around the whole Fermi surface. We begin Sec. 4.4 by discussing which frequencies are observed and which are allowed theoretically. We then discuss the dependence of these oscillations on the angle (Sec. 4.4.1) and on the magnetic field (Sec. 4.4.2). We finish with an analysis of the peculiar temperature dependence (Sec. 4.4.3).

At the end of the chapter, we present additional data collected in pulsed magnetic fields up to 66 T in Sec. 4.5, which were collected in order to follow the mass enhancement up to higher fields and look for signs of a possible QCP. We also present data from FIB-prepared crystals of ZrSiS in Sec. 4.6 and we finish this chapter with a discussion (Sec. 4.7), conclusion and outlook (Sec. 4.8).

4.1.1 Structure and Fermi surface of ZrSiS

Fig. 4.1(a) shows the crystal structure of ZrSiS. ZrSiS -like HfSiS- has the PbFCl-type structure (tetragonal space group P4/nmm), a common structure with layers of, in this case, Zr and S sandwiched between square nets of Si [28]. As the layers are weakly coupled, ZrSiS can be regarded as a stack of quasi-two-dimensional layers. The electronic band structure of bulk ZrSiS is shown in Fig. 4.1(b). Around E_F, four bands are visible that disperse linearly. The bands that cross Γ-X and Z-R are responsible for the hole pockets and those crossing Z-A and Γ-M for the electron pockets.

Due to spin-orbit coupling (SOC), there is a small gap ($\sim$0.02 eV) separating the valence and conduction bands and the Dirac-type band crossing is gapped out. However, following the line where the band crossing would take place, one can nevertheless draw a nodal line throughout the Brillouin zone. This is the red line in Fig. 4.1(c), where the Fermi surface (FS) of ZrSiS is drawn. The dispersion in energy of this nodal line appears in Fig. 4.1(d), which shows both the valence and conduction bands in the Z-R-A plane, as a function of energy. The gap along the crossing line between the two bands can be seen as an unshaded region and the electron and hole pockets are indicated at the Fermi level.

An additional Dirac crossing exists that arises from the square Si sub-lattice and is protected by non-symmorphic symmetry [5]. This crossing, located at the X-point, does not open a gap even in the presence of strong spin-orbit coupling.

The FS (Fig. 4.1(c)) has a diamond shape and consists of two highly warped cylindrical elements, one containing electrons, the other holes, both of which occur four times. This FS

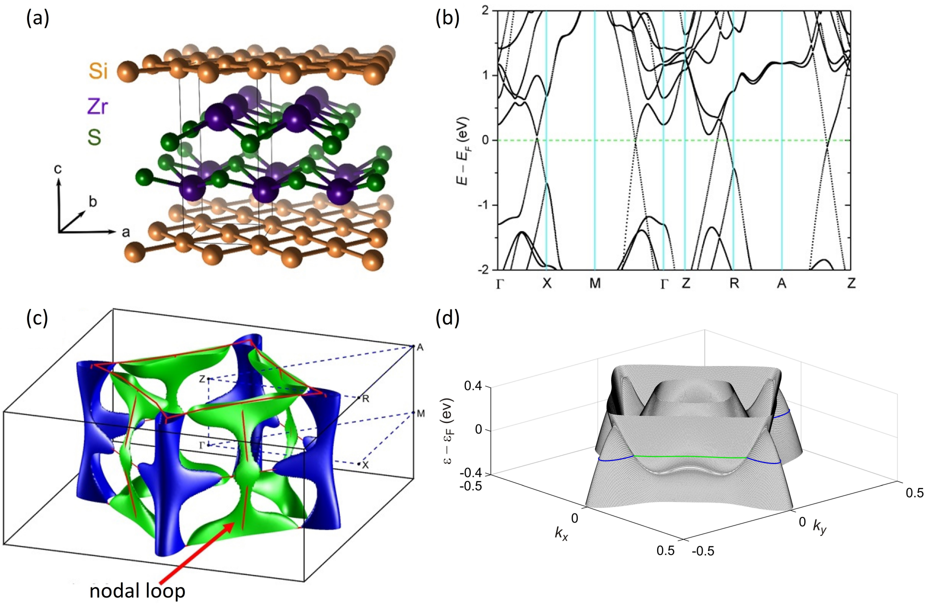

Figure 4.1: *(a) Crystal structure of ZrSiS, with the Si square net highlighted in brown. (b) Calculated bulk band structure of ZrSiS, including spin-orbit coupling. (c) Three-dimensional Fermi surface of ZrSiS. Hole pockets are shown in blue and electron pockets in green. The Dirac nodal loop is indicated by a red line. (d) Energy versus in-plane wavevectors at the top of the Brillouin zone. The blue and green lines mark the contours of the equally colored pockets in (c). Along the line where the bands cross, a gap (unshaded region) appears due to spin-orbit coupling.*

is quite similar to that which was discussed for HfSiS in chapter 3, with apparent differences found only away from the important Z-R-A plane. The electron pockets are located at the sides of the diamond and form an elongated shape along the nodal line in the Z-R-A plane, that we refer to as the "dog-bone". Below this plane, the pocket thins down considerably only to slightly broaden again in the Γ-X-M plane, where the remaining cross-sectional area is very small. The hole pockets occupy the corners of the diamond and, in the Z-R-A plane, have a shape that resembles a petal from a flower. Hence, we refer to this pocket as the "petal". This pocket disperses strongly around k_z and for the resulting shape in the Γ-X-M plane, we reserve the name "boomerang". The cross-sections of the different planes are shown in Figs. 4.2(a) and (b).

The main differences between ZrSiS and HfSiS appear in the Γ-M-X plane. In HfSiS, the electron pockets do not extend throughout the Γ-M-X plane and there is an opening in the hole pocket at the corner of the diamond. It is the absence of this opening that creates the

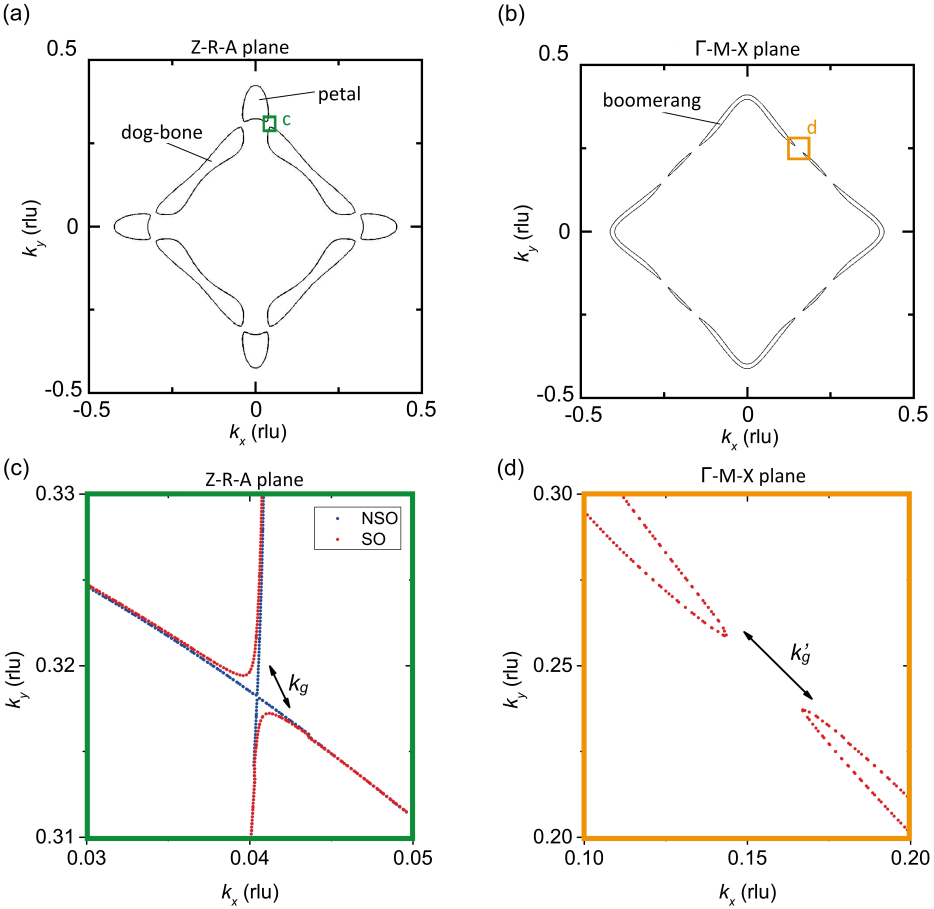

Figure 4.2: *Cross-sections of the FS of ZrSiS in (a) the Z-R-A plane and (b) the Γ-X-M plane. The green and orange slices correspond to the plots in (c) and (d), respectively. (c) Enlarged view of the section of the Brillouin zone marked in green in (a), in the Z-R-A plane. The calculation is shown both with (red) and without (blue) spin-orbit coupling included. The gap is indicated as k_g. (d) Detail of the section around the gap in the Γ-X-M plane marked in (b). The gap is indicated as k_g'. Note the different scales in panels (c) and (d); the gap k_g' is considerably larger than k_g.*

boomerang pocket in ZrSiS. Aside from this, the spherical pocket predicted in the center of the Brillouin zone of HfSiS does not appear in ZrSiS.

The gap, k_g, between the pockets in the FS of ZrSiS (highlighted in Fig. 4.2) is considerably smaller than that in HfSiS. As the breakdown field B_0 is proportional to k_g^2 [29] and the probability is proportional to $\exp(-B_0/B)$, magnetic breakdown is much more likely in the Zr-compound and indeed it has been shown before, that electrons may tunnel across the gap in momentum space [23], forming breakdown orbits. In this way, orbits can exist that include elements of both the dog-bone and petal orbits (within the Z-R-A plane) and it is even possible to make a single orbit around the whole diamond.

In Fig. 4.2(b), it is illustrated how the gap is opened under the influence of SOC. This gap in the Z-R-A plane is small ($k_g = 4.9 \times 10^{-3}$Å^{-1}), and is expected to enable tunneling between pockets at strong enough magnetic fields. MB orbits attributed to this plane were reported previously [23]. The gap in the Γ-M-X plane (shown in Fig. 4.2(c)), on the other hand, is expected to be too large for any viable breakdown orbit. According to our calculations, this gap is an order of magnitude larger than the one in the Z-R-A plane and so the tunneling probability should be small. Understanding these aspects of the FS is important for the interpretation of the data presented in the following sections.

4.1.2 Sample synthesis and characterization

Single crystals of ZrSiS were provided by Leslie Schoop from Princeton University. These crystals were grown out of their constituent elements using iodine vapor transport. Stoichiometric quantities of each element were placed in a carbon-coated quartz ampule, together with a small amount of iodine. This tube was heated to 1,100 °C with a gradient of 100 °C, for the duration of one week. The crystals were then annealed at 600 °C for four weeks afterwards. Finally, the ampule was opened and high quality single crystals with dimensions of the order of a few millimeters were obtained.

Sample	Contacts	Growth batch
A	Ag paste	1
B	Ag paste	1
4	Evaporated Au (2.3.2)	2
8	Evaporated Au (2.3.2)	1
9	Evaporated Au (2.3.2)	2
33	FIB Pt (2.1)	1
34	FIB Pt (2.1)	1
Torque	N/A	2

Table 4.1: *Overview of the different samples of ZrSiS discussed in this chapter.*

The structure of these crystals was then confirmed by means of single-crystal X-ray (XRD, see Sec. 2.6.3) and electron diffraction. Additionally, the crystals were examined by electron microscopy, also using back-scattered electron detectors, to look for evidence of inclusions. No sign of any such inclusions was found. The different samples of ZrSiS that were used in the measurements discussed in this chapter, are listed in table 4.1.

4.2 Magnetoresistance

The magnetoresistance (MR) of ZrSiS (shown in Fig. 4.3(a) for two of our best samples) shows two unusual features, the first of which is its large magnitude. We cannot calculate this magnitude exactly, as our measured zero-field resistance is unreliable, but we can make an estimate using literature data. A resistivity as low as 48 nΩcm at 2 K was reported for ZrSiS crystals grown by the same group [14]. Assuming the same resistivity for our samples, we estimate their zero-field resistance to be of order 10 $\mu\Omega$, suggesting that our MR is of the order of 10^5% at 10 T.

An MR as high as 10^4-10^5% is typically reported [7, 12, 14, 16, 30] for ZrSiS. Such values are typical not just for ZrSiS or NLSMs, but commonly occur in topological semimetals in general [31] and may be related to the linear energy dispersion. In the presence of smooth disorder and with a low density of states near the Fermi level, such dispersion naturally leads to a non-saturating, linear MR.

The large MR is also often attributed to electron-hole compensation and considered unrelated to the Dirac-type dispersion [30]. However, there are indications that ZrSiS is not compensated [12]. As we do not observe any Hall signal in our measurements, we cannot check the electron and hole concentrations for compensation. Another explanation offered in Ref. [16] for the large MR of ZrSiS, is the opening of a gap at the band touching points. This appears to be inconsistent with what we know of the bandstructure of ZrSiS, namely that a gap is opened by spin-orbit coupling without the requirement of high magnetic fields.

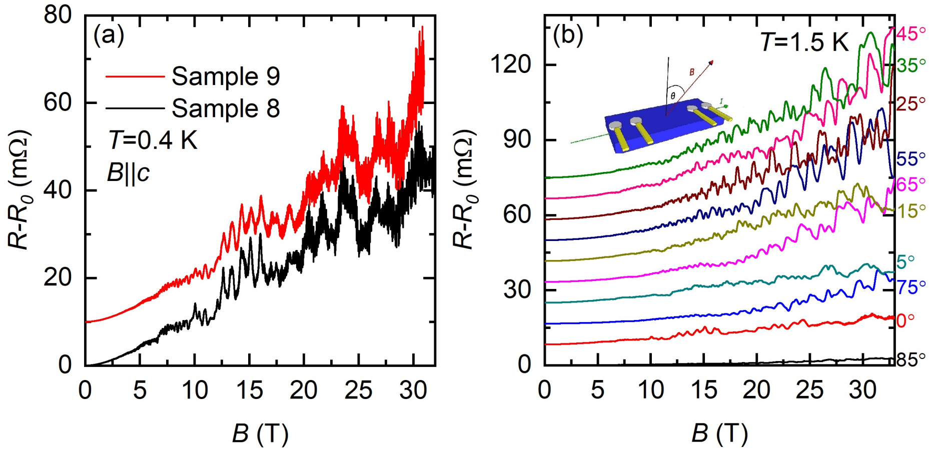

Figure 4.3: *(a) MR data from two of the samples used for this work. The measurements were done at $T = 0.4$ K and for $B \parallel c$. The data of sample 9 are offset by 10 mΩ. (b) Magnetoresistance of sample A for selected angles between the sample and the magnetic field, as indicated in the inset. Successive curves are offset by 8.3 mΩ for clarity.*

A particular aspect of the MR of ZrSiS was reported in Refs. [7, 14, 30, 32, 33], related to the shape of the MR magnitude as a function of the angle with respect to the magnetic field. When plotted over 360°, this shape resembles a butterfly and thus it was termed "butterfly" magnetoresistance in Ref. [14]. The origin of the "butterfly" MR is thought to be a combination of two- and fourfold symmetric elements in the band structure. We show angle dependent MR measurements of one of our samples in Fig. 4.3(b), from which qualitatively the same butterfly shape can be extracted.

The other noteworthy feature seen in Fig. 4.3(a) is the complex pattern of strong quantum oscillations that is superimposed on the MR background. These oscillations can be separated into two categories, those with frequencies below 1 kT and those between 7 and 12 kT. The low-frequency part of the spectrum will be discussed in detail in Sec. 4.3 and the high frequencies will be analyzed in Sec. 4.4.

4.3 Analysis of the low-frequency spectrum

4.3.1 Determination of the fundamental frequencies

We have studied the quantum oscillations in ZrSiS both via the Shubnikov-de Haas (SdH) effect in electrical transport, and via the de Haas-van Alphen (dHvA) effect using torque magnetometry (described in Sec. 2.6.1). The FFTs resulting from these experiments at low temperature are shown in Fig. 4.4.

The two spectra reproduce many of the same features. Particularly the frequencies at 180, 240, 300 and 600 T are well resolved with both techniques. There is, however, a number of frequencies that appear in the transport data, but not in torque. On the other hand, in torque, three very low frequencies are visible, which are difficult to resolve in transport measurements due to the large background MR. Aside from these, 420 T stands out as the only frequency that appears clearly in dHvA data, but is barely visible in SdH.

Comparing our results to the literature, and we see that the 240 T frequency is very consistently observed in Shubnikov-de Haas [7, 12, 14, 16, 32, 33], de Haas-van Alphen [33, 34] and thermoelectric oscillations [35]. Most other frequencies above 100 T, however, have never been reported. The exception is the 600 T frequency, which was also observed in a study of thermoelectric quantum oscillations [35].

All previous studies additionally reported one or more low frequencies (F<25 T), with limited agreement between them. In most cases, values between 8 and 9 T, 14 and 19 T, or 22 and 25 T are reported. Frequencies outside these ranges are not reproduced by more than one study. In our SdH data, we do not have resolution in this frequency range, but in dHvA, we see 8 T (and its harmonic at 16 T) and 22 T, in good agreement with previous reports.

In order to assign the observed frequencies to parts of the FS, angle dependent measurements are crucial. When the angle between the magnetic field and the sample is varied, the extremal

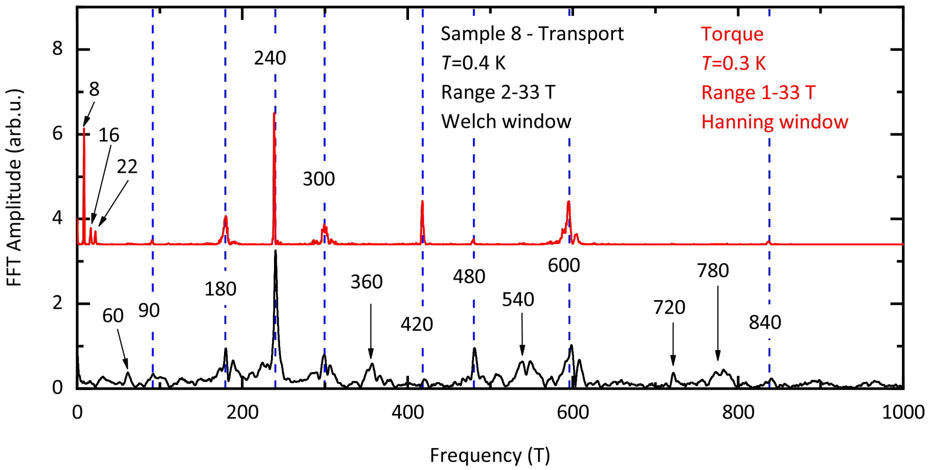

Figure 4.4: *FFTs of both SdH (black) and dHvA (red) data of ZrSiS. Frequencies that occur in both spectra are marked with dashed blue lines. Some frequencies are only observed with one technique.*

orbits around the different pockets of the FS change accordingly. From the FS that is calculated with Density Functional Theory (DFT, see Sec. 2.6.4), shown in Fig. 4.1(c), we can predict how these orbits will behave. From that, a theoretical plot of frequency versus angle can be made. By comparing the experimental data to this plot, we are then able to connect observed frequencies with the FS.

Angle dependent MR data over the whole angular range of 0-90° was previously shown in Fig. 4.3(b), where we discussed the shape of the MR. As we now focus on the behavior of the oscillation frequencies, we show FFTs of the data in Fig. 4.5(a), taken at 5° intervals. It is difficult to draw conclusions based on this, as there are many different frequencies, especially at intermediate angles. Several of these appear to be harmonics, however, which can simplify the interpretation.

At $B \parallel c$ (0°), the DFT calculations predict two large (F>200 T) frequencies arising from the petal and dog-bone pockets in the Z-R-A plane of the FS. Several small frequencies are expected to arise from the Γ-X-M plane or from an intermediate plane. For the petal, a frequency of 240 T is predicted as well as an angle dependence that agrees well with the data. This allows us to assign this orbit with confidence. However, the dog-bone is not as clear. This orbit is predicted to induce oscillations with a frequency of 515 T, which does not agree with any seen in the experimental data, while also its angle dependence is not obviously found within the data of Fig. 4.5(a).

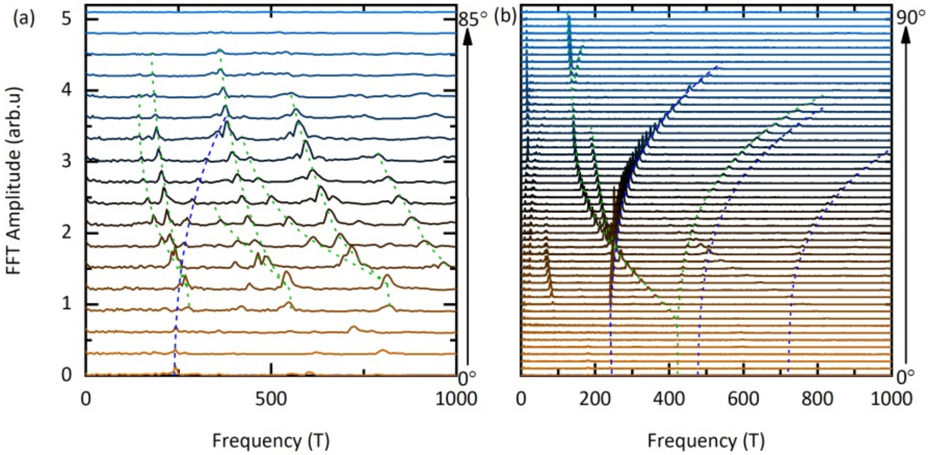

Figure 4.5: *FFTs as a function of angle for (a) transport data on sample A and (b) torque data. The data used to calculate the FFTs in (a) was measured up to 33 T, with 5° steps in the angle between the sample and the field. A rectangular window function over a 4-33 T range was used for the calculation. The FFTs in (b) result from measurements up to 16 T using a Hanning window function. This data was taken with steps of 2°. In both (a) and (b), the dashed lines are guides to eye, to follow specific frequencies in angle.*

We reported on the same dataset in Ref. [23]. In that paper, we presented SdH data on ZrSiS with a lower resolution than the data we present in this chapter. Within the low frequency region of the FFT spectrum, only frequencies of 240 T and 600 T were clearly resolved. For this reason, we interpreted the 600 T as arising from the dog-bone. However, our dHvA oscillation data prove that this assignment needs to be revised.

In Fig. 4.5(b), we show FFTs from the torque data taken with angle intervals of 2°. Compared to the transport data, this data is much cleaner. The noise level is lower, and fewer harmonics are observed. The frequencies of the main peaks

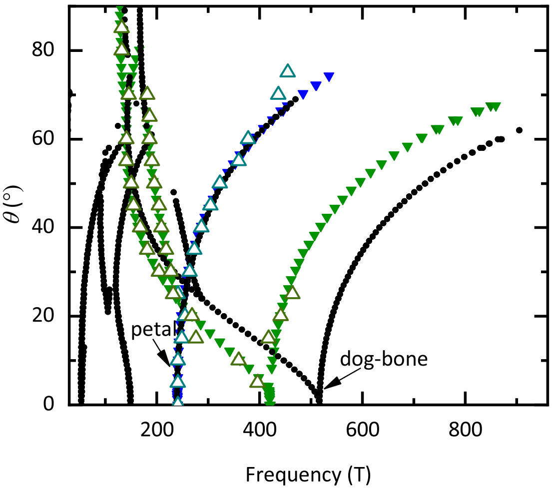

Figure 4.6: *Angle dependence of the frequencies seen in the FFTs. Black dots are calculated with DFT, filled triangles are collected from torque (dHvA) data and open triangles from transport (SdH). Blue and green triangles represent orbits arising from different parts of the FS, as indicated in this figure and illustrated in Fig. 4.1(c).*

(excluding harmonics) above 100 T that we extract from this data are shown together with the DFT prediction in Fig. 4.6. Several of the peaks seen at $B \parallel c$ cannot be traced in angle, as they disappear with only a small deviation from $B \parallel c$. These frequencies are also not included.

When plotting the experimental and theoretical frequencies together as a function of angle, it becomes clear that the frequency that is 420 T when $B \parallel c$, must arise from the dog-bone. In Fig. 4.6, we can see excellent agreement between transport and torque, as well as with the calculation for the petal. For the lower branch of the dog-bone, the frequency at small angles is less than what was predicted, but the agreement above 30° is good. The higher branch has a consistently lower frequency than calculated, but has the same shape. In general, the behavior of the experimental curve matches very well with the predictions. The observation of the two branches coming together is particularly clear. This allows us to assign the frequency of 420 T to the dog-bone with confidence, and forces us to reinterpret the peak assignment made in Ref. [23].

It is interesting to note that the DFT calculations agree with the data remarkably well, with the magnitude of the larger orbit being the only exception. This deviation can have a number of causes, including a lack of stoichiometry or an inaccuracy of the input parameters to the DFT calculations due to the temperature. The former seems unlikely, as the well-resolved quantum oscillations suggest a very high crystalline quality; the latter was discussed for the case of HfSiS in Sec. 3.1.2 and probably does play a role. This is expected to have only a small effect on the frequency however.

To explain the significant discrepancy between the predicted and measured size of the dog-bone, we must therefore consider the effect of possible electronic correlations. It is known within the field of correlated electron systems, that DFT does not capture the behavior of correlated systems with a high degree of accuracy. As correlation effects are predicted in the proximity of the nodal line, it is probable that the dog-bone pocket, which closely follows the nodal line, is indeed affected by correlations. As DFT does not take this into account, it overestimates the size of this orbit.

Finally, the very low frequencies that we observed in the dHvA FFT are not included in Fig. 4.6, because they do not appear in the SdH data at any angle and the theoretical predictions are not as clear in this frequency range. We can, however, associate these frequencies with orbits in the Γ-M-X plane or in an intermediate plane between Z-R-A and Γ-M-X.

4.3.2 Magnetic breakdown orbits

Now that we have identified the fundamental frequencies in our FFT spectrum, we turn again toward the SdH FFT spectrum. We show the spectrum in Fig. 4.7(a), where we refer to the petal as 'α' and the dog-bone as 'β', with frequencies F_α and F_β, respectively. Fig. 4.7(b) shows the FS of ZrSiS in the Z-R-A plane, indicating these two pockets. Also shown are the direction of the rotation of charge carriers around the pockets and the gap between the different pockets. In this plane, the situation is completely symmetric and there are eight identical gaps.

Aside from the α and β peaks, there are many others visible in our spectrum. Some of the other frequencies appear as sharp peaks at integer multiples of the fundamentals (i.e. $2F_\alpha$, $3F_\alpha$ and $2F_\beta$) and can be easily explained as harmonics. For the α orbit, we see the amplitude of the harmonics progressively decreasing in amplitude, whereas 2β actually has a slightly large amplitude than β. This may be due to the fact that β is close to the noise level and its amplitude is therefore very uncertain.

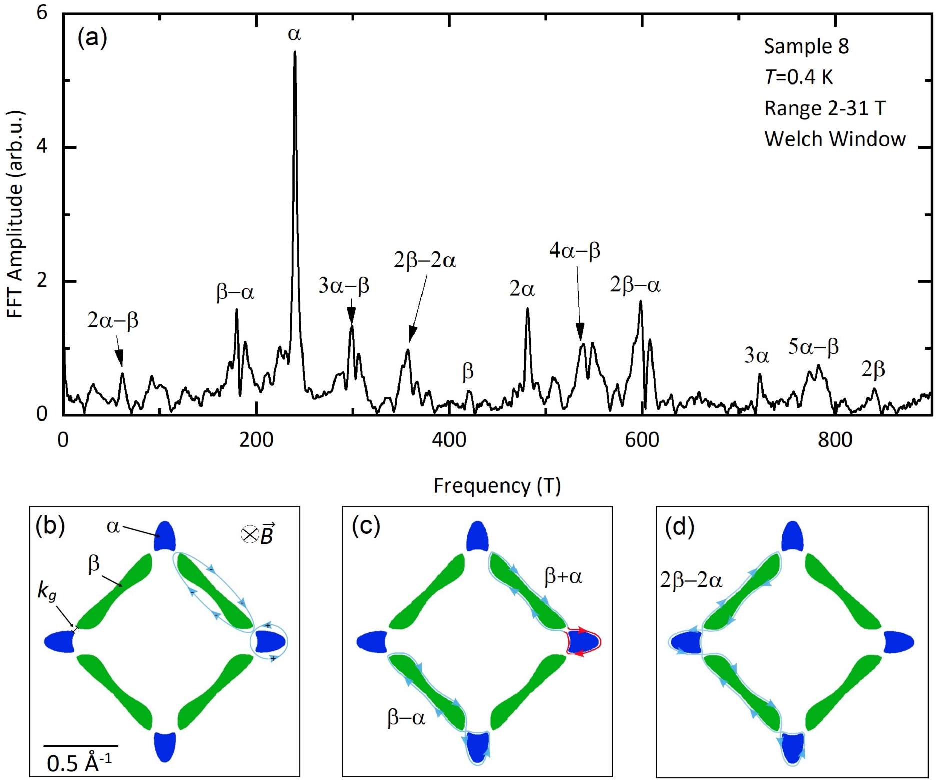

Figure 4.7: *(a) FFT of MR data of sample 8, taken at* $T = 0.4$ *K and* $B \parallel c$*. A Welch window over a range of 2 to 31 T was used for this FFT. (b) Two-dimensional cut of the FS in the Z-R-A plane. The hole pockets are shown in blue and marked* α*, the electron pockets are green and marked* β*. The gap between the two pockets is* k_g*. Also indicated is the direction of the cyclotron rotation around the pockets, for a magnetic field going into the page. (c) Illustration of the* $\beta - \alpha$ *and the forbidden* $\beta + \alpha$ *pockets. (d) Sketch of the* $2\beta - 2\alpha$ *orbit, as an example.*

The remaining frequencies are combinations of the form $|nF_\alpha - lF_\beta|$, with integer n and l. The corresponding orbits can exist due to tunneling between the two kinds of pockets, enabled by the small size of the gap, k_g. As discussed earlier, this process is called magnetic breakdown

[29, 36] and has been demonstrated in several materials, including organics [37–39] and even elemental metals such as Mg [40]. The common factor between these materials is the presence of closely spaced orbits within the Fermi surface. The crucial difference between previously reported systems and ZrSiS (as well as HfSiS, see Ref. [41] and chapter 3), is the fact that the latter has breakdown between electron and hole pockets, instead of electron and electron, or hole and hole. Because of this, we may speak of Klein tunneling in momentum space as discussed in Chapter 3 and we must consider the difference of the frequencies, not the sum.

Another aspect of the MB in ZrSiS (and HfSiS) that sets it apart from the MB in other known systems, is the presence of the nodal line. As shown in Fig. 4.1(c), the nodal line runs around the whole diamond shape in both the Z-R-A and the Γ-X-M planes. It thereby passes through each of the pockets and through the gaps between them. When a carrier tunnels through one of these gaps, it crosses the nodal line. The crossing point is therefore the point where correlation effects are most likely to occur.

Fig. 4.7(c) shows the simplest allowed breakdown orbit, $\beta - \alpha$ (180 T). As illustrated in the figure, the rotation directions of the two pockets are different, due to their different character. The fact that we have to subtract the frequencies because of this, is perhaps more intuitively clear if we consider two overlapping orbits. The rotation around the overlapping part must cancel out in that case. The same is true for the two separated orbits we have here. It should also be clear now why a sum of orbits is forbidden. The simplest of such forbidden orbits, $\beta + \alpha$ (660 T) is also drawn in Fig. 4.7(c). This requires a reversal of the rotation direction around one of the orbits, which is unphysical.

Frequencies with n and/or l larger than one are more complex. For example, the frequency $2\beta - 2\alpha$ (360 T) can look like the sketch in Fig. 4.7(d), or it can be the harmonic of the $\beta - \alpha$ orbit drawn in Fig. 4.7(c). As long as $|n - m| \leq 1$, these orbits are all semi-classically allowed. Some orbits, however, such as $5\alpha - \beta$, require that a single pocket is orbited more than once. To make this frequency, either five turns are made around one α pocket, or around two different α pockets. There cannot be more than two α pockets involved, as they both have to border the same β pocket for tunneling to be possible. No known mechanism exists for this kind of orbit that involves multiple rotations around a single pocket. In fact, this is semi-classically forbidden and has, to our knowledge, not been observed previously. It does, however, describe our data very well and may be enabled by a hitherto unknown quantum mechanical mechanism.

Going back to the FFT spectrum in Fig. 4.7(a), we now have an explanation for all of the observed frequencies. One thing that remains peculiar, however, is the fact that the difference frequencies tend to have split peaks. One peak corresponds to the calculated difference of frequencies, and the other is approximately 10 T larger. This is especially clear for $2\beta - \alpha$. A possible explanation for these split peaks could be that they are an artifact of the FFT procedure. However, if this were the case, also α and its harmonics would be expected to exhibit some splitting, but these peaks are well-defined. The splitting may therefore be caused by an unknown mechanism relating to the magnetic breakdown.

4.3.3 Effective masses

By determining the effective cyclotron masses and comparing them with theoretical predictions, we can corroborate our assignments of certain frequencies to certain orbits. First of all, the effective masses of the petal and dog-bone orbits (m^*_α and m^*_β, respectively) may be estimated directly from the DFT calculated bandstructure, using the derivative of the Fermi surface area to the energy (see Eq. B.5). Doing so, we can predict $m^*_\alpha = 0.16m_e$ and $m^*_\beta = 0.55m_e$, with m_e the free electron mass.

From the temperature dependence of the magnetoresistance data (shown in Fig. 4.8(a)), we can then determine the experimental cyclotron masses of the carriers for each orbit. We do this by plotting the amplitude of each peak in the FFT against temperature (over a fixed field window) and performing a Lifshitz-Kosevich (LK) fit as described in Appendix B. This is shown for some selected frequencies in Fig. 4.8(b). In the case of split peaks in the FFT, which occur for most breakdown frequencies, we have determined effective masses for both peaks, and found them to be the same.

The resulting masses are shown in table 4.2 for different samples and orientations. There is quite some spread in the observed masses between the different samples, and even between measurements of the same sample under different angles with the magnetic field. It is not clear why this should be the case, but it is consistently so under different ranges of magnetic field and field windows used for the FFT. It may be due to the presence of many different frequencies in close proximity, leading to leakage of the amplitudes from one peak to another. The fact that small changes in angle can have drastic consequences, not just in the mass, but in the spectrum itself, also does not help. Certain peaks may be observable at one angle, but not 3° away from it. These factors all contribute to the uncertainty in the mass determination. A further discussion of this uncertainty is included in Appendix C.

The value for m^*_α that we find experimentally for each orientation, is larger than the predicted value. Masses reported for the same frequency in literature ($0.15m_e$ [33], $0.16m_e$ [7, 14] or $0.18m_e$ [35]), however, agree well with this prediction. Therefore, we can be confident that 240 T does indeed match the α pocket, despite the larger mass we observe. The situation is different for the β orbit. Due to the low amplitude of the β peak, we are not able to determine the mass for every configuration, but for those cases where we do extract m^*_β, the theoretical and experimental values are in good agreement. This serves as a confirmation of our assignment of the 420 T frequency to the dog-bone orbit.

Now we are ready to consider the difference frequencies that we observe. According to theoretical predictions for MB, the masses of combined electron and hole orbits should add up as:

$$m^*_{n\alpha - l\beta} = n|m^*_\alpha| + l|m^*_\beta|. \tag{4.1}$$

We may check our experimental masses for agreement with this relation in order to reinforce our assignments, provided we can determine masses for α and β. For the harmonics of F_α and F_β, we see that often the masses are not the expected two (or three) times the fundamental mass, which suggests that either these masses suffer from experimental error in excess of our

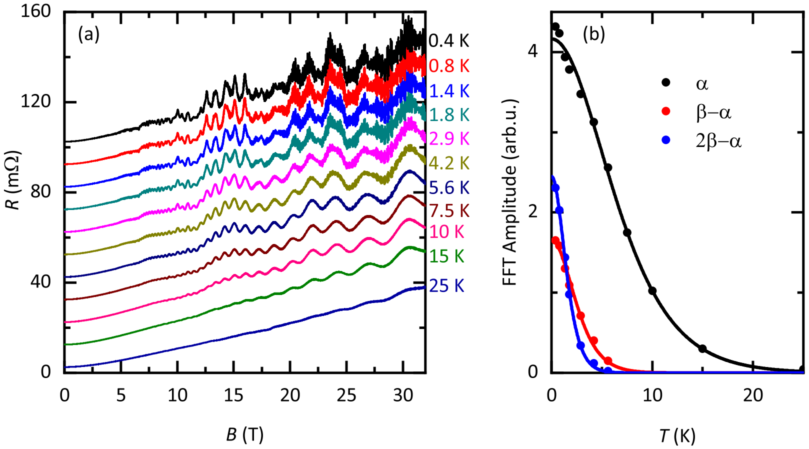

Figure 4.8: *(a) Magnetoresistance data of sample 8 at different temperatures, with $B \parallel c$. Successive curves are offset by 10 mΩ. (b) Temperature dependence of the amplitude of selected frequencies, with LK fit.*

estimate, or the harmonic masses are being adjusted by an unknown mechanism beyond the standard LK theory.

However, for all configurations in which we can find a mass for β, we see that, $m^*_{\beta-\alpha} = m^*_{\beta} + m^*_{\alpha}$, as predicted. This is the same result as that reported for HfSiS in chapter 3 and Ref. [41]. However, in ZrSiS, we can extend this result to $n, l > 1$. In that case, the masses still work out for most combinations of α and β, with exceptions only for the $4\alpha - \beta$ orbit in sample 8 and the $2\beta - \alpha$ in torque. This means the relationship of Eq. 4.1 usually holds even for the forbidden orbits where $|n - l| > 1$. It is not clear what is the physical mechanism behind these orbits, but this result suggests that carriers can indeed make multiple turns around one orbit when breakdown to another orbit is involved. In general, the fact that the masses of most α and β combinations add up as theoretically expected, confirms our assignment of these orbits to magnetic breakdown.

4.3.4 Angle dependence of breakdown orbits

The probability of magnetic breakdown depends strongly on the size of the gap between the pockets, k_g. As the magnetic field is tilted away from the c-axis, the extremal orbits tilt together, as they always exist in planes perpendicular to the magnetic field. This means they will no longer have the shape illustrated in Figs. 4.3(b)-(d). For this reason, the gap is expected to increase significantly with angle and at some point can no longer be crossed because α and β are in different planes. Experimentally, this means we expect the breakdown orbits to vanish within a few degrees away from $B \parallel c$.

F (T)	Orbit	Sample 8 ($\theta=0°$)	Sample 8 ($\theta=3°$)	Sample 9 ($\theta=0°$)	Sample 9 ($\theta=3°$)	Sample 4 ($\theta=1°$)	Torque ($\theta=0°$)
240	α	0.31±0.03	0.19±0.02	0.21±0.01	0.217±0.008	0.245±0.009	0.2±0.1
420	β	-	0.6±0.1	-	0.47±0.04	-	0.60±0.09
480	2α	0.45±0.09	0.6±0.2	0.38±0.03	0.38±0.04	0.41±0.02	-
720	3α	-	-	0.71±0.06	-	-	-
840	2β	-	1.01±0.04	-	0.97±0.02	-	-
180	$\beta-\alpha$	0.8±0.2	0.7±0.2	0.74±0.06	0.63±0.05	0.58±0.01	0.73±0.06
360	$2\beta-2\alpha$	1.43±0.09	-	1.2±0.3	-	1.0±0.3	-
600	$2\beta-\alpha$	1.38±0.06	1.18±0.05	1.2±0.1	1.0±0.1	1.04±0.04	1.02±0.04
300	$3\alpha-\beta$	1.2±0.1	-	-	-	-	1.02±0.09
540	$4\alpha-\beta$	2.1±0.1	1.69±0.07	1.81±0.04	-	-	-
780	$5\alpha-\beta$	1.61±0.05	1.66±0.05	1.2±0.1	1.6±0.2	-	-

Table 4.2: *Frequencies <1000 T and their associated masses (in units of the free electron mass, m_e), for different samples and orientations. The table is divided into three categories. From top to bottom: fundamental frequencies and their harmonics, allowed breakdown orbits, and semi-classically forbidden breakdown orbits.*

We verify this theory by measuring MR in sample 8 at small tilt angles with respect to the magnetic field. The resulting FFTs are plotted in Fig. 4.9. In contrast to what we have seen for magnetic breakdown in HfSiS (Chapter 3), breakdown orbits are not all obviously vanishing within this angle range. For this reason, we consider their amplitudes in the FFT.

For most of the breakdown frequencies (look, for example, to 180 T and 300 T), a reduction in amplitude is seen with at least 1° of misalignment, although the amplitude does not go to zero within 3°. As the gap in ZrSiS is considerably smaller than that in HfSiS, this is in line with the expected behavior for breakdown orbits. One of the orbits that we attribute to magnetic breakdown, however, shows a very different behavior. The 600 T frequency (assigned $2\beta-\alpha$) is peculiar, as it presents a minimum at 0°, and a maximum at 1.5°.

Not only the breakdown orbits are affected by the tilting of the field, but so are the fundamentals and their harmonics. In fact, the amplitudes of β depends strongly on the angle. For $-1<\theta<1$, β is in the noise level. Outside this range, however, β and especially 2β grow strongly in amplitude.

It is possible to explain this effect qualitatively by assuming that, at $\theta=0°$, the probability of completing a β orbit is low due to the large density of states and the strong curvature of the pocket near the point where the gap opens. At that point, the band bends over and becomes horizontal in the energy plane, thus producing a spike in the density of states. This then leads to a marked increase in the scattering probability at this 'hot spot' exactly where the Fermi level crosses the nodal line. Because of this, the carriers are unlikely to close a β orbit.

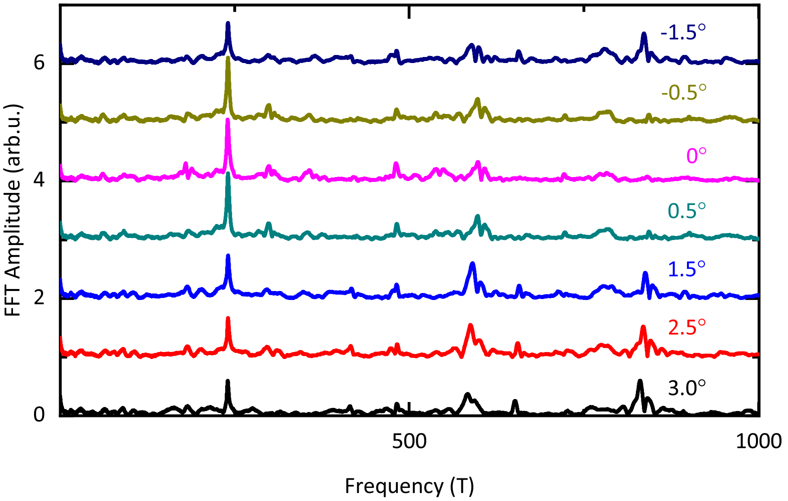

Figure 4.9: *FFTs of MR data of sample 8, for different small angles away from* $B \parallel c$*. The measurements were done at 1.4 K and a Welch window with a 2-31 T range was used for the FFTs.*

They can, however, tunnel to the α pocket and complete a breakdown orbit thereby avoiding the scattering 'hot spot' and crossing the nodal line. Therefore, β (and even more so 2β) are suppressed, while breakdown orbits that do not involve multiple turns around one β pocket, are not.

Then, upon tilting the field, the local curvature of the pocket changes and the scattering probability is reduced and so one or more orbits around β become more likely. This explains a rise of the β and 2β amplitudes, as well as an initial rise of $2\beta - \alpha$ (when the increased probability of an orbit around β outweighs a reduced probability to tunnel to α) followed by a decrease (when the tunneling probability becomes too low).

One observed frequency was so far not discussed, and that is the one of 660 T. This corresponds to $F_\beta + F_\alpha$ and is semi-classically forbidden. However, we see that a peak at 660 T appears for $\theta > 1°$, together with β. A possible explanation for this may be magnetic interaction, which will be discussed in Sec. 4.3.6.

4.3.5 Development of the oscillations in a magnetic field

Next we study the development of the quantum oscillation spectrum under the influence of a rising magnetic field. We do this by taking FFTs over increasing field windows, starting with a window of 1-2 T while incrementing the upper limit one tesla at a time until 31 T. The result is shown in Fig. 4.10.

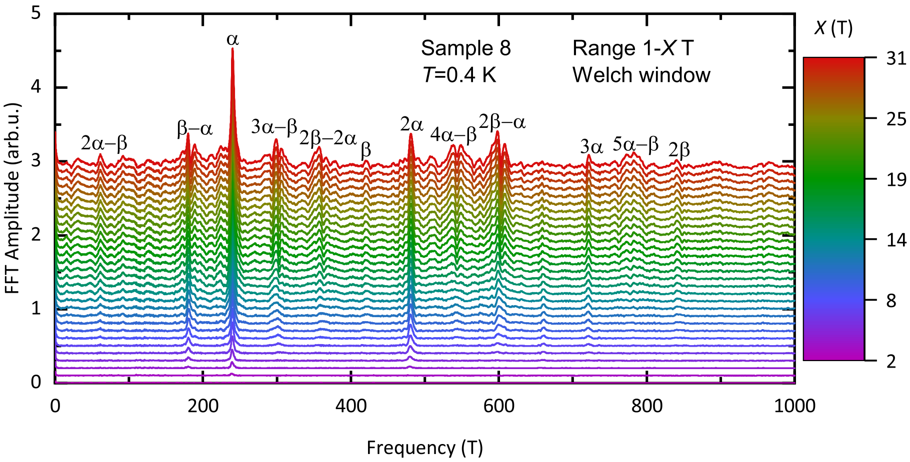

Figure 4.10: *Low frequency FFT of sample 8 at $T = 0.4$ K, for increasing field ranges from 1 T to X T.*

Fig. 4.10 allows us to determine the onset of each of the low frequency orbits. The results are shown in Table 4.3. The first frequency to appear when incrementing the field is, not surprisingly, F_α. For the other fundamental, F_β, we have to go up to at least 8 T in order to see it. In fact, several of the breakdown orbits appear at lower fields than β. However, aside from this, there appears to be a general trend of a higher number of gaps involved in breakdown (or a larger number of turns around a single pocket) leading to a higher onset field, as expected.

There is one anomaly present in Table 4.3, namely the frequency of 660 T. This frequency is in fact forbidden and should not be observed. In Fig. 4.10, we can see that it does appear at a certain field. However, since it grows very little in field, it disappears into the noise level when the FFT range extends up to higher fields. A possible explanation for this frequency is offered in Sec. 4.3.6.

Frequency (T)	Assignment	Number of gaps	Onset field (T)
240	α	0	3
420	β	0	8
480	2α	0	4
720	3α	0	6
840	2β	0	8
180	$\beta - \alpha$	1	4
600	$2\beta - \alpha$	1 or 2	6
60	$2\alpha - \beta$	1 or 2	7
360	$2\beta - 2\alpha$	1, 2 or 3	8
300	$3\alpha - \beta$	1 or 2	6
540	$4\alpha - \beta$	1 or 2	8
780	$5\alpha - \beta$	1 or 2	11
660	$\beta + \alpha$	-	5

Table 4.3: *Minimal magnetic fields required to observe each orbit, correlated with the number of gaps involved in breakdown.*

4.3.6 Magnetic interaction effects

In Sec. 4.3, it was explained that an orbit $\beta + \alpha$ is strictly forbidden. However, under some circumstances, it is possible to observe a small peak at this frequency (660 T). While in Fig. 4.3(a) it is below the noise level, one can perceive some amplitude at this frequency in Figs. 4.9 and 4.10. This can be explained with magnetic interaction (MI, see also Sec. 3.5 for more details), which occurs because the oscillations are a function of B, rather than H. As $B = \mu_0(H + M)$ and M is an oscillating quantity, this leads to different frequencies. For example, if M is to first order oscillating with two frequencies, then taking into account MI, oscillations are possible with frequencies that are combinations of the two fundamentals.

It is straightforward to simulate this effect; the result is shown in Fig. 4.11. We start out by simulating M using the LK equation (see appendix B) depending on H, using the two frequencies F_α and F_β. We take into account all unknown damping factors, such as the Dingle term, (we cannot extract these parameters by directly fitting the data to the LK equation, as there are too many different frequencies to make an acceptable fit) as a constant that we adjust such that the ratio of the two fundamental amplitudes in the FFT matches to the experimental data. For the second order, we use the same LK equation, but as a function of $H + M$.

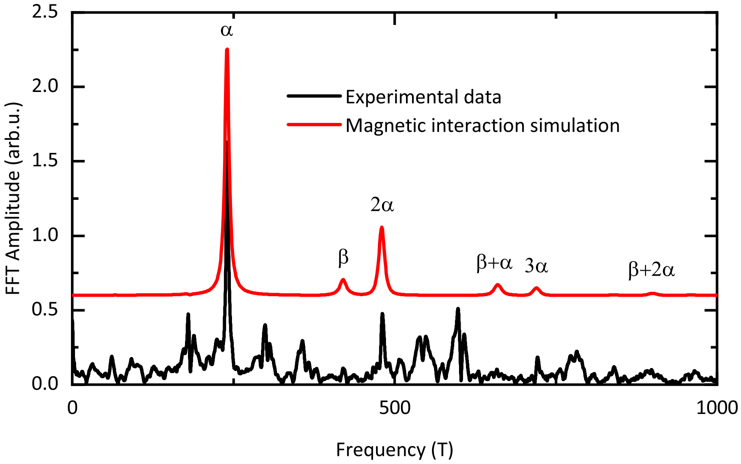

Figure 4.11: Simulation of the effect of magnetic interaction in our system, with a comparison to experimental data. The simulated data is offset for clarity.

The resulting FFT reproduces β and α with its harmonics, with relative amplitudes in good agreement with the experimental data. Two additional frequencies, $F_\beta + F_\alpha$ and, very weakly, $F_\beta + 2F_\alpha$, appear. These frequencies are semi-classically forbidden and can therefore not result from magnetic breakdown. The fact that the $F_\beta + F_\alpha$ frequency does arise from our MI simulation, suggests that MI is a valid explanation of why we observe this frequency under certain conditions.

4.3.7 Analysis of the possible mass enhancement

We reported an enhancement of the cyclotron mass of the 600 T frequency in Ref. [23]. Such a field-induced mass enhancement may be a sign of correlation effects, and is therefore of considerable interest. In Ref. [23], the frequency of 600 T was attributed to the dog-bone pocket which runs parallel to the nodal loop, where the Coulomb interaction is only partially screened. This suggests that residual Coulomb interactions lead to an enhancement in m^*, contrary to what is known to occur in graphene, where a partial screening of Coulomb interaction leads to a reduction in m^* [42, 43]. Within our present understanding, we interpret 600 T as $2\beta - \alpha$ instead of β, but the same considerations continue to apply. Nevertheless, the question arises whether there is an enhancement of β individually. We address this question below.

First we consider the data for the 600 T frequency. The data shown in Ref. [23] were collected using sample A, and confirmed in sample 33. Since then, we have gathered additional SdH data on three more samples in multiple orientations, as well as dHvA data on one sample. For each of these configurations, we have looked for this mass enhancement. Fig. 4.12(a) shows the LK fittings we performed with different field ranges, for one of these samples. The quality of these fits is good, but errors may arise from the same sources as discussed previously. Since we are looking at small field windows, the resolution of this data is significantly reduced, and thus the problem of amplitude leaking between peaks is exacerbated.

Each of the curves in Fig. 4.12(a) makes for one point in the m^* versus B plot of Fig. 4.12(b). The field windows are chosen to have equal size in B^{-1} (i.e. $B_1^{-1} - B_2^{-1}$ is constant) and the average fields are determined as $\overline{B} = 2/(B_1^{-1} + B_2^{-1})$.

Within our current interpretation of the 600 T frequency, we expect an effective mass of approximately 1.2-1.4m_e, based on the experimental masses of α and β. Many of the masses shown in Fig. 4.12(b) are within this range, so any mass enhancement is likely to be weak. This is in contrast with our report in Ref. [23], where the band mass was predicted to be 0.55m_e as expected when $F_\beta = 600$ T and a clear enhancement was seen. The present dataset is still broadly consistent with the notion of an increasing m^* in field as reported in Ref. [23], but it is difficult to quantify due to the spread of the data.

Partially screened Coulomb interactions due to the proximity to the nodal line were previously mentioned as a possible explanation for a field-induced mass enhancement of the β pocket. We note that, for the $2\beta - \alpha$ orbit, this effect should be stronger. In order to make this orbit, a charge carrier tunnels through two gaps and thus crosses the nodal line twice. This increases the probability of correlation effects for this orbit.

A possible alternative explanation for a trend of increasing mass in field could be the onset field of the orbit. As we now believe the 600 T frequency arises due to magnetic breakdown, it must have a certain onset field, B_0, associated with it. This onset field depends on the square of the gap between the pockets and therefore depends on the angle of the sample with the field. For this reason, the orbit will start to appear at a different field in every experiment (because no two samples are ever *exactly* at the same angle, even if we make every effort to align $B \parallel c$). This has consequences for the determination of the field-dependent mass, as we need to make FFTs over different field windows, which may or may not contain B_0. The consequence of such an effect would be a mass that first appears to increase with field and then stabilizes. Only when it is stable would we obtain the real mass. However, there is no guarantee that this point is always reached.

Finally, we turn to the field dependent masses of the α and β orbits, shown in Fig. 4.12(c). Having made the correct assignment of β, it is clear that there is no obvious enhancement in m^* for either the petal or the dog-bone orbits, although we note the large spread in m^* for β.

4.4 High frequency breakdown orbits

We now turn to the high frequency part of the FFT spectrum. In Fig. 4.13, we show the SdH FFT spectrum of sample 8, where a large number of frequencies between 7.5 and 11.5 kT is visible. Based on the DFT calculations, there exists no single pocket in the FS of ZrSiS that can account for such large frequencies. This strongly suggests that these frequencies results

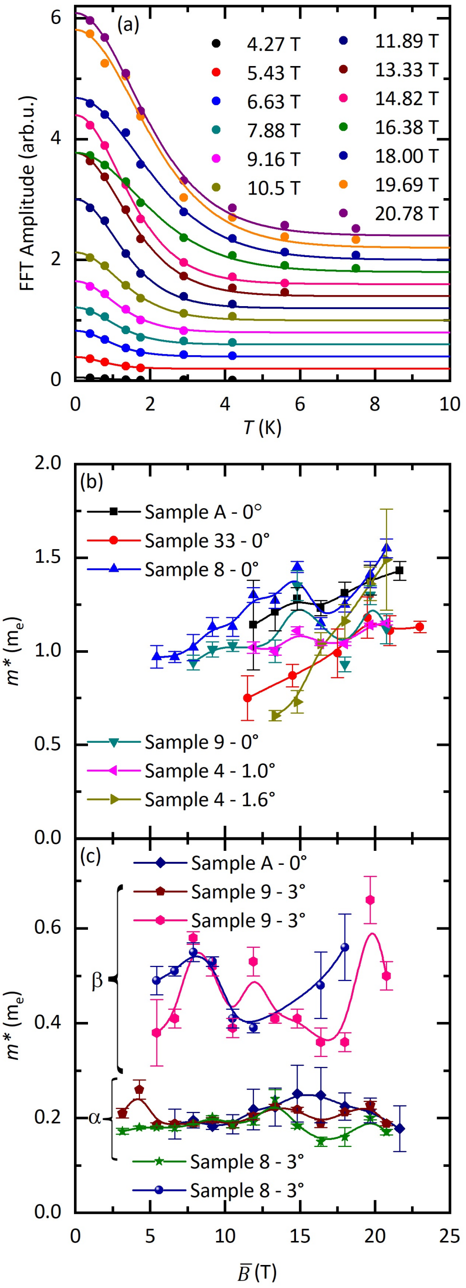

Figure 4.12: *(a) FFT amplitude of the 600 T ($2\beta-\alpha$) frequency for different field windows, with LK fitting. Data are from sample 8, with $\theta = 0°$. The legend lists the average fields of the window. Successive curves are offset for clarity. (b) Determined masses associated with the 600 T frequency for several configurations, as a function of the average magnetic field. (c) Field dependences of the masses of the α and β in different configurations.*

from magnetic breakdown around the full diamond shape of the FS, because only when the area in between the four electron and four hole pockets is included, can such a large frequency appear. This process then involves tunneling through each of the eight gaps in the Brillouin zone and is possible under the same conditions as the low-frequency breakdown, only with a lower probability.

According to DFT calculations, the area in between the pockets should be ~6 kT. We call this area A (illustrated in Fig. 4.14 in gray). Fig. 4.14(a) and (b) show the two simplest orbits that included A and are allowed, $A + 4\alpha$ (DFT: 6.9 kT) and $A + 4\beta$ (DFT: 8.1 kT). Other orbits around A, such as $A + 2\alpha$, $A + 3\beta$ or A itself, are semi-classically forbidden for the same reason as $\beta + \alpha$ being forbidden. It would require a reversal of the rotation direction of the charge carrier. Orbits that *are* allowed are of the form $A + 4\alpha - n\beta$ or $A + 4\beta - n\alpha$, with integer n. Fig. 4.14(c) and (d) illustrate examples of this kind of orbit.

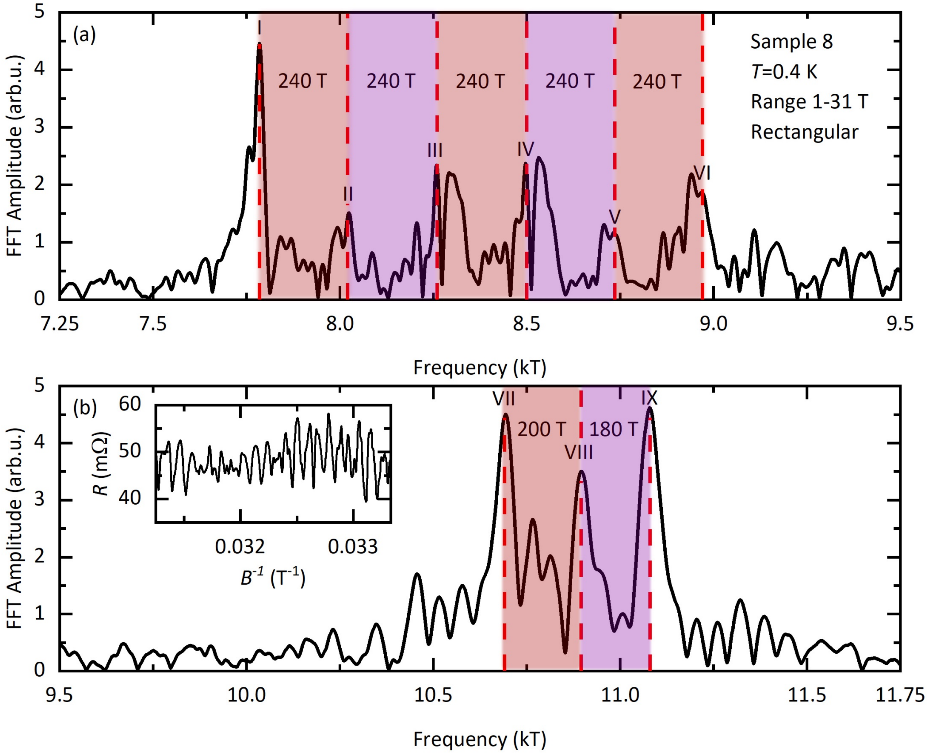

Figure 4.13: *(a) The "A" group of high frequency oscillations in the FFT, over a range of 7250 to 9500 T. (b) The "B" group, over 9500 to 11750 T. Inset: magnetoresistance showing the high frequency oscillations between 30 and 31 T, plotted as a function of* B^{-1}.

For a more detailed analysis, we have divided the high frequency FFT of the SdH data

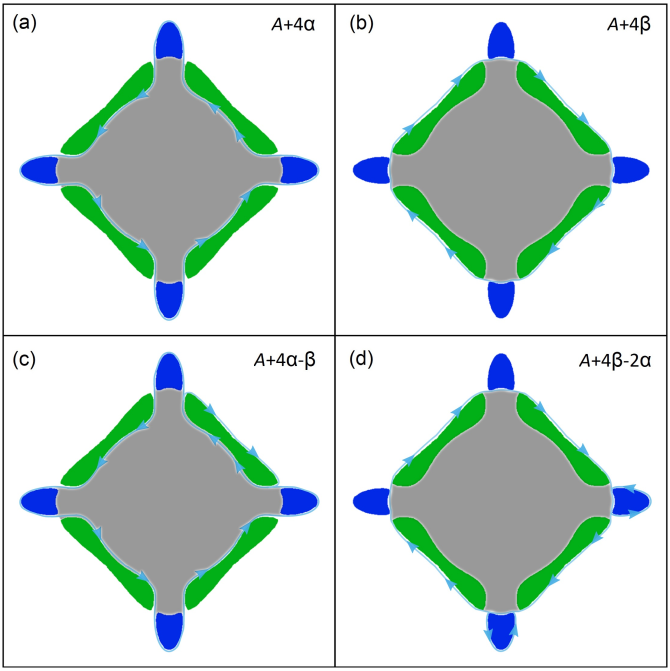

Figure 4.14: *Examples of allowed high frequency orbits in the Z-R-A plane of the FS. The gray area is A. (a) $A+4\alpha$, (b) $A+4\beta$, (c) $A+4\alpha-\beta$ and (d) $A+4\beta-2\alpha$. The orbits shown in (a) and (b) are the most fundamental allowed high frequency orbits; the others are formed by subtracting individual pockets from them.*

(Fig. 4.13) into two (equally sized) parts; one $7250<F<9500$ T and the other $9500<F<11750$ T. In this way, we highlight the existence of two different groups of frequencies, that we refer to as the "A" and "B" groups, respectively. When comparing Fig. 4.13(a) and (b), it is immediately apparent that these two groups are different, as the typical spacing between adjacent peaks is distinctive.

Six of the tallest peaks in group A are marked I-VI in Fig. 4.13(a). The most important observation here, is the fact that each of the marked peaks has a frequency 240 T larger or smaller than its neighbors. This is consistent with the addition or subtraction of F_α, implying that consecutive orbits enclose an ever increasing number of α pockets (e.g. $A+4\beta-n\alpha$). However, this pattern is not continued in the B group (Fig. 4.13(b)), where the spacing between the largest peaks is ~200 T for VII and VIII, and ~180 T for VIII and IX.

Each of these peaks has another tall peak beside it, separated by approximately 30 T. This is especially clear for peaks III and IV. Based on the FS with the two pockets α and β participating in magnetic breakdown orbits, the origin of this 30 T spacing is not obvious. The smallest linear combination of α and β is 60 T, so an orbit made of these two elements cannot, in principle, have frequency differences less than 60 T. However, a ~10 T splitting was observed for the low frequency breakdown frequencies and may be related.

When comparing the experimental results to the theoretical predictions, we see that the present theory describes many of our observations. In particular the 240 T separation between the major peaks suggest orbits of the form $A + 4\beta - n\alpha$ for the A group. Evidently, the real magnitude of the A orbit must be larger than calculated by DFT for this scenario to work. Considering the fact that the β orbit is actually overestimated by DFT, this seems reasonable. The large number of observed peaks other than the six major ones, may however require the inclusion of semi-classically forbidden orbits.

In principle, frequencies that are semi-classically forbidden, can still be observed through the magnetic interaction effect. This was discussed in Sec. 4.3.6 for the low frequencies, and was found to be a possible explanation of the forbidden $\alpha+\beta$ frequency. We attempted to simulate this effect also for the high frequencies, and we see that it can lead to additional frequencies, beside the ones that are included in the simulation. However, since we do not know which of the observed frequencies correspond to which orbits, we cannot determine which of them are allowed or not and we cannot perform an accurate simulation of this specific situation. In any case, MI cannot explain peaks separated by less than 60 T in the A group.

Finally, the fact that the A and B groups are well separated and have a different density of peaks, suggests that the B group originates from a different part of the FS, specifically the Γ-M-X plane. The gap in this plane is predicted to be an order of magnitude larger than in the Z-R-A plane, so breakdown should be considerably less probable, but not forbidden. However, in Sec. 4.3, we attributed only frequencies lower than 100 T to the Γ-M-X plane. This means that breakdown in this plane would lead to a small range of closely spaced high frequencies, and cannot explain the >1 kT breadth of either group, unless an additional larger pocket is present.

4.4.1 Suppression of MB with small changes in angle

When we tilt the magnetic field, we see that the high frequency orbits are rapidly suppressed, consistent with the notion of magnetic breakdown. Raw data and FFTs demonstrating this fact can be found in Fig. 4.15(a) and (b). It is noteworthy that the B group is less sensitive to angle changes than the A group, as it confirms it has a different origin. Assuming these B frequencies are still caused by magnetic breakdown, this suggests that a different gap is involved, with a different local curvature. This gap may grow more slowly with angle, or the curvature can be more favorable to breakdown.

We performed a simulation of the gap size in the Z-R-A plane as a function of angle and determined how much attenuation of the breakdown frequencies should take place as a consequence of this increase in gap. The results of these simulations are shown in Fig. 4.16(a) and (b), respectively. As can be seen, k_g increases almost linearly as the angle increases. With no other influence on the breakdown field, it would therefore be quadratic in θ. However, this also

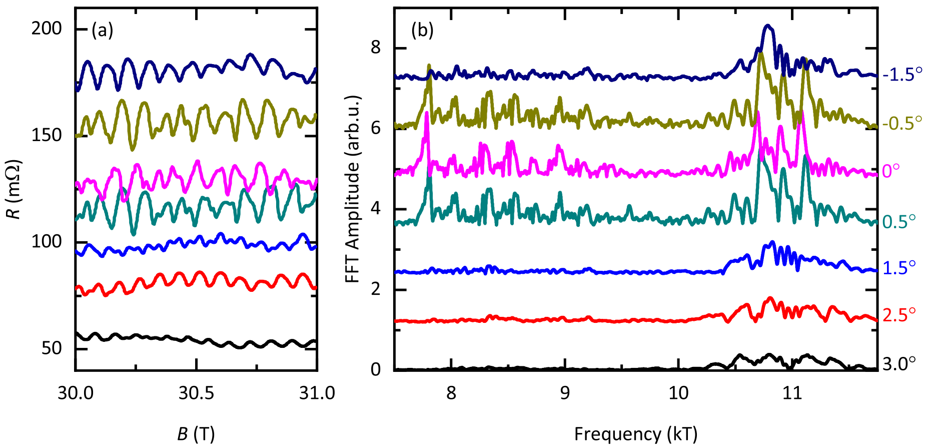

Figure 4.15: *Angle dependence of the high frequency oscillations. (a) MR data highlighting part of the high field region where fast oscillations occur. Successive curves offset by 25 mΩ for clarity. (b) Corresponding FFT spectra, made over a 1-31 T range using a rectangular window function.*

depends on the curvature. As the angle changes, so does the shape of the orbit.

In Fig. 4.16(b), we show the attenuation together with the normalized amplitude of peak I, as well as the normalized, integrated amplitudes of the whole A and B groups. We only plot the integrated amplitude for B, because we are not able to include an individual peak from the B group, as the frequencies in this group disperse strongly with angle. It is therefore not straightforward to follow a single frequency and determine how its amplitude decays. For the A group, we integrate over a range of 7.25 to 9.5 kT and for the B group over 9.5 to 11.75 kT. Before normalizing to the $\theta = 0°$ value, we subtract a background determined by integrating over the same size of range, but without any oscillation amplitude.

Looking at both the I frequency and the A group, we see a reasonable agreement with the calculation. The agreement between the single frequency and the group is also good, confirming that it is a fair comparison to consider the whole group, with the only exception being the data point at 1°. This point is enhanced when looking at the integrated amplitude, because some of the frequencies (such as II and VIII) increase in amplitude over this range. For the B group, on the other hand, we see a clear deviation from the theory, suggesting that a different gap is involved in the B group breakdown.

Considering that the simulation was done for the gap in the Z-R-A plane and the A group agrees fairly well with it, it makes sense to attribute this group to a number of orbits in the Z-R-A plane. This attribution also fits well with the 240 T spacing seen between the major peaks in the FFT spectrum. Most likely, the B group then arises from the Γ-M-X plane. However,

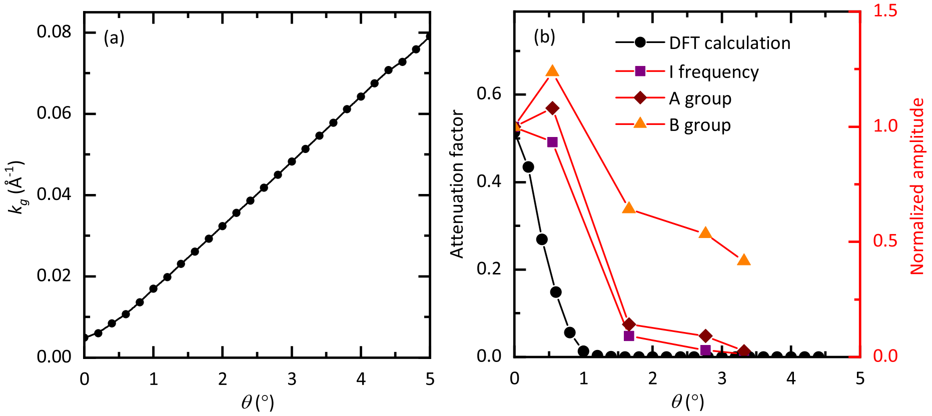

Figure 4.16: *(a) Simulation of the gap size in the Z-R-A plane as function of the angle between the magnetic field and the c-axis. (b) Corresponding attenuation factor of the magnetic breakdown, plotted together with the normalized amplitudes of the frequency I from the A group and the integrated, background-subtracted A and B groups.*

we lack a simulation of the attenuation in this plane to compare with the angle dependence of the B group amplitude in order to confirm this.

4.4.2 Onset fields of high frequency breakdown orbits

In Fig. 4.17, we show the development of the high frequency FFT spectrum in increasing magnetic field, allowing us to make an estimate of the onset fields of the magnetic breakdown. These onset fields are shown in Table 4.4. All peaks in either group come up together, with low amplitude peaks becoming visible at higher fields.

Group	Onset field (T)
A	9
B	13

Table 4.4: *Onset fields of the high frequency magnetic breakdown orbits by group.*

The higher onset field of the B group is evident from Fig. 4.17 and suggests that the breakdown gap that is being bridged to form this group of frequencies is larger than that of the A group by approximately 20%, as the breakdown field is ∼45% larger (and $B_0 \propto k_g^2$). Considering the DFT calculated FS, there is only one possibility of a larger gap in the system and that is in the Γ-M-X plane. According to DFT, this gap is an order of magnitude larger than that in the Z-R-A plane, though this is clearly an overestimation. A more serious concern is the fact that the frequencies we have identified as belonging to orbits in the Γ-M-X plane are all smaller than 100 T. It is unlikely that breakdown involving these orbits can account for the peak spacing or

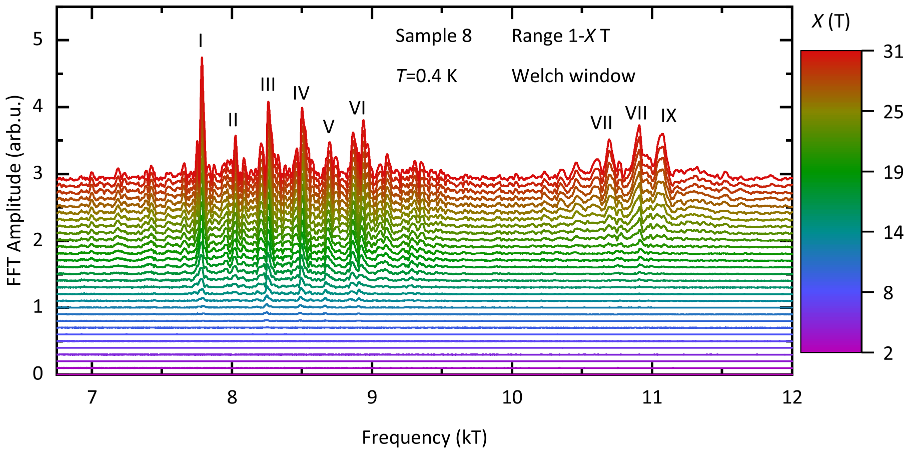

Figure 4.17: *High frequency FFT of sample 8 at $T = 0.4$ K, for increasing field ranges from 1 T to X T.*

the overall breadth of the B group. For these reasons, assignment of the B group to this plane is not obvious and perhaps requires the presence of a larger pocket in the Γ-M-X plane whose fundamental is not detected in our measurements or coincides with another orbit within the Z-R-A plane.

4.4.3 Effective masses and survival to high temperatures

In Fig. 4.18, we show the development in temperature of the high frequency SdH oscillations and their spectrum. The most striking observation here is the persistence of certain frequencies up to very high temperatures. This effect will be discussed in detail below, but first we take a look at the largest peaks (I-IX) and study the temperature dependence of their amplitudes. From this, we are able to determine effective masses, using the Lifshitz-Kosevich (LK) equation (described in detail in Appendix B).

In order to achieve an accurate determination of the mass, we choose the field range of our FFT such that the relevant oscillations exist throughout the whole window, but the range is large enough to allow good resolution. A range from 15.624 to 31 T ($\overline{B} = 20.78$ T), with a rectangular window function, is a good compromise. As an example, Fig. 4.19 shows the resulting data together with the LK fitting for peaks I, III and VII. The frequency marked as III is split into two peaks that behave differently in temperature. We denote these two as IIIa and IIIb for the lower and higher of the two frequencies, respectively. The masses associated with these and other major peaks determined for samples 8 and 9, and for the torque measurement, are shown in table 4.5. Some frequencies are not observed in particular configurations, or have too little resolution; in those cases, we could not determine a mass.

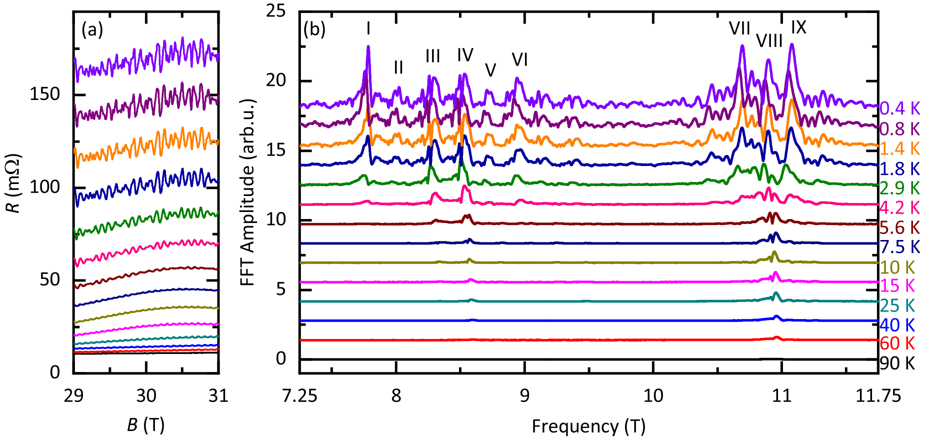

Figure 4.18: Temperature dependence of the high frequency SdH oscillations in sample 8. (a) Raw data, showing only the highest field range. The curves are offset for clarity. (b) Corresponding FFT spectra, made with a rectangular window function over a field range of 15.624-31 T.

Overall, the masses show a fair agreement between the samples. The largest deviations are found for peak I, which in torque has a significantly higher mass. This may be related to the fact that the amplitude of I is strongly reduced in torque as compared to either of the two transport samples.

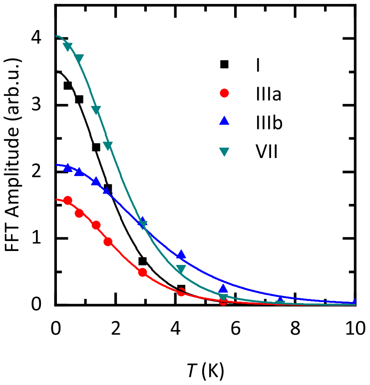

Figure 4.19: Amplitudes of selected SdH peaks as a function of temperature, with LK fitting.

It is interesting to note that the two peaks of a pair always have markedly different effective masses associated with them. This suggests that we are not looking at an artifact of the FFT procedure, but at two similar, but different frequencies corresponding to actual physical effects. However, we are not aware of any effect that could lead to the observation of two peaks with significantly different masses, and a spacing of ∼30-40 T.

As the most likely explanation for the major peaks is breakdown of the form $A + 4\beta - n\alpha$, the masses should differ by m^*_α for frequencies spaced by F_α. Such addition is not obvious in the data (see table 4.2), but nevertheless these high masses (for a Dirac system) likely originate from the combination of the masses of numerous pockets involved in the MB.

	Frequency (T)	Sample 8	Sample 9	Torque
I	7780	1.8±0.06	1.61±0.05	2.1±0.1
IIa	7990	1.6±0.1	1.52±0.08	-
IIb	8020	1.9±0.2	-	1.4±0.2
IIIa	8260	1.5±0.1	1.3±0.1	1.2±0.1
IIIb	8290	0.98±0.07	0.86±0.06	-
IVa	8500	1.20±0.03	0.91±0.07	0.9±0.3
IVb	8530	0.81±0.06	0.73±0.06	-
Va	8690	-	-	1.7±0.2
Vb	8730	1.5±0.1	1.3±0.1	-
VI	8940	1.4±0.1	1.1±0.1	1.2±0.2
VII	10690	1.5±0.1	1.36±0.08	-
VIII	10900	1.1±0.1	1.2±0.1	-
IX	11080	1.4±0.1	1.3±0.1	-

Table 4.5: *Frequencies I-IX and their associated masses (in units of the free electron mass, m_e), for different samples with $B \parallel c$. Frequencies designated with a or b are the lower and higher of a split frequency, respectively. The frequencies listed in the table are those of sample 8. Sample 9 has frequencies that are systematically ∼30 T larger, and the torque sample exhibits deviations of maximum 20 T from sample 8. The exception is frequency Va, which is only observed in torque.*

Persistence of the oscillations up to high temperatures

Already in Fig. 4.18, it is possible to see certain frequencies persisting to very high temperature, both in the A and in the B group. In Figs. 4.20(a) and (b), we highlight the relevant parts of the FFT spectrum in order to study this effect in more detail. It is clear now that most high frequencies do not survive beyond $T = 4.2$ K, with only five exceptions, some of which are not fully suppressed even at 90 K.

The high-T frequencies follow the same pattern of pairs of peaks, separated by ∼30-40 T, but cannot be connected with any of the major frequencies (I-IX) discussed for the low-T spectrum. Following the development of these peaks with decreasing temperature is in fact difficult, because there are small shifts in frequency with changes in temperature and the major peaks dominate at low T. Below 4.2 K, those peaks that appear to survive to high T, are typically smaller side-peaks of the major ones. Nevertheless, it is possible to make a

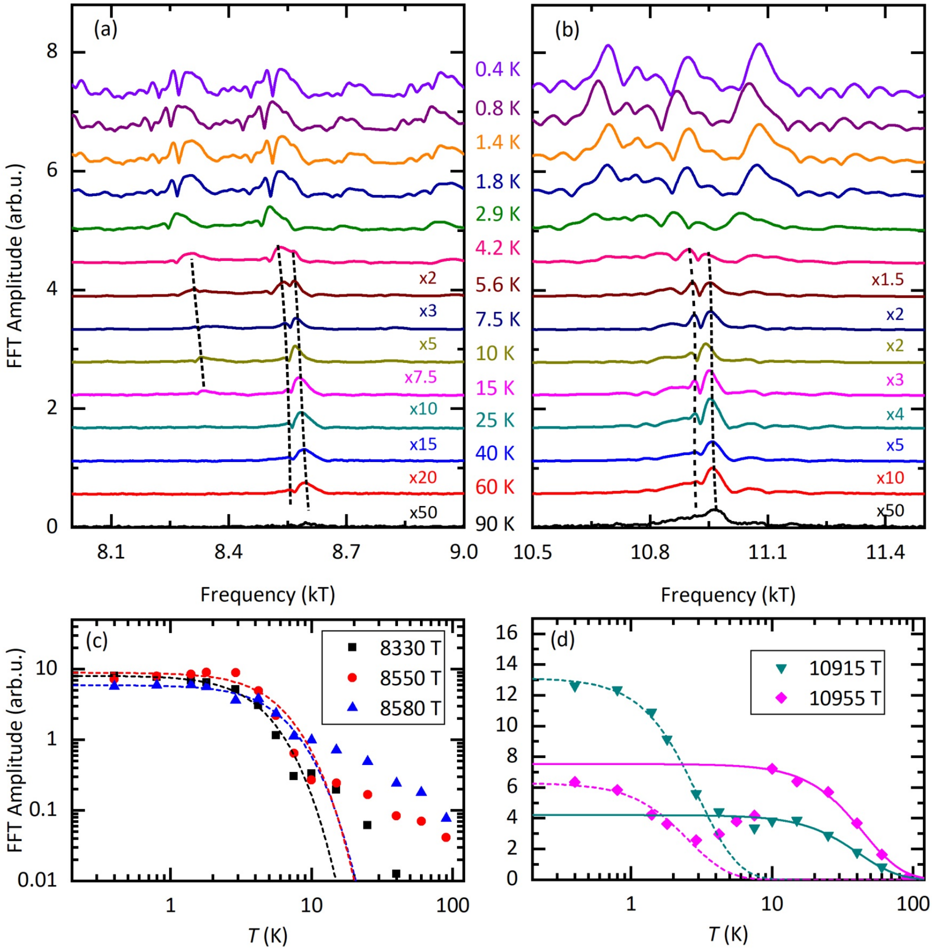

Figure 4.20: *Highlights of Fig. 4.18(b), showing the high temperature tail of the SdH oscillations for (a), the A group and (b), the B group. The dashed lines are guides to the eye. (c) Amplitude versus temperature for the high temperature frequencies in the A group, with LK fitting over the low-T range. (d) Amplitudes in the B group, with fitting over two different ranges.*

reasonable estimate of the amplitudes of each of the peaks over the whole temperature range. The results of this are shown in Figs. 4.20(c) and (d).

The amplitudes as a function of temperature of the five high-T peaks have a quite anomalous behavior. They do not follow the standard LK behavior (see appendix B), but instead they appear to first decrease as usual, and then start a much slower decline. Within the B group

(Fig. 4.20(d)), the amplitude even increases between 4 and 10 K. In the A group, the 8330 T frequency survives over a smaller temperature range and no amplitude increase is seen.

The data in Fig. 4.20(d) is reminiscent of that predicted in Ref. [44], which discusses a kind of quantum oscillation with anomalous temperature dependence similar to our observation that can occur in narrow-gap insulators with band inversion. ZrSiS does have a small spin-orbit coupling-induced gap, so this scenario could apply. Within this model, when the chemical potential is inside the gap, but asymmetric between the two bands, numerical calculations reveal that a phase shift occurs at a certain magnetic field and a suppression of the oscillation amplitude occurs at a certain temperature. These effects should be different between quantities derived from the grand canonical potential, such as the magnetization, and quantities that depend on the DOS, such as the resistivity.

As seen in Fig. 4.21, we do indeed have a temperature-induced phase shift around 6 K. Below ∼30 T, the low- and high-temperature oscillations are in phase, but above ∼30 T, they are shifted by π. Such a phase shift, though different in detail from the predictions, suggest that a scenario such as that proposed by Ref. [44] may explain the anomalous temperature dependence that we observe.

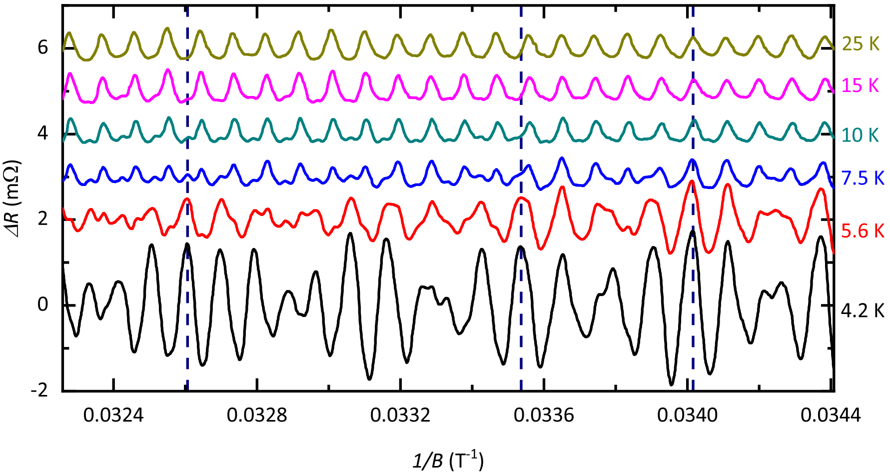

Figure 4.21: *MR data of sample 8 after subtraction of a smooth background and low frequency oscillations, for different temperatures, plotted for high field as a function of* B^{-1}*.*

Furthermore, the signals in the transport and torque are indeed very different. This is highlighted in Fig. 4.22(a), where we show a segment of an MR curve taken at 90 K and a torque curve at 30 K. While the high frequency oscillation is unmistakable in the MR data, the low frequency oscillations are no longer seen. The torque data, on the other hand, shows no sign of any high frequency oscillations even at 30 K. The FFTs of the torque data, shown in Fig. 4.22(b), confirm that the high frequencies vanish above 10 K.

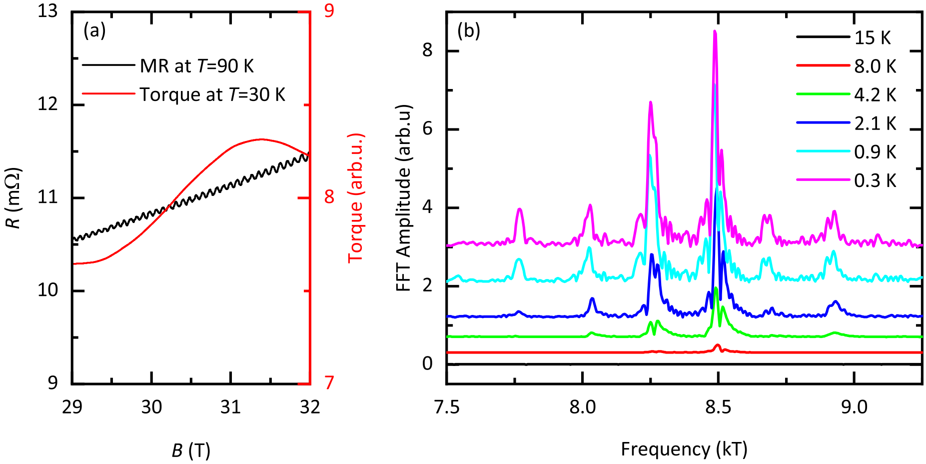

Figure 4.22: *Comparison of the oscillations at high temperature in torque and in transport. (a) MR of sample 8 at $T = 90$ K, together with torque at only 30 K. (b) High frequency FFTs of the torque data at different temperature, showing the absence of any high-T peaks. FFTs were done with $B \parallel c$, over a field range of 10-33 T and using a Hanning window.*

We can extract masses for the different temperature regimes of amplitude decay by fitting multiple times to the LK equation, for different ranges. This is the same procedure that we followed in Ref. [23]. The first range starts at $T = 0$ K until the amplitude reaches a minimum, and the second starts from the following maximum. This procedure gives us two different masses for most frequencies. We show these masses in table 4.6 for samples 8 and 9.

Frequency (T)	Sample 8 (low T)	Sample 8 (high T)	Sample 9 (low T)	Sample 9 (high T)
8330	0.8±0.2	0.16±0.01	0.87±0.04	0.18±0.02
8550	-	0.036±0.006	0.89±0.06	0.078±0.008
8580 (8610)	0.7±0.1	0.049±0.005	0.69±0.03	0.085±0.007
10915 (10940)	1.1±0.1	0.043±0.005	1.07±0.08	0.066±0.008
10955 (10990)	1.3±0.2	0.049±0.007	-	0.083±0.009

Table 4.6: *Effective masses at low and high temperatures for samples 8 and 9, determined from LK fittings over different ranges. The number in brackets in the first column is the frequency for sample 9, which is not always the same as for sample 8. Masses are in units of m_e.*

The masses that we find at low temperatures are generally close to those determined for the nearest of the major peaks I-IX, although the frequencies are typically not exactly the same. This is why the low-T masses show a good agreement between samples 8 and 9, while most of the high-T masses are mismatched. What appears to be happening, is that the large number of peaks that exists at low temperature dominates the spectrum there. Only when the amplitudes of these peaks have sufficiently diminished, can we properly address the high-T frequencies.

Going back to Fig. 4.21, there is another observation we can make, regarding the somewhat unusual shape of the oscillations at higher temperatures. It appears that the peak of each oscillation is sharper than the valley. A similar effect was seen for Mg [45], in a slightly misaligned magnetic field, and related to a so-called quantum interferometer, or Stark interferometer effect [36, 46]. A Stark interferometer is essentially analogous to a regular interferometer, with waves traveling along different paths and arriving at the same point, where they interfere with each other. The difference is that, in our case, the two paths are different routes along the FS, such as illustrated in Fig. 4.23. Moreover, in order to observe an oscillation due to a Stark interferometer, the paths needs to be quite precisely the same length, so that constructive interference takes place.

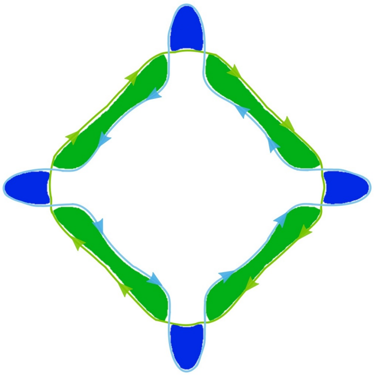

Figure 4.23: *Illustration of different possible paths around the FS that may interfere.*

Stark interferometers are known to exist not only in pure Mg [46, 47], but also in organic metals [48, 49]. This effect may be a possible explanation for the presence of oscillations persisting to very high temperatures, as it leads to temperature-independent oscillations. Furthermore, it can be observed in SdH experiments, but not in dHvA, which agrees very well with our data. A Stark interferometer therefore seems a viable explanation.

Due to this sensitivity to the difference in length between its two paths, the interferometer can be strongly affected by small changes in the angle between the sample and the magnetic field. For example, in Mg, the oscillation pattern changes drastically with an angle change of only 0.054° [45]. The high-temperature oscillations in ZrSiS, however, can be observed up to at least 60 K with an angle of 3°. It follows then, that any interferometer within the FS of ZrSiS, should be symmetric so that both paths change equally with angle. Despite this information, it is not clear what would be the arms of the interferometer. Due to the fixed rotation direction around each pocket, it is difficult to imagine interferometers that include the area A and can lead to large frequencies.

4.5 Pulsed field measurements

In order to gain more information regarding the mass enhancement reported in Ref. [23], we performed measurements in a pulsed magnetic field up to $B = 66$ T. Unfortunately, two limitations of the pulsed field setup limited the resolution of our data. The first was the fact that the crystals could not be rotated. Considering the angle sensitivity of the magnetic breakdown effect, it is crucial to obtain $B \parallel c$ with the maximum possible accuracy. Aligning ex-situ as is required in pulsed field, can easily cause errors of the order of $\sim 1°$. Most likely, this is the reason that we almost do not observe high frequency oscillations within the magnetic fields we normally access (see Fig. 4.24(a) for data).

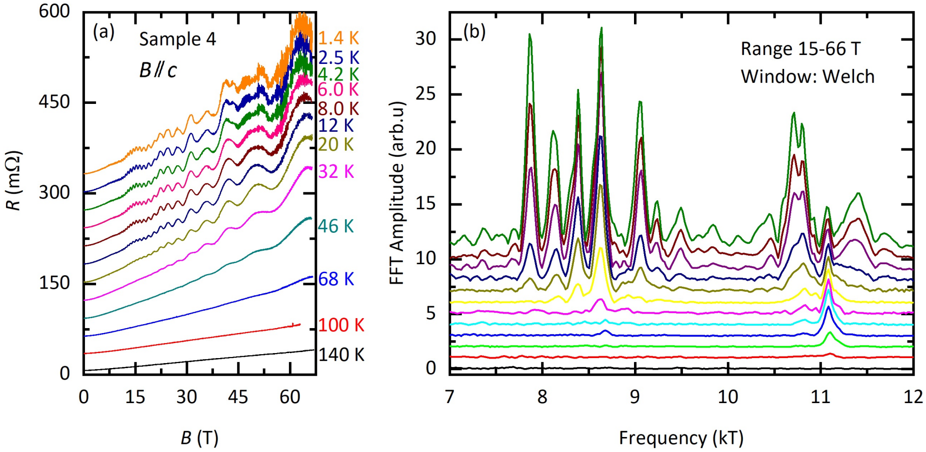

Figure 4.24: *(a) MR data from sample 4 up to $B = 66$ T, for $B \parallel c$ and different temperatures. (b) High frequency regions of the corresponding FFT spectra.*

The second problem is the fact that a measurement takes only milliseconds. Despite the use of very fast electronics, such a high rate of sweeping the field causes us to lose resolution on our fast oscillations. It is necessary to use a low integration time to observe these oscillations, which has the side-effect of higher noise. Because of these two complications, the pulsed field measurements unfortunately did not give us any new information.

Fig. 4.24(b) shows the FFT spectra from our pulsed field data. In the A group, there are five major peaks, albeit with different spacings than reported in Sec. 4.4. This could be due to a small misalignment of the sample, or the different field scale causing different parts of the spectrum to dominate. Group B, which is expected to be less sensitive to angle (as we saw in Sec. 4.4.1), has a lower resolution with fewer peaks resolved. This reduced resolution in fact occurs over the whole spectrum, and is most likely a consequence of the very high sweep rate of the magnetic field.

The low frequency spectrum (not shown here), reproduces the same main frequencies as those measured in steady field. These were analyzed for a possible mass enhancement, but no conclusive result was obtained.

4.6 Microsamples of ZrSiS

Measurements were also performed on microscopic samples prepared with FIB (samples 33 and 34, method described in Sec. 2.1). The data collected on these samples show a good agreement with that for macroscopic crystals, with key features in both the low frequency and high frequency spectra being reproduced. However, the contact resistances were ∼100 Ω, possibly resulting in a reduced resolution of the measurement. Some data is shown in Fig. 4.25. Overall, the quality of the data is slightly lower than that of Ref. [23].

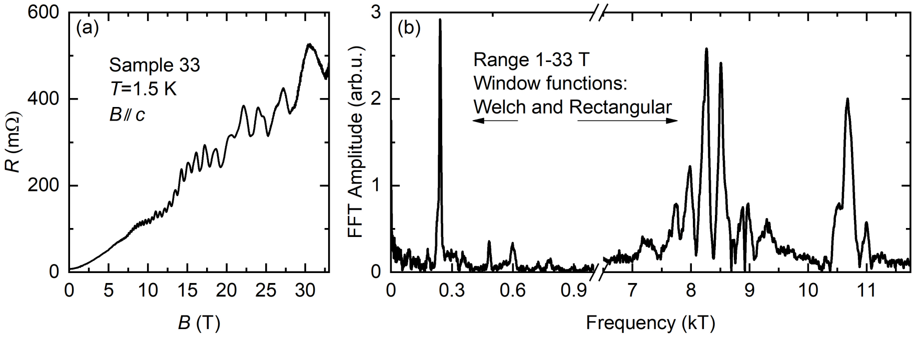

Figure 4.25: *Data collected on a FIB-prepared microsample of ZrSiS (number 33). (a) MR data at* $B \parallel c$ *and* $T = 1.3$ *K. (b) Corresponding FFT spectrum, divided in low and high frequency parts.*

In the FFT spectrum (Fig. 4.25(b), we can recognize the same peaks at 240 T (α) and 600 T ($2\beta - \alpha$) Harmonics of F_α are also seen, as well as a weak 180 T ($\beta - \alpha$) peak. F_β is not seen. In the high frequency region, we can recognize the A and B groups. Within A, we see the typical spacing of 240 T between major peaks, while in B, the number of peaks is reduced.

The good agreement between the data collected on FIB-contacted samples and conventionally contacted samples validates the use of FIB as a tool for the structuring of ZrSiS. It is likely that the reduction in resolution of the data from the FIB-prepared samples can be remedied by further optimization of the fabrication procedure for this material. In particular, an improvement of the contact resistance is desirable, as those samples with the best contacts (4, 8 and 9) show the highest resolution of data. This could be achieved by evaporating Au onto a freshly cleaved crystal surface, and then cutting the crystal into the desired shape with FIB, while removing the Au outside the intended contact areas.

After such optimization, FIB can be a powerful tool for the fabrication of novel, miniaturized devices using ZrSiS. For example, with these devices, one may be able to address the surface states of ZrSiS or to measure under high pressure. In the latter case, the small size of the devices is an advantage due to the limited sample space available in such experiments. Additionally, the zero-field resistance and Hall effect, which we cannot observe in our macroscopic crystals, could be measured more easily in an optimized device prepared with FIB.

4.7 Discussion

Within this chapter, we have identified the full diamond-shaped Fermi surface of the nodal-line semimetal ZrSiS and conclusively demonstrated both its shape and its character. We have additionally confirmed its character as a nodal-line semimetal and revealed a great many oscillatory phenomena within this compound.

We have confirmed the existence of two different pockets within the FS of ZrSiS, each occurring four times. Hole pockets are located in the corner of the diamond and elongated electron pockets at its sides. Within the Z-R-A plane of the Fermi surface, these different pockets have frequencies $F_\alpha = 240$ T and $F_\beta = 420$ T; within the Γ-X-M plane, they are much smaller. We identify these pockets through their angle dependence, which is accurately predicted by DFT even if F_β is overestimated, possibly due to correlation effects not taken into account by DFT.

Identifying these two frequencies as the fundamentals, we have been able to explain many others as combinations of the α and β orbits, leading to frequencies that are the difference of their individual frequencies (i.e. $|nF_\alpha - lF_\beta|$, with integer n and l). This is made possible through the mechanism of magnetic breakdown at the small gaps between the electron and hole pockets. We have confirmed this by showing that the combination frequencies are rapidly suppressed with small changes in angle, as they should be, due to the increase in gap size.

These gaps are in fact the only parts of the FS where carriers cross the nodal line, as these gaps only exist because the nodal line itself is gapped out by spin-orbit coupling. This means that the carriers crossing the gap are most likely to be affected by correlation effects, which we may indeed observe. One indication of that is the very low amplitude of β for $B \parallel c$, which we believe to be due to a scattering 'hot spot' located near the crossing of the Fermi level with the nodal line. Another indication may be a field-induced mass enhancement as reported in Ref. [23], which is broadly consistent with our data for multiple samples.

The assignment of breakdown frequencies to combinations with specific n and l is further supported by the analysis of their masses, which add up as $n|m_\alpha^*| + l|m_\beta^*|$. The one remaining frequency that cannot occur due to magnetic breakdown, $F_\alpha + F_\beta$, is attributed to magnetic interaction, which may produce a small amplitude for this oscillation. It is quite remarkable that so many frequencies have been generated by only two single fundamentals, albeit fundamentals that are each associated with four pockets. This is a consequence of the location of these pockets along the nodal line.

High frequency oscillations arise from magnetic breakdown along the entire nodal loop within the Z-R-A plane (the A group) and quite likely, the nodal loop in the Γ-M-X plane too (the

B group). Such complete traversal is rare and indicates that the (spin-orbit induced) gaps in ZrSiS are smaller than predicted by DFT. Otherwise, the probability of tunneling through eight consecutive gaps would be vanishingly small.

The breadth of the B group as well as the spacing between the major peaks in B (which is in fact larger than in A) suggests that perhaps some of the frequencies in the Γ-M-X plane are not resolved in our data. This is consistent with a report of a 130 T frequency in Ref. [14] as well as the prediction of 150 T from DFT. However, if there is indeed an unresolved fundamental frequency arising from the Γ-M-X plane, then there are likely to be additional, low-frequency breakdown orbits in this plane. Such orbits are also not observed.

The temperature dependence of the high frequency peaks does not clarify the assignment of specific frequencies to specific orbits, but it does lead to one interesting observation. That is the existence of certain high frequencies in both the A and the B group, that continue to exist up to very high temperatures (∼90 K). The persistence of such oscillations up to high temperatures can possibly be explained in terms of a Stark interferometer, which is known to cause temperature-independent oscillations.

4.8 Conclusions and outlook

This chapter represents, without doubt, the most extensive study of the Fermi surface of ZrSiS performed until now. Our work confirms the presence of a diamond-shaped FS with electron and hole pockets arising from the dispersion of robust Dirac bands through the Fermi level and the formation of a Dirac-like nodal loop. A rich tapestry of magnetic breakdown phenomena are also observed, indicating that the gaps opened up in the Dirac spectra by spin-orbit coupling are small, which may be due renormalization caused by correlation effects.

The topological nature of ZrSiS, already well established in previous work, for example using ARPES [5, 6] or studying the Berry phase [23], is confirmed by our data. We additionally report indications of correlation effects, such as a possible anomalous mass enhancement, which was first presented in Ref. [23]. Such effects have been predicted theoretically for NLSMs and there have been some experimental indications. However, based on this much more extensive study, the signatures of mass enhancement are weaker than originally found.

In the end, it is remarkable that the whole set of oscillatory phenomena discussed in this chapter can be described in terms of the Fermi surface ‘cage’ that follows the contours of the nodal-line around the whole Brillouin zone. It appears that there are no other contributions to the Fermi surface, confirming the DFT calculations. Nevertheless, despite the fact that the Fermi level is very close to the nodal line, we have only seen indirect indications of correlation effects, such as the loss of the β orbit near $B \parallel c$ due to the presence of a scattering ‘hot spot’ right where the Fermi level crosses the nodal line. This suggests that it may be necessary to go extremely close to the nodal line before significant correlation effects can be observed.

Overall, our investigations confirm that ZrSiS (and possibly other member of the same family) are ideal platforms on which to study the physics of the Dirac nodal line or loop and the interplay between topology and correlation. We note that the possibility of gating a very thin layer of ZrSiS is very interesting. Such a study may help us to extract topological aspects of ZrSiS or enable us to induce stronger correlation effects as the Fermi level is tuned closer to the nodal line. Such investigations are ongoing.

References

[1] R. Chen, H. C. Po, J. B. Neaton, and A. Vishwanath. *Nature Physics*, 14(1):55–61, 2018.

[2] S.-M. Huang, S.-Y. Xu, I. Belopolski, et al. *Nature Communications*, 6(7373), 2015.

[3] D. Sapkota, R. Mukherjee, and D. Mandrus. *Crystals*, 6(12):160, 2016.

[4] C. L. Zhang, Z. Yuan, G. Bian, et al. *Physical Review B*, 93(054520), 2016.

[5] L. M. Schoop, M. N. Ali, C. Straßer, et al. *Nature Communications*, 7(11696), 2016.

[6] M. Neupane, I. Belopolski, M. M. Hosen, et al. *Physical Review B*, 93(201104(R)), 2016.

[7] X. Wang, X. Pan, M. Gao, et al. *Advanced Electronic Materials*, 1600228, 2016.

[8] A. Topp, R. Queiroz, A. Grüneis, et al. *Physical Review X*, 041073, 2017.

[9] M. M. Hosen, K. Dimitri, I. Belopolski, et al. *Physical Review B*, 95(161101(R)), 2017.

[10] B. Fu, C. Yi, T. Zhang, et al. *ArXiv*, 1712.00782, 2017.

[11] C. Chen, X. Xu, J. Jiang, et al. *Physical Review B*, 95(125126), 2017.

[12] R. Sankar, G. Peramaiyan, I. P. Muthuselvam, et al. *Scientific Reports*, 7(40603), 2017.

[13] Y.-Y. Wang, Q.-H. Yu, and T.-L. Xia. *Physical Review B*, 94(041103), 2016.

[14] M. N. Ali, L. M. Schoop, C. Garg, et al. *Science Advances*, 2(e1601742), 2016.

[15] J. Hu, J. Y. Liu, D. Graf, et al. *Scientific Reports*, 6:18674, 2016.

[16] R. Singha, A. Pariari, B. Satpati, and P. Mandal. *Proceedings of the National Academy of Sciences*, 114(10):2468–2473, 2017.

[17] A. Topp, J. M. Lippmann, A. Varykhalov, et al. *New Journal of Physics*, 18(125014), 2016.

[18] J. Liu and L. Balents. *Physical Review B*, 95(075426), 2017.

[19] Y. Huh, E.-G. Moon, and Y. B. Kim. *Physical Review B*, 93(035138), 2016.

[20] B. Roy. *Physical Review B*, 96(041113), 2017.

[21] S. V. Syzranov and B. Skinner. *Physical Review B*, 96(161105(R)), 2017.

[22] L. Aggarwal, C. K. Singh, M. Aslam, et al. *ArXiv*, 1802.07993, 2018.

[23] S. Pezzini, M. R. van Delft, L. Schoop, et al. *Nature Physics*, 14:178–183, 2018.

[24] P. Gegenwart, J. Custers, C. Geibel, et al. *Physical Review Letters*, 89(056402), 2002.

[25] J. Paglione, M. A. Tanatar, D. G. Hawthorn, et al. *Physical Review Letters*, 91(246405), 2005.

[26] A. N. Rudenko, E. A. Stepanov, A. I. Lichtenstein, and M. I. Katsnelson. *Physical Review Letters*, 120(216401), 2017.

[27] M. M. Scherer, C. Honerkamp, A. N. Rudenko, et al. *ArXiv*, 1809.02962, 2018.

[28] W. Tremel and R. Hoffmann. *Journal of the American Chemical Society*, 109(1):124–140, 1987.

[29] D. Shoenberg. *Magnetic Osillation in metals.* Cambridge University Press, 1984.

[30] Y.-Y. Lv, B.-B. Zhang, X. Li, et al. *Applied Physics Letters*, 108(244101):5, 2016.

[31] I. A. Leahy, Y.-P. Lin, P. E. Siegfried, et al. *Proceedings of the National Academy of Sciences*, 115(42):10570–10575, 2018.

[32] C.-C. Su, C.-S. Li, T.-C. Wang, et al. *New Journal of Physics*, 20(103025), 2018.

[33] T. Zhang, Y. Jiang, Z. Song, et al. *ArXiv*, 1807.08756, 2018.

[34] J. Hu, Z. Tang, J. Liu, et al. *Physical Review B*, 96(045127), 2017.

[35] M. Matusiak, J. R. Cooper, and D. Kaczorowski. *Nature Communications*, 8(15219), 2017.

[36] M. I. Kaganov and A. A. Slutskin. *Physics Reports*, 98(4):189–271, 1983.

[37] X. Yan, M. J. Naughton, R. V. Chamberlin, et al. *Synthetic Metals*, 27:145–150, 1988.

[38] A. Audouard, J.-Y. Fortin, D. Vignolles, et al. *Journal of Physics: Condensed Matter*, 27(315601), 2015.

[39] F. A Meyer, E Steep, W Biberacher, et al. *Europhysics Letters*, 32(8):681–686, 1995.

[40] M. G. Priestley, L. M. Falicov, and G. Weisz. *Physical Review*, 131(2):617–622, 1963.

[41] M. R. van Delft, S. Pezzini, T. Khouri, et al. *ArXiv*, 1806.10592, 2018.

[42] D. C. Elias, R. V. Gorbachev, A. S. Mayorov, et al. *Nature Physics*, 7(9):701–704, 2011.

[43] G. L. Yu, R. Jalil, B. Belle, et al. *Proceedings of the National Academy of Sciences*, 110(9):3282–3286, 2013.

[44] H. K. Pal, F. Piéchon, J. N. Fuchs, M. Goerbig, and G. Montambaux. *Physical Review B*, 94(125140), 2016.

[45] R. W. Stark and R. Reifenberger. *Journal of Low Temperature Physics*, 26(5-6):819–826, 1977.

[46] R. W. Stark and C. B. Friedberg. *Journal of Low Temperature Physics*, 14(1-2):111–146, 1974.

[47] J. W. Eddy and R. W. Stark. *Physical Review Letters*, 48(4), 1982.

[48] M. V. Kartsovnik. *Chemical Reviews*, 104(11):5737–5781, 2004.

[49] D. Vignolles, A. Audouard, V. N. Laukhin, et al. *European Physical Journal B*, 71(2):203–209, 2009.

CHAPTER 5

Surface and bulk superconductivity at ambient pressure in the Weyl semimetal TaP

5.1 Introduction

Since the discovery of Weyl semimetals, a great deal of work has been devoted to understanding the properties of these topological materials, whose band structure includes specific points known as Weyl nodes where non-degenerate bands touch each other and disperse linearly. Weyl semimetals differ from the related Dirac semimetals in that they require either time-reversal or inversion symmetry to be broken in order to lift the degeneracy of the nodes. Consequently, Weyl nodes always exist in pairs of opposite chirality that are connected through Fermi arcs running along the surface of the material, as has been observed experimentally in several candidate materials using Angle Resolved Photoemission Spectroscopy (ARPES) [1–6]. The chiral nature of the Weyl nodes can furthermore manifest itself in electrical transport, in the form of the chiral anomaly, leading to a negative longitudinal magnetoresistance. The observation of this effect has been reported in several materials [7–9], though its origin remains uncertain [10, 11].

Part of the work presented in this chapter has been published in: M. R. van Delft *et al.*, *Surface and bulk superconductivity at ambient pressure in the Weyl semimetal TaP*. arXiv:1808.09702

In addition to the intrinsic transport properties of Weyl semimetals, the combination of Weyl physics and superconductivity may support Majorana [13] or other exotic surface states [14] as a result of their topological nature. These states are of fundamental interest and may eventually be applicable in the field of quantum computation. For this reason, there is an ongoing effort aimed at achieving superconductivity in such materials and investigating their properties, either through the use of the proximity effect [13, 15] or by other means.

The family of compounds comprising TaP, TaAs, NbAs and NbP are all experimentally confirmed as Weyl semimetals [2, 3, 5, 16–18] and are now among the most ardently studied compounds in this class. As TaAs was the first family member to be identified as a Weyl semimetal, the family is often named after this compound. Fig. 5.1 shows the crystallographic structure of the TaAs family, the members of which are isostructural with space group $I4_1md$. The lack of inversion symmetry is apparent from this figure.

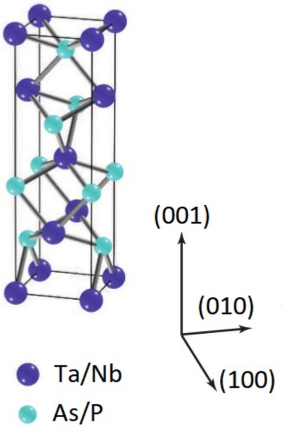

Figure 5.1: *Crystal lattice structure of the materials in the TaAs family. From Ref. [12].*

The bandstructures of the members of the TaAs family are quite similar. Here we only show the calculated bandstructure of TaP, in Fig. 5.2 (bandstructures for each of the four family members can be found in Ref. [19]). When spin-orbit coupling (SOC) is excluded from the calculation, the valence and conduction bands cross along closed rings. With SOC included, the bands become gapped along all high symmetry directions and the rings disappear. Instead, 12 pairs of Weyl nodes can be uncovered in the first Brillouin zone [12, 19]. These pairs exist in two inequivalent planes, $k_z = 0$ (generally called W1) and $k_z \approx \pm\pi/c$ (W2).

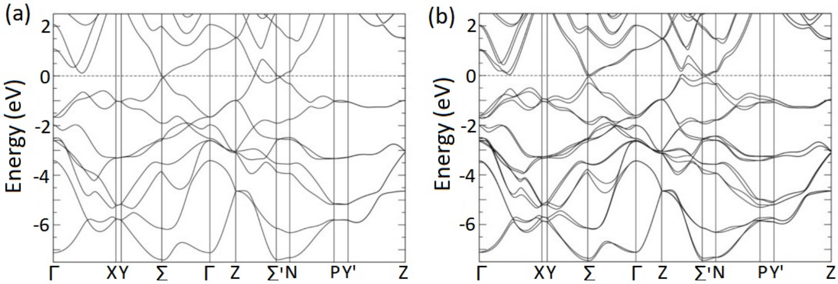

Figure 5.2: *Electronic band structure of TaP from first-principles calculations, (a) without and (b) with spin-orbit coupling. Adapted from Ref. [19].*

Under the right conditions, each member of the TaAs family has shown trace signatures of superconductivity. In TaAs, a superconducting onset has been induced through contact with a sharp tip of either Ag [20] or PtIr [21], while in TaP, this onset was achieved under the application of extremely high pressures [22], as shown in Fig. 5.3. In each case, however, only partial reduction in the resistivity was observed. A state of zero resistance has only been reported in samples where superconductivity was induced in a thin surface layer by treatment with FIB [23].

In this chapter, we show the existence of intrinsic bulk superconductivity in TaP, in addition to the FIB-induced surface superconductivity that was previously reported [23]. We have prepared four samples of TaP for this study by cutting them from a single crystal using FIB according to the procedure outlined in Sec. 2.1. The as-grown parent crystal has an ill-defined shape, and as such it is difficult to perform a reliable resistivity measurement of this sample along a particular axis. For this reason, we mainly study the microsamples (an example of which is shown in Fig. 5.5(a)).

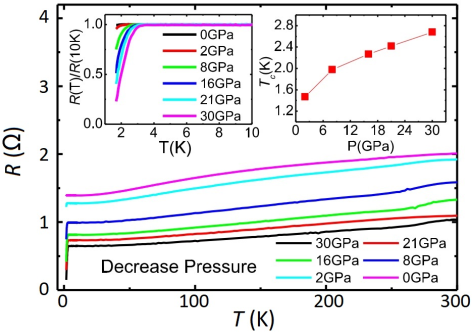

Figure 5.3: *$R(T)$ curves from Ref. [22] under different pressures. The left inset shows an enlarged view of the data at low T and the right shows the pressure dependence of the observed T_c.*

5.2 Characterization measurements

As a first characterization, we measured the resistivity as a function of temperature for each of the four microsamples. First, we compare a typical curve from our study with a previously reported example [26]. We see that the behavior of these two crystals is very different, with the one from our study being far more resistive. In fact, the resistivity of our sample is more similar to that reported for samples subjected to high pressure (see Fig. 5.3), in which superconductivity was induced [22]. This suggests that superconductivity is more likely to occur in TaP in a more highly resistive crystal.

The results for all of our samples are shown in Fig. 5.5(b) and they are strikingly different from most curves that were previously reported in the literature [24–26]. The resistivity is usually found to decrease by more than one order of magnitude between 300 and 4 K (without applied magnetic field). In our data, on the other hand, samples 1, 3 and 4 show very little variation in resistivity between room temperature and 4 K. Each of these samples shows a slow increase of the resistivity with decreasing temperature to approximately 50 K. Below this temperature, the resistivity either decreases or increases more slowly.

The data of sample 2 are quite different. Down to $T = 50$ K, the resistivity displays similar behavior to the other samples, albeit with a considerably lower magnitude. Below 50 K, however, it exhibits a sharp upturn in the resistivity, reaching a maximum around 3.5 K. The reason for this disparity in behavior is not clear, as sample 2 was cut from the same crystal plane as 1 and 4 and prepared in the same procedure as all the others. The only sample that is expected to be distinct is number 3, as this one was cut from a plane perpendicular to that of the other samples, i.e. along the c-axis.

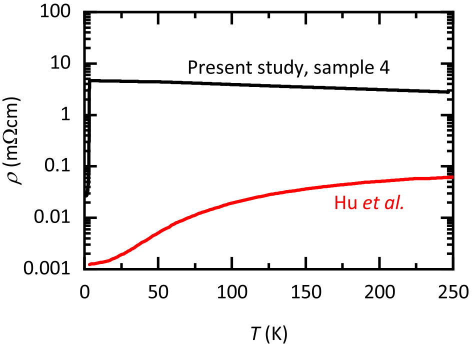

Figure 5.4: *Comparison of data from the present study (sample 4) with data that is typical for TaP, taken from Ref. [26].*

The residual resistivity ratio (RRR) is defined as the ratio of the resistivity at room temperature to that at 0 K, with a larger RRR indicating a higher sample quality. For our samples, we use the data just above T_c instead of the 0 K resistivity and find RRR≈1 for our samples, with the exception of sample 2 (RRR≈0.04). These values are considerably lower than the typical RRRs of 31 to 96 reported previously for macroscopic crystals [22, 24–26], but similar to what can be deduced from Fig. 5.3 at any pressure. It appears that after applying pressure, the crystals have a significantly reduced RRR. Knowing this, we might associate superconductivity in TaP with a lower crystal quality.

In the inset of Fig. 5.5(b), we focus on the low-T part of the resistivity curves. Here, it can be seen that each of the four samples exhibits a resistive transition with a characteristic temperature, T_c, between 1.7 and 5.3 K. For sample 2, the increase in resistance turns over to a sharp decrease, but the final low-T ρ_{xx} is still higher than that at high T. Sample 3 distinguishes itself with a much broader transition and higher overall T_c. However, only sample 4 reaches a state of zero resistance.

Before turning to discuss these resistive transitions in detail, we first characterize our samples in terms of their normal state (Sec. 5.2.1) and oscillatory magnetoresistance (Sec. 5.2.3). Then we demonstrate in Secs. 5.3 and 5.4 that in our FIB-processed crystals, both bulk and surface superconductivity are present, while in the as-grown parent crystal only bulk but inhomogeneous superconductivity appears. We delineate and identify the two transitions in the microfabricated crystals based on the angle dependence of their characteristic magnetic fields. Finally, in Sec. 5.5, we study the critical current associated with the superconductivity and in Sec. 5.6, we discuss the possibility of our samples being in a BCS-BEC crossover regime.

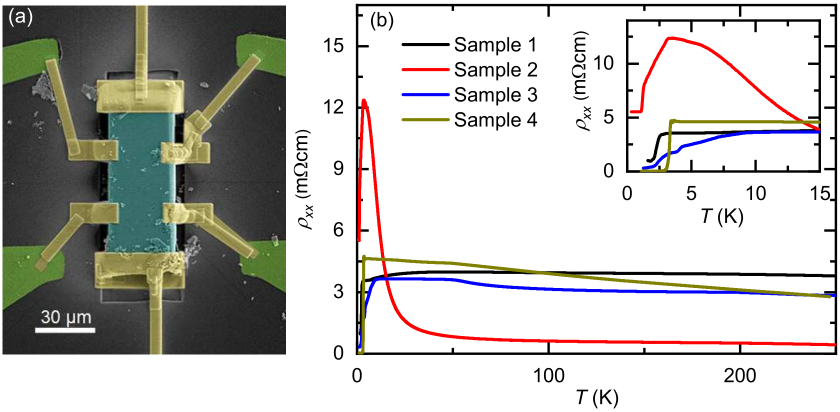

Figure 5.5: *(a) False color SEM image of a typical FIB contacted crystal. (b) Temperature sweeps of the resistivity of each of the four measured TaP crystals made with FIB. Inset: the same data, but focused on the low temperature part in order to show the superconducting transitions. The reason for the more semiconducting behavior of sample 2 is not understood. Sample 3 is oriented with the current along the c-axis while the other samples are mounted with the current aligned within the ab-plane. Apart from sample 2, all microsamples have an RRR≈1.*

5.2.1 Magnetoresistance

A frequently reported effect in topological semimetals, Dirac or Weyl, is a very large non-saturating magnetoresistance (MR) [18, 26–30]. At this time, there is no clear explanation for these observations, though charge compensation as well as a high mobility are considered to contribute. The lack of saturation may also be explained by the particular band structure, with linear dispersion around touching points between valence and conduction bands [31]. However, a recent study of elemental Sb showed that extremely large MR can be fully accounted for within a semi-classical framework, using an anisotropic, field-dependent mobility tensor [32].

Fig. 5.6 shows magnetoresistance measurements of microfabricated sample 1, for different angles between the magnetic field and the *c*-axis. The observed MR is larger for angles closer to the *c*-axis, but does not exceed 50% at 30 T for any angle, in stark contrast to the 10^5% or higher MR values reported by others for macroscopic single crystals of TaP [24, 26]. The reason for this marked difference is not well understood, but it is conceivable that FIB sample fabrication introduces both Ga^+ doping, thus disturbing the charge compensation, and a reduced crystalline quality, thus reducing the mobility. Certainly, the FIB plays a role, as in our as-grown crystal a MR larger than 4000% at 16 T and 1.3 K is observed.

Aside from the strong reduction the magnitude of the MR, the shape is different from what is commonly reported for TaP [25, 26, 30]. Here, we see a slight bending over of the MR at higher fields, suggesting a tendency towards saturation. This difference might also be explained through a lack of charge compensation in our samples.

As briefly mentioned before, one of the signatures of Weyl semimetal physics is the Adler-Bell-Jackiw anomaly, or chiral anomaly, which can be observed as a negative longitudinal magnetoresistance (NLMR) in parallel electric and magnetic fields [33]. This anomaly has its origin in the field of particle physics [34], and can be understood as a non-conservation of chiral particles under the influence of parallel magnetic and electric fields.

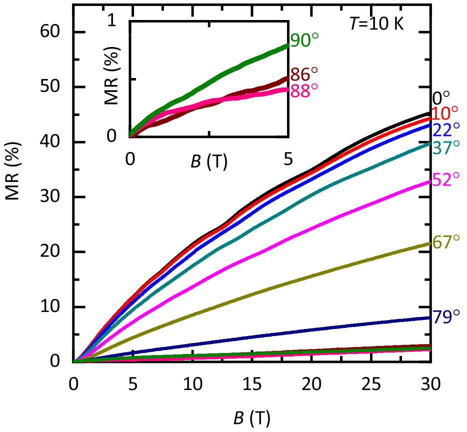

Figure 5.6: *Magnetoresistance measurements of sample 1 up to $B = 30$ T for different angles between the field and current directions. Top inset: highlighted data at low field for angles close to $B \parallel I$, demonstrating the absence of negative magnetoresistance. Center inset: sketch of the sample indicating the direction of the magnetic field.*

The experimental observation of the chiral anomaly through NLMR is non-trivial, as there are many effects other than the chiral anomaly that may induce NLMR, some of which having nothing to do with the topological properties of WSMs. For instance, it may arise from inhomogeneous current flow, due to a purely geometrical effect called current jetting [10, 11]. Current jetting can be minimized by careful definition of the electrical contacts, such that they cover the whole side of the sample.

When contacting our TaP microsamples, we took particular care that their sides were completely covered by the contacts, so that the current distribution would be homogeneous. In order to test for the chiral anomaly, we then measured the magnetoresistance for several angles between the magnetic field and the current close to $B \parallel I$. The results of these measurements for one of our samples are shown in the inset of Fig. 5.6. Clearly, no NLMR is present. This is the case for all of our microfabricated samples, and may be due to the same reasons as the absence of very large magnetoresistance in other orientations. Without NLMR, no evidence of Weyl semimetal physics is present in our samples, so it remains uncertain whether we can still speak of a WSM. For the as-grown crystal, we are not able to align the current and magnetic field precisely, and so we cannot look reliably for NLMR there. Therefore, we cannot compare our crystals before and after FIB to determine if the Weyl physics is being suppressed by FIB.

5.2.2 Carrier concentration

In order to determine whether charge compensation is present in our samples, it is necessary to find the concentrations of electrons and holes. For this reason, we attempted to fit our MR and Hall resistivity, ρ_{xy}, data to a two-carrier model. Unfortunately, this fitting turned out not to be a good description of our data.

Instead, we can use a single-carrier model to calculate a carrier density, n, from the Hall coefficient, R_H, as follows:

$$R_H = \frac{V_H t}{IB} = \frac{1}{ne}, \qquad (5.1)$$

where V_H/B is determined from a linear fit of the measured Hall voltage as a function of magnetic field (an example is shown in Fig. 5.7); I is the applied current and t the thickness of the sample. The resulting carrier concentrations for each of the samples are shown in table 5.1. For sample 3, no concentration could be determined because no significant Hall voltage was measured for this sample. The values we then obtain for the carrier concentrations are comparable to those from literature [24, 26, 35].

Sample	Concentration (cm^{-3})
1	(8.4±0.6)·10^{18}
2	(3.4±0.5)·10^{19}
3	N/A
4	(2.2±0.4)·10^{19}

Table 5.1: *Carrier concentrations at $T = 4$ K of the different samples*

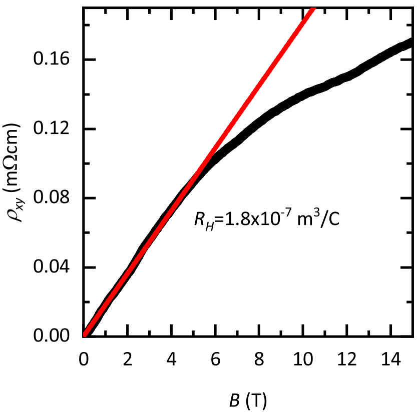

Figure 5.7: *Example of the fitting of the Hall data for the extraction of the Hall coefficient and carrier density, for sample 2.*

5.2.3 Quantum oscillations

Fig. 5.8(a) shows data from our Shubnikov-de Haas study of microstructured sample 1. The oscillations are well-resolved in ρ_{xy} for $B \parallel c$, but are suppressed gradually when the field is tilted away from this orientation. The fact that we are able to see these quantum oscillations in our microstructured samples suggests that the crystalline quality remains high, even if the FIB processing induced some damage.

Fig. 5.8(b) shows curves resulting from the subtraction of a smooth background from the data, plotted as a function of the inverse magnetic field. This allows for the direct observation of two frequencies $F_1 = 17$ T and $F_2 = 33$ T, as indicated in the graph. The same frequencies can also be extracted from the Fourier spectrum, shown in Fig. 5.8(c). Our observed frequencies are in excellent agreement with Ref. [36], which reports 17.3 and 36.7 T. Other studies report slightly larger, but comparable frequencies [26, 35].

Fig. 5.8(d) shows the Fermi surface of TaP, as determined in Ref. [35]. There are two inequiv-

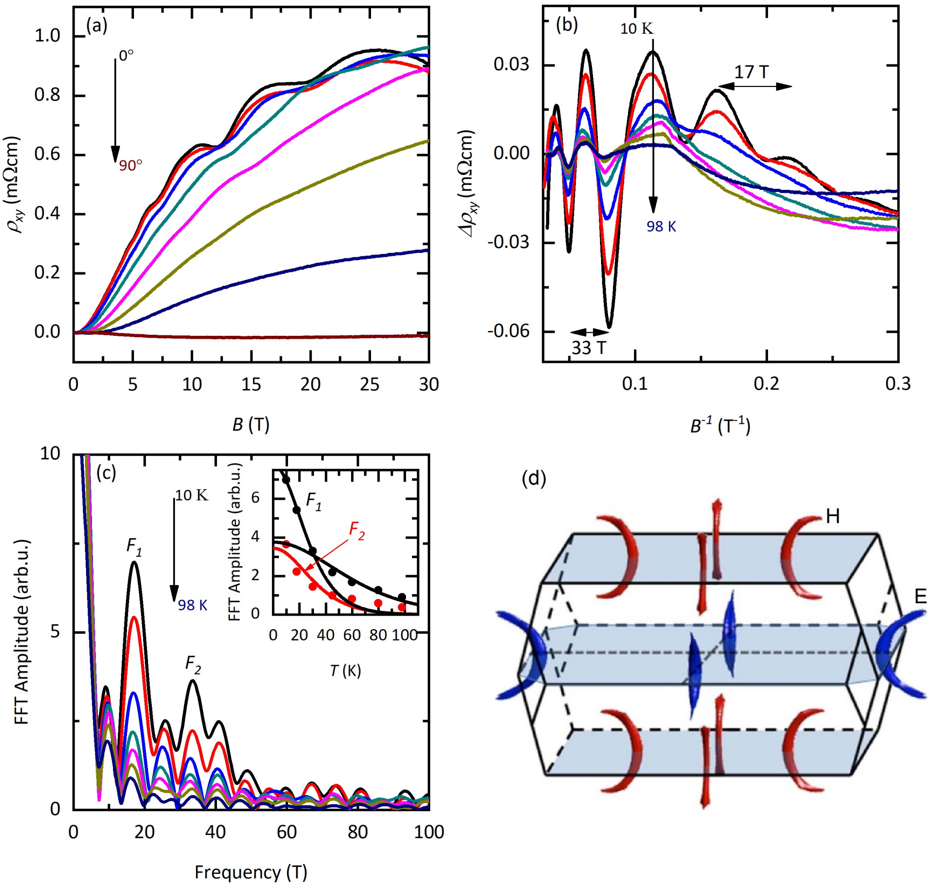

Figure 5.8: *(a) Shubnikov-de Haas oscillations in the Hall resistivity of microstructured sample 1. These measurements were done at $T = 10$ K. (b) Fermi surface of TaP based on a combination of calculations and experiment from Ref. [35]. Electron pockets are shown in blue, and hole pockets in red. (c) Hall resistivity after subtraction of smooth background, plotted against $1/B$ for different temperatures and $B \parallel c$. (d) Fourier transforms corresponding to the curves in (c), with a field range of 5 to 30 T and a Welch window function (see Appendix C for a discussion of Fourier analysis). Inset: FFT Amplitude as a function of temperature, with Lifshitz-Kosevich fitting in order to extract the effective mass.*

alent pockets, due to electrons and holes, both banana shaped. Band structure calculations performed in Ref. [36], suggest that F_1 can be attributed to an orbit around the electron pocket, and F_2 around the hole pocket. Finally, the cyclotron mass can be extracted using the Lifshitz-Kosevich (LK) formalism (described in detail in Appendix B). We show the temperature dependent data that is needed to do this in Figs. 5.8(b) and (c), for temperatures between 10 and 98 K and a constant angle $B \parallel c$. The resulting LK fitting is shown in the inset of Fig. 5.8(c).

For F_2, we find a mass of $(0.041\pm0.002)m_0$, considerably lower than previously reported. In our determination of the F_1 mass, on the other hand, we find that a single LK fit does not accurately describe the temperature decay. The temperatures below $T=35$ K and those above fall on different curves and can both be described well by separate fits. This results in masses of $(0.048\pm0.002)m_0$ below and $(0.038\pm0.002)m_0$ above 35 K, both agreeing well with those obtained in other studies [25, 35]. The unusual temperature dependence may arise due to two different orbits with similar frequencies and different masses, that we cannot resolve separately.

5.3 Superconductivity

Fig. 5.9(a) shows low-temperature resistivity curves for both the pristine crystal and microstructured sample 4. The parent crystal exhibits an incomplete, resistive transition at a transition temperature $T_c = 3.0 \pm 0.8$ K that resembles the one which had been observed previously in TaP under high pressure [22]. The microstructured crystal, on the other hand, exhibits a sharp transition to zero resistance with $T_c = 3.3 \pm 0.5$ K.

In order to confirm the presence of superconductivity in our samples, we studied the evolution of the resistive transition in the presence of a magnetic field. Fig. 5.9(b) shows temperature sweeps of the resistivity of one of the microstructured samples under different, constant magnetic fields. These fields are applied perpendicular to the current direction. Clearly, the resistive transition in the FIB-processed sample is suppressed with field, as is expected in the case of a superconducting transition. For $B_\perp = 10$ T, it vanishes completely. In the parent crystal, the transition is suppressed more strongly and vanishes under a very small magnetic field.

Superconductivity has been reported before in microfabricated samples of TaP, TaAs, NbP and NbAs [23], but in as-grown TaP it has never been observed at ambient pressure despite the large number of measurements at low temperature that have been carried out on this material [25, 26, 35, 37]. For the measurements done under high pressure that did find superconductivity, it was reported that the crystal was in the P-6m2 phase, the same structure that is found for

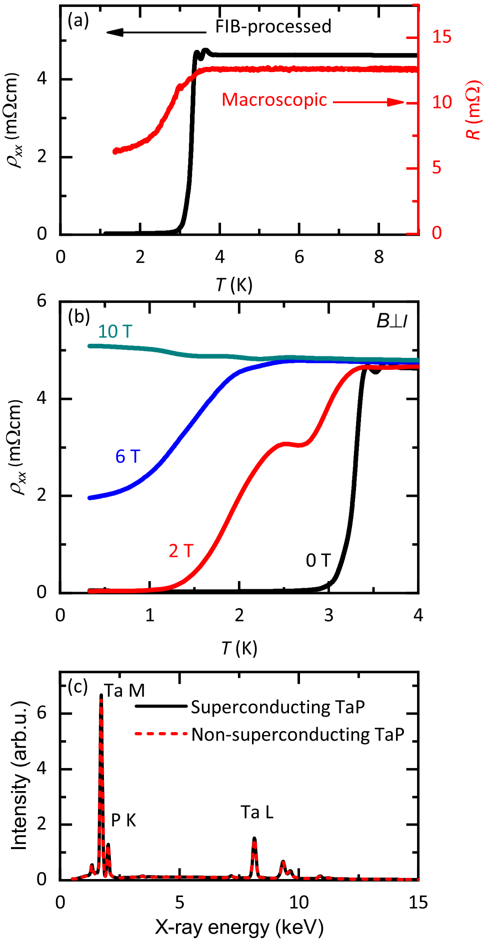

Figure 5.9: *(a) Temperature sweeps showing the resistive transition of the FIB-processed sample 4 and the macroscopic crystal from which all FIB samples were cut. (b) Resistivity curves at low temperature of FIB-processed sample 4 under different, constant magnetic fields perpendicular to the current direction. (c) EDX spectra of the bulk sample used in our experiments and a non-superconducting sample obtained from a different source. Within the experimental resolution, the compositions are the same.*

superconducting MoP [38]. For this reason, we investigated our bulk crystal for any signs of deviation in terms of structure that might be related to superconductivity. However, our XRD (X-Ray Diffraction, described in Sec.2.6.3) measurements demonstrate that our TaP crystal is in the $I4_1md$ space group, as is usual for TaP under ambient conditions [16, 39, 40]. Thus the superconducting state that develops in our crystals appears to be distinct from what has been observed before.

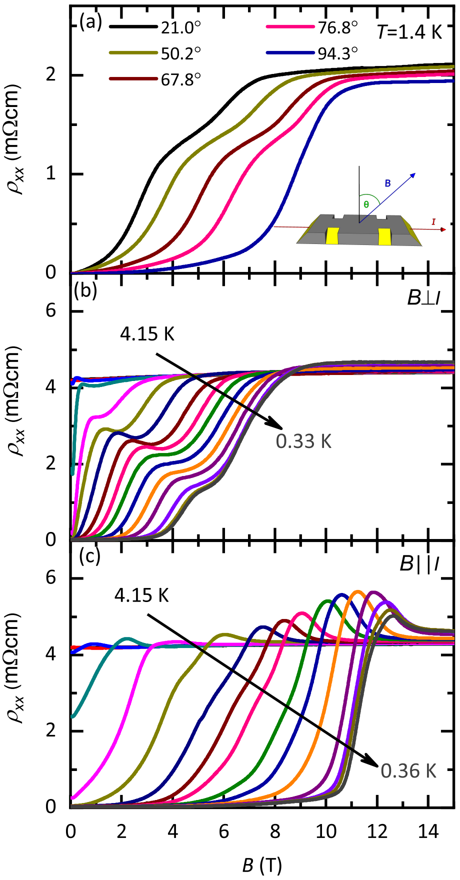

Figure 5.10: *Field sweeps of the resistivity of FIB-processed sample 4 for (a) different angles as defined in the inset and (b) different temperatures in a magnetic field parallel to the current direction and (c) in a field perpendicular to the current.*

We also studied the composition of the parent crystal with EDX (Energy Dispersive X-ray spectroscopy, described in Sec.2.6.2) and compared its stoichiometry to that of a crystal of TaP from a different source that did not display any sign of superconductivity. The two bulk crystals were measured in the same EDX system during a single run to exclude any difference in signal other than from the material itself and care was taken to ensure that a flat crystal surface was facing towards the electron beam. The resulting spectra are shown in Fig. 5.9(c). From these we find that the two crystals have a stoichiometry that is identical to within an experimental error of about 1%, implying that our material is very similar to that used in other studies. Despite our best efforts, however, we could not determine the precise Ta:P ratio with real confidence due to the inherent difficulties associated with quantitative EDX measurements. Such a measurement requires a reference sample that is certain to be stoichiometric TaP. Our reference sample is known to be not superconducting, but its stoichiometry is not guaranteed.

Fig. 5.10(a) shows field sweeps of the resistivity of one of the microstructured crystals (sample 4) under different orientations of the magnetic field. Here, the angle 90° denotes a field parallel to the direction of the applied current (see inset of Fig. 5.10(a)), which in this case is the crystallographic *ab*-plane. For angles away from 90°, there is a clear double transition that we associate with distinct superconducting phases. Close to 90°, the characteristic fields of the two superconducting phases are assumed to merge, causing the two transitions to become indistinguishable.

Figs. 5.10(b) and (c) show the temperature dependence of the resistive transitions in field, for fields perpendicular and parallel to the current direction, respectively. In perpendicular field (Fig. 5.10(b)), there are two distinct superconducting features separated by a broad shoulder. In the parallel field configuration on the other hand, the shoulder is much weaker. This suggests that the characteristic fields of the two phases are of similar magnitude, but have a different temperature dependence. The data also reveal an upturn of the resistivity before the normal state is fully restored. Such an upturn is frequently observed in inhomogeneous superconductors [41–44] due to current redistribution as some parts of the crystal turn superconducting while others remain resistive [45]. It was also seen recently, for example, in the pressure-induced superconducting transition in MoP [38].

5.4 Dimensional analysis

The data in Fig. 5.10 can be used to extract characteristic fields for both transitions as a function of angle and temperature. The two field scales are determined here by defining the field at which the resistance has risen to 90% of the normal state (H_2) and the field that minimizes the second derivative of the resistivity (H_1). This procedure is outlined in Fig. 5.11.

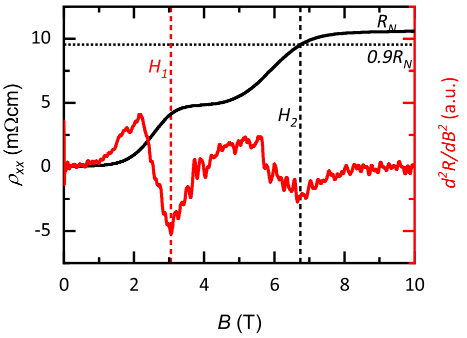

Figure 5.11: *Illustration of how the identification of the characteristic fields is done: H_2 is the field where the resistance reaches 90% of the normal state value and H_1 is identified by the negative peak in the second derivative.*

In the following, any conclusions made regarding the dimensionality of the superconducting states depend strongly on the degree of uncertainty resulting from the determination of H_1 and H_2, so it is important to estimate how accurate this is. In the case of H_1, an estimate of the uncertainty can be made from the width of the dip in the second derivative. A sharper dip corresponds to a smaller error. In the case of H_2, the uncertainty depends on the determination of R_N. The resistance in fields just above the characteristic field is fairly flat, but still there is a finite positive magnetoresistance that introduces some uncertainty. In parallel field, the resistive upturn above H_2 increases the uncertainty.

5.4.1 Angle dependence of the characteristic fields

In Fig. 5.12, we show both H_1 and H_2 as a function of the angle between the magnetic field and the ab-plane at $T = 1.4$ K. The four panels of the figure demonstrate fits using different models that represent either three-or two-dimensional superconducting states. The first model, shown in Fig. 5.12(a), is the three-dimensional Ginzburg-Landau (GL) model [46], of the form

$$\left(\frac{H_c \sin\theta}{H_{c\perp}}\right)^2 + \left(\frac{H_c \cos\theta}{H_{c\|}}\right)^2 = 1, \tag{5.2}$$

where θ is as defined in the inset of Fig. 5.10(a) and $H_{c\perp}$ ($H_{c\|}$) represents the characteristic field in the perpendicular (parallel) field configuration. This model describes the dependence of the critical field of a bulk superconductor on the angle of an applied magnetic field. If the superconductor is completely isotropic, then $H_{c\|} = H_{c\perp}$ and it is automatically satisfied. For an anisotropic superconductor, this model interpolates between the two extremes.

The model gives an excellent fit of H_2, both at small and at large angles. The values of $H_{c\|}$ and $H_{c\perp}$ resulting from the fit are shown in table 5.2. For H_1, it approaches the data quite well, but not as well as the 2D Tinkham model for thin films [47] (shown in Fig. 5.12(b)). This model has the form:

$$\frac{H_c \sin\theta}{H_{c\perp}} + \left(\frac{H_c \cos\theta}{H_{c\|}}\right)^2 = 1. \tag{5.3}$$

The Tinkham model describes the angle dependence of the critical field in the case of a thin superconducting film with $d \ll \xi_{GL}$ (ξ_{GL} is the out-of-place coherence length) and can be derived based on quantization of fluxoids, small superconducting current loops around a non-superconducting region. The magnetic field, H, through such a loop is quantized in units of Φ_0, the magnetic flux quantum. Depending on the orientation of the magnetic field relative to the superconducting film, a different size of fluxoids is induced in the film. In a field parallel to the film, the dimension of the loops is limited by the film thickness. The energy then increases as H^2. In a perpendicular field, on the other hand, the size of the current loops decreases with increasing H. From this, it can be seen that the critical field versus angle relationship should look like Eq. 5.3[47].

A derivation of the Tinkham model starts from the linearized Ginzburg-Landau differential equation, with a magnetic field in the xz plane (with the x-axis defined perpendicular to the plane) at an angle θ from the plane of the superconducting film. A vector potential can then be chosen that has only a y-component, but is independent of y. Furthermore, in the case of $d \ll \xi_{GL}$, the potential also becomes independent of x. With these assumptions, the equation is solvable and Eq. 5.3 is obtained.

The two models give a similar fit, but differ in important details, mainly for small angles or angles close to 90°. Based on this, it is found that the 2D Tinkham model gives the best description of the behavior of H_1, covering not only the cusp at 90° which the 3D GL misses, but also its behavior in near-perpendicular fields. Conversely, the angle dependence of H_2 does not have as sharp a cusp as H_1 does and is better described by the 3D GL model, which more accurately captures the behavior at angles away from 90°.

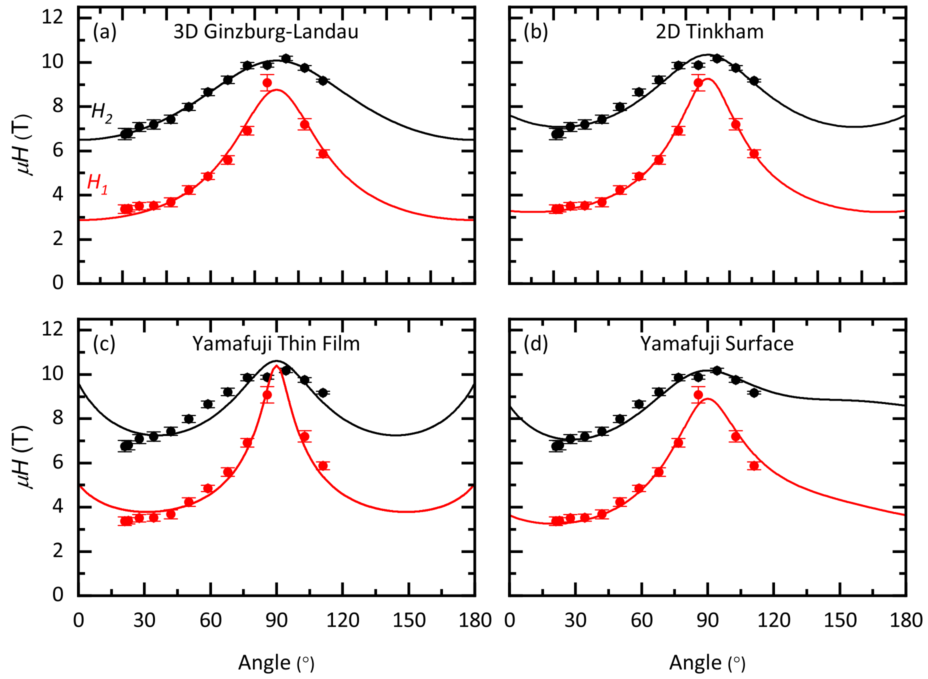

Figure 5.12: *Angle dependence of characteristic fields at $T = 1.4$ K, fitted with (a) the 3D Ginzburg-Landau model, (b) the 2D Tinkham model, (c) the Yamafuji model for thin films and (d) the Yamafuji model for surface superconductivity.*

Method	$H_{1\|\|}$	$H_{1\perp}$	$H_{2\|\|}$	$H_{2\perp}$
Ginzburg-Landau	2.87±0.09	8.8±0.3	6.50±0.05	10.08±0.05
Tinkham	3.28±0.04	9.3±0.1	7.6±0.1	10.3±0.1
Yamafuji thin film	5.1±0.1	10.5±0.7	9.6±0.3	10.6±0.3
Yamafuji surface	3.6±0.1	8.9±0.2	8.6±0.2	10.2±0.1

Table 5.2: *Parallel and perpendicular characteristic fields as determined from the four different fitting methods.*

For specific situations, there exist refinements of the 2D Tinkham model: one for the case of intrinsic surface superconductivity (Eq. 5.4) and another for a thin superconducting film (Eq. 5.5). Both of these models are derived from the linearized GL equation, with slightly different conditions. In the former, a thick film is considered, where nucleation occurs on the surface, leading to a deformation of the magnetic field. In the latter, the equation is solved with a loosened condition on the layer thickness, such that it should be less than or comparable to the out-of-plane coherence length ξ_{GL} (while the Tinkham model requires a thickness $d \ll \xi_{GL}$)[48, 49].

$$\frac{H_c \sin\theta}{H_{c\perp}} + \left(\frac{H_c \cos\theta}{H_{c||}}\right)^2 [1 + \tan\theta(1 - \sin\theta)] = 1. \tag{5.4}$$

$$\frac{H_c \sin\theta}{H_{c\perp}} + \left(\frac{H_c \cos\theta}{H_{c||}}\right)^2 \left[1 - 3(1+\sqrt{2}) \left(\frac{H_{c\perp}}{H_{c||}}\right)^2 \frac{H_c \sin\theta}{H_{c\perp}}\right] = 1. \tag{5.5}$$

As shown in Fig. 5.12(c) and (d), both of these adapted models lead to a less accurate fitting for H_1 and H_2. In particular, the thin film model is found to be a bad fit of the data overall, while the outcome of the surface model resembles that of the Tinkham model. The pronounced asymmetry in this model, however, leads to a reduced quality of fit. Thus, with the GL and Tinkham models giving the most accurate descriptions of H_2 and H_1 respectively, we can conclude that H_2 arises from the bulk crystal while H_1 is characteristic of a 2D superconducting state. This state presumably arises from a very thin layer on the surface that satisfies the criterion of $d \ll \xi_{GL}$.

5.4.2 Phase diagram

Fig. 5.13 shows the phase diagram of FIB-processed TaP, in both parallel and perpendicular field configurations. H_1 is only shown for perpendicular field, as it is not distinguishable in the parallel field configuration. The behavior of H_2 in both configurations can be well described by the empirical expression $H_2 = H_2(0)(1 - (T/T_c)^2)$, in agreement with the description of the critical field of a three-dimensional GL superconductor. H_1 on the other hand, is better described with a linear temperature dependence, consistent with the GL model for two-dimensional superconductors: $\mu H_{1,\perp} = \Phi_0/(2\pi\xi_{GL}^2)(1 - T/T_c)$ [50]. Associating H_1 with the upper critical field for the two-dimensional superconducting layer, we can estimate the out-of-plane coherence length, ξ_{GL} to be approximately 7.7 nm.

In order to make an estimate of the thickness d of the superconducting layer, we use the SRIM-2013 code to simulate the ion milling process. With the low acceleration voltage of 8 kV that is used for the final polishing of the sample, the Ga^+ ions penetrate about 5.0 nm below the surface of the sample. As P is sputtered approximately two times more readily than Ta, an average composition is expected in this thin layer of $Ta_{2.1}P$. Of course, the thickness of the superconducting layer cannot simply be assumed to be the same as the ion penetration depth; if anything, this depth gives an upper limit. Considering this, it is not unreasonable to expect that the condition $d \ll \xi_{GL}$ is indeed satisfied.

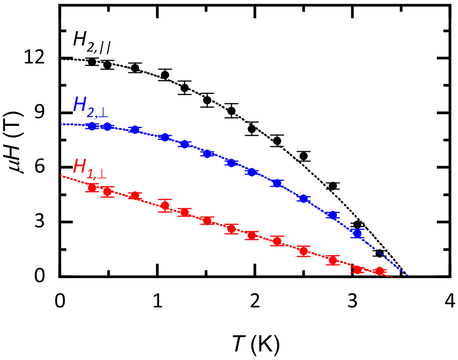

Figure 5.13: *Temperature dependence of the characteristic fields for parallel and perpendicular fields. H_2 is fitted using a three-dimensional model and H_1 with the two-dimensional Ginzburg-Landau model. H_1 in parallel field cannot be unambiguously identified and is thus omitted from this figure.*

5.5 Critical currents

We can gain additional information by looking at the critical currents associated with the transitions. To find these currents, we measured the current-voltage (IV) characteristics and differential resistivity curves in different magnetic fields and temperatures. In Fig. 5.14, the data are shown for zero field at $T = 1.3$ K.

Several clear transitions can be seen in the differential curves shown in Fig. 5.14(b). Around 1.0 and 1.1 mA, there are two distinct features that do not lead to a significant change in resistance. We presume that these correspond to parts of the bulk crystal becoming superconducting while others remain resistive and they are likely to be a consequence of strong inhomogeneity present in the sample. The transition at 0.7 mA then represents the majority of the bulk crystal becoming normal, leading to a strong increase in the resistivity. The state of zero resistance, however, can only be seen below a much smaller bias current of about 60 μA, as seen in the IV curve in the inset of Fig. 5.14(a). The associated differential resistivity (inset Fig. 5.14(b)) does not go to zero due an experimental offset of unknown origin. As the IV curve does have zero slope in this regime, dV/dI would be expected to go to zero as well.

Considering the two-dimensional nature of the surface layer superconductivity, this small bias current corresponds to a current density of approximately $8{\cdot}10^4$ A$\cdot$cm^{-2}, much larger than

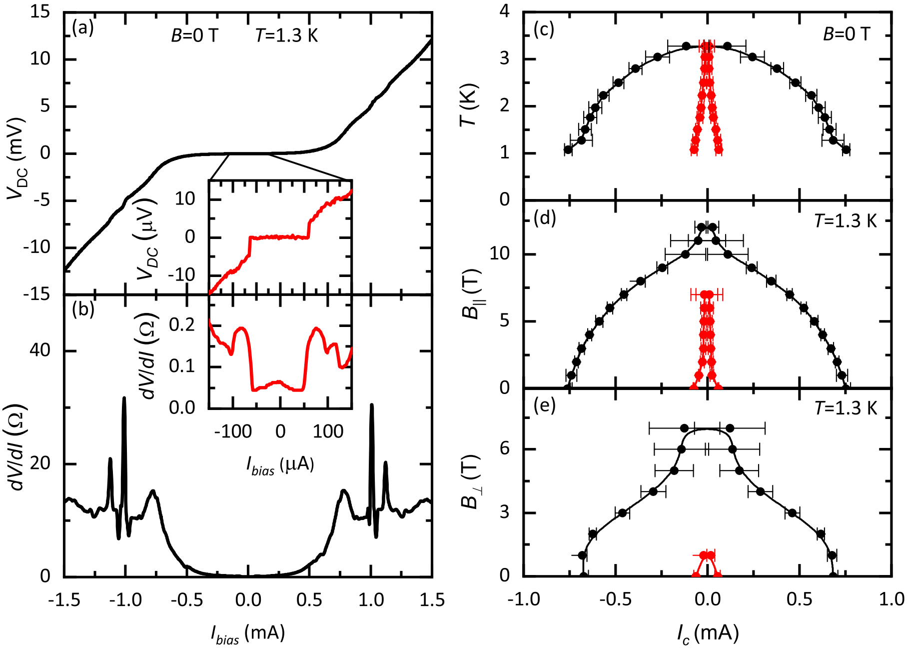

Figure 5.14: (a) IV curve of sample measured at $T = 1.3$ K and $B = 0$ T. Inset: expanded view on the low-current region where the transition due to the surface can be seen. (b) Differential resistance measured simultaneously with the IV curve. Inset: differential resistance corresponding to the inset of (a). (c)-(e) Critical currents of the bulk (black) and surface (red) as a function of (c) the temperature, (d) parallel magnetic field and (e) perpendicular magnetic field.

that associated with the bulk transition (about $1{\cdot}10^3$ A·cm^{-2}).

Figs. 5.14(c)-(e) show the critical currents for bulk and surface TaP as a function of temperature and magnetic field. The error bars in these figures are extracted from the width of the region in the differential resistance curves where the resistance drops strongly. At higher temperatures or fields, this region becomes more smeared out and less well defined, leading to larger error bars.

This is a further confirmation of Fig. 5.13 as the two transitions are suppressed at the same temperature, but at different values of magnetic field. In perpendicular field, the feature associated with surface superconductivity can be seen up to 1 T, whereas in parallel field, it survives up to 7 T. The difference is less apparent for the bulk superconductivity, but also this feature can be seen to persist to higher fields in the parallel than is evident in the perpendicular configuration, in agreement with Fig. 5.13(b).

5.6 Possible BCS-BEC crossover regime

As found in Sec. 5.2.2, the carrier concentration n of microstructured sample 1 as determined from a simple Drude analysis is $4.5{\cdot}10^{18}$ cm^{-3}. For a semimetal such as TaP, this is a typical value, in agreement with the literature [26, 35]. However, for a superconducting material, it is unusually low. For comparison, we consider $SrTiO_3$, for which a T_c of 180 mK is realized for a carrier concentration of $4.1{\cdot}10^{18}$ cm^{-3}[51]. The T_c of our TaP is at least 10 times higher despite the fact that the carrier density is comparable. For these reasons, we consider the possibility of a crossover between a Bardeen-Cooper-Schrieffer state and a Bose-Einstein condensate (BCS-BEC) for the observed superconductivity.

The BCS theory was developed to describe superconductors with a pairing instability due to an arbitrarily weak attractive interaction in a system of fermions. The formation of pairs and their condensation occur at the same temperature. The BEC paradigm, on the other hand, describes fluids of strongly interacting bosons, that condense into a single quantum state [52, 53]. Here, pairing occurs at higher temperature than condensation. These two systems appear distinct, but are in fact two extremes of a continuum. The crossover between the two can be described by two length scales: the pair size (coherence length ξ) and the interparticle distance.

Typically, a BCS superconductor has a high density (i.e small interparticle distance), such that many thousands of pairs overlap in the coherence volume $V_{coh} = 4/3\pi\xi^3$. A BEC superconductor, however, may be very dilute and have less than one pair in V_{coh}. In that case, there is no interaction between different pairs.

Using the value of $n = 2.6{\cdot}10^{19}$ cm^{-3} for sample 4 and the value of 7.7 nm obtained from the fitting of Fig. 5.13 for the out-of-plane coherence length ξ, we calculate the number of pairs in V_{coh}. This amounts to approximately 25 pairs, suggesting there is limited overlap between them. With a number of 25 pairs in V_{coh}, sample 4 is similar to FeSe (with 31 pairs [54]), which is considered to be in a BCS-BEC crossover regime [55–57]. These findings therefore suggest that this new breed of semi-metals is a good playground for the observation of possible exotic superconductivity.

5.7 Conclusions

In conclusion, we have observed signatures of bulk superconductivity at ambient pressure in a crystal of TaP and confirmed the appearance of FIB-induced surface superconductivity. The bulk superconductivity does not extend throughout the entire crystal, but appears to be either inhomogeneous or filamentary in nature. In other studies, it was found that TaP typically contains a large density of defects and can be off-stoichiometric with an excess of Ta [37, 39]. Our EDX data do not exclude off-stoichiometry in our samples, but considering the similarity between the superconducting and non-superconducting samples, any overall off-stoichiometry cannot explain the superconductivity we observe.

It is, however, apparent that the superconductivity in our sample is strongly inhomogeneous as we see multiple partial superconducting transitions, as well as an upturn of the resistance just above critical field in the parallel field configuration. This suggests that there may exist domains with a local excess of Ta or defect structures that support superconductivity. Nevertheless, our findings call for a thorough study of the growth of TaP and related compounds in order to establish under what conditions superconductivity is optimized. Further research is also required to ascertain whether superconducting TaP retains any of the characteristics of a Weyl semimetal. If it does, TaP may well become an ideal platform for the study of Weyl superconductivity.

References

[1] K. Deng, G. Wan, P. Deng, et al. *Nature Physics*, 12:1105–1110, 2016.

[2] B. Q. Lv, H. M. Weng, B. B. Fu, et al. *Physical Review X*, 5(031013), 2015.

[3] S.-Y. Xu, N. Alidoust, I. Belopolski, et al. *Nature Physics*, 11:748–754, 2015.

[4] S.-Y. Xu, I. Belopolski, N. Alidoust, et al. *Science*, 349(6248):613–617, 2015.

[5] D. F. Xu, Y. P. Du, Z. Wang, et al. *Chinese Physics Letters*, 32(107101), 2015.

[6] S. Souma, Z. Wang, H. Kotaka, et al. *Physical Review B*, 93(161112(R)), 2016.

[7] A. C. Niemann, J. Gooth, S.-C. Wu, et al. *Scientific Reports*, 7(43394), 2017.

[8] X. Huang, L. Zhao, Y. Long, et al. *Physical Review X*, 5(031023), 2015.

[9] C.-L. Zhang, S.-Y. Xu, I. Belopolski, et al. *Nature Communications*, 7(10735), 2016.

[10] R. D. Dos Reis, M. O. Ajeesh, N. Kumar, et al. *New Journal of Physics*, 18(085006), 2016.

[11] Y. Li, Z. Wang, P. Li, et al. *Frontiers of Physics*, 12(3):127205, 2017.

[12] B. Yan and C. Felser. *Annual Review of Condensed Matter Physics*, 8:337–354, 2016.

[13] A. Chen and M. Franz. *Physical Review B*, 93(201105), 2016.

[14] B. Lu, K. Yada, M. Sato, and Y. Tanaka. *Physical Review Letters*, 114(096804), 2015.

[15] U. Khanna, A. Kundu, S. Pradhan, and S. Rao. *Physical Review B*, 90(195430), 2014.

[16] S.-Y. Xu, I. Belopolski, D. S. Sanchez, et al. *Science Advances*, 1(10):e1501092, 2015.

[17] S.-M. Huang, S.-Y. Xu, I. Belopolski, et al. *Nature Communications*, 6(7373), 2015.

[18] C. Shekhar, A. K. Nayak, Y. Sun, et al. *Nature Physics*, 11:645–649, 2015.

[19] C.-C. Lee, S.-Y. Xu, S.-M. Huang, et al. *Physical Review B*, 92(235104), 2015.

[20] L. Aggarwal, S. Gayen, S. Das, et al. *Nature Communications*, 8(13974), 2017.

[21] H. Wang, H. Wang, Y. Chen, et al. *Science Bulletin*, 62:425–430, 2017.

[22] Y. Li, Y. Zhou, Z. Guo, et al. *npj Quantum Materials*, 2(66), 2017.

[23] M. D. Bachmann, N. Nair, F. Flicker, et al. *Science Advances*, 3(e1602983), 2017.

[24] C. Zhang, C. Guo, H. Lu, et al. *Physical Review B*, 92(041203(R)), 2015.

[25] J. Hu, J. Y. Liu, D. Graf, et al. *Scientific Reports*, 6:18674, 2016.

[26] J. Du, H. Wang, Q. Mao, et al. *Science China*, 59(5):657406, 2016.

[27] D. Wu, J. Liao, W. Yi, et al. *Applied Physics Letters*, 108(042105), 2016.

[28] Y.-Y. Wang, Q.-H. Yu, and T.-L. Xia. *Physical Review B*, 94(041103), 2016.

[29] N. Kumar, Y. Sun, N. Xu, et al. *Nature Communications*, 8(1642), 2017.

[30] C. Shekhar, V. Süß, and M. Schmidt. *ArXiv*, 1606.06649, 2016.

[31] A. A. Abrikosov. *Physical Review B*, 58(5):2788–2794, 1998.

[32] B. Fauqué, X. Yang, W. Tabis, et al. *ArXiv*, 1803.00931, 2018.

[33] H. B. Nielsen and M. Ninomiya. *Physics Letters B*, 130(6):389–396, 1983.

[34] D. Kharzeev. *Physics Letters B*, 633(2):260–264, 2006.

[35] F. Arnold, C. Shekhar, S.-C. Wu, et al. *Nature Communications*, 7(11615), 2016.

[36] C.-L. Zhang, S.-Y. Xu, C. M. Wang, et al. *Nature Physics*, 13:979–986, 2017.

[37] T. Besara, D. A. Rhodes, K.-W. Chen, et al. *Physical Review B*, 93(245152), 2016.

[38] Z. Chi, X. Chen, C. An, et al. *npj Quantum Materials*, 3(28), 2018.

[39] J.-O. Willerström. *Journal of The Less-Common Metals*, 99:273–283, 1984.

[40] N. Xu, H. M. Weng, B. Q. Lv, et al. *Nature Communications*, 7(11006), 2016.

[41] J. Jaroszynski, F. Hunte, L. Balicas, et al. *Physical Review B*, 78(174523), 2008.

[42] P. Santhanam, C. C. Chi, S. J. Wind, M. J. Brady, and J. J. Bucchignano. *Physical Review Letters*, 66(2254), 1991.

[43] A. Nordström and Ö Rapp. *Physical Review B*, 45(12577), 1992.

[44] T. Klimczuk, T. Plackowski, W. Sadowski, and M. Plebańczyk. *Physica C: Superconductivity*, 387:203–207, 2003.

[45] R. Vaglio, C. Attanasio, L. Maritato, and A. Ruosi. *Physical Review B*, 47(22):15302, 1993.

[46] M. Tinkham. *Introduction to superconductivity.* McGraw-Hill, Inc., 2nd edition, 1996.

[47] M. Tinkham. *Physical Review*, 129(6), 1963.

[48] K. Yamafuji, T. Kawashima, and F. Irie. *Physics letters*, 20(2), 1966.

[49] K. Yamafuji, E. Kusayanagi, and F. Irie. *Physics Letters*, 21(1), 1966.

[50] J. M. Lu, O. Zheliuk, I. Leermakers, et al. *Science*, 350(6266), 2015.

[51] X. Lin, Z. Zhu, B. Fauqué, and K. Behnia. *Physical Review X*, 3(021002), 2013.

[52] M. Randeria and E. Taylor. *ArXiv*, 1306.5785, 2013.

[53] Q. Chen, J. Stajic, S. Tan, and K. Levin. *Physics Reports*, 412:1–88, 2005.

[54] H. Yang, G. Chen, X. Zhu, J. Xing, and H. H. Wen. *Physical Review B*, 96(064501), 2017.

[55] S. Kasahara, T. Watashige, T. Hanaguri, et al. *Proceedings of the National Academy of Sciences*, 111(46):16309–16313, 2014.

[56] S. Kasahara, T. Yamashita, A. Shi, et al. *Nature Communications*, 7(12843), 2016.

[57] T. Watashige, S. Arsenijević, T. Yamashita, et al. *Journal of the Physical Society of Japan*, 86(014707), 2017.

CHAPTER 6

Low-temperature thermal conductivity study of the quasi-one-dimensional superconductor $Li_{0.9}Mo_6O_{17}$

6.1 Introduction

The purple bronze material $Li_{0.9}Mo_6O_{17}$ has been a subject of study for nearly 50 years [1], both because of its superconducting properties [2–4] and its quasi-one-dimensionality [5–7]. Here we address both of these aspects through their influence on the thermal and electrical conductivities at low temperatures. The study of the superconductivity (SC) is of particular interest due to recent proposals of triplet SC in $Li_{0.9}Mo_6O_{17}$ [8–11]. Triplet SC is an unusual phenomenon that is known from the class of unconventional quasi-one-dimensional superconductors called Bechgaard salts [12, 13] and is associated with re-entrant superconductivity [14] and the possibility of exotic phases [11].

An important question relating to the nature of the SC in $Li_{0.9}Mo_6O_{17}$, is whether there are nodes in superconducting gap, as this can give us information on the superconducting pairing symmetry. We address this question through a study of the thermal conductivity in the $T \to 0$ K limit, where a nonzero value suggests the presence of nodes.

The one-dimensionality is studied through the Wiedemann-Franz (WF) law, a longstanding empirical law that relates the ratio between the electronic thermal conductivity and the electrical conductivity to the temperature and the Lorenz number L [15]. The WF law has the form $\kappa_e/\sigma = LT$ and is considered to be obeyed as long as L is equal to the theoretical value $L_0 = (\frac{\pi^2}{3})(\frac{k_B}{e})^2$. It can be derived from the Drude model for a free electron gas, but remains valid when electron-electron interactions are active, i.e. in the case of a Fermi liquid (FL). This can be understood in terms of fermionic quasiparticles that are responsible for the transport of both charge and entropy.

At temperatures approaching 0 K or exceeding 300 K, the WF law has been shown to hold in a wide range of materials [16–21]. Although it is frequently violated at intermediate temperatures (for example in $Bi_2Sr_2CaCu_2O_8$ [21] or graphene [22]), those violations are not larger than a few tens of percent and typically show an effective L smaller than L_0. To date, no definitive violation of this law has been reported in the important 0 K limit.

However, this situation is predicted to be very different in one-dimensional materials. In such systems, where the electrons are confined to just one spatial dimension, the FL theory breaks down and the Tomonaga-Luttinger Liquid (TLL) theory is required for an accurate description. In the TLL theory, the fundamental excitations are holons, that only carry charge, and spinons, that only carry spin. As the holons transport purely electrical current, whereas the spinons transport thermal current, this spin-charge separation can lead to a violation of the WF law [23, 24].

$Li_{0.9}Mo_6O_{17}$ is one material in which this enhancement is expected to occur, as it has shown quasi-1D behavior in agreement with TLL theory in several spectroscopic probes, including ARPES [7, 25–27]. $Li_{0.9}Mo_6O_{17}$ was previously investigated for a possible violation of the WF law and a strong deviation was reported in the temperature range 25-300 K, with $L > L_0$ [28] (see Fig. 6.1(a)), again consistent with TLL theory. In this study, we investigate the low temperature limit and determine thermal and electrical conductivities of $Li_{0.9}Mo_6O_{17}$ at temperatures down to 80 mK with magnetic fields applied either parallel or perpendicular to the conducting chains and we observe a strong WF violation in one sample. Unfortunately, another sample did not reproduce this result.

In this chapter, we first discuss possible mechanisms for WF law violation (Sec. 6.1.1) and then describe the specifics of the material $Li_{0.9}Mo_6O_{17}$ in terms of its structure (Sec. 6.1.2), its resistivity (Sec. 6.1.4) and the samples we use for this study (Sec. 6.1.3). In Sec. 6.2, we then describe the thermal and electrical conductivity measurements on our two samples.

In order to perform subsequent analysis, it is necessary to separate the two contributions to the thermal conductivity, arising from phonons and electrons. In Sec. 6.3 we therefore extract the electron contribution, which we use to study the superconducting properties of $Li_{0.9}Mo_6O_{17}$ in Sec. 6.4 and to test the validity of the WF law in Sec. 6.5, where we see an order of magnitude violation at $T = 0$ K. In Sec. 6.6, we then confirm this violation by comparing differences in the conductivities in magnetic fields in order to find L over the whole temperature range. Finally, our conclusions for this chapter are described in Sec. 6.8.

6.1.1 Violation of the Wiedemann-Franz law

A strong violation of the WF law in $Li_{0.9}Mo_6O_{17}$ was reported previously, in Ref. [28]. In that work, the Lorenz number was determined both from both longitudinal and Hall conductivities (L_{xy}). We reproduce their data in Fig. 6.1(a). As can be seen, there is a violation with $L > L_0$ that increases as the temperature is decreased, and a much larger violation in L_{xy}. Such violations may be understood from TLL theory, based on the idea of spin-charge separation,

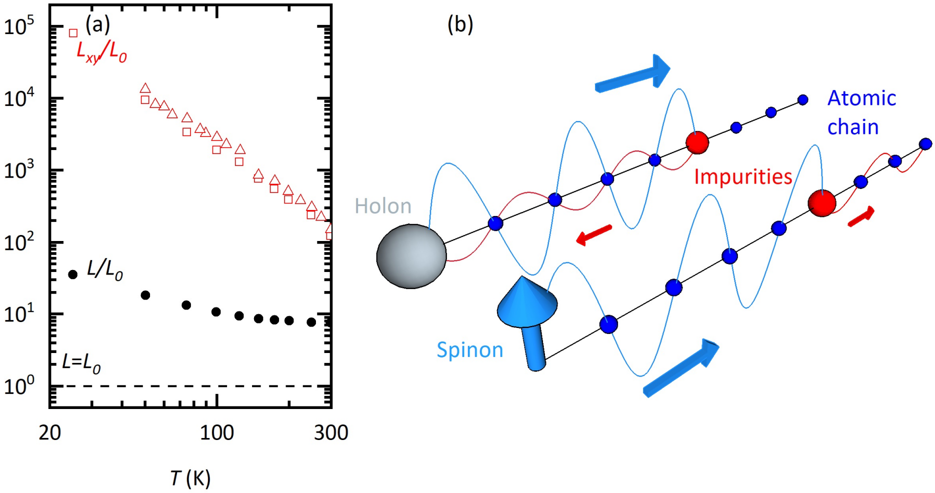

Figure 6.1: *(a) Previously reported data on the violation of the WF law, from Ref. [28]. (b) Illustration of the spin-charge separation process with impurity scattering. After Ref. [30].*

i.e. the separation between carriers of charge and of spin.

There exists more than one way in which spin-charge separation can lead to a violation of the WF law. One way is illustrated in Fig. 6.1(b). In this case, transport of holons is suppressed relative to that of spinons due to their stronger propensity for backscattering from impurities along the 1D chains. This effect causes an enhancement of L at low temperatures. The degree of enhancement then depends on the strength of electron interactions in the system, set by the Luttinger parameter or dimensionless conductance K. In the noninteracting case where $K = 1$, WF is obeyed, but in the case of repulsive interactions, $K < 1$, L is increased [23]. Beyond a critical interaction strength (when $K < 1/2$), it will even diverge.

A value of K can be estimated from the anomalous exponent α obtained from scanning tunneling microscopy [29] and angle-resolved photoemission spectroscopy [7], giving a value of 0.2-0.25. Therefore, within this framework, the value of L/L_0 is expected to diverge, as found experimentally [28].

Another route to WF law violation in a TLL is related to the formation of a charge gap without an accompanying spin gap. This idea is proposed for $Li_{0.9}Mo_6O_{17}$ based on previous measurements of the magnetic susceptibility, χ, and the Hall coefficient, R_H. The former can be taken as a measure for the spin density, while the latter is inversely proportional to the charge density. As seen in Figs. 6.2(a) and (b), the susceptibility is approximately constant over a wide temperature range, while the Hall coefficient begins to increase strongly with decreasing temperature below $T \approx 100$ K, where the material undergoes an incomplete Mott transition. This suggests a constant spin density, and strongly suppressed charge density at low T. Below 10 K, the Hall coefficient (and thus the charge density), is seen to saturate (see the inset of

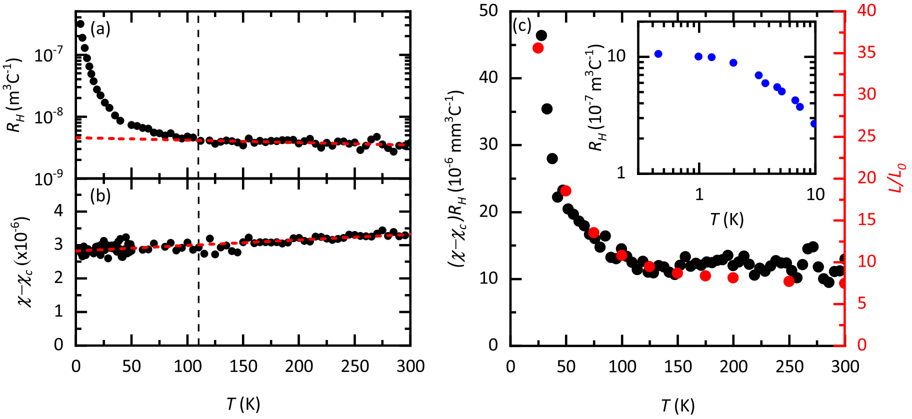

Figure 6.2: *(a) Hall coefficient as a function of temperature. Below a certain* T *(indicated by the black dashed line),* R_H *is enhanced. The red dashed line is a linear fit of the data above the enhancement of* R_H*. (b) Magnetic susceptibility, with subtracted Curie term, versus temperature. The red dashed line is a linear fit of the data, with intercept,* $(\chi - \chi_C)|_{T=0K} = 2.8 \times 10^{-6}$*. (c) Comparison between the product of the susceptibility and the Hall coefficient and the violation of the WF-law from Ref. [28]. A clear correlation is observed between the two. Inset:* R_H *data extended down to low temperatures, demonstrating a saturation. The* R_H *and* χ *data in (a), (b) and (c) are from Wakeham, Robinson* et al. *(unpublished work).*

Fig. 6.2(c)).

In the general theory for a TLL at commensurate electron fillings (such as half filling or quarter filling, relevant to $Li_{0.9}Mo_6O_{17}$), the presence of finite repulsive interactions destroys the metallic state by opening a Mott gap. For zero interchain hopping ($t_\perp = 0$), the Fermi surface that would exist in the absence of electron repulsion is essentially composed of two flat Fermi sheets, as represented by the dashed lines in Fig. 6.3(a). In the presence of interactions, the quasiparticle residue is then destroyed at every point on the Fermi surface.

When $t_\perp$ is finite, however, the Fermi surface becomes warped. In the case of no interactions, this is the situation of the dotted line in Fig. 6.3(a). The intersection of the Fermi surface with the line of zeros in the quasiparticle Green functions now becomes confined to isolated points. For small Coulomb repulsion, U, only quasiparticle states at these loci are destroyed. As U increases, however, quasiparticle states at progressively larger distances from these loci are also destroyed (by Umklapp processes), and as a consequence, the number of Landau quasiparticles becomes progressively smaller and the Fermi surface is transformed from a large warped sheet to small electron and hole pockets, thereby resembling a semi-metal. This is the case of the solid lines in Fig. 6.3(a). This overall scenario appears consistent with the saturation of the in-chain resistivity and Hall coefficient with decreasing temperature.

Fig. 6.2(c) shows the reported L/L_0 values from Ref. [28] together with χR_H. This quantity

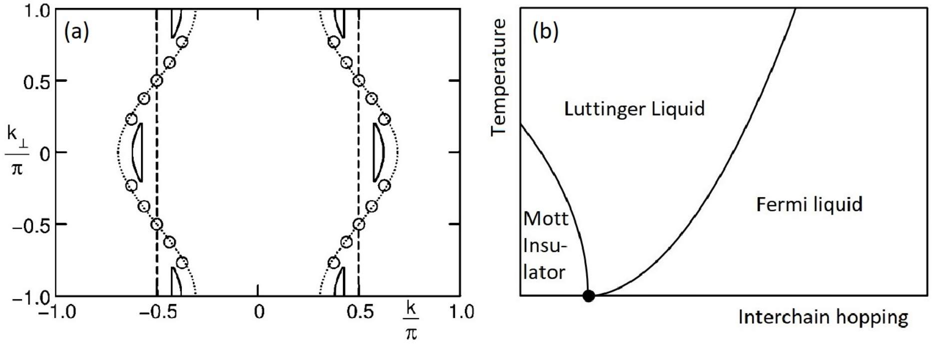

__Figure 6.3:__ (a) Schematic phase diagram of a quasi-one-dimensional system, as function of the the temperature and the interchain hopping. Lines between the different states indicate crossovers, so that the only phase transition is the $T=0$ K transition from a Mott insulator to a FL. This Mott insulator phase is only present for commensurate fillings. (b) Theoretical FS in the half-filled case, compared to the non-interacting case (dotted lines) and the purely one-dimensional case ($t_\perp = 0$, dashed lines). Both figures from Ref. [31].

χR_H is proportional to the ratio of the spin and charge densities and we can see that it follows the same behavior as L/L_0. With this correspondence, the proposed explanation for WF violation is strongly supported. If it remains valid down to very low temperatures, a saturation value of the order of $\sim$1000 might be expected for L/L_0.

There exists an alternative scenario, however, namely that $Li_{0.9}Mo_6O_{17}$ undergoes a dimensional crossover from quasi-1D to 3D at low temperature. In that case, FL behavior will be restored, and thus the WF law is expected to be recovered. This possibility was proposed in Ref. [31] and is also illustrated in Fig. 6.3(b), which depicts a general phase diagram of a quasi-one-dimensional system. As seen in Fig. 6.3(b), there always exists a crossover from a TLL to a FL as long as the interchain hopping is sufficiently large. If it is small, a crossover to a Mott insulating state is expected. However, while the resistivity of $Li_{0.9}Mo_6O_{17}$ increases significantly with decreasing temperature (below 25 K), it does not diverge, suggesting the presence of a low-carrier metallic state at low temperature. Therefore, we may expect that $Li_{0.9}Mo_6O_{17}$ becomes a FL at low temperature and the WF law is in fact obeyed (i.e. $L/L_0 = 1$) at T=0 K.

6.1.2 Structure of $Li_{0.9}Mo_6O_{17}$

$Li_{0.9}Mo_6O_{17}$ has a monoclinic unit cell ($P2_1/m$ structure), shown in Fig. 6.4(a). Within this unit cell, there are six crystallographically independent positions with Mo atoms. Two of these atoms, Mo(3) and Mo(6) are located within MoO_4 tetrahedra and the other four in MoO_6 octahedra [5, 32]. The Mo(1) and Mo(4) atoms are placed on the zigzag chains along the *b* direction, which are formed by four corner-linked octahedra.

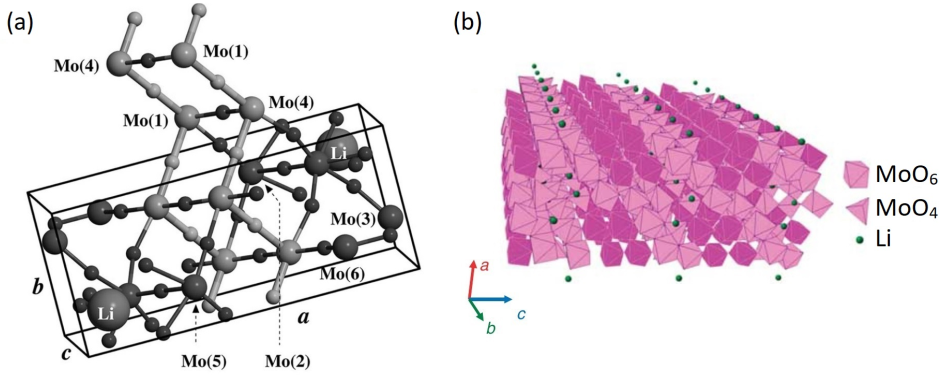

Figure 6.4: *(a) Unit cell of $Li_{0.9}Mo_6O_{17}$ indicating the 1D zigzag chains running along the b direction. Reproduced from Ref. [32]. (b) Three-dimensional crystal structure showing the conducting zigzag chains as MoO_6 octahedra along the b axis in dark purple and non-conducting octahedra and MoO_4 tetrahedra in light pink. Li ions are shown as green spheres. Adopted from Ref. [28].*

Within each unit cell, there is a pair of these chains, connected by an O atom between Mo(1) and Mo(4). Each pair of chains is well separated from that in the adjacent unit cells. Fig. 6.4(b) shows a wider view of the structure of $Li_{0.9}Mo_6O_{17}$, with the tetra- and octahedra highlighted. Those forming the conducting chains are given a darker color. The large spatial separation of the conducting elements gives rise to the highly anisotropic properties. The Li atoms are located at intermediate sites, which typically exhibit ~10% of vacancies. The variation in this is fairly small, such that there are typically between 0.87 and 0.93 Li atoms per Mo_6O_{17} unit.

6.1.3 Samples

Single crystals of $Li_{0.9}Mo_6O_{17}$ were grown using a temperature gradient flux method [33]. sample 1 was supplied by Prof. Hidenori Takagi from the Max Planck Institute for Solid State Research in Stuttgart and sample 2 by Prof. Martha Greenblatt from Rutgers University in New Jersey, USA. A mixture of Li_2MoO_4, MoO_3 and MoO_2 was sealed in evacuated quartz ampules and heated in a two-zone furnace. The mix was first preheated to a temperature below the melting point for three days, then heated further in a temperature gradient for more than seven days. Afterwards, the ampules were cooled down to room temperature over the course of one hour and opened. The resulting crystals were then checked with XRD in order to identify the crystallographic axes, so that each sample could be cleaved along either the *a*- or *b*-axes.

For the measurements described in this chapter, both samples were measured along their crystallographic *b*-axes. Sample 1 has dimensions 0.95x0.67x0.16 mm^3, while sample 2 is a bit larger at 2.1x1.1x0.06 mm^3. Both samples demonstrate superconductivity with $T_c = 1.4$ K and 1.2 K, respectively. The appearance of SC (inset of Fig. 6.5(b)) can be taken as a sign of high quality in this material.

6.1.4 Resistivity of $Li_{0.9}Mo_6O_{17}$

Due to its quasi-one-dimensional character, $Li_{0.9}Mo_6O_{17}$ has a very large resistive anisotropy, such that $\rho_a : \rho_b : \rho_c = 80 : 1 : 1600$ at room temperature [34]. When cooling from 300 K, its in-chain resistivity initially shows metallic behavior, until it reaches a minimum around $T = 25$ K. Below this temperature, the resistivity exhibits a strong upturn, which ends with the onset of SC around $T = 1$-2 K.

Fig. 6.5(a) shows the resistivity of $Li_{0.9}Mo_6O_{17}$ measured along each of its axes, from the work of Ref. [34]. The sample used in that study, exhibits a high T_c of 2.2 K and a small resistive upturn. In our samples, T_c is lower and the upturn is larger (Fig. 6.5(b)). The resistivity along the b-axis (the only direction measured in our experiments) of sample 1, is also higher by a factor of ~2, for temperatures above the upturn. Sample 2 was not measured in this temperature range.

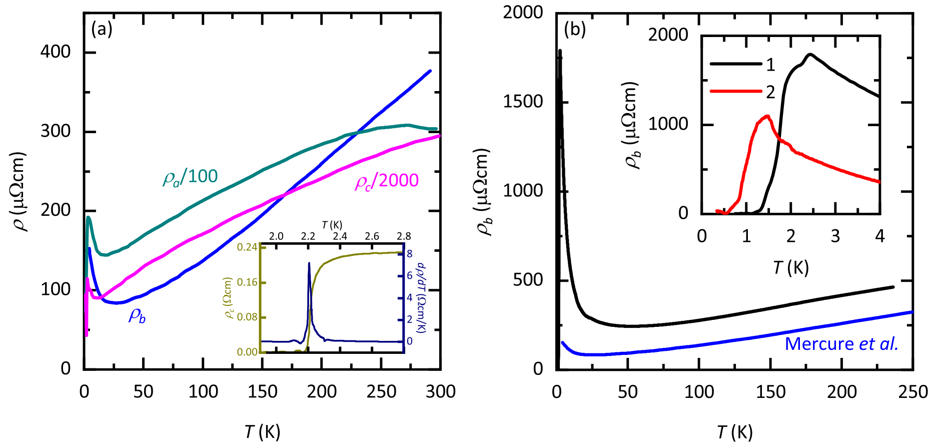

Figure 6.5: (a) Previously reported zero-field resistivity curves for $Li_{0.9}Mo_6O_{17}$ along each of its three crystallographic axes. ρ_a and ρ_c are scaled for clarity. The inset shows the superconducting transition as seen in ρ_c and its derivative. From Ref. [34]. (b) Zero-field b-axis resistivity curve from the present work (sample 1, black) and from Ref. [34] (blue). The inset highlights the superconducting transition in sample 1 and compares it with sample 2.

The upturn of the resistivity remains a topic of discussion, as no consensus exists about its origin. One commonly suggested explanation is a charge density wave (CDW). The CDW scenario is supported by transport data from various sources [35–37], and several materials related to $Li_{0.9}Mo_6O_{17}$ are known to exhibit CDW behavior. However, this scenario seems unlikely in $Li_{0.9}Mo_6O_{17}$, as no signs of a CDW are seen in optical [38] or STM experiments [29]. Furthermore, the structural changes that are expected with a Peierls-type CDW are not seen in X-ray or neutron diffraction [39, 40].

Another explanation that has been suggested is localization [42], but this too leaves parts of the data unexplained [43]. However, more recently, the proposal of dark excitons that are ordered by repulsive Coulomb interaction at low temperature, was made theoretically [44]. This theory provides a natural explanation for the upturn as well as many other properties of $Li_{0.9}Mo_6O_{17}$ and is strongly supported by recent experimental work [45].

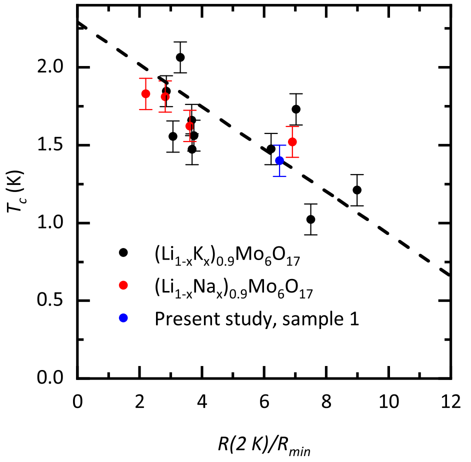

Figure 6.6: *T_c of doped $Li_{0.9}Mo_6O_{17}$ plotted as a function of $R|_{T=2K}/R_{min}$. This data is independent of the value of x. From Ref. [41]. The ratio that we determined for sample 1 is included.*

While every crystal of $Li_{0.9}Mo_6O_{17}$ exhibits the resistive upturn, not every one of them is superconducting, and those that are often vary in their value of T_c. This appears to be related to the size of the upturn, as Ref. [41] reported an anti-correlation between T_c and the upturn size, with a linear relation between T_c and the ratio of the resistivity at 2 K to the minimal resistivity, as shown in Fig. 6.6. With the values of $T_c = 1.4$ K and $R|_{T=2K}/R_{min} \approx 6.5$, our result for sample 1 agrees well with this relation. This shows that, despite the relatively high value, the resistive behavior of sample 1 is in good agreement with previous reports.

For sample 2, all measurements were done in the experimental setup for thermal conductivity (see Sec. 2.4.1), which has a maximum temperature range of operation of approximately 5 K. For this reason, we did not measure near the temperature of minimal resistivity. However, in order to compare the data of this sample with previous measurements, we can estimate the minimum resistivity, R_{min}, using the findings of Ref. [41]. For a T_c of 1.2 K, we should have $R_{T=2K}/R_{min} = 7$-9 and 80-110 $\mu\Omega$cm. This value is consistent with previous reports [28, 34], but smaller than that of sample 1 (see Fig. 6.5(b)).

6.2 Thermal and electrical conductivities

In order to compare the data between our two samples as well as previously published data, we show the electrical and thermal conductivities (σ and κ, respectively) of both samples in zero

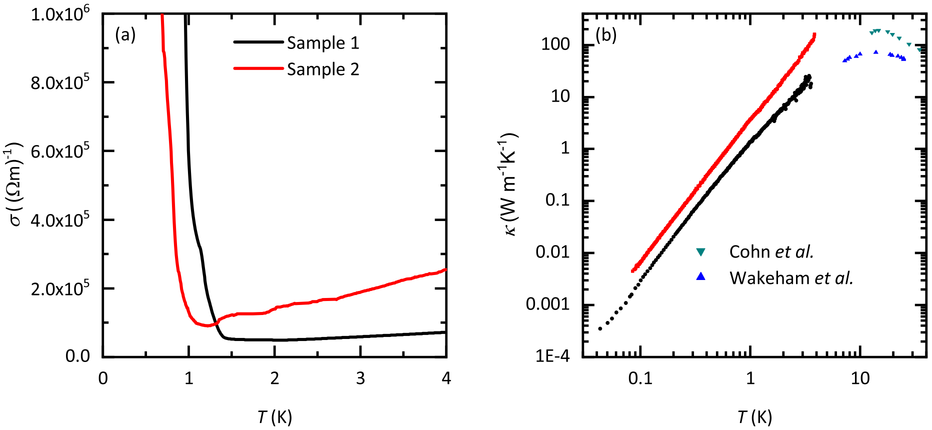

Figure 6.7: *Comparison of the (a) electrical and (b) thermal conductivities of samples 1 and 2 in zero magnetic field. Data points from studies performed by Cohn* et al. *[46] and Wakeham* et al. *[28] are included for comparison.*

magnetic field in Fig. 6.7(a) and (b). From Fig. 6.7(a), we see that the electrical conductivity of sample 1 is lower. A possible explanation of this could be a mixing of the conductivity between the different crystallographic directions. The contacts were naturally prepared in such a way as to avoid this issue, but possibly not with complete success. We note, however, that the obtained ρ_b values are consistent with the previous reports.

The thermal conductivity (Fig. 6.7(b)) of sample 1 is also considerably lower than that of sample 2, by a factor of approximately 3. On a log-log scale, both curves are approximately parallel to each other. The data from Refs. [46] and [28], included in Fig. 6.7(b), are most consistent (in terms of their magnitude) with sample 1, with both of them showing a maximum beyond the range of our measurement. This suggests that sample 2 has an anomalously large thermal conductivity.

It is not clear whether the discrepancy between the two datasets is intrinsic (e.g. due to a higher phonon thermal conductivity in sample 2) or extrinsic (due to some error in one of the measurements). It is true that the two samples were grown in different laboratories under nonidentical conditions and as shown in Fig. 6.7(b) for Refs. [28, 46], the thermal conductivity of $Li_{0.9}Mo_6O_{17}$ can vary by a factor of 2-3 between samples from different sources.

Another possible origin of the discrepancy could be the contacts. In sample 1, no electrical measurement could be performed with the contacts that were used for the thermal measurement. In fact, a complete redoing of these contacts on a cleaned surface was required in order to obtain reasonable electrical data. It is not inconceivable then, that these bad contacts were also influencing the thermal measurement by adding spurious thermal resistances. In that case, the κ of sample 1 has a systematic error.

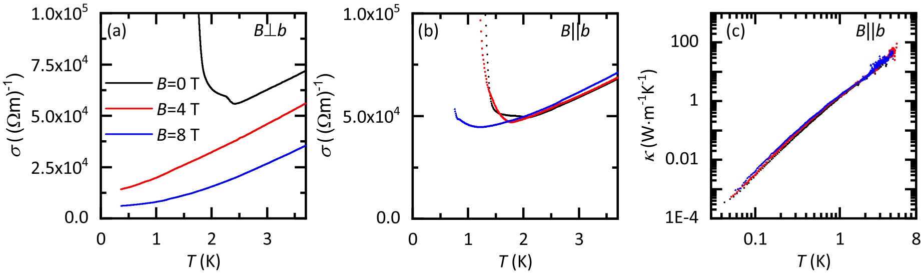

Figure 6.8: *Conductivities of sample 1 under magnetic fields of 0, 4 or 8 T, with (a) the electrical conductivity in perpendicular field; and (b) the electrical conductivity in parallel field and (c) the thermal conductivity in perpendicular field.*

However, if there is a thermal resistance between the sample and the thermometers, then this would lead to a measured ΔT that is smaller than the real ΔT over the sample, causing a κ that appears larger than it is. As sample 1 has the smaller κ of the two samples, this rather suggests that sample 2 suffered from this effect. For this sample, however, the contact resistances were sufficiently low to allow for a good electrical measurement. Furthermore, a sample with larger contact resistances is expected to reach a higher base temperature and exhibit a saturation of the thermometer resistances, which is not consistent with our measurements. The fact that the two samples have a qualitatively similar temperature dependence is also a further argument against this theory.

Thus, it appears that thermal contact resistances cannot explain the difference in κ between our samples. The samples were measured in the same setup, under the same experimental conditions, so a systematic error in the measurement of one sample seems unlikely. We therefore attribute the difference between our samples to the different growth conditions.

Next we discuss the data in an applied magnetic field, beginning with the conductivities of sample 1, shown in Fig. 6.8. For this sample, σ was measured for both $B \perp b$ and $B \parallel b$ (see Figs. 6.8(a) and (b) respectively). In the measured temperature range, σ can be seen to increase with increasing temperatures in both cases, as is known to occur in $Li_{0.9}Mo_6O_{17}$ below the metal-insulator transition. In zero field, the sample experiences a superconducting transition around a critical temperature of approximately 1.4 K.

In the perpendicular configuration, there is a strong negative magnetoconductivity and superconductivity is easily suppressed. With $B = 4$ T, there is no more sign of SC down to the lowest measured temperatures. On the other hand, when the field is parallel to the b-axis, superconductivity is only weakly suppressed and the MR is negligible or slightly positive. The higher critical field in the parallel field configuration is consistent with previous reports [47] and sample 1 is therefore likely to be bulk superconductor.

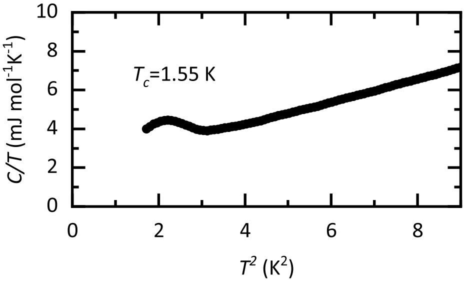

Figure 6.9: *Data from specific heat measurements of a sample of $Li_{0.9}Mo_6O_{17}$ with $T_c = 1.55$ K, showing the specific heat anomaly at the superconducting transition. From Walmsley* et al. *(unpublished work).*

This is corroborated by previous specific heat measurements, which demonstrated a clear anomaly at T_c for $Li_{0.9}Mo_6O_{17}$ crystals with T_c down to 1.55 K (see Fig. 6.9). This is clear evidence for the presence of bulk SC. This T_c is only slightly larger than that of sample 1, which is therefore likely to be in the same regime.

We now turn to the thermal conductivity of sample 1, shown in Fig. 6.8(c). As can be seen in the figure, κ decreases by over five orders of magnitude in the temperature range from 5 K down to 80 mK. Furthermore, on top of this strong temperature dependence, there is also a small positive thermal magnetoconductivity. We believe this effect is due to the thermal conductivity of electrons, κ_e, which is one of the two main contributions to the total κ. The other contribution is due to phonons, κ_{ph} and is generally unaffected by magnetic fields. In this case, at least for $B \parallel b$, we can attribute the positive thermal magnetoconductivity to the same mechanism as the positive electrical magnetoconductivity.

As shown in Fig. 6.10, sample 2 shows qualitatively the same behavior as 1, but with significant quantitative differences. One clear difference is the suppression of SC in sample 2 with lower parallel magnetic fields. In sample 2, the application of 4 T ($B \parallel b$) already reduces T_c considerably, and 8 T is sufficient to suppress any sign of SC. This difference in critical field can be associated with the observed difference in T_c and suggests that here the SC is likely to be filamentary in nature, in agreement with specific heat measurements which showed no anomaly for similarly low values of T_c. Another distinction between the two samples is the fact that the positive magnetoconductivity is larger in sample 2.

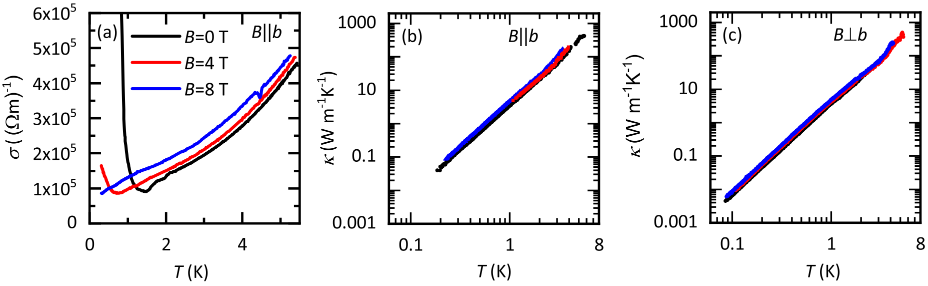

Figure 6.10: *Conductivities of sample 2 under magnetic fields of 0, 4 or 8 T, with (a) the electrical conductivity in parallel field and (b) in thermal conductivity in parallel field; and (c) the thermal conductivity in perpendicular field.*

Figs. 6.10(b) and (c) show the thermal conductivity of sample 2, with a magnetic field parallel or perpendicular to the *b*-axis, respectively. In either orientation, κ depends strongly on the temperature, dropping again by five orders of magnitude over less than 5 K.

One question arises regarding the thermal conductivity in perpendicular field. The behavior in this configuration is nearly the same as in the other, with a slight increase in κ as a function of the magnetic field. Attributing this increase to the thermal conductivity of electrons is in good agreement with σ in parallel field. In perpendicular field, however, σ decreases strongly with magnetic field. The increase in $\kappa_{B\perp b}$ with field is thus not understood.

6.3 Extraction of the electronic contribution to the thermal conductivity

Before we can proceed to study the superconducting properties, it is necessary to separate the electrical contribution to the thermal conductivity, κ_e, from the phonon contribution, κ_{ph}. Here we two discuss methods of extracting κ_e in the limit of $T \to 0$ through extrapolation of the data.

The conventional way to extract κ_e from the measured total κ is to plot κ/T as a function of T^2 and make a linear fit. The intercept of this fit then gives κ_e/T and the slope κ_{ph}/T^3, in the 0 K limit. In order to justify the use of this method, we need to assume that the phonon mean free path is limited by the sample dimensions at low temperatures. Why this should be so can be made clear by deriving the thermal conductivity from simple kinetic theory.

Consider first the rate of change of the energy of a phonon with velocity $\vec{v}$ under a thermal gradient ∇T:

$$\frac{\partial E}{\partial t} = c\vec{v} \cdot \vec{\nabla} T, \tag{6.1}$$

with c the heat capacity of the single phonon. The phonon travels an average distance $\lambda_{mfp} = v\tau$, with τ the relaxation time, before being scattered. λ_{mfp} is called the mean free path. Summing over all phonons, with concentration n, then gives the total heat flux:

$$\vec{Q} = -nc\tau\langle\vec{v} \cdot \vec{v}\rangle\vec{\nabla} T = -\frac{1}{3}nc\tau v^2\vec{\nabla} T, \tag{6.2}$$

where the brackets represent an average over all particles. Combining Eq. 6.2 with Fourier's law, $\vec{Q} = -\kappa\vec{\nabla} T$, then gives:

$$\kappa_{ph} = \frac{1}{3}nc\tau v^2 = \frac{1}{3}C_v v\lambda_{mfp}, \tag{6.3}$$

with $C_v = nc$ the total heat capacity.

As long as the sample dimensions allow it, λ_{mfp} increases with decreasing temperature, as overall scattering reduces. However, when λ_{mfp} becomes of the same magnitude as the sample size, it is expected to saturate due to scattering off the edges of the sample. With λ_{mfp} being boundary limited in this way, C_v becomes the only temperature dependent parameter and κ_{ph}

assumes its T^3 dependence. κ_e, on the other hand, has a different behavior and we can make use of this difference in temperature dependence to distinguish the two contributions. In a metal, $\kappa_e \propto T$ at low T. In an isotropic BCS superconductor, κ_e/T extrapolates to zero, while a superconductor with nodes in the order parameter, it is linear in T at low temperatures and thus becomes a constant offset in the plot of κ/T.

The assumption of a boundary limited mean free path is not necessarily valid, as specular reflection may lead to a λ_{mfp} that is than the sample size. Specular reflection differs from the usual diffusive reflection in that phonons are reflected elastically from the surface instead of being absorbed and re-emitted. This is more likely to occur when the crystal surface is very smooth. If specular reflection is important, κ_{ph} is no longer T^3 dependent due to the T-dependence of λ_{mfp} and the linear fitting does not work. Instead, a $T^{2\alpha}$ fit can be made, with $\alpha \lesssim 1$.

There is no general agreement in the literature about which fitting procedure should be used. In fact, this is a point of heated debate [48–52]. The linear method was used for, among others, the unconventional superconductors $YBa_2Cu_3O_y$ [53], LaFePO[54] and FeSe [55]. In each of these cases, a constant λ_{mfp} was found, consistent with the sample dimensions. The $T^{2\alpha}$ method, however, is also commonly employed, for example for cuprates $YBa_2Cu_3O_y$ and $La_{2-x}Sr_xCuO_4$ [56], iron pnictide $BaFe_2As_2$ [57], the low-dimensional quantum magnet $NiCl_2$-$4SC(NH_2)_2$ [58], or the quasi-one-dimensional spin chain material $(CH_3)_2NH_2CuCl_3$ [59]. In each of these examples, specular reflection is invoked as justification for the fit, sometimes together with scattering off grain boundaries or electrons [57]. As we have no information to say a priori that one method or the other should be used in our case, we use both of them and compare the results.

Examples of both the linear and the $T^{2\alpha}$ fittings are shown for sample 1 in Fig. 6.11(a), up to 0.05 K^2 (≈225 mK). Regardless of which fitting method is used, it is important to consider the range over which the fit is applied. For the linear fit, the temperature needs to be low enough for the phonon mean free path to be in the boundary limited regime. This typically happens only at very low temperatures, because only then does λ_{mfp} become of the order of the sample size. The temperature where this occurs, is different for each material. In $YBa_2Cu_3O_y$, for example, it is considered to be as low as 110 mK [52], while in IPA-$CuCl_3$ it is as high as 700 mK [60]. For our $Li_{0.9}Mo_6O_{17}$, we tried various different ranges from 0 up to 300 mK and found that above ∼225 mK, the linear fit does not accurately describe the data. Additionally, for ranges up to at most ∼120 mK, the fit parameters have large error bars due to the limited amount of data.

In Fig. 6.11(b), we show the extracted parameters for linear fits of the 0, 4 and 8 T datasets of sample 1, for different fitting ranges 0-X K^2. The slope (κ_2/T^3) that we determine with these fits shows very little dependence on the fitting range, but the intercept (κ_e/T) increases with larger fit ranges. The data at 4 T stands out, as it has a κ_e/T that is distinct from that which was determined for the other fields, particularly for higher range maxima, while it would be expected to show values between those at 0 and 8 T.

The $T^{2\alpha}$ fit is often employed for larger temperature ranges [52]. We made a number of fits

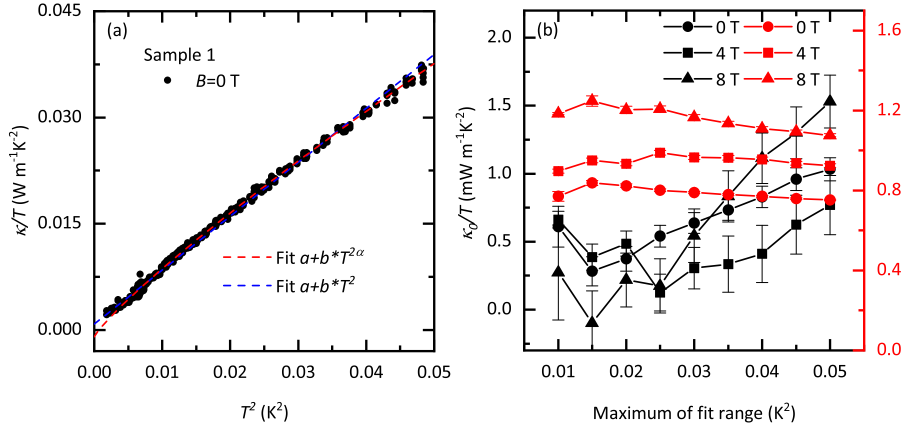

Figure 6.11: *(a) Thermal conductivity divided by temperature plotted against the square of the temperature for sample 1. Two different fitting methods are used to extract the electronic contribution at 0 K. (b) Parameters resulting from the linear fitting method applied to the data of sample 2, for different fitting ranges. The minimum of the range is fixed at 0 K^2, while the maximum is incremented by 0.005 K^2 up to 0.05 K^2.*

with this method (see Fig. 6.11(a)), using ranges from 0 K up to a maximum of 1 K. For the lowest maxima of the temperature ranges, up to approximately 180 mK, this method exhibits very large errors and does not accurately describe the data. For maxima larger than 0.5 K, the data at relatively high temperature is well described, but the fit does not capture the points below 100 mK. Since our goal is to estimate a value in the 0 K limit, these points at the lowest temperatures are crucial and a fit that does not capture them cannot be used. Finally then, using a range from 0 K to a maximum between 180 mK and 0.5 K results in a fair description of the data with χ^2 similar to the linear fit, however the intercepts of the fits fluctuate around 0 W m^{-1} K^{-2}, often even becoming negative (as for example in Fig. 6.11(a)). The calculated values of α are between 0.84 and 0.90.

B (T)	κ_e/T (mW m^{-1} K^{-2})	κ_2/T^3 (W m^{-1} K^{-4})
0	0.7±0.4	0.78±0.04
4	0.7±0.3	0.93±0.03
8	1.1±0.7	1.12±0.07

Table 6.1: *Results for sample 1 of the extrapolation to $T = 0$ K with the linear fitting method.*

As a negative κ_e/T is not physical, we use only the results of the linear fitting method for further analysis. We show the results for sample 1 in Table 6.1; these values are used for further analysis within this chapter.

6.4 Superconductivity in $Li_{0.9}Mo_6O_{17}$

Looking again to the thermal conductivity data of sample 1, but with an eye to the superconducting transition, reveals there is a suppression of κ when the crystal is superconducting (see Fig. 6.12(a)). This suppression is emphasized in Fig. 6.12(b), where we plot the difference between the normal state thermal conductivity, κ_N (estimated from the fit in Fig. 6.12(a)), and measured κ.

The observed suppression is consistent with conventional, isotropic s-wave superconductivity, where κ_e decreases exponentially when SC is induced, as seen in Nb [61] and $LaRhSi_3$ [62], for example. In other cases, κ_{ph} is known to increase strongly below T_c, as a result of a reduced electron-phonon interaction leading to an enhancement of λ_{mfp}. This has been reported, for example, in the high-T_c unconventional superconductor $YBa_2Cu_3O_{7-y}$ [63] and in the heavy fermion superconductor $PrOs_4Sb_{12}$ [64]. We see no sign of this type of behavior.

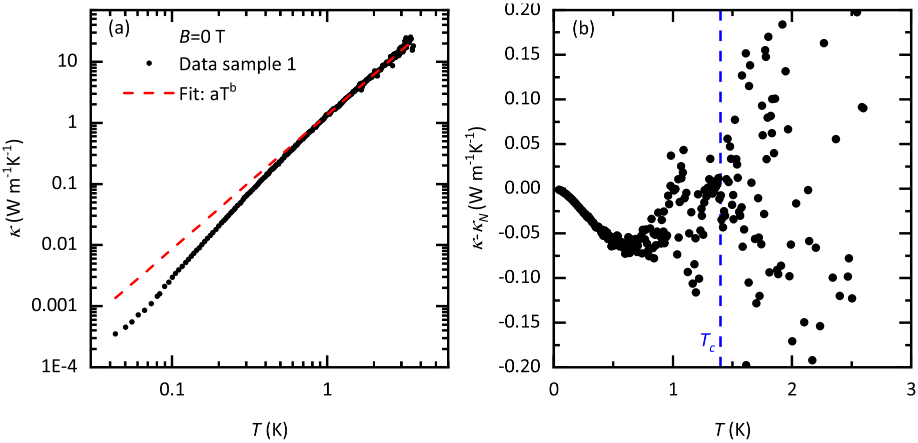

Figure 6.12: *(a) Zero-field κ of sample 1, fit with a power law in order to estimate the normal-state thermal conductivity. (b) Deviation of the normal-state estimate, κ_N, from the real experimental data. The blue dashed line indicates T_c.*

Our low-T thermal conductivity data can be used to study the presence of nodes in the superconducting gap (i.e. points where the gap closes). Generally, the value of κ/T in the zero kelvin limit is used as a diagnostic tool for this [55, 65, 66]. If $\kappa_0/T > 0$, the SC is nodal, if $\kappa_0/T = 0$, it is not (in which case it is s-wave or p-wave). The reason for this is the fact that an isotropic gap leads to an exponential suppression of κ_e/T while nodal SC creates excitations at low energy that can propagate heat. This leads to a finite κ_0/T, with a linear temperature dependence of κ_e/T due to the dual structure of the nodal gap. However, this classification only works for samples that are homogeneous and contain no non-superconducting regions, as those would also result in a residual linear term in κ.

The residual thermal conductivity of sample 1 is shown in Fig. 6.13. The value of κ_0/T is non-zero, but very small. Observations of nodal superconductivity, however, typically rely on much larger residual thermal conductivities [65, 68], such as seen in the nodal superconductor Sr_2RuO_4 [69], for example. Sr_2RuO_4 has a comparable T_c to $Li_{0.9}Mo_6O_{17}$ but a residual thermal conductivity that is three orders of magnitude larger. Because of this, we can conclude that the superconductivity of $Li_{0.9}Mo_6O_{17}$ is likely nodeless, consistent with isotropic s-wave SC or with a proposed scenario of nodeless triplet SC [10, 11, 70], illustrated in the inset of Fig. 6.13.

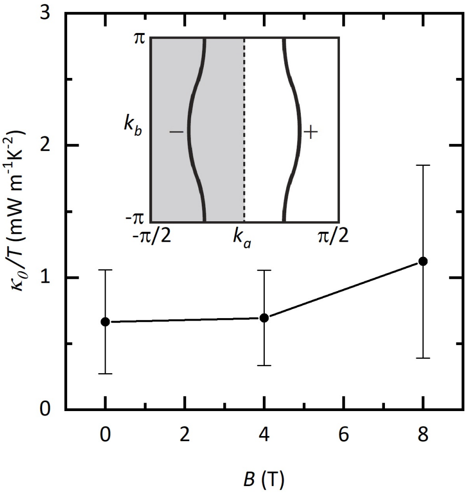

Figure 6.13: *Residual thermal conductivity of sample 1, as extracted from the linear fitting method described in Sec. 6.3. Inset: Illustration of the gap symmetry of nodeless p-wave superconductivity. The solid lines represent the Fermi surface, the dashed lines the nodes in the gap. As the nodes do not cross the FS, this situation is essentially nodeless. From Ref. [67].*

6.5 Validity of the Wiedemann-Franz law in the limit T → 0

Fig. 6.14(a) shows an example of the linear fitting procedure for sample 2. As with sample 1, we only use the outcomes of this fitting method for further analysis. In Fig. 6.14(a), we plot the extracted parameters for different field ranges, demonstrating that the fitting is valid also for this sample. The values of κ_0/T that we use in our assessment of the WF law validity are the averages of those in the figure, for each field strength. These values are shown in Table 6.2.

Having determined values of κ_e/T at 0 K, the next step towards an examination of the validity of the WF law is to find corresponding values of σ. For sample 2, we are able to extract these σ_0 from a simple linear fit of the data. As shown in Fig. 6.15, σ of sample 2 demonstrates linear behavior at low temperatures and can therefore be extrapolated to 0 K. Since σ diverges when SC sets in, the lower limit of our fitting range is fixed above T_c. The higher limit is set by the loss of linearity above approximately 2 K. For sample 1, we cannot perform this analysis, as the higher T_c leads to a minimum temperature that is too high to reach the linear regime. For

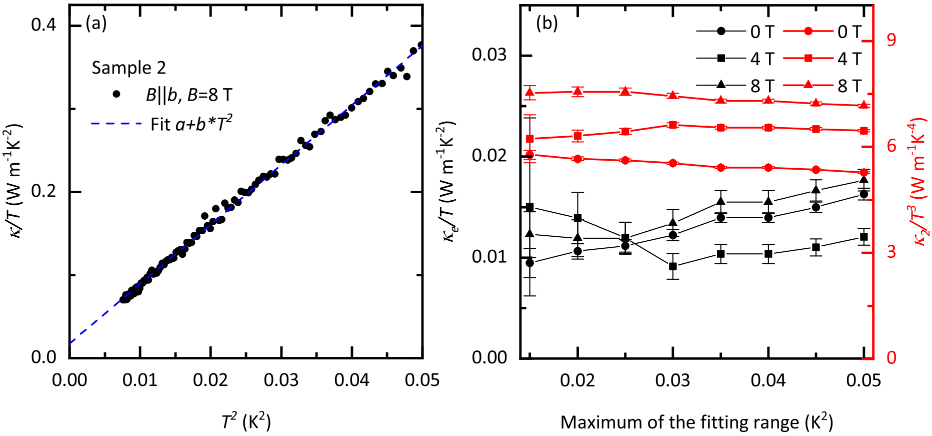

Figure 6.14: *(a) Thermal conductivity divided by temperature plotted against the square of the temperature for sample 2. Two different fitting methods are used to extract the electronic contribution at 0 K. (b) Parameters resulting from the linear fitting method applied to the data of sample 2, for different fitting ranges. The minimum of the range is fixed at 0* K^2*, while the maximum is incremented by 0.005* K^2 *up to 0.05* K^2*.*

this reason, we cannot extract σ_0 with any confidence and we only perform the extrapolation for sample 2. We have tried various different ranges for the linear fit of this sample, and found the resulting σ_0 to be range-independent. This shows that the linear fitting is justified.

Finally, we are able to determine $\kappa_0/(\sigma_0 T L_0)$, and assess the validity of the WF law in $Li_{0.9}Mo_6O_{17}$. The calculated L/L_0 values are shown together with the results of our fittings in Table 6.2. Combining the extracted σ_0 with the κ_e/T from the linear fit (under the assumption of a boundary limited λ_{mfp}), we see an order of magnitude violation of the WF law at any of the measured magnetic fields. In Sec. 6.6, we attempt to confirm this violation using a different method that does not rely on any assumptions concerning the phonon boundary scattering.

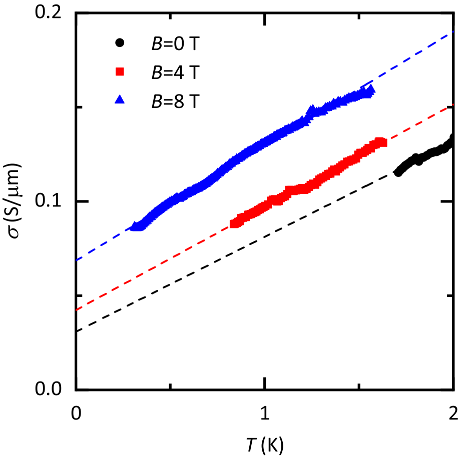

Figure 6.15: *Extrapolation of the electrical conductivity of sample 2 using a linear fit (dashed lines) of the data. The data is cut above* T_c*.*

B (T)	κ_e/T (mW m^{-1} K^{-2})	κ_2/T^3 (W m^{-1} K^{-4})	σ_0 (S/μm)	L/L$_0$
0	13±2	5.5±0.2	0.030±0.008	17±4
4	12±2	6.5±0.1	0.045±0.004	11±2
8	14±2	7.4±0.2	0.065±0.002	9±1

Table 6.2: *Results for sample 2 of the extrapolation to* $T = 0$ *K with the linear fitting method for* κ_e/T *and* σ*, together with the determined WF violation* L/L_0*.*

6.6 The differential Wiedemann-Franz law

Another way to separate the effects of electrons and phonons on the thermal conductivity, is by considering their dependence on the magnetic field. We saw in Fig. 6.10(c) that the total thermal conductivity increases in a magnetic field. As also the electrical conductivity is enhanced in a field, most likely the electrical contribution to κ is at least partially responsible for this. If we assume that it is fully responsible, and thus that κ_{ph} is field-independent, then we can separate the two contributions.

This assumption is not unfounded, as phonons are typically insensitive to magnetic fields, but we nevertheless must justify it carefully. Situations where κ_{ph} *does* depend on the magnetic field can occur mainly when the phonons are scattered by particles that are affected by magnetic fields, for example through the paramagnetic scattering effect [71–73]. In this case, phonons can scatter with paramagnetic spins, leading to a reduction of κ_{ph}. A sufficiently high magnetic field suppresses this scattering mechanism and therefore leads to an increasing κ_{ph} in field. This scenario is unlikely for $Li_{0.9}Mo_6O_{17}$, however, as no magnetic atoms are present in this compound. Furthermore, this type of magnetic scattering involving phonons is normally expected to lead first to a dip in κ_{ph} and only then to an enhancement [59, 74, 75]. We see no sign of such a dip. For these reasons, the assumption that κ_{ph} does not depend on the magnetic field, is well justified.

When κ_{ph} is field-independent, the difference between the values of κ at different magnetic fields is entirely electronic. We may then consider a differential version of the WF law, as follows:

$$\frac{\Delta\kappa}{\Delta\sigma} = LT, \tag{6.4}$$

where $\Delta\kappa = \kappa|_{B=B_2} - \kappa|_{B=B_1}$ and $\Delta\sigma = \sigma|_{B=B_2} - \sigma|_{B=B_1}$ and $B_2 > B_1$. $\Delta\kappa$ and $\Delta\sigma$ are shown in Fig. 6.16(a) for $B_1 = 8$ T and $B_2 = 4$ T, for sample 2. We could also use data recorded at 0 T, but then the sample is superconducting for a large part of the temperature range, so we cannot determine $\Delta\sigma$ at low temperatures. For this reason, it is better to use 4 T as the lower field in the calculation of the conductivity differences.

However, even at 4 T, the lowest temperature at which we can determine σ is limited to about 0.7 K by SC, while at 8 T, we have performed measurements of σ down to approximately 0.3 K. As the overall lowest temperature achieved during our experiments is 80 mK, for $\kappa_{B=8T}$, we extrapolate the electrical data down to 80 mK using a linear fit, in the same way as in Fig. 6.15. This extrapolation is justified, because σ does indeed follow a clear linear behavior, while $\Delta\sigma$ is nearly constant. The result of the comparison between $\Delta\kappa$ and $\Delta\sigma$ therefore does not strongly depend on this extrapolation. Finally, for $\kappa_{B=4T}$, the range of our measurements extends down to 100 mK, which we also extrapolate down to 80 mK.

Having done these extrapolations, we apply Eq. 6.4 and estimate L as a function of temperature. We show the result in Fig. 6.16(b), relative to the theoretical Lorenz constant, L_0. As can be seen, the WF law is violated over the whole range of our measurements. The violation is extremely large at higher temperatures, up to four orders of magnitude, but it plummets as the temperature decreases. Around 80 mK, the violation has dropped to $L/L_0 = 20 \pm 10$. This value appears small compared to the maximal values we observe, but it still represents a significant violation of the WF law. In this temperature range, any violation is rare and, when it does occur, typically has $L < L_0$. A 20 times violation of the WF-law at 80 mK is therefore a remarkable finding.

However, for a true test of the WF law, we have to explore the 0 K limit. Considering the observed rate of change of L, 80 mK is not a low enough temperature. For this reason, we need to find a suitable method of extrapolating the data of Fig. 6.16(b) to $T = 0$ K, which we may do by considering the temperature dependence of $\Delta\sigma$ and $\Delta\kappa$ separately. As seen in Fig. 6.16(a), the former varies little with temperature and can be taken as a constant. We then only need the form of the temperature dependence of $\Delta\kappa$. As explained in Sec. 6.3, the

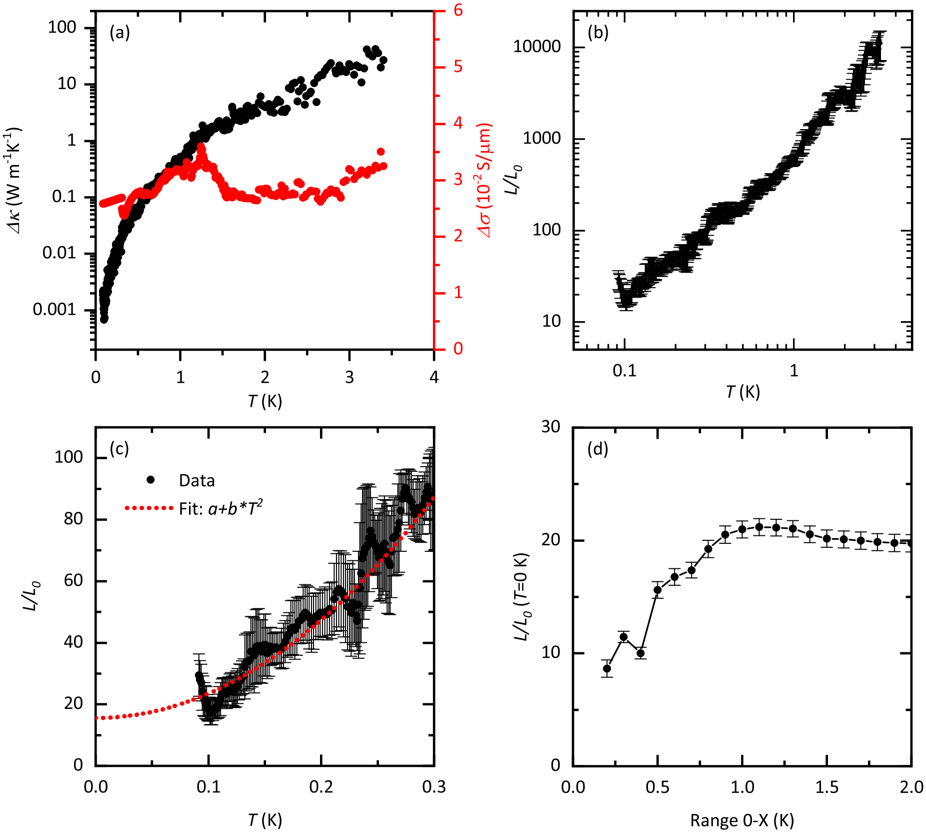

Figure 6.16: *(a) Differential values of the thermal and electrical conductivities, taken as the difference between data at 4 and 8 T. Data points below 0.3 K for* $\Delta\sigma$ *are based only on extrapolation. (b) The ratio of the experimentally observed L of sample 2, with the theoretical Lorenz constant,* L_0*, extracted from the comparison of* $\Delta\kappa$ *and* $\Delta\sigma$*, plotted over the whole temperature range. (c) Same data as (b), but shown only at low temperatures. A fit is made in order to estimate the* L/L_0 *ratio in the 0 K limit. (d) Extrapolated zero temperature values of* L/L_0 *for different fitting ranges (from* $T = 0$ *K to* $T = X$ *K) of* $a + b * T^2$*.*

temperature dependence of κ_e (and thus $\Delta\kappa$) is expected to be linear at the lowest temperatures. This, however, does not describe our data. Instead, $\Delta\kappa$ exhibits a somewhat surprising T^3-dependence. A T^3-dependence of the thermal conductivity is normally associated with phonons, but in this case there is an electronic component that has this same dependency, as also discussed in Sec. 6.7.

As per Eq. 6.4, the resulting L/L_0 then should be proportional to T^2. In Fig. 6.16(c), we show the same data as in (b), but only below $T = 0.3$ K, with a fit of the form $a + b * T^2$. We apply this fit procedure to the data over different ranges, in order to test its validity. The results of those tests are shown in Fig. 6.16(d). For ranges with upper limits above 1 K, we then consistently find $L/L_0|_{T=0K} = 20\pm1$, with the fit giving a reasonable description of the data. For lower range maxima, the extrapolated value of L/L_0 is reduced, but not lower than approximately 10. This means that even for the lowest accessible temperature ranges, we find an order of magnitude violation of the WF law.

The outcome of this procedure can be compared with the values listed in Table 6.2. Those results are determined at specific magnetic field strengths, while in the present discussion we compare two different strengths. L/L_0 does appear to depend on the magnetic field, mainly due to the contribution from σ, so the appropriate method of comparison between the two methods of determining L is to compare the extrapolated L/L_0 from the differential WF law to the average of the values determined at 4 T and 8 T by fitting κ/T versus T^2. Doing so, we find an excellent agreement between the two methods, when considering a small fit range of L/L_0. Even when looking at a larger fit range, the two methods still agree on the order of magnitude of WF violation.

However, if we correct for the anomalously large thermal conductivity of sample 2, the WF law is apparently obeyed in $Li_{0.9}Mo_6O_{17}$ for $T \rightarrow 0$ K. For this reason, it is important to verify through measurements of additional samples whether the obtained values of κ are accurate. The very strong temperature dependence, on the other hand, does remain even after such a correction. This is in agreement with the previous report of a large WF violation down to T=25 K [28].

So far, all discussion of the differential WF law has been related to sample 2. Naturally, we have performed the same study for sample 1. This study, however, is plagued by a number of issues. Firstly, the higher T_c of sample 1 means that analysis below $T = 2$ K is not possible, as SC cannot be fully suppressed. Secondly, κ in sample 1 exhibits considerably less field dependence than in sample 2, resulting in a small and strongly fluctuating $\Delta\kappa$. For these reasons, the calculation of L/L_0 from the differential WF law, does not give usable results for sample 1.

6.7 Analysis of the T^3-contribution to κ

The values of κ_2/T^3 that we extract from our fitting (see Tables 6.1 and 6.2) can be compared to theoretical estimates of the phonon contribution to the thermal conductivity, κ_{ph}/T^3. These estimates are made using Eq. 6.3 and experimentally determined parameters. We may use: $C_v = \beta T^3$, with $\beta = 0.9$ mJ/mol·K^4 (or 4.5 J/m^3·K^4) according to Ref. [76] and:

$$v_{ph} = \frac{k_B \theta_D}{\hbar} \left(\frac{V}{6\pi N} \right)^{1/3}, \tag{6.5}$$

with $\hbar$ and k_B the Planck and Boltzmann constants respectively, θ_D the Debye temperature, V the volume of the sample and N the total number of atoms (which can be calculated from the number of atoms in the unit cell and the number of unit cells in the crystal). Furthermore, previous studies have obtained values of approximately 365 K [77, 78] or 410 K [41] for the Debye temperature, which we can employ in our calculation. The resulting v_{ph} is then 2950 to 3300 m/s.

Assuming no specular reflection, we have $\lambda_{mfp} = 2\overline{w}/\sqrt{\pi}$, with $\overline{w}$ the geometric mean width of the sample (i.e. $\overline{w} = \sqrt{4hw/\pi}$, the diameter of a circle with an area equal to the rectangular cross-section). From this point on, the calculation is different for our two samples, so we will discuss them separately, beginning with sample 1, where $\overline{w} \approx 305$ μm and $\lambda_{mfp} \approx 345$ μm. Combining all numbers, we calculate $\kappa_{ph}/T^4 = 1.7 \pm 0.2$ W·m^{-1}K^{-4}, larger than the κ_2/T^4 we observed experimentally by a factor of 1.5-2.

For sample 2, we find $\kappa_{ph}/T^4 = 1.4 \pm 0.2$ W·m^{-1}K^{-4}. The outcome of the calculation is similar to that for sample 1, but approximately 4-5 times smaller than the experimental data. This comparison is often done for other materials as well, and typically the estimates agree with the experiment to within an an uncertainty band of order 50%, such as for example in the cuprate material family [53]. The large difference that we observe is therefore quite unusual.

It appears then, that we have an additional contribution to our thermal conductivity in sample 2, proportional to T^3. If this contribution arises solely due to phonons, the data has to be dominated by specular reflection. This seems unlikely, however, as it would imply a λ_{mfp} that saturates at 4-5 times the width of the sample. To our knowledge, there exists no precedent for such behavior in literature. Furthermore, our fitting results suggest that the scenario of purely diffusive scattering works well for our data. Because of this, we may conclude that the additional T^3 contribution to κ is likely electronic in nature, whose origin is also expected due to the T^2-dependence of σ.

6.8 Conclusions

In this chapter, we have analyzed the thermal and electrical conductivities of $\mathrm{Li_{0.9}Mo_6O_{17}}$ in order to study its superconducting properties and to look for a possible violation of the Wiedemann-Franz law. We studied two different samples of $\mathrm{Li_{0.9}Mo_6O_{17}}$. Sample 1 appears to be a bulk superconductor, as evidenced by the fact that its SC is not fully suppressed even in a magnetic field of 8 T and its T_c is in line with that of a sample from another study that demonstrated a clear specific heat anomaly.

We studied the residual thermal conductivity of this sample in the $T \to 0$ K limit. The thermal conductivity has contributions from both electrons and phonons, however, while it is only the former that is of interest. Separating the two components is therefore key to this study. In order to do this, we attempted two different fitting methods, both making use of the difference in temperature dependence. The first method requires plotting κ/T versus T^2 and fitting linearly; the intercept of the fit then gives us κ_e/T at $T = 0$ K. The second method is similar, but proportional to $T^{2\alpha}$.

The first method is expected to be valid in the case that specular reflection is not important, so that the phonon mean free path is limited by the sample size. This method provides a good description of our data. The second method, on the other hand, invokes specular reflection to explain a temperature dependence of the mean free path. However, this method leads to unphysical outcomes for κ_e/T at $T = 0$ K. Therefore, we extract the residual thermal conductivity, κ_0/T, only from the first method. As the values of κ_0/T are very small, we conclude that the superconducting gap of $Li_{0.9}Mo_6O_{17}$ is nodeless.

Sample 2, in which superconductivity is more easily suppressed and likely filamentary, is more suited for a study of a possible WF law violation. Such a violation was predicted for one-dimensional systems obeying Tomonaga-Luttinger liquid theory [23], of which $Li_{0.9}Mo_6O_{17}$ is an example. We looked for a violation in the $T \to 0$ K limit, by comparing the residual κ_e/T with the extrapolated $T = 0$ K value of σ. In this way, we found an L one order of magnitude larger than L_0.

We attempted to confirm this WF law violation by making use of the difference in magnetic field dependence. The assumption made here is that κ_{ph} is independent of B and can be taken out of the equation by subtracting the overall values of κ at different field strengths from each other. After doing the same for σ, we were able to determine L/L_0 from a differential version of the WF law, over the full temperature range of our measurements. For sample 2, this analysis yielded clear data showing that the WF law is violated by four orders of magnitude at temperatures of a few kelvin, but partially recovers as the temperature decreases. At the lowest experimentally accessible temperature of 80 mK, the violation is still one order of magnitude and a fit of the data suggests that this violation persists to $T = 0$ K.

The temperature dependence of L/L_0 that we find in this way is different from what was predicted based on the mechanism of spin-charge separation. We have discussed two different possible consequences of this mechanism, which suggest that L/L_0 either diverges for $T \to 0$ K or saturates around $L/L_0 \approx 1000$. Neither of these is observed; instead, there appears to be a partial recovery of the WF law at the lowest temperatures, possibly due to a dimensional crossover from a quasi-one-dimensional TLL to a three-dimensional FL.

In conclusion, we have seen signs of nodeless superconductivity in one sample of $Li_{0.9}Mo_6O_{17}$ and an order of magnitude violation of the Wiedemann-Franz law in the $T = 0$ K limit in another. However, the superconducting gap structure cannot be studied in the second sample due to the filamentary nature of its superconductivity and the WF law violation cannot be confirmed in the first because we cannot fully suppress its superconductivity. Furthermore, there are large discrepancies in the thermal conductivities of the two samples, despite the fact that we have carefully excluded systematic errors. Therefore, additional measurements are required to verify both observed phenomena and to reconcile the data from the two samples from different sources.

References

[1] J.-M. Réau, Cl. Fouassier, and P Hagenmuller. *Journal of Solid State Chemistry*, 1(3-4):326–331, 1970.

[2] C. Schlenker, H. Schwenk, C. Escribe-Filippini, and J. Marcus. *Physica B: Condensed Matter*, 135B:511–514, 1985.

[3] M. Sato, Y. Matsuda, and H. Fukuyama. *Journal of Physics C*, 20:137–142, 1987.

[4] M. Boujida, C. Escribe-filippini, J. Marcus, and C. Schlenker. *Physica C*, 153-155:465–466, 1988.

[5] M. Onoda, K. Toriumi, Y. Matsuda, and M. Sato. *Journal of Solid State Chemistry*, 66:163–170, 1987.

[6] K. Smith, K. Breuer, M. Greenblatt, and W. McCarroll. *Physical Review Letters*, 70(24):3772–3775, 1993.

[7] F. Wang, J. V. Alvarez, S. K. Mo, et al. *Physical Review Letters*, 96(196403), 2006.

[8] W. Cho, C. Platt, R. H. Mckenzie, and S. Raghu. *Physical Review B*, 92(134514), 2015.

[9] N. Lera and J. V. Alvarez. *Physical Review B*, 92(174523), 2015.

[10] A. G. Lebed and O. Sepper. *Physical Review B*, 87(100511(R)), 2013.

[11] O. Sepper and A. G. Lebed. *Physical Review B*, 88(094520), 2013.

[12] S. Bouffard, M. Ribault, R. Brusetti, D. Jerome, and K. Bechgaard. *Journal of Physics C:*, 15:2951–2964, 1982.

[13] M.-Y. Choi, P. M. Chaikin, S. Z. Huang, et al. *Physical Review B*, 25(10):6208–6217, 1982.

[14] A. G. Lebed. *Physical Review B*, 59(2):721–724, 1999.

[15] R. Franz and G. Wiedemann. *Annalen der Physik*, 165(8):497–531, 1853.

[16] V. Bayot, L. Piraux, J. P. Michenaud, and J. P. Issi. *Physical Review Letters*, 65(20):2579–2582, 1990.

[17] F. Ronning, R. W. Hill, M. Sutherland, et al. *Physical Review Letters*, 97(067005), 2006.

[18] H. R. Ott, O. Marti, and F. Hulliger. *Solid State Communications*, 49(12):1129–1131, 1984.

[19] A. F. Bangura, X. Xu, N. Wakeham, et al. *Scientific reports*, 3(3261), 2013.

[20] Y. Machida, K. Tomokuni, K. Izawa, et al. *Physical Review Letters*, 110(236402), 2013.

[21] X. Du, L. Mihaly, and P. B. Allen. *Physica B*, 194-196:1507–1508, 1994.

[22] J. Crossno, J. K. Shi, K. Wang, et al. *Science*, 0343(February):1–10, 2016.

[23] C. Kane and M. Fisher. *Physical Review Letters*, 76(17):3192–3195, 1996.

[24] A. Garg, D. Rasch, E. Shimshoni, and A. Rosch. *Physical Review Letters*, 103(096402), 2009.

[25] G. H. Gweon, J. D. Denlinger, J. W. Allen, et al. *Journal of Electron Spectroscopy and Related Phenomena*, 117-118:481–502, 2001.

[26] F. Wang, S. K. Mo, J. W. Allen, et al. *Physical Review B*, 74(113107), 2006.

[27] J. D. Denlinger, G.-H. Gweon, J. W. Allen, et al. *Physical Review Letters*, 82(12):2540–2543, 1999.

[28] N. Wakeham, A. F. Bangura, X. Xu, et al. *Nature communications*, 2(396), 2011.

[29] J. Hager, R. Matzdorf, J. He, et al. *Physical Review Letters*, 95(186402), 2005.

[30] T. Commissariat. Spinons take the heat, 2011.

[31] S. Biermann, A. Georges, A. Lichtenstein, and T. Giamarchi. *Physical Review Letters*, 87(276405), 2001.

[32] Z. S. Popović and S. Satpathy. *Physical Review B*, 74(045117), 2006.

[33] W. H. Mccarroll and M. Greenblatt. *Journal of Solid State Chemistry*, 54:282–290, 1984.

[34] J.-F. Mercure, A. F. Bangura, X. Xu, et al. *Physical Review Letters*, 108(187003), 2012.

[35] J. Dumas and C. Schlenker. *International Journal of Modern Physics B*, 7(23n24), 1993.

[36] C. Escribe-filippini, J. Beille, M. Boujida, J. Marcus, and C. Schlenker. *Physica C*, 162-164:427–428, 1989.

[37] X. Xu, A. F. Bangura, J. G. Analytis, et al. *Physical Review Letters*, 102(206602), 2009.

[38] L Degiorgi, P. Wachter, M. Greenblatt, et al. *Physical Review B*, 38(9):5821–5826, 1988.

[39] J. Merino and R. H. McKenzie. *Physical Review B*, 85(235128), 2012.

[40] M. S. Da Luz, J. J. Neumeier, C. A. M. Dos Santos, et al. *Physical Review B*, 84(014108), 2011.

[41] Y. Matsuda, M. Sato, M. Onoda, and K. Nakao. *Journal of Physics C*, 19(30):6039, 1986.

[42] J. Choi, J. Musfeldt, J. He, et al. *Physical Review B*, 69(085120), 2004.

[43] L. Dudy, J. D. Denlinger, J. W. Allen, et al. *Journal of physics. Condensed matter*, 25:014007, 2013.

[44] P. Chudziński. *European Physical Journal B*, 90(148), 2017.

[45] J. Lu, X. Xu, M. Greenblatt, et al. *submitted*, 2018.

[46] J. L. Cohn, B. D. White, C. A. M. Dos Santos, and J. J. Neumeier. *Physical Review Letters*, 108(February):1–5, 2012.

[47] J. F. Mercure, A. W. Rost, E. C. T. O'Farrell, et al. *Physical Review B*, 81:1–12, 2010.

[48] X. F. Sun, S. Ono, Y. Abe, et al. *Physical Review Letters*, 96(017008), 2006.

[49] S. Li, J.-B. Bonnemaison, A. Payeur, et al. *Physical Review B*, 77(134501), 2008.

[50] X. F. Sun and Y. Ando. *Physical Review B*, 79(176501), 2009.

[51] S. Li, J.-B. Bonnemaison, A. Payeur, et al. *Physical Review B*, 79(176502), 2009.

[52] Y. Ando, X. F. Sun, and K. Segawa. *Journal of Physics: Conference Series*, 108:012001, 2008.

[53] L. Taillefer, B. Lussier, R. Gagnon, K. Behnia, and H. Aubin. *Physical Review Letters*, 79(3):483–486, 1997.

[54] M. Sutherland, J. Dunn, W. H. Toews, et al. *Physical Review B*, 85(014517), 2012.

[55] P. Bourgeois-Hope, S. Chi, D. A. Bonn, et al. *Physical Review Letters*, 117(097003), 2016.

[56] M. Sutherland, D. G. Hawthorn, R. W. Hill, et al. *Physical Review B*, 67(174520), 2003.

[57] N. Kurita, F. Ronning, C. F. Miclea, et al. *Physical Review B*, 79(214439), 2009.

[58] X. F. Sun, W. Tao, X. M. Wang, and C. Fan. *Physical Review Letters*, 102(167202), 2009.

[59] L. Chen, X. Wang, W. Ke, et al. *Physical Review B*, 84(134429), 2011.

[60] Z. Y. Zhao, B. Tong, X. Zhao, et al. *Physical Review B*, 91(134420), 2015.

[61] L. S. Sharath Chandra, M. K. Chattopadhyay, S. B. Roy, V. C. Sahni, and G. R. Myneni. *Superconductor Science and Technology*, 25(035010), 2012.

[62] N. Kurita, C. F. Miclea, C. Putzke, et al. *Journal of Physics: Conference Series*, 273(012077), 2011.

[63] S. J. Hagen, Z. Z. Wang, and N. P. Ong. *Physical Review B*, 40(13), 1989.

[64] G. Seyfarth, J. P. Brison, M.-A. Méasson, et al. *Physical Review Letters*, 97(236403), 2006.

[65] H. Shakeripour, C. Petrovic, and L. Taillefer. *New Journal of Physics*, 11(055065), 2009.

[66] M. X. Wang, Y. Xu, L. P. He, et al. *Physical Review B*, 93(020503(R)), 2016.

[67] K. Kuroki and Y. Tanaka. *Journal of the Physical Society of Japan*, 74(6):1694–1697, 2005.

[68] K. Hashimoto, M. Yamashita, S. Kasahara, et al. *Physical Review B*, 81(220501(R)), 2010.

[69] M. Suzuki, M. A. Tanatar, N. Kikugawa, et al. *Physical Review Letters*, 88(227004), 2002.

[70] Y. Fuseya and Y. Suzumura. *Journal of the Physical Society of Japan*, 74(4):1263–1269, 2005.

[71] X. F. Sun, I. Tsukada, T. Suzuki, S. Komiya, and Y. Ando. *Physical Review B*, 72(104501), 2005.

[72] X. F. Sun, A. A. Taskin, X. Zhao, A. N. Lavrov, and Y. Ando. *Physical Review B*, 77(054436), 2008.

[73] Z. Y. Zhao, X. M. Wang, B. Ni, et al. *Physical Review B*, 83(174518), 2011.

[74] Y. Tokiwa, T. Yamashita, M. Udagawa, et al. *Nature Communications*, 7(10807), 2016.

[75] S. Scharffe, G. Kolland, M. Valldor, et al. *Journal of Magnetism and Magnetic Materials*, 383:83–87, 2014.

[76] C. Schlenker, J. Dumas, C. Escribe-filippini, et al. *Philosophical Magazine B*, 52(3):643–667, 1985.

[77] M. Greenblatt. *Chemical Reviews*, 88(1):31–53, 1988.

[78] M. Greenblatt, H. Vincent, M. Marezio, et al. *Low-dimensional electronic properties of molybdenum bronzes and oxides*, volume 11. Kluwer Academic Publishers, Dordrecht, 1989.

Summary

In this thesis, we discuss experimental work on four different materials: two nodal-line semimetals, one Weyl semimetal, and one quasi-one-dimensional (semi)metal. Each of these material systems is shown to exhibit novel, and indeed emergent, phenomena.

The first group of materials studied in this thesis is the group of nodal-line semimetals, represented by HfSiS in Chapter 3 and ZrSiS in Chapter 4. These materials are of interest due to their particular topology, with linearly dispersing bands touching along an extended line in the Brillouin zone. Additionally, it has been predicted that nodal line semimetals may be predisposed towards various types of order due to a vanishing density of states near their Fermi level

For HfSiS, we report the first experimental observation of Klein tunneling in momentum space. This effect was predicted for type-II Weyl semimetals, but can in fact occur in any material that has electron and hole pockets in close proximity. We detect it through measurements of the Shubnikov-de Haas effect, performed at different temperatures and under different angles.

In the low frequency regime of our measurements, we primarily detect two fundamental frequencies, F_α and F_β, which we can associate with orbits around the individual hole and electron pockets, respectively. By following these frequencies as they change with the angle of the magnetic field and comparing them with theoretical predictions, we are able to confirm this assignment. From the temperature dependence of the oscillation amplitudes, we then determine the effective masses of these two orbits, which are in good agreement with our calculations.

Aside from the fundamentals and harmonics, we detect several other frequencies, including a frequency $F_\beta - F_\alpha$. This frequency arises due to magnetic breakdown between the electron and hole pockets, and thus can be called momentum space Klein tunneling, in an orbit that we refer to as the 'figure of eight'. As predicted, the effective mass associated with this orbit is the sum of the masses of β and α. Furthermore, the orbit is found to be rapidly suppressed as the angle between the field and the sample c-axis is increased slightly away from 0°. These facts support the interpretation of $\beta - \alpha$ as a magnetic breakdown orbit.

We also observe a number of high frequency oscillations. These frequencies appear due to magnetic breakdown enabling an orbit around the whole Brillouin zone. Because the central

area between the pockets is included, the orbit becomes very large. At the same time, because a number of α and β pockets may or may not be added to the orbit, many different frequencies are possible. In HfSiS, these frequencies are difficult to study independently as we do not have sufficient resolution to resolve their small spacing. This effect is therefore easier to study in ZrSiS, in which the resolution is higher.

The data on ZrSiS resemble those on HfSiS in many ways, with a similar behavior of the fundamental frequencies F_α and F_β, but they have a higher degree of complexity. This is a consequence of the fact that the Fermi surface has essentially the same shape, but with a smaller gap between the pockets. As the probability of magnetic breakdown depends crucially on the size of this gap, it occurs more frequently in ZrSiS and we can see many more frequencies, both low and high.

Another interesting phenomenon was previously reported for ZrSiS, namely an enhancement of the effective mass associated with a particular orbit in a magnetic field. Such an enhancement may be indicative of correlation effects leading up to a quantum critical point. For this reason, we study this effect in several samples. The resulting data have a large spread, and unfortunately cannot confirm the observation of a mass enhancement.

The high frequency oscillation spectrum of ZrSiS exhibits a plethora of emergent phenomena. The frequencies come in two separate groups originating from different planes, with distinct behavior. The lower frequency group arises due to magnetic breakdown in Z-R-A plane, including the α and β pockets, and the higher frequency group likely comes from the Γ-M-X plane.

A particularly unusual effect within the high frequency oscillations of ZrSiS, is the temperature dependence of the Shubnikov-de Haas spectrum. Whereas most frequencies are suppressed with little more than 4 K, certain specific ones remain observable even at T=90 K. Furthermore, the nature of the oscillations appears to change in temperature, as evidenced by changes in the shape and amplitude. Finally, these high-temperature oscillation only appear in electrical transport measurements, not in magnetic torque measurements. A possible explanation could be the development of a so-called Stark interferometer effect on the Fermi surface.

What is exceptional about ZrSiS and HfSiS, is the fact that their whole set of observed oscillatory phenomena can be described in terms of a simple Fermi surface ‘cage’ that follows the contours of the nodal-line. Despite this, however, we have only seen indirect indications of electron correlation, suggesting that it may be necessary to get even closer to the nodal line to enhance the correlation effects. For this reason, future studies of the ZrSiS-family under high pressure or of gated thin layers are of interest. Such studies may help to induce stronger correlation effects as the Fermi level is tuned towards to the nodal line.

The next phenomenon, discussed in Chapter 5, is the occurrence of superconductivity in the Weyl semimetal Tantalum Phosphide (TaP), which appears to be filamentary, but bulk. This is an important observation, as the combination of Weyl physics and superconductivity may lead to exotic surface states, such as Majorana fermions. We investigate this effect through magnetotransport measurements on four different microsamples prepared with a Focused Ion

Beam (FIB), cut from a single crystal. FIB is a powerful technique (described in detail in Appendix A) for the shaping and contacting of microscopic crystals, but carries with it the risk of damaging the surfaces of the crystals.

Considering the superconducting behavior of the samples, there is indeed reason to believe the surface has been modified: in the microsamples, two (partial) resistive transitions can be seen, whereas in the parent crystal, only one appears. We investigate the origin of these two transitions by determining their characteristic magnetic fields as a function of angle and temperature and describing them with two- or three-dimensional models. For the transition with the lowest characteristic field, we find that a 2D model gives an excellent description, while the angle dependence of the higher characteristic field is best fitted with a 3D model.

The fitting strongly suggests that one of the transitions arises from the (3D) bulk of the sample and the other from the (2D) surface. From this we conclude that the surface state is introduced by the FIB processing, as supported by simulations, and the bulk state is an intrinsic property of our TaP crystal. Additionally, we can state that the bulk superconductivity must be very inhomogeneous, because we see several different critical currents that can be associated with the bulk, as well as an upturn of the resistance in magnetic field as superconductivity is suppressed.

The origin of the superconductivity remains uncertain, however. We compare the composition of our crystal with that of a non-superconducting crystal, and find no measurable difference. Similarly, we have determined the crystal structure and found it be the same as previously reported. The most likely explanation, therefore, appears to be that our crystal has a large number of defects (which is known to be common in this type of material). Structures of defects within the crystal could induce a very inhomogeneous superconductivity.

Future studies should aim to determine under what conditions superconductivity of TaP is optimized, as well as to ascertain whether superconducting TaP retains the characteristics of a Weyl semimetal. If these questions are answered, TaP may become an ideal platform for the study of Weyl superconductivity.

The final material being studied in this thesis, in Chapter 6, is the quasi-one-dimensional (semi)metal $\mathrm{Li_{0.9}Mo_6O_{17}}$. We study two aspects of this material using two different samples, namely the superconductivity and the one-dimensionality. In order to draw conclusions on either aspect, the first requirement is to obtain a good estimate of the electronic contribution to the thermal conductivity (κ_e) in the limit $T \to 0$ K. To do this, κ_e needs to be separated from the phonon contribution through the linear fitting of a plot of κ/T versus T^2. The intercept then gives κ_e/T for $T \to 0$ K (i.e. κ_0/T).

Using the thus extracted negligible values of κ_0/T for one of our samples, we can conclude that the superconducting gap is nodeless. The same values, but for the other sample, can be used to assess the validity of the Wiedemann-Franz (WF) law. This law relates the electrical and thermal conductivities to the Lorenz constant L and the temperature and is generally valid for $T \to 0$ K. However, in a one-dimensional material such as $\mathrm{Li_{0.9}Mo_6O_{17}}$, this law is expected to be violated. We therefore combine our κ_0/T with extrapolated values of the electrical conductivity in order to test the WF law.

Doing so, we calculate an L that is one order of magnitude larger than the theoretical value. We confirm this remarkable violation of the WF law by making use of the magnetic field dependence of the data to estimate L over the whole temperature range of our experiments. We then find a WF-violation of four orders of magnitude at temperatures of a few kelvin, dropping to one order at the lowest accessible temperature of approximately 80 mK. This suggests a (partial) recovery of the WF law, suggestive of a crossover from a one-dimensional to a three-dimensional (semi)metal.

However, due to the large discrepancies in the thermal conductivities of the two samples, additional measurements are required to verify both observed phenomena and to reconcile the data from the two samples from different sources.

In general, the work presented in this thesis may lead to further investigations of the combination of topology and electron correlations. In the cases of the topological nodal line semimetals HfSiS and ZrSiS, the observed indications of correlation effects warrant further research. Some steps that could be taken to bring these effects to the fore, include measurements under pressure or of gated thin layers. For the case of TaP, it is important to determine how the superconductivity arises, and how it can be controlled. If superconducting TaP can be shown to preserve the topological properties of regular TaP, it will be an excellent material for the study of topological superconductivity.

Samenvatting

In dit proefschrift bespreken we experimenteel werk met betrekking tot vier verschillende materialen: twee nodal-line ("knooppunten-lijn") halfmetalen, één Weyl halfmetaal en één quasi-ééndimensionaal (half)metaal. Van elk van deze drie materiaalsystemen tonen wij aan dat zij nieuwe, en inderdaad emergente, fenomenen vertonen. Dat wil zeggen, nieuwe fenomenen die niet beschreven kunnen worden als een som van alle ingrediënten, maar die ontstaan als gevolg van de complexe interactie tussen microscopische bestanddelen.

De eerste groep materialen die we bestuderen binnen dit proefschrift zijn de nodal-line halfmetalen, vertegenwoordigd door HfSiS in Hoofdstuk 3 en door ZrSiS in Hoofdstuk 4. Deze materialen zijn interessant vanwege hun topologie, met banden met lineaire dispersie die elkaar raken langs een lijn binnen de Brillouin zone. Bovendien is het voorspeld dat nodal-line halfmetalen een neiging kunnen hebben tot verschillende types van orde door een verwaarloosbare toestandsdichtheid nabij het Fermi niveau.

Voor HfSiS rapporteren we de eerste experimentele observatie van Klein tunnelen in de impulsruimte. Dit effect was voorspeld voor type-II Weyl halfmetalen, maar kan in principe in elk materiaal voorkomen dat nabijgelegen elektron- en gat-zones heeft. We hebben dit ontdekt door middel van metingen van het Shubnikov-de Haas effect, uitgevoerd bij verschillende temperaturen en onder verschillende hoeken.

In het laagfrequente regime van onze metingen, detecteren we voornamelijk twee fundamentele frequenties, F_α en F_β, die we kunnen toewijzen aan respectievelijk de individuele gat- en elektron-zones. Door deze frequenties te volgen wanneer zij veranderen met de hoek tussen het magneetveld en het sample, bevestigen we deze toewijzing. Via de temperatuursafhankelijkheid van de oscillatie-amplitude bepalen wij vervolgens de effectieve massa's van beide orbitalen, die in goede overeenkomst blijken met onze berekeningen.

Naast de fundamentele frequenties, meten wij nog verscheidene andere, waaronder een frequentie $F_\beta - F_\alpha$. Dit is mogelijk door magnetische doorbraak tussen elektron- en gat-zones en kan ook Klein tunnelen in impulsruimte genoemd worden, in de zogenaamde figuur-acht orbitaal. Zoals voorspeld, is de effectieve massa van deze orbitaal gelijk aan de som van de massa's van β en α. Bovendien blijkt dat deze orbitaal zeer snel onderdrukt wordt zodra de hoek tussen het magneetveld en de c-as van het sample afwijkt van $0°$. Deze feiten ondersteunen de interpretatie van $\beta - \alpha$ als een magnetische doorbraak orbitaal.

Wij hebben ook een aantal oscillaties met zeer hoge frequenties ontdekt. Deze frequenties verschijnen doordat magnetische doorbraak een orbitaal mogelijk maakt rond de gehele Brillouin zone. Omdat de centrale zone tussen de elektron- en gat-zones inbegrepen is bij de totale orbitaal, wordt deze zeer groot. Tegelijkertijd zijn er veel verschillende grote frequenties mogelijk, omdat een aantal keren α of β wel of niet aan de orbitaal kan worden toegevoegd. In HfSiS is het moeilijk om deze frequenties onafhankelijk van elkaar te bestuderen omdat de resolutie van onze metingen onvoldoende is om de pieken met hun kleine tussenruimte van elkaar te onderscheiden. Dit effect is daarom gemakkelijker te bestuderen in ZrSiS, waar de resolutie hoger is.

De data over ZrSiS lijken op veel manieren op die over HfSiS, met een vergelijkbaar gedrag van de fundamentele frequenties F_α en F_β, maar met een grotere mate van complexiteit. Dit is een consequentie van het feit dat het Fermi oppervlak grotendeels dezelfde vorm heeft, maar met een kleinere ruimte tussen de zones. Aangezien de kans op magnetische doorbraak sterk afhangt van de grootte van deze tussenruimte, komt dit dus veel vaker voor in ZrSiS en kunnen we meer frequenties meten.

Een ander interessant fenomeen werd eerder al gerapporteerd voor ZrSiS, namelijk een toename van de effectieve massa voor een specifieke orbitaal in een magneetveld. Een dergelijke toename is een mogelijke indicatie van correlatie effecten die leiden tot een kwantum kritisch punt. Om deze reden bestuderen we dit effect in meerdere samples. De data die hieruit resulteert, heeft echter een grote spreiding en kan helaas de observatie van een massa toename niet bevestigen.

Het hoogfrequente deel van het oscillatie spectrum van ZrSiS vertoont een overvloed aan emergente fenomenen. De frequenties kunnen worden opgedeeld in twee verschillende groepen, met elk een ander gedrag. De groep met lagere frequentie ontstaat door magnetische doorbraak in het Z-R-A vlak, met daarin de α en β zones, en de groep met hogere frequentie is waarschijnlijk afkomstig uit het Γ-M-X vlak.

Een bijzonder effect binnen de hoogfrequente oscillaties van ZrSiS, is de temperatuursafhankelijkheid van het Shubnikov-de Haas spectrum. Terwijl de meeste frequenties onderdrukt kunnen worden met niet veel meer dan 4 K, blijven een aantal zichtbaar tot zelfs bij T=90 K. Bovendien blijkt dat de aard van oscillaties verandert met de temperatuur, zoals aangetoond met een verandering van de vorm en een amplitude die eerst afneemt met de temperatuur en vervolgens weer toeneemt. Tot slot zijn deze hoge-temperatuur oscillaties alleen zichtbaar in elektrische transportmetingen, niet in magnetische moment metingen. Een mogelijke verklaring zou een zogenaamd Stark interferometer effect in het Fermi oppervlak kunnen zijn.

Het bijzondere aan ZrSiS en HfSiS, is het feit dat hun gehele verzameling geobserveerde oscillerende fenomenen beschreven kan worden in termen van een simpele Fermi-oppervlak 'kooi' die de contouren van de nodal-line volgt. Desondanks hebben we alleen indirect indicaties van correlatie effecten waargenomen, wat suggereert dat het noodzakelijk is om de nodal-line nog dichter te benaderen om correlatie effecten te versterken. Om deze reden zijn toekomstige onderzoeken naar de ZrSiS-familie onder hoge druk of met gating interessant. Zulke experimenten kunnen helpen om sterkere correlatie effecten te induceren als het Fermi niveau dichter tot de nodal-line komt.

Het volgende fenomeen, besproken in Hoofdstuk 5, is de verschijning van supergeleiding in het Weyl halfmetaal tantaal fosfide (TaP). Deze blijkt niet volledig te zijn, maar bevindt zich wel in de bulk van het kristal. Dit is een belangrijke ontdekking, omdat de combinatie van Weyl fysica en supergeleiding exotische oppervlaktetoestanden tot gevolg kan hebben, zoals Majorana fermionen. Wij onderzoeken dit effect met behulp van magnetotransport metingen aan vier verschillende microscopische samples, gesneden uit één kristal met behulp van een gefocusseerde ionen-straal. De gefocusseerde ionen-straal is een krachtige techniek (beschreven in detail in Appendix A) voor het bewerken en contacteren van microscopische kristallen, maar brengt het risico met zich mee om het oppervlak van de kristallen te beschadigen.

Gezien het supergeleidende gedrag van de samples, is er inderdaad reden om te geloven dat het oppervlak is gemodificeerd: in de micro-samples zijn namelijk twee (gedeeltelijke) weerstands-overgangen zichtbaar, terwijl in er in het moederkristal slechts één verschijnt. We onderzoeken de oorsprong van deze overgangen door hun karakteristieke magneetvelden te bepalen bij verschillende temperaturen en onder verschillende hoeken. Vervolgens beschrijven we deze hoekafhankelijke data met verschillende modellen. Voor de overgang met het laagste karakteristieke veld, blijkt dan dat een tweedimensionaal model een uitstekende beschrijving geeft, terwijl de hoekafhankelijkheid van het hogere karakteristieke veld het beste past binnen een driedimensionaal model.

De modellering suggereert sterk dat één van de overgangen ontstaat vanuit de (3D) bulk van het sample, en de andere vanuit het (2D) oppervlak. Hiermee kunnen we concluderen dat de supergeleidende oppervlaktetoestand wordt geïnduceerd door de gefocusseerde ionen-straal, in overeenstemming met simulaties, en dat de bulk toestand een intrinsieke eigenschap vertegenwoordigt van ons TaP kristal. Bovendien kunnen we stellen dat de bulk supergeleiding zeer inhomogeen moet zijn, omdat we meerdere verschillende kritieke stromen zien die geassocieerd kunnen worden met de bulk van het sample, evenals een toename van de weerstand in een magneetveld wanneer de supergeleiding wordt onderdrukt.

De oorsprong van de supergeleiding blijft echter onzeker. We vergelijken de samenstelling van ons kristal met een niet supergeleidend kristal en vinden geen meetbaar verschil. Verder bepalen we de kristalstructuur; deze is hetzelfde als eerder gepubliceerd. De meest waarschijnlijke verklaring lijkt daarom te zijn dat ons kristal een groot aantal defecten heeft (het is bekend dat dit gebruikelijk is in dit soort materiaal). Structuren van defecten binnen het kristal zouden een zeer inhomogene supergeleiding kunnen veroorzaken.

Toekomstige studies zouden erop gericht moeten zijn om te bepalen onder welke omstandigheden de supergeleiding van TaP wordt geoptimaliseerd, en om vast te stellen of supergeleidend TaP nog steeds de eigenschappen van een Weyl halfmetaal behoudt. Als deze vragen zijn beantwoordt, dan kan TaP een ideaal platform worden voor de studie van Weyl supergeleiding.

Het laatste materiaal wat wordt bestudeerd in dit proefschrift, in hoofdstuk 6, is het quasi-eendimensionale (half)metaal $\mathrm{Li}_{0.9}\mathrm{Mo}_6\mathrm{O}_{17}$. We onderzoeken twee aspecten van dit materiaal, namelijk de supergeleiding en de eendimensionaliteit. Om conclusies te kunnen trekken over elk van beide aspecten, is de eerste vereiste om een goede schatting te maken van de elektronische bijdrage aan de thermische geleiding (κ_e) in de limiet $T \to 0$ K. Hiervoor moet κ_e gescheiden worden van de bijdrage door fononen met behulp van een lineaire fit van κ/T als functie van T^2. Het snijpunt met de y-as geeft dan de waarde κ_e/T voor $T \rightarrow 0$ K (oftewel κ_0/T).

Met de zo bepaalde verwaarloosbare waardes voor κ_0/T van één van onze samples, kunnen we concluderen dat er geen knooppunten aanwezig zijn binnen de supergeleidende kloof. Dezelfde waardes voor het andere sample kunnen gebruikt worden om de geldigheid van de Wiedemann-Franz (WF) wet te beoordelen. Deze wet relateert de elektrische en thermische geleidbaarheid aan de Lorenz constante, L, en aan de temperatuur en is in het algemeen geldig voor $T \rightarrow 0$ K. Echter, voor een eendimensionaal materiaal zoals $\mathrm{Li_{0.9}Mo_6O_{17}}$, bestaat de verwachting dat deze wet geschonden wordt. Om deze wet te testen combineren wij daarom onze κ_0/T met geëxtrapoleerde waardes voor de elektrische geleidbaarheid.

Op deze manier berekenen we een L die één orde van grootte groter is dan de theoretisch voorspelde waarde. Dit is een opvallende schending van de WF wet, die wij verder bevestigen voor dit sample door L in te schatten over het gehele temperatuurbereik van de meting, met behulp van de magnetische veldafhankelijkheid van de data. Wij vinden zo een L die vier ordes van grootte groter is dan de theoretische voorspelling, bij temperaturen van enkele kelvin. Echter, bij afnemende temperatuur zien we ook een sterke afname van L, wat wijst op een (gedeeltelijk) herstel van de WF wet. Een dergelijk herstel suggereert een overgang van een eendimensionaal naar een driedimensionaal (half)metal.

Echter, door de grote verschillen tussen de thermische geleiding van de twee samples zijn er verdere metingen nodig om beide geobserveerde fenomenen te verifiëren en de data van de beide samples met elkaar in overeenstemming te brengen.

In het algemeen kan het werk uit dit proefschrift leiden tot verder onderzoek naar de combinatie van topologie en correlatie effecten. In het geval van de topologische halfmetalen, ZrSiS en HfSiS, verdienen de geobserveerde indicaties van correlatie effecten een diepere studie. Enkele stappen die genomen kunnen worden om deze effecten naar voren te brengen, zijn metingen onder hoge druk of van dunne lagen voorzien van een gate elektrode. In het geval van TaP is het belangrijk om te bepalen hoe de supergeleiding ontstaat en hoe deze kan worden gecontroleerd. Als supergeleidend TaP nog steeds de topologische eigenschappen heeft van normaal TaP, dan is het een uitstekend materiaal voor de studie van topologische supergeleiding.

APPENDIX A

Focused Ion Beam (FIB)

A Focused Ion Beam (FIB) is a tool that enables the structuring of microscopic samples. It is able to do this by focusing a beam of ions onto a small spot on a sample, thereby locally sputtering the material. By scanning this spot over the sample, the FIB is able to sputter the materials in a programmed pattern and thus produce the desired structure. Additionally, the ions that impact the surface will excite secondary electrons that can be detected in order to generate an image similar to that generated by a scanning electron microscope (SEM).

If it is used together with a precursor material, the ion beam can also be used to deposit various materials, such as platinum (Pt). This can be used for example to make electrical contacts to a sample, to protect it against sputtering damage or to attach it mechanically to a substrate or probe. The sputtering and deposition capabilities of the FIB give it a wide range of applicability, which is further increased by the addition of an SEM column to the FIB system. Combining SEM and FIB in one system makes it possible to observe the system in a nondestructive manner and to view it from multiple angles simultaneously, while retaining the full capabilities of the standalone FIB.

FIB has found applications in many different areas. The most common application is in the semiconductor industry, where FIB is used to repair or modify photolithography masks [1], or to analyze and repair faults in devices. In materials science, it is frequently used to prepare transmission electron microscope (TEM) samples [2]. In that process, a thin plate of material is cut from a larger sample and extracted from it. This thin plate can then be transferred to the TEM (which requires very thin samples) to allow the structure of the material to be studied.

Outside of industry or materials science, application of the FIB is less common, but still many different uses have been demonstrated, such as three-dimensional destructive imaging of layered structures [3], implanting ions as a way to dope semiconductors [4] or even analyzing banana peel [5]. FIB is also used in the field of biology, for example to observe the interfaces between cells and evaluate the processes that take place there [6] or to cut into human brains [7].

The particular application of this work, microstructuring and contacting of mesoscopic crystals for transport measurements, has been demonstrated before. The first demonstrations were by Cheng [8] and Jaroszynski [9] in 2008. Since 2010, Moll has improved on the basic work of Cheng and Jaroszynski and started patterning crystals in ways that allow measurements that would otherwise have bene impossible [10], for example by cutting a long and thin channel into $PdCoO_2$ to study electron hydrodynamics [11].

A.1 Advantages of FIB

The main competitor of FIB in the field of microstructuring and contacting is E-Beam Lithography (EBL). For EBL, the sample is covered in a thin, uniform layer of a polymeric resist material that the electron beam is scanned over in order to create the desired pattern. EBL has the highest resolution and it is cleaner than FIB, as it can not pollute unirradiated parts of the sample. Using EBL, the evaporation of metals (or other films) onto the sample is done in a dedicated external system, allowing for a much wider range of materials that can be used as well as a higher purity. However, FIB has a number of advantages over EBL, that make it a better option for the project of this thesis.

First of all, while FIB can handle samples of any shape, EBL requires a smooth surface in order to spin the layer of resist, typically with a thickness of the order of 100 nm. With the micron-sized samples we use, a uniform resist layer covering sample and substrate is out of the question. Furthermore, the resist needs to be processed chemically, which may be harmful to the sample or the glue that holds it in place.

While with EBL it takes several processing steps before the result can be evaluated, FIB allows for in-situ observation of the sample during the exposure. This means the result of any action with the ion beam is immediately visible, and the beam settings can be directly adjusted to be appropriate for the treatment of the sample. Using EBL on the other hand, it can take many iterations to find the right settings for a particular application. Every time a new material is used, a whole new optimization process is necessary.

Although EBL is more commonly used for micro- and nanostructuring, FIB offers additional possibilities to work on all sorts of materials in any shape desired. When weighing up the advantages and disadvantages, it is clear FIB is the technique of choice for this project.

A.2 The dual-beam FIB-SEM machine

The FIB machine used for this work is a FEI Nova-600 Nanolab dual beam FIB and SEM instrument, located at the MESA+ institute for nanotechnology in Enschede, the Netherlands.

The main components of this machine are the ion and electron columns as well as the vacuum chamber with the sample stage and additional equipment such as detectors or gas injectors. The electron column is placed in the vertical position, while the ion column has an angle of 52° with respect to it.

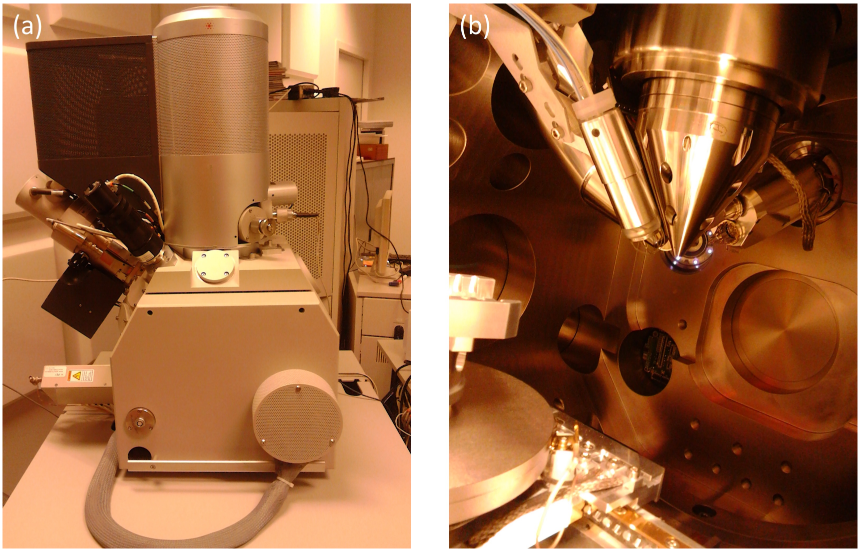

Figure A.1: *Picture of the FEI Nova-600 Nanolab dualbeam FIB/SEM used for this work, at the MESA+ institute for nanotechnology in Enschede, the Netherlands. Seen from (a) outside and (b) inside.*

The most important component of the ion column is the ion source. The type of ions that is used in most FIB machines, including the one that is used for this project, is Ga^+ from a Liquid Metal Ion Source (LMIS). The LMIS consists of a tungsten needle attached to a reservoir of gallium, which can be heated to liquidity. The liquid gallium then flows along the tungsten needle, which has a tip radius of a few μm. An electric field is then applied, causing the Ga to form a cone due to the balance between the electrostatic force and the surface tension. The apex of this cone typically has a diameter of only 2-5 nm, small enough that an extraction voltage can pull Ga^+-ions out of the tip through field evaporation, a process where atoms are ionized in high electric fields and ejected. For this process to work, the tip needs to be sufficiently sharp. This is ensured by the liquidity of the Ga, causing a continuous flow of Ga that replaces the ejected ions.

The reasons gallium is used are many [12]. It has a melting point only slightly above room temperature (29.8 °C), meaning it requires very little heating to become liquid and can easily stay liquid for extended times without further heating. Since the melting point of the needle material (tungsten) is extremely high, there is little or no reaction or diffusion between the tungsten needle and the liquid gallium. Additionally, the low volatility at the melting point, the low surface free energy and the low vapor pressure of gallium are also favorable for use in FIB. Finally, the emission characteristics of gallium are such that the ions can be focused to a fine spot size with a current density that can be well controlled [13]. The only downside to the use of gallium arises when milling a compound that itself contains gallium.

After the ions are emitted from the source, they are accelerated down through the ion column with an acceleration voltage of typically 30 kV. The column has two magnetic lenses, one to form the ions into a probe and the other to focus the beam of ions onto the sample. Different apertures can be used to attain different beam currents between 1.5 pA and 20 nA. The column also contains two octopoles that can align the beam, scan it over the sample and correct for stigmation effects. Finally, it has a beam blanker that can deflect the ion beam away from the axis of the column in order to protect the sample when needed.

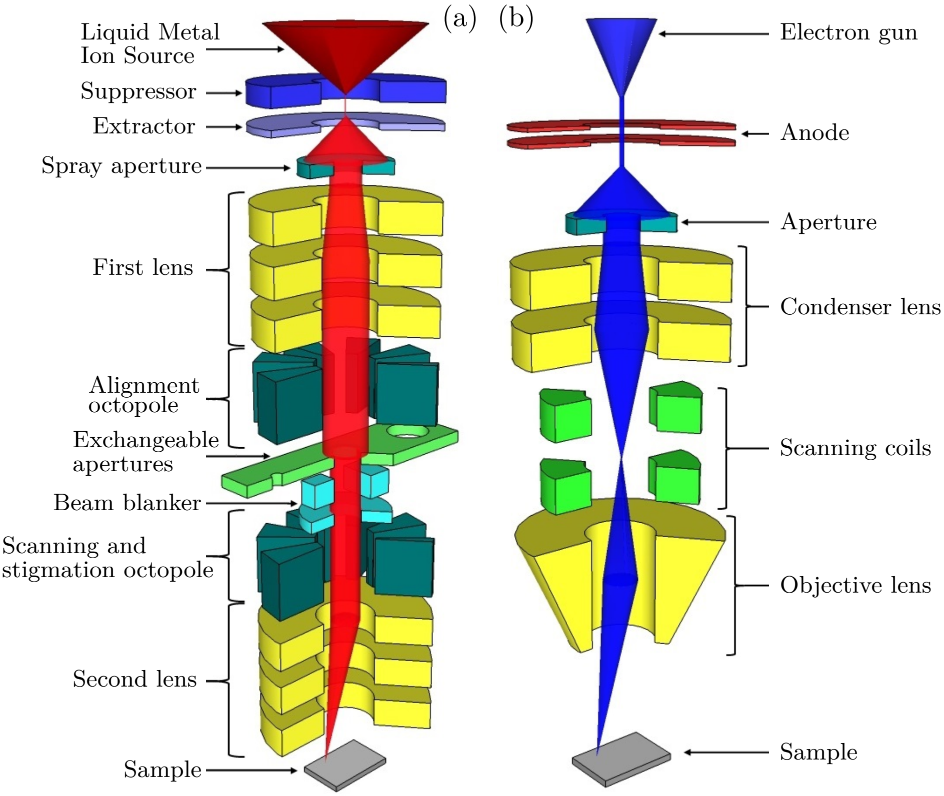

Figure A.2: *Schematic of (a), the FIB column, and (b), the SEM column.*

The SEM column of the dual-beam FIB-SEM uses the same mechanisms as a conventional SEM. The electrons are emitted from a field emission electron gun with a tungsten cathode and then focused onto the sample. This happens in a similar way to the ion beam, using two lenses. The beam can be scanned over the sample by a set of electromagnetic coils.

The detectors in the system can be used for imaging with both ions or electrons. The system has three independent detectors that can be used in different modes. The main modes of operation are secondary electron detection, or backscattered electron or ion detection. The former mode makes use of the fact that as an electron or ion impacts a material, it causes secondary electrons to be emitted from this material. These electrons are then picked up by the detector. The latter mode detects the electrons or ions that are reflected back from the sample that is being imaged. These two modes give different contrast and thus provide slightly different information. The detectors themselves are each located in a specific part of the system, and are more or less sensitive to particular parts of the signal. This is a result of the fact that the electrons or ions that are emitted from the sample via different mechanisms are emitted with distinctive angle dispersions.

When imaging an insulating sample with the ion beam, charge from the incoming ions will accumulate on the sample, causing a number of problems. The most obvious one is a shifting and distortion of the image that can severely hinder operation. The reason this happens is that the accumulated charge deflects the new charges coming on to the surface. Because of this, the ions do not impact where they should and the image is shifted. Additionally, the charge attracts emitted secondary electrons, that thus do not reach the detector. Another problem is the potential for damage to a sample as it gets highly charged. It has been reported in several cases, that charging can reduce the crystallinity of a sample [14] and even cause it to break apart [12]. A common way to deal with this problem is to deposit a conducting layer on top of the sample, but if this is not an option, there exists another solution in the form of a particular add-on to the FIB machine. That is the charge neutralizer (CN). The CN bombards the sample with a broad beam of low-energy electrons while it is being imaged by the FIB. In this way, the positive charge from the Ga^+ ions is compensated by the negative charge of the electrons and charging problems can be avoided. Using the CN does have consequences for the operation of the FIB though; it is not possible to use the SEM together with the CN, and the available detection modes are limited since only secondary ions can be detected.

The stage can be moved in the x, y and z directions, tilted from -10° to 52° and rotated compucentrically over 360°. When using the FIB, the stage should be about 5 mm below the electron column, at the eucentric height. Operation at this height is essential, not only because the position on the sample that is being observed remains the same under tilting of the stage at this height, but also because this is the height where the electron and ion beams cross. This means that one should image the same feature when scanning with either the electron beam or the ion beam.

Another important component of the machine is the gas injection system (GIS). This part is required to deposit materials with the FIB and contains the sources of precursor gases. In order to use these, they are heated up and a nozzle is injected into the chamber through which the gas can flow. It is important that the end of the nozzle is very close to the sample, so that the gas does not compromise the vacuum of the whole chamber, but does reach the target area. This is another reason why the FIB should be operated at the eucentric height. The machine that is used for this project has sources of platinum and tungsten available, but other options exist too.

On top of these systems, there are several other add-ons available that can be used with a FIB/SEM. These include, for example, Electron Backscatter Diffraction (EBSD), which enables the user to determine crystal orientations of a sample and Energy-Dispersive X-ray spectroscopy (EDX), which can be used to study the local composition of a sample. The only installed add-on to the Nova-600 system however is in-situ micromanipulation. This is done with a Kleindiek micromanipulator probe that can be placed inside the chamber. This probe can be moved up or down, left or right and in or out with high accuracy and can thus be used to move or probe things inside the chamber. Unfortunately, usage of this probe does restrict the range of the stage motion to lower tilt angles.

A.3 Applications of FIB

In general, there are three applications of a focused ion beam, illustrated in Fig. A.3. The simplest application is to use the FIB in the same way as an SEM, to make images. The contrast of a FIB image is different from that of an SEM image, and so FIB can provide different information about the surface of a sample.

In addition to imaging, FIB can also be used to mill material away or to deposit material. These applications are explained in detail below.

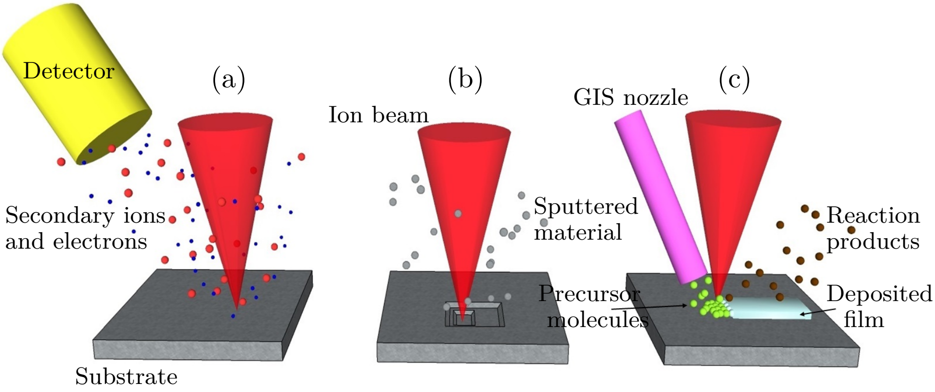

Figure A.3: *Illustration of the different FIB processes. (a) Imaging. (b) Milling. (c) Deposition.*

Milling with FIB

In principle, the milling process is very simple. The ions impact the sample and cause atoms to be ejected from it. This is a process that inevitably takes place at any acceleration voltage or current, even very low ones. Because of this, FIB is in most cases inferior to SEM for imaging as it damages the sample. However, the milling process can also be very useful as it can be used to remove material on a scale as small as the beam size, about 6 nm. In this way, microstructures can be created, faults can be removed from devices or small pieces of material can be cut from a larger sample.

There are potential problems with the milling process, however, that have to be taken into account when using it. One issue is the fact that the surface of the milled material is being damaged by and contaminated with the Ga-ions that it is bombarded with. This means that the top 5 to 40 nm of the material contains implanted Ga-ions and defects induced in the crystal structure. This can significantly affect any surface sensitive properties of the material, but considering that the samples used for this work are typically of micrometer thickness, the bulk most likely remains unaffected.

Another possible problem is caused by sputtered material that is not effectively removed. The atoms that are ejected from the material can impact on it again and form a layer of redeposited material. This can have multiple consequences. For example, the layer could be conductive and cause unintended shortcuts between different parts of a device.

The effect of redeposition is strongest if there is some structure near to the ion beam spot that the atoms can impact on. Such a structure could be, for example, the sidewalls of a milled trench. In particular, this has to be taken into account when milling quite deep trenches. As the trench gets deeper, more and more redeposition will occur on the sidewalls, causing the milling process to become less and less effective. If the ratio between the depth and width of the trench is large enough, further milling can even become impossible. Therefore, it is advisable to make a trench wide enough that the ejected material can leave the trench without having a large chance of redepositing.

Material deposition with FIB

The third application of FIB, material deposition, requires a precursor gas in addition to the ion beam. This gas consists of molecules that can be split into two components as they are impacted by ions. One component is the material that is to be deposited, while the other is a volatile reaction product that can be removed by the pump attached to the vacuum chamber. In principle, the resolution of this process is the same as that of the milling process, but it can be limited by certain unintended effects.

One effect that limits the deposition resolution is caused by collisions between ions and precursor molecules in the gas above the substrate. The probability of a collision like this is small compared to that of a collision on the substrate, but it does occur. The molecular fragments resulting from these collisions are highly reactive and can cause the formation of a halo of material deposited around the desired area. This halo is typically very thin, and the material is of poor quality. However, if a large deposition is to be made in one area, the halo around it can become problematic. Such unintended deposition is referred to as 'overspray'.

Aside from the overspray, the FIB-induced material deposition is in fact a competition between two processes. The breaking up of the precursor molecules causing material to be deposited and simultaneous milling causing the same material to be removed. In order to achieve the desired balance between these processes, there are several parameters that need to be considered.

One such parameter is the flow rate of the precursor gas. If it is too low, the broken molecules on the surface will not be replaced fast enough and ions will frequently impact the surface when there is no precursor. When that happens, the milling will counteract the deposition. If the flow is too high, not only is a large fraction of the gas wasted, the probability of unintended collisions above the substrate is also increased. Essentially, the flow rate needs to be balanced with the ion current. A larger current can make the deposition faster, but only if there is enough precursor present on the substrate.

Another key parameter is the acceleration voltage. It needs to be high enough that the precursor molecules are effectively broken, but not so high as to damage the substrate below. Other parameters are less straightforward to understand, such as the way the ion beam is scanned over the substrate. The scanning speed, direction and pattern all matter. As does the dwell-time, the time that the ion beam spends in one spot, and the overlap between each spot. Furthermore, each parameter can not only affect the deposition rate, but also the properties of the deposited film, such as its composition and conductivity.

Films deposited by FIB are often not very pure. Usually, they contain a large percentage of undesirable elements. Most commonly, the materials get polluted by carbon atoms that come from the precursor molecules. Those molecules consist of typically large organic groups in addition to the material that is to be deposited. Additionally, the ions themselves can also contaminate the deposition. As the material is being bombarded by gallium ions, the chance of those ions being implanted is not negligible. When depositing platinum using the precursor $(CH_3)_3Pt(CpCH_3)$, for example, the composition of the deposit has been reported to be about 60-70% carbon, 10% gallium and only 20-30% platinum [15].

References

[1] T. Amano, Y. Nishiyama, H. Shigemura, et al. *Proceedings of SPIE*, 7379(73792L), 2009.

[2] L. A. Giannuzzi and F. A. Stevie. *Micron*, 30:197–204, 1999.

[3] J. M. Zajac and W. Langbein. *Physical Review B*, 86(195401), 2012.

[4] H. C. Mogul, A. J. Steckl, Gyles Webster, M. Pawlik, and S. Novak. *Applied Physics Letters*, 61(5):554–556, 1992.

[5] J. R. Memon, G. Z. Memon, P. J. Heard, K. R. Hallam, and G. C. Allen. *Pakistan Journal of Analytical and Environmental Chemistry*, 16(1):24–30, 2015.

[6] E. Lamers, X. F. Walboomers, M. Domanski, et al. *Tissue Engineering Part C-Methods*, 17(1), 2011.

[7] G. Knott, H. Marchman, D. Wall, and B. Lich. *Journal of Neuroscience*, 28(12):2959–2964, 2008.

[8] P. Cheng, H. Yang, Y. Jia, et al. *Physical Review B*, 78(134508), 2008.

[9] J. Jaroszynski, F. Hunte, L. Balicas, et al. *Physical Review B*, 78(174523), 2008.

[10] P. J. W. Moll. *The role of anisotropy in iron-pnictides addressed by focused ion beam sample fabrication.* Phd thesis, ETH Zurich, 2012.

[11] P. J. W. Moll, P. Kushwaha, N. Nandi, B. Schmidt, and A. P. Mackenzie. *Science*, 351(6277), 2016.

[12] L. A. Giannuzzi and F. A. Stevie. *Introduction to Focused Ion Beams: Instrumentation, Theory, Techniques and Practice.* Springer, New York, 2005.

[13] Z. M. Wang. *FIB Nanostructures*, volume 20 of *Lecture Notes in Nanoscale Science and Technology.* Springer, 2013.

[14] W. Siemons, C. Beekman, J. D. Fowlkes, et al. *APL Materials*, 2(022109), 2014.

[15] J. M. De Teresa, R. Córdoba, A. Fernández-Pacheco, et al. *Journal of Nanomaterials*, 2009(936863), 2009.

APPENDIX B

Lifshitz-Kosevich equation

The Lifshitz-Kosevich (LK) equation describes the amplitude, $A(B)$, of the p^{th} harmonic of a certain quantum oscillation of frequency F (where $F = (\hbar/2\pi e)A_F$, with A_F the area of Fermi surface encircled by the orbit) as a function of the magnetic field B. It is equally applicable to both Shubnikov-de Haas oscillations in the magnetoresistance (after subtraction of a smooth background) and de Haas-van Alphen oscillations in the magnetization, as well as to other quantum oscillatory phenomena. For a system with multiple frequencies, a sum over all frequencies of the LK equation gives a valid description. The LK equation has the following form [1, 2]:

$$A(B) = A_0\sqrt{B}R_sR_TR_D\cos\left[2\pi p\left(\frac{F}{B} - \gamma - \delta\right)\right], \tag{B.1}$$

with $\gamma = 1/2 - \Phi_B/2\pi$, where Φ_B is the Berry phase [3]. The value of δ is $\pm1/8$ for a 3D system, with the sign depending on whether the oscillation arises from a maximal($-$) or minimal($+$) extremal cross-section of the Fermi surface. It is possible to extract Φ_B from experimental data either through direct fitting, or by making a Landau level fan diagram.

R_T is the temperature damping factor:

$$R_T = \frac{p\alpha Tm^*/B}{\sinh\left(p\alpha Tm^*/B\right)}, \tag{B.2}$$

R_D the Dingle factor:

$$R_D = \exp\left(-\frac{p\alpha T_D m^*}{B}\right) \tag{B.3}$$

and R_s the spin-splitting factor:

$$R_s = \cos\left(\frac{p\pi g m^*_{spin}}{2m_e}\right). \tag{B.4}$$

In each of these equations m^* is the effective cyclotron mass, which is often expressed in terms of m_e, the free electron mass. Eq. B.2 is often employed to determine m^* based on experimentally determined oscillation amplitudes at different temperatures. m^* is related the energy derivative of the Fermi surface area as follows:

$$m^* = \frac{\hbar^2}{2\pi} \frac{d}{dE} A_F. \tag{B.5}$$

Eq. B.3 accounts for a reduction in amplitude due to electron scattering causing a broadening of the Landau levels. The effect on the amplitude is similar to that of an increase in temperature from the true temperature [1, 4]. This additional temperature is T_D.

For both Eq. B.2 and Eq. B.3, the following simplification was used:

$$\alpha = \frac{2\pi^2 k_B}{e\hbar}. \tag{B.6}$$

For practical purposes, this can be further simplified using $\alpha m_e = 14.69$ while writing m^* as a fraction of m_e.

Eq. B.2 is often used independent from Eq. B.1 in order to determine the effective mass. In that case, all parameters other than the temperature are considered constant and the equation is fit to experimental data of the oscillation amplitude. Ideally, this should be done by identifying a single period of a particular oscillation from the raw data (after subtraction of the non-oscillatory background) and following its amplitude in temperature. However, in multi-frequency systems, this is near impossible to do and instead the FFT amplitude related to the frequency of interest needs to be used. In that case, it is important to choose a field range ($B_{min} \leq B \leq B_{max}$) for the FFT in which the oscillation is always present and replace the magnetic field in Eq. B.2 with an appropriate average, $\overline{B}$, defined as follows:

$$\frac{1}{\overline{B}} = \frac{1}{2} \left(\frac{1}{B_{max}} + \frac{1}{B_{min}} \right). \tag{B.7}$$

The average has to be taken over the inverse of the magnetic field, as the oscillations are periodic in $1/B$.

In Eq. B.4, g is the g-factor. The reduction factor R_s arises from the energy difference between spin-up and spin-down electrons, as the spin degeneracy is lifted in a magnetic field [5, 6]. Spin-splitting can under the right circumstances be observed as a splitting of the magnetic oscillations close to the quantum limit, but more commonly leads only to reduction of the amplitudes according to Eq. B.4.

An additional damping factor is added to the LK equation in the case of magnetic breakdown, that is:

$$R_b = l(ip_t)^{n_t} p_r^{n_r}, \tag{B.8}$$

with $n_t(p_t)$ the number(probability) of tunneling events, $n_r(p_r)$ the number(probability) of reflections and l the degeneracy of the orbit. This factor describes the reduction in amplitude of a certain breakdown orbit depending on its probability. For the probability, we have:

$$p_t \propto e^{B_0/B}, \tag{B.9}$$

with the breakdown field, $B_0 \propto k_g^2$ and k_g the size of the tunneling gap in reciprocal space.

References

[1] D. Shoenberg. *Magnetic Osillation in metals.* Cambridge University Press, 1984.

[2] I. Lifshitz and A. Kosevich. *Sov. Phys. JETP*, 2(4):636, 1956.

[3] M. V. Berry. *Proceedings of the Royal Society A*, 392(1802):45–57, 1984.

[4] R. B. Dingle. *Proceedings of the Royal Society A*, 211(1107):517, 1952.

[5] E. H. Sondheimer and A. H. Wilson. *Proceedings of the Royal Society A*, 210(1101):173, 1951.

[6] R. B. Dingle. *Proceedings of the Royal Society A*, 211(1107):500, 1952.

APPENDIX C

Fast Fourier Transform

Throughout this thesis, a large number of Fast Fourier Transforms (FFTs) is performed in the analysis of quantum oscillations. Often, the interpretation crucially depends on the accuracy of the resulting FFT spectra. It is important, therefore, to optimize the FFT procedure for each case, so that the spectrum has both the highest resolution and the greatest accuracy.

C.1 Field range and interpolation

In our case, an important consideration when taking an FFT is which field range from the original dataset to use. Typically, certain frequencies do not exists over the whole dataset, but they only start beyond a certain field. For certain applications (such as determining an effective mass), it is important not to include any data in the FFT that does not include the relevant frequency. In other cases, however, including more data is actually desirable as it can lead to a higher resolution. Data collected at very low magnetic fields before oscillations set in, is typically very noisy and should thus not be included in the FFT.

For each application in this thesis, we choose the magnetic field range such that the resulting FFT is optimized for the particular feature we are studying. Over the chosen range, we then interpolate the data in order to generate equally spaced data-points for the FFT (as the measurements are done as a function of B, the relevant spacing in $1/B$ is normally not equal). In this interpolation, a large enough number of points needs to be used to avoid aliasing. Aliasing occurs when the data is sampled at a rate that is less than twice the highest frequency present in the signal. Additional, non-physical, frequencies could be generated due to aliasing.

C.2 Window functions

When performing an FFT, there is the implicit assumption that the dataset is finite and its two endpoints are interpreted as if they are connected. When an integer number of periods of a periodic signal fill the dataset, this assumption is correct and the FFT will work well. Typically, however, this is not the case and a discontinuity occurs in the signal that is being transformed. This discontinuity appears in the FFT as additional frequencies. The resulting spectrum is then not the real spectrum of the dataset, but a smeared out version.

A way to mitigate this effect, is windowing. Essentially, the dataset is multiplied by a window function (WF) with a smoothly varying amplitude that tends to zero at the edges. In this way, the endpoints of the dataset are connected and no more discontinuity takes place. A large number of different WFs exists, and is useful for different applications.

After windowing, a certain frequency in the signal will usually appear in FFT as a large peak centered around this frequency, with progressively smaller peaks (side lobes) beside it on both sides. Depending on which WF is used, a different balance is struck between the amplitude and width of the main peak, and those of the side lobes. Lower side lobes lead to a reduced leakage of amplitude from the main peak, but may also increase its bandwidth.

For each series of FFTs done in this thesis, several WFs are tested before choosing one, in order to see which one gives us the best resolution. We judge the accuracy of the resulting spectrum by comparing spectra made with different window functions, and seeing which features are reproducible in all spectra. Examples of this are shown in Fig. C.1. The conclusions of these tests often differ for different situations, such as for the low and high frequencies seen in ZrSiS and HfSiS. For example, the rectangular window (which is essentially the same as no window), usually gives unreliable results for the low frequencies, but actually works well for the high ones. In those cases that different spectra are directly compared, for example when studying a temperature or angle dependence, we naturally always use the same window for each of those spectra.

We have tested seven different windows, which can be divided into three groups. Within each group, the different WFs give nearly identical results. The Hanning, Welch and rectangle windows shown in Fig. C.1 represent these three groups. In Fig. C.1(a), we show a comparison between different WFs for frequencies up to 1000 T (in this case for SdH data on ZrSiS). Most of the frequencies are reproduced for each WF, but the rectangle window has a higher overall noise level, while the Hanning window has quite low amplitude for certain peaks. The Welch window is a good compromise between the two and is therefore used for low frequencies in most cases throughout this thesis.

When looking at high frequencies (Fig. C.1(b)), the situation is somewhat different. In this case, the group of frequencies around 11 kT is suppressed when using Hanning, while the 8-9 kT group is comparable between the different functions. The rectangular window results in the highest amplitude of the main frequencies in the 11 kT group and is therefore the most useful in this situation.

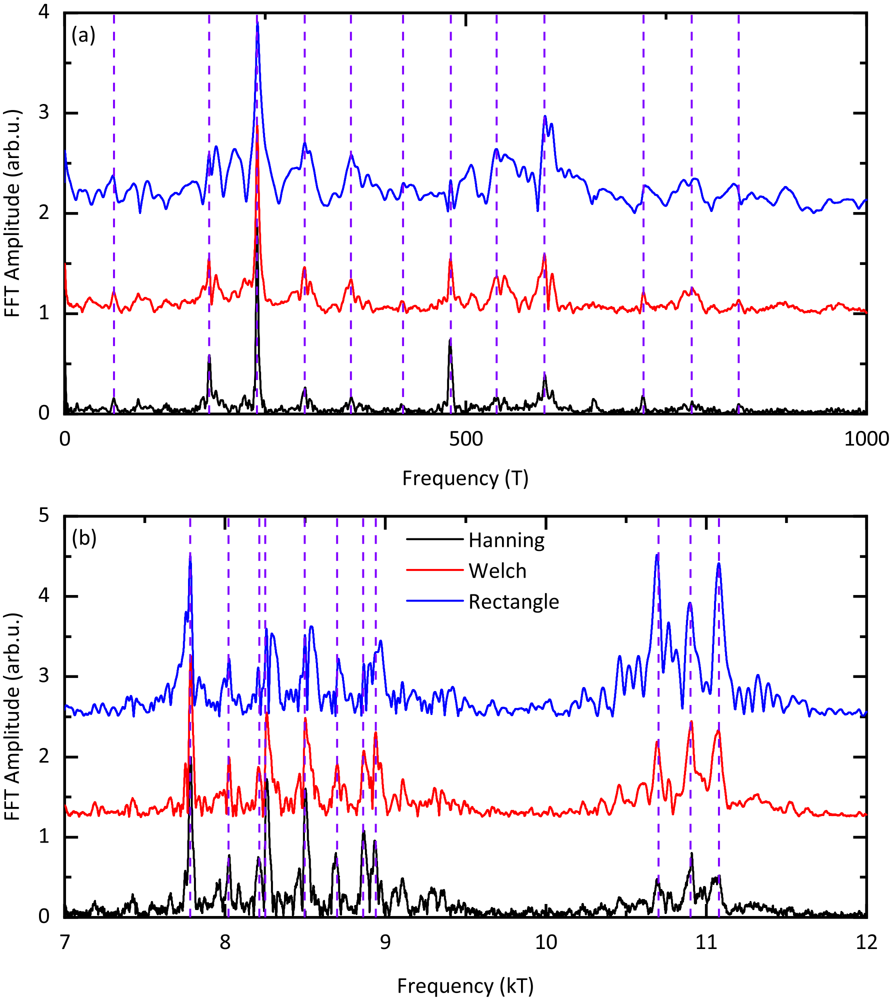

Figure C.1: *Comparison of different window functions for (a) low frequencies and (b) high frequencies. Purple dashed lines indicate main peaks seen with each WF.*

C.3 Zero padding

One way to increase the number of points in an FFT spectrum, is zero padding. In order to do this, one simply adds a number of zeros to the dataset. The advantage of doing this, is that it leads to more frequency bins in the FFT spectrum. That is, essentially, more points. This is often very helpful especially in the low-frequency parts of our FFT spectra, where otherwise there is a very low density of points and important peaks may be represented by only two or three points. Using zero padding, our spectrum appears smoother and we can see the shape of peaks and separate closely spaced frequencies. However, zero padding in principle adds no additional information and it is typically not useful for high frequencies.

C.4 Uncertainty in the amplitude

In order to calculate an effective mass for a certain frequency seen in the FFT spectrum, a fit of the amplitude as a function of temperature can be made using the Lifshitz-Kosevich equation (see Appendix B). There are, however, a number of factors causing uncertainty in these amplitudes, and therefore in the determined effective masses. The main contribution that can lead to a large error, is leakage of amplitude from other peaks in the FFT spectrum, close to the one of interest. The FFT spectra based on different configurations tend to reproduce the same peaks, but the relative amplitude varies considerably. Because of this, it may happen that in the spectrum of one sample, a certain peak is very well resolved, while in another sample, a nearby peak is much larger. Side-peaks of this large peak can then add up with the first peak, causing a large error in the amplitude determination. In some cases, it is not even possible to determine a mass. Other sources of uncertainty are the noise level in the FFT, affecting mainly those peaks with very low amplitude.

Aside from errors in the FFT amplitudes, there is an additional contribution to the uncertainty of the mass, arising from the LK fitting procedure. This is an inherent (typically small) error in calculating the fit parameters, depending on the number of points and their spread. The numbers reported for effective masses throughout this these come with estimates of the total uncertainty caused by all of these factors.

List of publications

S. Pezzini*, **M. R. van Delft*** (*contributed equally), L. M. Schoop, B. Lotsch, A. Carrington, M. I. Katsnelson, N. E. Hussey and S. Wiedmann. *Unconventional mass enhancement around the Dirac nodal loop in ZrSiS.* Nature Physics 14:178–183 (2018)

M. R. van Delft, S. Pezzini, T. Khouri, C. S. A. Müller, M. Breitkreiz, L. M. Schoop, A. Carrington, N. E. Hussey and S. Wiedmann. *Electron-hole tunneling revealed by quantum oscillations in the nodal-line semimetal HfSiS*, Physical Review Letters 121:56602 (2018)

M. R. van Delft, S. Pezzini, M. König, P. Tinnemans, N. E. Hussey and S. Wiedmann. *Surface and bulk superconductivity at ambient pressure in the Weyl semimetal TaP*, under review

C. Q. Xu*, B. Li*, **M. R. van Delft*** (*contributed equally), W. H. Jiao, W. Zhou, B. Qian, N. D. Zhigadlo, D. Qian, R. Sankar, F. C. Chou, N. E. Hussey and X. Xu. *Extreme magnetoresistance and pressure-induced superconductivity in the topological semimetal candidate YBi*, Physical Review B 99:024110 (2019)

M. R. van Delft, C. S. A. Müller, T. Khouri, S. Pezzini, M. Breitkreiz, L. M. Schoop, A. Carrington, N. E. Hussey and S. Wiedmann. *De Haas-van Alphen oscillations due to magnetic breakdown in ZrSiS*, in preparation

M. Shahrokhvand, S. Pezzini, **M. R. van Delft**, U. Zeitler, N. E. Hussey and S. Wiedmann. *Bulk and in-gap states in SmB_6 revealed by high-field magnetotransport.* Physical Review B 96:205125 (2017)

J. Lu, X. Xu, M. Greenblatt, R. Jin, P. Tinnemans, S. Licciardello, **M. R. van Delft**, J. Buhot, P. Chudzinski and N. E. Hussey. *Emergence of a real-space symmetry axis in the magnetoresistance of $Li_{0.9}Mo_6O_{17}$*, under review

W. Zhou, B. Li, C. Q. Xu, **M. R. van Delft**, Y. Chen, X. C. Fan, B. Qiang, N. E. Hussey and X. Xu, *Nonsaturating magnetoresistance and nontrivial band topology of type-II Weyl semimetal $NbIrTe_4$*, under review

Curriculum vitae

Name: Maarten van Delft
Place of birth: ‘s-Hertogenbosch
Data of birth: 7th June 1991

2003-2009: Preparatory Scientific Education (VWO) at the Willem van Oranje College in Waalwijk, the Netherlands

2009-2012: Bachelor of Science in Applied Physics at the Eindhoven University of Technology in Eindhoven, the Netherlands

2012-2014: Master of Science in Applied Physics at the Eindhoven University of Technology, in Eindhoven, the Netherlands

2014-2018: PhD researcher at the High Field Magnet Laboratory in Nijmegen, the Netherlands